https://doi.org/10.15388/vu.thesis.286
https://orcid.org/0000-0003-1432-3866

VILNIUS UNIVERSITY
CENTER FOR PHYSICAL SCIENCES AND TECHNOLOGY

Simonas
RAMANAVIČIUS

Formation, modification and new applications of orderly structured titanium oxide nanostructures

DOCTORAL DISSERTATION

Natural sciences,
Chemistry (N 003)

VILNIUS 2022

This dissertation was written between 2017 and 2021 in Center for Physical Sciences and Technology.
The research was supported by Research Council of Lithuania.
Stipends – P-DAP-19-342; P-DAP-20-370; P-DAP-21-299
Mobility funding – 09.3.3.-LMT-K-712-13-0298; 09.3.3.-LMT-K-712-21-0091; P-DAK-19-198; P-DAK-20-99.

Academic supervisor:
dr. Arūnas Jagminas (Center for Physical Sciences and Technology, Natural Sciences, Chemistry, N 003).

This doctoral dissertation will be defended in a public meeting of the Dissertation Defence Panel:

Chairman – prof. habil. dr. Aivaras Kareiva (Vilnius University, Natural Sciences, Chemistry, N 003).

Members:
doc. dr. Renata Butkutė (Center for Physical Sciences and Technology, Natural Sciences, Physics, N 002).
prof. dr. Vytautas Getautis (Kaunas University of Technology, Natural Sciences, Chemistry, N 003).
habil. dr. Zenonas Jusys (Ulm University, Natural Sciences, Chemistry, N 003).
prof. habil. dr. Rimantas Ramanauskas (Center for Physical Sciences and Technology, Natural Sciences, Chemistry, N 003).

The dissertation shall be defended at a public meeting of the Dissertation Defence Panel at 2 p. m. on 25th February 2022 in meeting room D401 of the Center for Physical Sciences and Technology.

Address: Saulėtekio av. 3, D 401, Vilnius, Lithuania
Tel. +37052648884; e-mail: office@ftmc.lt

The text of this dissertation can be accessed at the libraries of Center for Physical Sciences and Technology and Vilnius University, as well as on the website of Vilnius University: *www.vu.lt/lt/naujienos/ivykiu-kalendorius*

https://doi.org/10.15388/vu.thesis.286
https://orcid.org/0000-0003-1432-3866

VILNIAUS UNIVERSITETAS
FIZINIŲ IR TECHNOLOGIJOS MOKSLŲ CENTRAS

Simonas
RAMANAVIČIUS

Tvarkios struktūros titano oksido nanodarinių formavimo, modifikavimo ir naujų taikymų paieška

DAKTARO DISERTACIJA

Gamtos mokslai,
Chemija (N 003)

VILNIUS 2022

Disertacija rengta 2017 – 2021 metais Fizinių ir technologijos mokslų centre.
Mokslinius tyrimus rėmė Lietuvos mokslo taryba:
Stipendijos – P-DAP-19-342; P-DAP-20-370; P-DAP-21-299
Parama išvykoms – 09.3.3.-LMT-K-712-13-0298; 09.3.3.-LMT-K-712-21-0091; P-DAK-19-198; P-DAK-20-99.

Mokslinis vadovas:
dr. Arūnas Jagminas (Fizinių ir technologijos mokslų centras, gamtos mokslai, chemija, N 003).
Gynimo taryba:
Pirmininkas – prof. habil. dr. Aivaras Kareiva (Vilniaus universitetas, gamtos mokslai, chemija, N 003).
Nariai:
doc. dr. Renata Butkutė (Fizinių ir technologijos mokslų centras, gamtos mokslai, fizika, N 002).
prof. dr. Vytautas Getautis (Kauno technologijos universitetas, gamtos mokslai, chemija, N 003).
habil. dr. Zenonas Jusys (Ulmo universitetas, gamtos mokslai, chemija N 003).
prof. habil. dr. Rimantas Ramanauskas (Fizinių ir technologijos mokslų centras, gamtos mokslai, chemija, N 003).

Disertacija ginama viešame Gynimo tarybos posėdyje 2022 m. vasario mėn. 25 d. 14 val. Fizinių ir technologijos mokslų centro D 401 auditorijoje.

Adresas: Saulėtekio al. 3, Vilnius, Lietuva tel. +37052648884; el. paštas: office@ftmc.lt.

Disertaciją galima peržiūrėti Fizinių ir technologijos mokslų centro bei Vilniaus universiteto bibliotekose ir VU interneto svetainėje adresu: *https://www.vu.lt/naujienos/ivykiu-kalendorius*

Acknowledgments/Padėka

Studijų metu sutikti profesoriai, mokslų daktarai ir doktorantai, kiti kolegos negailėdami savo laiko stengėsi išaiškinti man kilusius klausimus ir vienaip ar kitaip prisidėjo prie galutinio šios disertacijos varianto. Nuoširdžiai jiems dėkoju.

Nuoširdus ačiū savo moksliniam darbo vadovui dr. Arūnui Jagminui už visokeriopą pagalbą, palaikymą, padrąsinimą, nuoširdumą žmogiškumą, ir galimybę iš arčiau susipažinti su nanotechnologijomis ir jų praktiniu taikymu.

Širdingas ačiū visiems savo kolegoms – už draugiškumą ir pagalbą visais gyvenimo klausimais, už vertingus patarimus, ir moralinį palaikymą. Ačiū visiems Nanostruktūros laboratorijos kolegoms už žinias ir palaikymą.

Nuoširdus ačiū Vidui, Vitalijai, Arnui, Sonatai, Mantui už atliktus XRD, XPS, SEM, SERS, EPR tyrimus bei pagalbą analizuojant gautus duomenis.

Ačiū mamai ir tėčiui, už motyvaciją visada siekti daugiau.

Abbreviations

SERS – surface enhanced Raman spectroscopy
SEM – scanning electron microscopy
FIB – focus ion beam system
EDX – energy dispersive X-ray analysis
CCD – charged-coupled device
XRD – X-ray diffraction
EMA – effective Medium Approximation
XPS – X-ray photoelectron spectroscopy
EPR – electron paramagnetic resonance spectroscopy
DFT – density functional theory
VOC – volatile organic compound
PPy – polypyrrole
PANI – polyaniline
DNA – deoxyribonucleic acid
DCT – direct charge transfer
CEM – chemical enhancement mechanism
EEM – electromagnetic enhancement mechanism
GCE – glassy carbon electrode
HER – hydrogen evolution reaction
MXenes - ($Ti_3C_2T_x$) „accordion-like“ structures
QDs – quantum dots

CONTENTS

INTRODUCTION

To date, a lot of studies and practical applications of titanium dioxide (TiO_2) was done. However, there is a need for extended applications of these materials and the limiting factor here is material properties [1]. To extend titanium dioxide properties, one of the strategies is the formation of various non-stoichiometric titanium oxides (TiO_{2-x}) and Magnéli phases (Ti_nO_{2n-1})-based structures [2]. As well, more and more studies coming out with a new class of titanium carbides ($Ti_3C_2T_x$) so-called „MXenes“ as it is known that these structures have interesting but still unexploited optical properties which rely on Ti^{3+} and its oxides formed in the structures [3]. The main problem for the formation of such structures is the stabilization during formation. In this study, attention is paid towards the formation of various nanostructured stoichiometric titanium dioxide (TiO_2), non-stoichiometric titanium oxide (TiO_{2-x}) and Magnéli phase (Ti_nO_{2n-1})-based structures which are suitable for applications as optically active materials, sensing materials or components for heterostructures formation [2, 4].

Stoichiometric TiO_2 is n-type semiconducting material and exist in three main solid phases (anatase, rutile and brookite); therefore, for applications in sensorics during the formation of sensing layer phase transformations are very often exploited to modify the sensitivity and selectivity of formed TiO_2 layers [5]. In addition to stoichiometric TiO_2, recently, various nanostructured non-stoichiometric titanium oxides, which by different authors are abbreviated as TiO_n, or TiO_{2-x} and Magnéli phases (Ti_nO_{2n-1}), have received significant attention in the development of various sensors [6].

In the case of gas sensors, the sensitivity of these sensors is high; however, the selectivity is still not sufficient, and in addition to that, some of them still have a rather high demand for electrical power due to the necessity to power heating element, which almost always is required for the achievement of high temperatures required for the efficient operation of gas and VOC sensitive semiconducting layer. Therefore, some strategies were developed to overcome drawbacks: (i) the possibility to apply the ‘self-heating’ mode in some gas and VOC sensors [7]; (ii) the engineering of advanced morphology, which offers better selectivity [8]; (iii) the formation of core-shell structures [9], e.g. quantum dots [10], where a core-forming material is covered by a shell of a particular material, which elicits advanced properties of the resulting hybrid sensing structure [11].

Recent progress in the formation of optically active titanium carbides ($Ti_3C_2T_x$) so-called MXenes encourage applications of these new 2D materials in the design of biosensors, biofuel cells and bioelectronics and some breakthrough in these areas are foreseen. Advantageous properties of MXenes are suitable for biosensing applications but it is not the limitation. The other important property of MXenes is their high and near metallic conductivity altered by their surface termination groups [12], leading to a possible application as supercapacitors [13], resistive sensors [14] and other applications in electrochemistry [15], electronics [16]. As a result of the relatively high concentration of free electrons, the plasmonic effect of MXenes reclassifies these materials into a class of metals because the plasmon frequency depends on the density of free electrons [17]. For this reason, MXenes might be used as a substitute for metallic nanostructures with the ability to enhance internal vibrations of molecules at near proximity as is in surface-enhanced Raman spectroscopy (SERS) [18].

Major goal

To synthesize narrow bandgap titanium oxide based nanostructures, characterize and investigate their possible applications.

Objectives

- ✓ To synthesize narrow bandgap titanium suboxide thin films and particles via hydrothermal synthesis method with further annealing in an oxygen-free atmosphere.
- ✓ To synthesize MXenes (Ti_3C_2) structures in a diluted hydrofluoric acid aqueous solution from Ti_3AlC_2 precursor.
- ✓ To characterize titanium suboxide and MXenes (Ti_3C_2) structures.
- ✓ To find applications for designed TiO_x and MXenes structures in sensorics and catalysis.

Scientific novelty

- ✓ It was first time determined that hydrothermal synthesis and subsequent calcination under oxygen-free atmosphere allow the formation of high surface area titanium suboxide nanostructures with controllable surface morphology, phase composition and bandwidth.
- ✓ For the first time, it was shown that hydrothermally formed titanium suboxides with high porosity and surface area could be used as substrates for nanoplatelet MoS_2-based electrocatalysts fabrication and application for a hydrogen evolution in acidic solutions. It was determined that

electrocatalysts formed on titanium suboxide substrates are more stable than those formed directly on metal substrates.

- ✓ For the first time, it was shown that titanium suboxide-based gas sensors are suitable not only for the determination of organic volatile compounds but as well can heat itself and reach high operating temperatures.
- ✓ For the first time, surfaces suitable for the detection of salicylic acid by enhanced Raman spectroscopy were formed from Ti_3C_2 Mxenes

Statements of defence

- ✓ Hydrothermal method in an alkaline selenious acid solution is suitable for the formation of nanoplatelet morphology titanium suboxide nanostructures on titanium surface.
- ✓ Titanium suboxides nanostructures hydrothermally formed in selenious acid alkaline solution possess high porosity and narrow bandgap in comparison to other titanium oxides.
- ✓ Titanium substrates with non-stoichiometric oxides on top are suitable for the formation of MoS_2 based electrocatalyst for a hydrogen evolution reaction.
- ✓ MXenes ($Ti_3C_2T_x$) „accordion-like“ structures might be obtained from its precursor of Ti_3AlC_2 after selective etching in a diluted hydrofluoric acid solution.
- ✓ Titanium suboxide and MXenes ($Ti_3C_2T_x$) structures could be used in the formation of various sensors.
- ✓ Substrates made from MXenes ($Ti_3C_2T_x$) structures could be used for the detection of salicylic acid by surface enhanced Raman spectroscopy.

Contribution of the author

All structures were fabricated, fractioned and collected by the author of this dissertation. The author also conducted the preparation of the samples for SEM, TEM, XPS, EPR and Raman spectroscopy analysis. Furthermore, the author took part in the analysis of experimental results, design of graphical illustration and preparation of scientific publications. Additionally, the obtained results were referenced by the author in numerous international conferences and, of course, the author wrote this dissertation himself. All non-original works are referenced.

Publications

The main results of the doctoral thesis were published in 6 scientific publications (P: 1-6) and 19 conference reports (C: 1-19).

Scientific publications

P1. Arunas Jagminas., **Simonas Ramanavicius**, Vitalija Jasulaitienė , Mantas Šimėnas, "Hydrothermal synthesis and characterization of nanostructured titanium monoxide films", *RSC Advances*, 2019, *9*, 40727; https://doi.org/10.1039/C9RA08463K

P2. Arunas Jagminas, Arnas Naujokaitis, Paulius Gaigalas, **Simonas Ramanavicius**, Marija Kurtinaitiene, Romualdas Trusovas, Substrate Impact on the Structure and Electrocatalyst Properties of Molybdenum Disulfide for HER from Water, *Metals* 2020, *10*, 1251; https://doi.org/10.3390/met10091251

P3. **Simonas Ramanavicius**, Alla Tereshchenko, Renata Karpicz, Vilma Ratautaite, Urte Bubniene, Andrius Maneikis, Arunas Jagminas, Arunas Ramanavicius A. "TiO_{2-x}/TiO_2-Structure Based 'Self-Heated' Sensor for the Determination of Some Reducing Gases", *Sensors* 2020, *20*, 74; https://doi.org/10.3390/s20010074

P4. **Simonas Ramanavičius**, Arūnas Ramanavičius, Insights in the Application of Stoichiometric and Non-Stoichiometric Titanium Oxides for the Design of Sensors for the determination of Gases and VOCs (TiO_{2-x} and Ti_nO_{2-n} vs. TiO_2), *Sensors* 2020, *20*(23), 6833; https://doi.org/10.3390/s20236833

P5. Sonata Adomavičiūtė-Grabusovė, **Simonas Ramanavičius**, Anton Popov, Valdas Šablinskas, Oleksiy Gogotsi, Arūnas Ramanavičius, Selective Enhancement of SERS Spectral Bands of Salicylic Acid Adsorbate on 2D $Ti_3C_2T_x$-Based MXene Film, Chemosensors 2021, *9(8)*, 223; https://doi.org/10.3390/chemosensors9080223

P6. **Simonas Ramanavičius**, Arūnas Ramanavičius, Progress and Insights in the Application of MXenes as New 2D Nano-Materials Suitable for Biosensors and Biofuel Cell Design, *Int. J. Mol. Sci.* 2020, *21*(23), 9224; https://doi.org/10.3390/ijms21239224

Other publications

O1. **Simonas Ramanavicius**, Milda Petruleviciene, Jurga Juodkazyte, Asta Grigucevičiene, Arunas Ramanavicius, Selectivity of Tungsten Oxide

Synthesized by Sol-Gel Method Towards Some Volatile Organic Compounds and Gaseous Materials in a Broad Range of Temperatures, *Materials* 2020, *13*, 523-539; https://doi.org/10.3390/ma13030523

O2. Milda Petruleviciene, Jurga Juodkazytė, Maliha Parvin, Alla Tereshchenko, **Simonas Ramanavicius**, Renata Karpicz, Urte Samukaite-Bubniene, Arūnas Ramanavicius, Tuning of photo-luminescence properties of WO3-based layers by the adjustment of layer formation conditions, *Materials* 2020, *13*(12), 2814; https://doi.org/10.3390/ma13122814

O3. **Simonas Ramanavicius**, Carla Bittencourt, Arnas Naujokaitis,Vidas Pakstas, Arunas Jagminas, Interfacing perovskite strontium molybdate tomolybdenum disulfide nanoplatelts for boosting HER from water, *International journal of hydrogen energy* 2021, *46*, 14359-14368.

O4. **Simonas Ramanavičius**, Arūnas Ramanavičius, Conducting Polymers in the Design of Biosensors and Biofuel Cells, *Polymers* 2021, *13*(1), 49; https://doi.org/10.3390/polym13010049

O5. **Simonas Ramanavičius**, Arūnas Ramanavičius, Charge Transfer and Biocompatibility Aspects in Conducting Polymer-Based Enzymatic Biosensors and Biofuel Cells, *Nanomaterials* **2021**, *11*(2), 371; https://doi.org/10.3390/nano11020371

O6. **Simonas Ramanavičius**, Arūnas Jagminas, Arūnas Ramanavičius, Recent advances in molecularly imprinted polymers based affinity sensors, *Polymers* 2021, *13(6)*, 974; https://doi.org/10.3390/polym13060974

O7. Eivydas Andriukonis, Raimonda Celiesiute-Germaniene, **Simonas Ramanavicius**, Roman Viter, Arunas Ramanavicius, From Microorganism-based Amperometric Biosensors towards Microbial Fuel Cells, *Sensors* 2021, *21*(7), 2442; https://doi.org/10.3390/s21072442

O8. Viktoriia Fedorenko, Daina Damberga, Karlis Grundsteins, Arunas Ramanavicius, **Simonas Ramanavicius**, Emerson Coy, Igor Iatsunskyi, Roman Viter, Application of Polydopamine Functionalized Zinc Oxide for Glucose Biosensor Design, *Polymers* 2021, *13(17),* 2918; https://doi.org/10.3390/polym13172918

Conference reports

C1. „10th Nano-conference „Current Trends in Electrochemistry and Material Science““, Vilnius, Lietuva. 2017.10.26, **Simonas Ramanavičius**, Arūnas Jagminas. „Synthesis of Differently Capped Superparamagnetic Cobalt Ferrite Nanoparticles and Its Application as Antibacterial Agents”.

C2. „PITTCON 2018”, Orlando, JAV, 2018.03.01, **Simonas Ramanavičius**, Arūnas Jagminas. „Synthesis of Titanium Oxide Layer on Titanium by Hydrothermal Method”.

C3. „Open Readings 2018” Vilnius, Lietuva, 2018.03.21, **Simonas Ramanavičius**, Arūnas Jagminas. „Titanium monoxide thin films formation by hydrothermal oxidation„.

C4. “NanoBio2018” Heraklionas, Graikija, 2018.09.26, **Simonas Ramanavičius**, Rokas Žalnėravičius, Arūnas Jagminas. „Shell-dependent antimicrobial efficiency of cobalt ferrite nanoparticles”.

C5. 77th International scientific conference program devoted to 100th anniversary of University of Latvia, Ryga, Latvija, 2019.02.08, **Simonas Ramanavičius**, Arūnas Jagminas. „A simple hydrothermal method for synthesis of titanium oxide with new properties”.

C6. ”1st INTERNATIONAL CONGRESS on ANALYTICAL and BIOANALYTICAL CHEMISTRY”, Antalija, Turkija, 2019.03.29, **Simonas Ramanavičius**, Arūnas Jagminas. „Synthesis of Advanced Titanium Oxide based Structures”.

C7. The 14th International School and Symposium on Synchrotron Radiation in Natural Science (ISSRNS’2019), Zakopanė, Lenkija, 2019.06.12, **Simonas Ramanavicius**, Arunas Jagminas. “Hydrothermal synthesis and characterization of molybdenum disulfide and strontium molybdate nanocomposite on titanium oxide substrates”.

C8. AAAFM-UCLA International Conference on Advances in Functional Materials, Los Angeles, JAV, 2019.08.22., **Simonas Ramanavicius**, Arunas Jagminas. „Titanium suboxides synthesis by direct oxidation method”.

C9. "3rd Global summit on Nanotechnology, NanoMedicine & Material science", Barselona, Ispanija, 2019.09.19, **Simonas Ramanavicius**, Arunas Jagminas. „Synthesis and advanced applications of TiOx based nanostructures“.

C10. 9-oji Fizinių ir technologijos mokslų centro (FTMC) doktorantų ir jaunųjų mokslininkų konferencija FizTeCh2019, Vilnius, Lietuva, 2019.10.24, **Simonas Ramanavičius**, Arūnas Jagminas. „Tvarkios struktūros titano oksido nanodarinių formavimo, modifikavimo ir naujų taikymų paieška“.

C11. The 78 th International Scientific Conference of the University of Latvia „LU78”, Ryga, Latvija, 2020.02.14, **Simonas Ramanavicius**, Alla Tereshchenko, Renata Karpicz, Vilma Ratautaite, Urte Bubniene, Andrius Maneikis, Arunas Jagminas, Arunas Ramanavicius, Roman Viter. „TiO 2-x /TiO 2 nanostructures formation and application in a gas sensing”.

C12. Nanostrucured Bioceramic Materials „NBCM2020”, Vilnius, Lietuva, 2020.12.03, **Simonas Ramanavicius**, Arūnas Jagminas, „Formation of Various TiO2-x nanostructures for Application in Biomedicine”.

C13. 2021 IEEE 11th International Conference on "Nanomaterials: Applications & Properties" (NAP-2021), Odessa, Ukraine, 2021.09.09, **Simonas Ramanavicius**, Alla Tereshchenko, Renata Karpic, Vilma Ratautaite, Urte Bubniene, Andrius Maneikis, Arunas Ramanavicius, Arunas Jagminas, „Titanium suboxide based self-heating gas sensor for detection of VOC's".

1. LITERATURE REVIEW

1.1. Titanium suboxides a new class of materials

Titanium dioxide, TiO_2, belongs to the group of materials that were most intensely investigated during the past three decades due to their unique optical, dielectric, catalytic properties, chemical resistance, mechanical hardness, nontoxicity and simple processing at a low cost. The crystalline forms of TiO_2-anatase, TiO_2-rutile and TiO_2-brookite polymorphs are well documented [1]. As it is known, anatase and rutile possess bandgap values of 3.23 eV and 3.02 eV, respectively, these materials are considered excellent optical absorbers for UV light [1]. These characteristics are successfully used in modern photocatalysis, solar cell devices [19], gas sensors [20], protective creams and multilayered coatings [1]. To tune the absorption edge of TiO_2 in the visible light region some most common techniques are used such as (I) the doping of titania with various elements both in the Ti and O sublattice positions [21], (II) hybridization of titania with lower bandgap semiconductor nanoparticles and quantum dots [22], (III) defective suboxides structures with a lack of oxygen formation [23].

The formation of nonstoichiometric semiconducting titanium oxides, namely titanium suboxides, are the freshest research direction to narrow titanium oxides bandgaps. These materials contain structural vacancies in both titanium and oxygen sublattices with a general formula Ti_nO_{2n-1}, where $n \geq 2$ [2].

1.2. Theoretical background for titanium dioxide and suboxide structures application in a gas sensing

The discovery of the semiconducting properties of TiO_2 facilitated the application of TiO_2 in the sensor design. Therefore, various TiO_2-based structures have been applied in chemical sensors [5, 24, 25] and even in biosensors [26, 27]. TiO_2 is a semiconductor of n-type [21] characterized by the charge mobility of 0.4 $cm^2/V\ s$ [28]. Three main phases of TiO_2 have different bandgaps: (i) 3.23 eV for anatase, (ii) 3.02 eV for rutile and (iii) 2.96 eV for brookite [29]. TiO_2 of all here mentioned phases can be simply formed and easily converted into any here mentioned form by annealing procedure. In addition to those three main phases, titanium oxide is forming various ‘non-stoichiometric’ structures e.g., TiO_{n-2} and/or TiO_n and so-called Magnéli phases, which have the formula Ti_nO_{2n-1}, where n = 4, ..., 10. The most nonstoichiometric structures of titanium oxide are exhibiting rather good electrical conductivity and possess sensing properties suitable for the development of gas VOC sensors [30]. Magnéli phases are very often advanced by a 'close neighbour' of the Magnéli phase titanium pentoxide (Ti_3O_5) with n = 3 for the formula of Ti_nO_{2n-1}. Titanium pentoxide is found in different polymorphic (α–, β–, γ–, δ–, and λ-forms) [31– 35] and it is sometimes mentioned as the very first Magnéli phase member because it has the stoichiometric chemical formula, which is consistent with Magnéli phase formula—Ti_nO_{2n-1} (where n = 3). Ti_3O_5 has a monoclinic crystal cell structure (with lattice constants of a = 9.9701 Å, b = 5.0747 Å, c = 7.1810 Å, β = 109.865°). Ti_3O_5 is exhibiting superconductivity at temperatures below 3 K, like some other Magnéli phases, e.g., Magnéli phase with n = 4 (Ti_4O_7) which is the 'most respectful' member of Magnéli phases [36]. Ti_4O_7 and other 'respectful' members of Magnéli phases in the crystal structure are having $TiO_{2(rutile)}$-based shear planes [37, 38], which is not the case for Ti_3O_5 [36]. Therefore, there is research where Ti_3O_5 and $TiO_{2(anatase)}$ were observed clearly without any signs of $TiO_{2(rutile)}$ in XRD-diffractograms [30]. It was reported that such Ti_3O_5 form of TiO_{2-x}/TiO_2-based heterostructures can be formed at a temperature of 400 °C, which is suitable for the formation of Ti_3O_5 with $TiO_{2(anatase)}$-intergrowths [39, 40] at very different formation conditions. The formation of the above-mentioned $TiO_{2(anatase)}$-intergrowths within Ti_3O_5 is valuable for the improvement of both electrical and optical sensing properties by the advancement of electrical conductivity and photoluminescence, which are enhanced by formed $TiO_{2(anatase)}$ [30]. However, despite clear advantages, the formation protocols of TiO_{2-x}/TiO_2- and Ti_nO_{2n-1}-based heterostructures are still not well elaborated and most of these structures tend to be oxidized in an air atmosphere at higher temperatures. Therefore, such challenges are important to be solved during further research on the development of TiO_{2-x}/TiO_2- and Ti_nO_{2n-1}-based heterostructures and some other materials suitable for the application in gas and VOC sensor design.

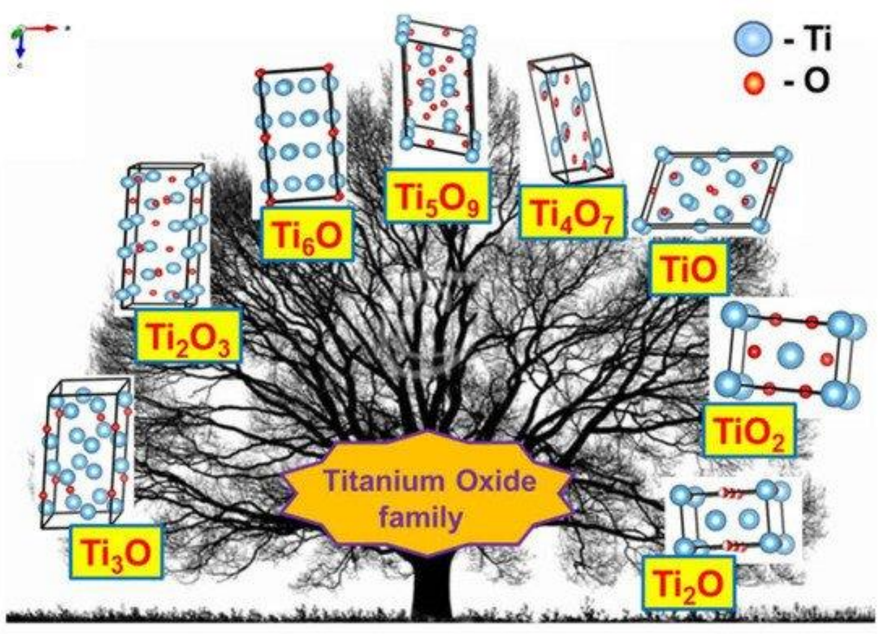

Figure 1. Crystal structures of various titanium oxides. Adapted from [2].

Table 1. Variation of the crystal structure of titanium oxides with O/Ti stoichiometry. Adapted from [2].

Compound	X in TiO_x	Structure
TiO_2	2	Rutile
$Ti_{10}O_{19}$	1.9	Anatase
Ti_9O_{17}	1.89	Triclinic
Ti_8O_{15}	1.875	Triclinic
Ti_7O_{13}	1.857	Triclinic
Ti_6O_{11}	1.833	Triclinic
Ti_5O_9	1.8	Triclinic
Ti_4O_7	1.75	Triclinic
γTi_3O_5	1.67	Monoclinic
Ti_2O_3	1.5	Tetragonal
TiO	1	Hexagonal Cubic Monoclinic
Ti_2O	0.5	Hexagonal
Ti	0	Hexagonal

1.3. Application of Stoichiometric TiO_2 in the Design of Gas and VOC Sensors

Gas and VOC sensors based on TiO_2 are cheap, easily developed. In these sensors rather basic analytical signal registration and assessment methods have been applied for the gas- and VOC-detection procedures. Some TiO_2-based sensors have rather good sensitivity towards various gaseous materials, which due to their different sensing mechanisms are divided into two major types: (i) reductive materials—H_2S, H_2, CO, NH_3, CH_3OH, C_2H_5OH, some other gasses and VOCs, (ii) oxidative gases—O_2, NO_2 and CO_2 [41–43]. It should be noted that resistivity- or current-based responses of TiO_2-sensors towards reductive or oxidative gaseous materials are opposite and, due to a rather low selectivity of sensing layers' analysis of gas and VOC mixtures, is still very complicated. Among many different options to measure analytical signals by semiconductor-based gas and VOC sensors, one of the simplest methods is to measure the electrical resistivity of the layer. Here, it should be noted that in order to increase the reliability of gas and VOC sensors in the analysis of gaseous compounds mixtures, in addition to basic resistivity measurements, it is reasonable to add some additional physicochemical methods, such as an evaluation of photoluminescence signals [30, 44, 45], which can be applied due to remarkable optical properties of a TiO_2 semiconductor [43]. It is worth noting that various TiO_2–based structures can be designed and enhanced by laser pulses, which improve the photocatalytic and photovoltaic performance of designed nano-structures [46].

1.4. Development of 'Hybridized' Heterostructures Based on TiO_2 and Application in the Design of Gas and VOC Sensors

Heterostructures based on TiO_2 are rather often applied in the design of gas and VOC sensors; among them, many different TiO_2-based heterostructures were investigated: V_2O_5/TiO_2 for chemi-resistive ozone sensors [47], TiO_2/perovskite heterojunctions for CO gas [48], TiO_2/(graphene-carbon)-based toluene VOC sensor operating at room temperature [49], TiO_2/SnO_2 for CO and NO_2 [50, 51], TiO_{2-x}/TiO_2-structure-based self-heated sensor for various reducing gases and VOCs [30]. A good demonstration of the improved gas-sensing performance of TiO_2 by graphene oxide (GO) was presented by Lee et al. [52] (Figure 2a,b), which was achieved by UV radiation. The authors claimed that n-n junction had been formed and proposed the band diagram of the GO/TiO_2, which represent an energetic diagram of the hetero-junction.

The authors also stated that in such a hetero-junction, the work function of GO was around 4.7 eV [53], which is higher than 4.4 eV, more typical for GO [54]. The accumulation and depletion layers were formed in this heterostructure [55] (Figure 2b), where, due to the establishment of the Schottky barrier, the depletion layer of TiO_2 became thicker, and for this reason, the electron number in GO interface increased. The main influence on the change of electrical resistance of this TiO_2/GO structure was induced by interaction of adsorbed VOC molecules on the oxygen-based GO functional groups. Moreover, negatively charged adsorbed oxygen molecules support the catalytic activity of TiO_2 by lowering the activation energy [56]. TiO_2 contributed to this heterostructure by its increased gas-adsorption sites and prevention of GO from agglomeration [57, 58]. Due to the above-mentioned properties, such a structure is sensitive to many reducing gasses, including ammonia gas. However, the active sites of GO were extremely sensitive to moisture, which increased resistance by the interaction of oxygen-based functional groups, such as hydroxyl, carboxylic and carboxyl [59]. This problem was solved by applying UV irradiation, which enabled the increase of both (i) the depletion layer of TiO_2 and (ii) the accumulation layer of GO (Figure 2c). Therefore, electrons were attracted to GO, where there are reduced oxygen-based groups, and in this way, moisture was removed [60]. The reduced GO formed, with TiO_2, a p-n junction, which had a decreased junction width at the interface (Figure 2d). Moreover, photolysis of TiO_2 led to the injection of electrons into GO, which prevented the recombination of electron-hole pairs [61]. Moreover, the amount of adsorbed oxygen decreased, which also reduced the adsorption of water [62]. The authors of [53] reported that the number of oxygen-based GO groups was partly restored by photocatalytic action of TiO_2, and these groups were suitable for the adsorption of reducing VOCs and remained sensitive for over the month.

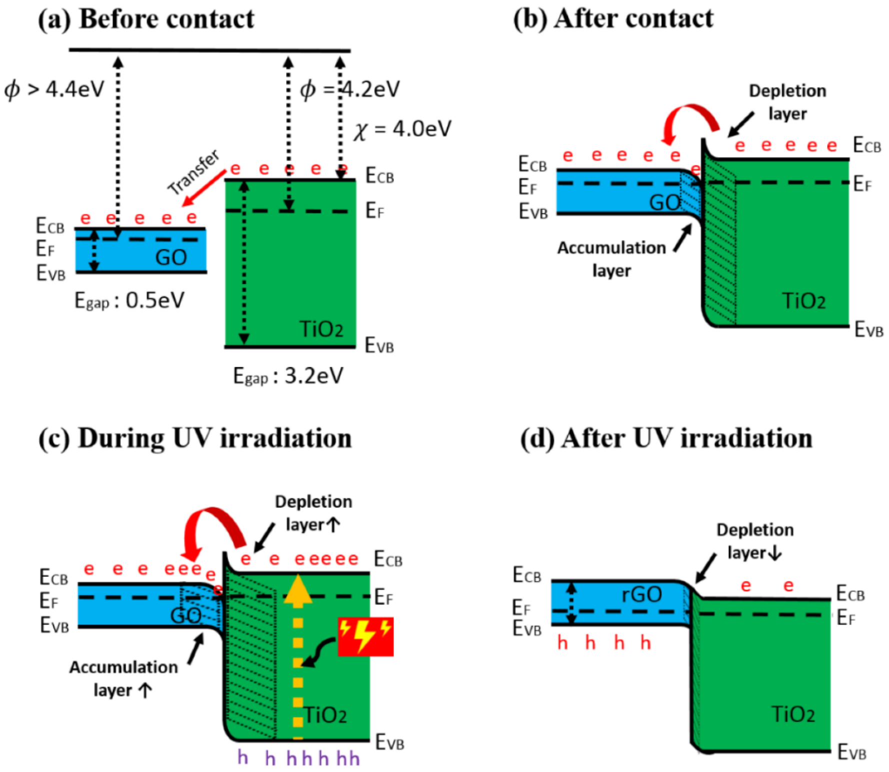

Figure 2. Band diagram of GO/TiO_2 composite (**a**) before contact, (**b**) after contact, (**c**) during UV irradiation, and (**d**) after UV irradiation. (e: electron, h: hole), adapted from [53].

TiO_2/SnO_2-based heterostructures also seem very attractive; due to the peculiarities of the energetic layers of molecular orbitals in TiO_2, the depletion of electrons is observed when it makes contact with SnO_2 [51]. Grains of some semiconductors and the most commonly used quantum dots, which are applied in forming the gas- and/or VOC-sensitive layer, are in the range of the Exciton Bohr radius; therefore, they have suitable physicochemical characteristics for the development of various gas and VOC sensors [10]. Therefore, advanced sensing properties can be established by small-grain-based structures [11]. SnO_2 is characterized by high charge-carrier mobility, which is critically important for the resistivity measurement-based gas and VOC sensors [52, 63]. In addition, SnO_2 is chemically stable, cheap and forms gas- and VOC-sensing layers; therefore, even in the pristine form it is used in various gas and VOC sensors [64]. However, gas- and VOC-sensing temperatures of pristine forms of TiO_2 and SnO_2 are rather high, e.g., for pristine SnO_2 QDs, it is 225 °C [10], but for some SnO_2-based core-shell structures (e.g., Au/SnO_2 [65]), these temperatures can be decreased down to 25–80 °C, which makes such structures attractive for real applications because enables to save a considerable amount of energy. Therefore, there are some expectations that formation of SnO_2 and TiO_2-based heterostructures will reduce the working temperature of gas and VOC sensors. In the formation of TiO_2/SnO_2 heterostructures dedicated for gas and VOC sensors, a variety of different nano-structures were developed: SnO_2-coated TiO_2 nanobelts [66], core-shell TiO_2/SnO_2 nanofibers [67], TiO_2-doped SnO_2 thick films [68], thin films based on layered SnO_2/TiO_2 structures [69], and SnO_2 nanoparticles covered by TiO_2 nanofibers [51]; SnO_2 QDs deposited a thin layer of TiO_2 [70]. In the previously mentioned research, both pristine and modified SnO_2 QDs were tested in gas and VOC sensors operating in two different modes: (i) at external heating and (ii) and at self-heating mode, while applying voltages in the range of 1–20 V. Optimal voltage was 20 V and these sensors were sensitive towards NO_2 and CO. The atomic layer deposition (ALD) method was applied to form TiO_2-based layers of precise thickness and the authors showed that the selectivity towards both gases and VOCs can be tuned by the variation of TiO_2 layer thickness, by the increase of TiO_2 up to 30 nm the best performance towards CO was yielded. Moreover, an anodic one-dimensional TiO_2 nanotube provided a large surface area and unidirectional electron transport pathway as a platform for the accommodation of thin SnO_2 coating, which was sensitive towards NO_2 [70].

Such a finding opens an avenue to tuning the selectivity of sensors based on TiO_2 layer-modified QDs by rather simple ‘morphology engineering’ procedures.

1.5. Strategies to Reduce Energy Consumption in Gas and VOC Sensors

One strategy to overcome high energy consumption is based on the reduction of the sensing element dimension; another one is based on the application of ‘low temperature’ sensors, which are operating at the temperature of the environment where target gases and VOCs are determined, while one additional recently emerging strategy relies on the possibility to apply so-called self-heating mode in some gas and VOC sensors [6, 29]. When the sensing layer has relatively low resistance, if sufficient voltage is applied to the sensing layer and the continuous transfer of charges along this layer is induced by this voltage, then some kinetic energy portion of these moving charges is converted into the heat due to interaction with various structural elements of the layer. Therefore, during this process, the generated heat can be exploited for the increase of sensing layer temperature. 'Self-heating' is beneficial in the application of TiO_{2-x}/TiO_2-based structures, because only at a temperature range of 72–180 °C has sufficient sensitivity of TiO_{2-x}/TiO_2-based heterostructure towards reducing gases and VOCs has been observed. Such a self-heating strategy reduces power consumption, increases the sensitivity of the sensor and minimizes the adsorption of water vapour, which is mostly present as moisture in the environment of interest, and at low temperatures may significantly decrease the sensitivity and selectivity of sensors towards gases and VOCs. Despite this fact, some researchers are searching for gas- and VOC-sensing materials, which are sensitive towards gases and VOCs at low temperatures [71].

Stoichiometric TiO_2-based structures have a rather high band-gap and, for this reason, they are not well conducting; therefore, it is not always easy to measure the electrical resistance of such layers and even elevation of temperature also does not always sufficiently increase the conductivity up to the suitable conductivity region. 'Self-heating' is also not possible if conductivity is low, because in order to get sufficient power, which will heat the sensor until it reaches a suitable temperature, very high voltages should be applied to the TiO_2-based structures.

Due to the suitable combination of chemical and semiconducting properties, TiO_2 has catalytic activity and even photocatalytic activity, both of which can be expressed by the 'water splitting ability' or 'oxidational activity'; these phenomena significantly strengthen when the sensing TiO_2 structure is irradiated by UV light [18, 72]. It was demonstrated that the pulsed laser modification can be successfully employed as a large-scale method enhancing the electronic properties of TiO_2 nanotubes. Such structure can contribute to the improved photocatalytic or photovoltaic performance of these TiO_2 nanotubes [73]. Therefore, the additional application of catalytic activity in TiO_2-based gas and VOC sensors is foreseen; however, it is still rarely exploited, due to significant complexity in the operation of such structures. TiO_2 has been used as a sensing material in room-temperature sensors for formaldehyde [73, 74], ozone [46], O_2 [69], CO [47], C_7H_8 [48], ethanol [66, 68, 75], H_2 [76, 77], and some other gases and VOCs [78].

However, at room temperature (25 °C), the operating sensors are sensitive towards humidity, which is present in the atmosphere. It should be noted that the analytical signals towards humidity and target-gases or VOCs can be very different, e.g., in the presence of humidity (water), the conductivity of the sensing layer increases, while the presence of the VOC conductivity of the sensing layer has decreased. Such a difference is observed due to different conductance mechanisms realized in the presence of water and the VOCs evaluated here. Water and VOCs adsorbed on the surface of the heterostructure tends to fill the 'gaps' between the TiO_{2-x} and/or TiO_2 grains and in such a way that it increases the conductivity of heterostructures, while the VOCs mostly have significantly lower conductivity compared with gas molecules that are replaced. In order to decrease sensitivity towards humidity, in most cases, the temperature of the sensing layer should be elevated over a room temperature, because the humidity at higher temperatures does not condense well on the sensing structure. An interesting UV irradiation-based approach to reduce the influence of humidity was demonstrated by Lee et al. [52], which was discussed in the previous chapter. The differing sensitivity towards different gases and VOCs at different temperatures enables the design of sensor-arrays, consisting of similar TiO_{2-x}/TiO_2-based heterostructures, where the individual sensor will operate at the most reliable but different temperatures, and hence will provide different signals towards the same mixture of gasses and VOCs [29]. The 'fingerprint' of analytical signals generated by the array can be assessed by ANOVA-based approaches and concentrations of individual gases can be decoded.

1.6. Sensing Mechanism of Some TiO_2-Based Heterostructures

The sensing mechanism of TiO_2-sensors is rather complex and it is based on the superposition of several processes, such as: (i) target-gas or -VOC adsorption to TiO_2-surface and (ii) desorption of pre-adsorbed gas or VOC from the TiO_2-surface. These adsorption/desorption processes depend on the nature of gases and lead to the formation of chemical bounds between adsorbed gas, and then the enrichment/depletion of TiO_2 upper layer by electrons, which are capable of being involved in the charge transfer process and, in such a way, are changing electrical conductivity of TiO_2-based layer. The conductivity of TiO_2-layer is based on two main variations: intrinsic conductivity of TiO_2-grains and the transfer of charge through the boundaries between separated grains. Therefore, both the (i) ratio of grain surface/volume and (ii) the number of such boundaries are very important for the development of the resistivity measurement-based analytical signal. The mechanism of conductance variation in the presence and absence of target gases (e.g., CO) has been discussed in detail by several research groups [79, 80] (Figure 3.). The electrostatic interaction between the particular parts of the target analyte and TiO_2 surface, as well as with the surface of other similarly behaving semiconductors (e.g., WO_3 [43, 44], also play a significant role in the development of both (i) changes of resistivity [29, 43] and (ii) variations of photoluminescence spectra [25, 44], which can both be applied for the assessment of the analytical signal [29]. The 'Debay radius/length' ratio and the size of grains are the factors that are significantly affecting charge-transfer efficiency in TiO_2- and TiO_{2-x}-based layers. The TiO_{2-x}/TiO_2-based heterostructure was highly porous and contained embedded 'nano-plates' and 'nano-sponges', which enhanced significantly the ratio between surface area and volume. Such advanced surface-formations are very useful, because a significantly larger area is available for the target gas or VOC absorption and, in this way, the sensitivity of the sensing layer is enhanced. The above-mentioned factors should be controlled during the development of gas and/or VOC sensors based on TiO_2 nanostructured layers [42, 81–83].

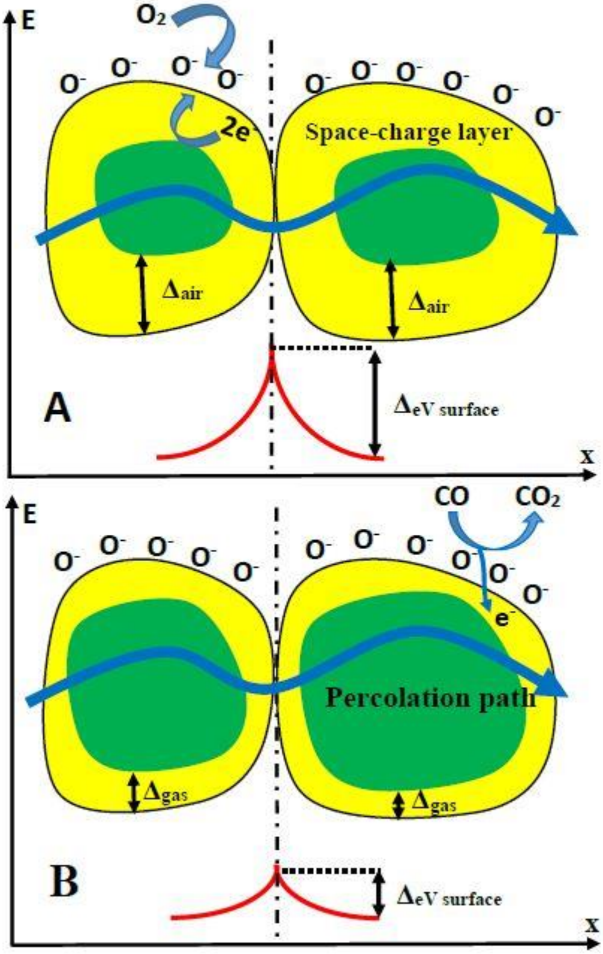

Figure 3. Structural and band models of conductive mechanism upon exposure to CO gas. **(A)** in the absence of CO, **(B)** in the presence of CO.

cfrather complex process and is mainly based on electrostatic and Van der Waals interactions (sometimes called ‘physical-adsorption/desorption’), without the formation/braking of chemical bounds and ‘chemisorption’, which is based on stronger chemical bound formation [84]. The physical sorption is mainly based on electrostatic and Van der Waals interactions between the adsorbed gas or VOC molecules and the TiO_2 surface. Gases (e.g.,: oxygen), which are present in the environment before the appearance of target gasses play a critical role in the sensing mechanism, because even before the measurement, they are pre-adsorbed on the surface of the semiconducting layer and, therefore, they affect the initial conductivity of the semiconducting layer. Later, during the course of measurement, these gas molecules are replaced by target (analyte) gas molecules and/or by some interfering gas molecules, when these are present in the environment, which is under investigation. In both cases, the adsorbed/desorbed molecules dependently on their abilities to donate/accept electrons to TiO_2-based structures and/or electrostatically interact with defect sites, which, in the TiO_2 structure, are responsible for the charge transfer and emission of photoluminescence photons [25], increase/decrease the electrical conductivity and photoluminescence efficiency and some other spectral properties of the TiO_2-based layer, both of which can be interpreted as analytical signals. However, bare TiO_2-based gas and VOC sensors have rather high electrical resistance and low dynamic range, which determine rather low sensitivity and selectivity. Therefore, heterostructures based on TiO_2 and other metal oxides, carbides and other materials have been designed [82, 85–87]. Conducting polymers (such as polypyrrole (Ppy) and polyaniline (PANI)) can be applied in the formation and modification of TiO_2-based heterostructures sensitive to gasses. The TiO_2/Ppy-based sensing heterostructures are able to operate at rather low temperatures. The TiO_2/Ppy-based sensor is suitable for the detection of gaseous NH_3 [88, 89] and the main LPG components (propane and butane) [90]. The TiO_2/PANI-based sensors for the determination of NH_3 has been reported [90–93]. The advanced sensitivity of TiO_2/Ppy and TiO_2/PANI-based sensors is based on the establishment of n/p-junction at TiO_2/Ppy interphase.

1.7. Recent Achievements and Perspectives in the Application of Non-Stoichiometric Titanium Oxides for Gas and VOC Sensor Design

The conductivity of TiO_{2-x} is considerably higher than that of stoichiometric TiO_2, especially if stoichiometry of Ti_nO_{2n-1} (where ‘n’ is between 4 and 10) is achieved because, at this stoichiometry, Magnéli phases can be formed rather easily [94], these phases possess metallic conductivity, superconductivity and some other valuable properties [95, 96], which can be applied in the design of gas and VOC sensor. It was determined that Magnéli phases are forming in TiO_{2-x}-based layers [97] planes based on Ti_nO_{2n-1} moieties, which penetrate through a matrix of TiO_2, and along this shear-plane, rather good conducting zones with electron-transfer-based conductivity are observed [96]. Even the presence of not-real members of Magnéli phases (Ti_2O_3 and/or Ti_3O_5) significantly increases the conductivity of titanium oxide-based heterostructures [29, 35]. Such conductivity variations are well exploited in the memristor-type logical elements, where the electrical resistivity of TiO_2 is increased and/or decreased by the reduction and/or oxidation of TiO_2-based structure when the corresponding potentials are applied [98].

The Ti^{3+}-containing TiO_{2-x}/TiO_2-based heterostructure possesses some ‘oxygen vacancies’ that are responsible for the electron mobility in this n-type semiconducting structure [99]. It is predicted that such ‘oxygen vacancies’ provide increased sensitivity towards some reducing and oxidizing gases and VOCs [29]. TiO_2-based structures can be reduced and form non-stoichiometric titanium oxides (TiO_{2-x}) and even Ti_nO_{2n-1}-based Magnéli phases [95]. In the TiO_{2-x} structure characterized by a low ‘x’ value, which varies in the range of $0 < x < 0.10$, ‘point defects’ dominate in the crystal structure, which possesses a great number of ‘oxygen vacancies’ and interstitials based on Ti^{3+} and Ti^{4+} [100]. The number of defects increases together with the increased ‘oxygen deficiency’ rate. In some research, it is reported that in Magnéli phases with an ‘x’ value of $0.10 < x < 0.34$, crystallographic shear planes and planar defects are extended [97, 101]. Magnéli phase-based titanium oxide structures conduct well and are chemically stable; therefore, they have found many application areas in the development of fuel cells, batteries and waste water decontamination [102–104], the same advantageous properties are suitable for the development of gas and VOC sensors. Hence, the presence of TiO_{2-x}/TiO_2-based heterostructures in TiO_2-based sensors can improve the sensitivity of the semiconducting layer, due to the advanced conductivity.

The design and technical procedures applied during the creation of TiO_2-based sensors at a high extent determined the sensitivity and selectivity of developed gas and VOC sensors. Non-conducting substrates with formed interdigitated electrodes are mostly used for the deposition of TiO_2- and TiO_n- and TiO_{2-x}-based sensors. TiO_2/TiO_{2-x} TiO_{2-x}/TiO_2 heterostructure can be formed by hydrothermal oxidation (in aqueous alkaline solution) of metallic titanium layer, which should be pre-deposited by magnetron sputtering. Therefore, additional strategies for the increase of conductivity should be elaborated, and one of such strategies is the modification of stoichiometric TiO_2-based structures by some non-stoichiometric TiO_2 [29]. TiO_{2-x}/TiO_2-based structures, which, due to the formation of Ti^{3+}, has some Ti_nO_{2n-1} clusters characterized by significantly advanced electrical conductivity, can be formed using many different approaches, e.g., metallic zinc-based reduction [21], plasma treatment [105], laser irradiation [106], high-energy particle bombardment [107] and thermo-chemical treatment [108]. The growing of large Ti_3O_5 crystals is still very challenging due to the polymorphism of titanium oxides [35]. XRD diffractograms (Figure 4) of designed TiO_{2-x}/TiO_2-based heterostructures, represents well some dispersion of Ti-based oxides [29], which form the TiO_{2-x}/TiO_2-structure, but some research [109] confirms the broad 'XRD peak-reach area' between 27° and 37° in the XRD-diffractogram [29] is assigned to Ti_3O_5, Ti_4O_7 and/or Ti_8O_{15}, which reveals the formation of the Magnéli phases within the TiO_{2-x}/TiO_2-based heterostructure. Meanwhile, the XRD peak between 34° and 37° reveals the presence of γ-Ti_3O_5, similar peaks were present in XRD-PDF file '00-040-0806 for γ-Ti_3O_5′ and by some other researchers [35], where the γ-Ti_3O_5 was formed by pulsed laser deposition. Low-temperature superconductivity was reported for both Ti_4O_7 and γ-Ti_3O_5 layers [35]; moreover, this research reports rather broad peaks in XRD-diffractograms of γ-Ti_3O_5 and of Ti_4O_7 at 36–38° and at 42–43°, respectively. XRD peaks and some other shape-like features in the same area of XRD-diffractograms at a very similar signal to noise ratio were also registered in the research, which is dedicated for sensing application of TiO_{2-x}/TiO_2-based heterostructures [29]. It should be noted that here commented XRD-diffractograms of TiO_{2-x}-based layers [29, 35, 110] despite of the here-mentioned very distinct similarities in all XR-diffractograms have also some differences, which appeared due to the different preparation procedures of TiO_{2-x}-based layers during each of the here-mentioned research. This fact reveals that there is a lot of space to change/vary the intrinsic morphology and composition of TiO_{2-x}/TiO_2-based heterostructures and to tune selectivity a sensitivity of such heterostructures by the establishment of different TiO_{2-x}/TiO_2-stoichiometry that is achieved by different annealing temperatures and/or durations [29].

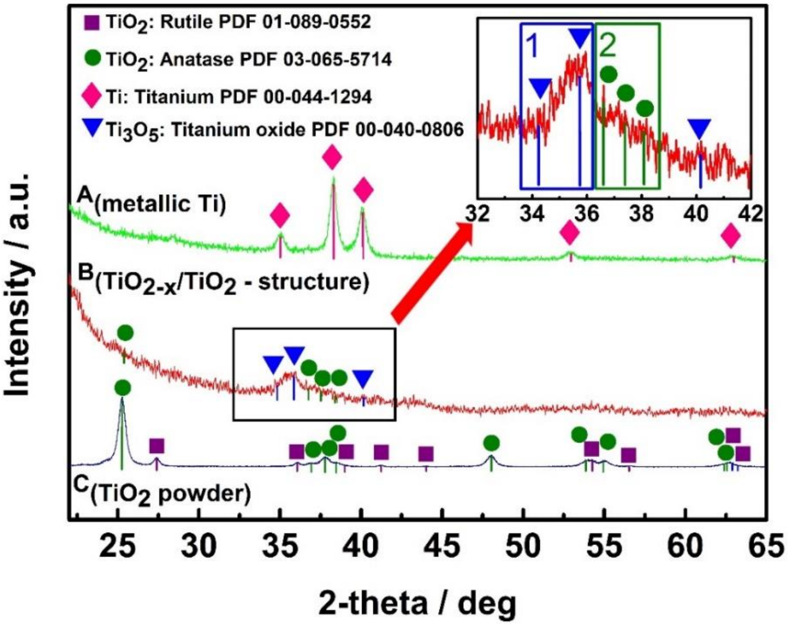

Figure 4. XRD patterns of: **A**$_{\text{(metallic Ti)}}$—metallic Ti layer of 100 nm thickness, which was formed by magnetron sputtering; **B**$_{(TiO2-x/TiO2\text{-structure})}$—$TiO_{2-x}/TiO_2$(400 °C)-based heterostructure, which was formed from above mentioned metallic 100 nm thick Ti layer; **C**$_{\text{(TiO2 powder)}}$—TiO_2-powder, which was used as 'control sample' and by the supplier (Sigma-Aldrich) was declared as 99.3% TiO_2 in anatase phase. Figure adapted from [29].

It should be noted that a significant part of the here-covered research on Magnéli phases has been based on the evaluation of powders and little research was performed on other structures, such as fibers [98] or planar structures [29]. Also TiO_n-based 'Magnéli phase like structures' might be formed by using the hydrothermal oxidation of a thin metallic layer of titanium sputtered by magnetron deposited [29]. Differently from the above-mentioned research, in some particular cases, the ratio of non-stoichiometric titanium oxides vs. stoichiometric titanium oxides in TiO_{2-x}/TiO_2-based heterostructures and/or in TiO_2-based layers can be increased by the treatment based on heating at a high temperature in the presence of reducing gasses and VOCs [110]. Some studies were dedicated for the investigations of transition between metal and insulator states of Ti_3O_5 that were performed: (i) applying visible-light pulses that have induced transition between β and λ forms of Ti_3O_5 [33], (ii) thermal treatment induces transition between α and β forms at 450 K [30] and between δ and γ at 240 K [31–34]. The transition between metal and insulator states at 350 K was observed [35]. Various research illustrates that the temperature range between 240 and 450 K is important for the phase changes of Ti_3O_5 and is important for the tuning of the titanium oxide layer conductivity and the adaptation of this layer for the determination of gaseous compounds. Hence, TiO_2 can be turned into Ti_nO_{2n-1} by proper doping, reduction and/or partial oxidation of metallic titanium [29] and later particular temperature-based treatment enables the establishment of the optimal TiO_{2-x}/TiO_2-based heterostructures. Therefore, such structures after some further adjustments can be applied in the design of sensors, which will have different levels of sensitivity and selectivity; therefore, such sensors with different levels of selectivity will be suitable for the establishment of sensor arrays. However, despite their advantageous conductivity, catalytic activity and sensing performance, which are all very suitable for the development of gas and VOC sensors, non-stoichiometric titanium oxides have a significant disadvantage in comparison to stoichiometric ones, which is that it is based on lower stability at the atmospheric condition, due to the continuous oxidation into stoichiometric TiO_2. Moreover, the selectivity of all the above-mentioned sensors is still rather low.

1.8. Analytical Signal Registration Protocols

The selection of a suitable method for the registration of the analytical signal is an important issue in the design of gas and VOC sensors; therefore, for this purpose, various methods can be applied: most of them are based on galvanostatic, potentiostatic and a variety of potentiodynamic measurements. Some of these electrical signal registration methods can, at the same time, be useful for the self-heating of sensing structure and/or, if well-adjusted, are suitable for the increase of sensitivity and selectivity of sensors. Electrical conductivity measurements are the most frequently applied for determination of the analytical signal by sensors based on all types of stoichiometric and non-stoichiometric titanium oxides [4, 9, 29, 41, 75, 88, 89, 92, 111–116]. The conductivity of TiO_{2-x}/TiO_2-based gas- and/or VOC-sensitive structure is rather high in comparison to that of stoichiometric TiO_2, therefore, the current passing through TiO_{2-x}/TiO_2-based structure heats-up sensing layer, which is very useful for the achievement of different selectivity at different temperatures, while the analytical signal can be based on changes of current registered at the same constant potential, which is applied for the heating of system and/or the evaluation of photoluminescence spectra [29]. However, it should be noted that stoichiometric titanium oxide-based sensors are characterized by rather low electrical conductivity ($\sim 10^{-10}$ S/m); therefore, the significant elevation of temperature up to 200–400 °C is required to increase the conductivity, in order to reach optimal sensing conditions. This requirement is typical for most of the sensors based on stoichiometric TiO_2-based semiconducting materials; therefore, in most of the stoichiometric TiO_2-based sensors, significantly higher temperatures should be applied in comparison to optimal temperatures for nonstoichiometric TiO_2-based sensors [29]. Operation at higher temperatures increases the energy consumption of the sensor, which becomes very actual if the sensors are operating at autonomous powering.

Despite its very good sensitivity, the selectivity of electrical resistance measurement-based any type of titanium oxide-based sensors is still rather poor. Therefore, additional signal registration methods are very beneficial, especially if they are applied simultaneously with electrical resistance measurements. The application of photoluminescence detection-based analytical methods in the development of TiO_2- and TiO_{2-x}/TiO_2-based gas and VOC sensors can significantly advance analytical information, which can be gathered by electrochemical methods. Most of the stoichiometric and nonstoichiometric titanium oxide structures are characterized by photoluminescence spectra with a maximum in the range between λ = 415–500 nm. Differences of photoluminescence spectra of titanium oxide structures depend on annealing conditions (mainly on the duration of heating and temperature changing protocol), both of which are applied during the formation of the structures because dependently on these conditions, different phases of stoichiometric and/or nonstoichiometric titanium oxide are formed, e.g., when TiO_{2-x}/TiO_2-based structure is formed using annealing at 400 °C, then significantly more intense photoluminescence signal (higher about 10 times) has been created in comparison to that determined for the TiO_{2-x}/TiO_2-based heterostructure formed using annealing at 600 °C, and if TiO_{2-x}/TiO_2-based structure is formed by annealing at 800 °C the photoluminescence of such a structure is very weak—over hundred times lower than that of TiO_{2-x}/TiO_2 -based heterostructure prepared at 400 °C [29]. Therefore, during the design of stoichiometric and nonstoichiometric titanium oxide-based structures for optoelectronics-based sensors preparation conditions should be followed and photoluminescence and sensing properties of these structures can be rather easily tuned by the adapting proper annealing conditions.

The increase of heating voltage, which is simultaneously used for the measurement of conductivity of the TiO_{2-x}/TiO_2-based heterostructure, gradually decreases photoluminescence peak intensity [29], due to the temperature-dependent reduction of a number of photoluminescence emitting centers at higher temperatures and temperature-based photoluminescence quenching [104, 117, 118]. In addition, the shift of peak maximum (λ_{max}), which is usually determined as a maximum of Gauss function, towards shorter wavelengths was observed [29]; this fact reveals that photoluminescence emitting centers, which are located close to the surface of TiO_{2-x}/TiO_2-based heterostructure are electrostatically affected by adsorbed gaseous material [25]. The evaluation of $TiO_{2(anatase)}$ photoluminescence was evaluated in some research and it was determined that photoluminescence is excited at shallow trap levels that have energy levels in the range of 0.41–0.64 eV, which is below the conduction band of this oxide [119]. Narrow photoluminescence emission bands were determined for $TiO_{2(anatase)}$ powder; they were emitted by self-trapped excitons that are appearing in the crystal structure of $TiO_{2(anatase)}$, which is based on octahedral sheets of 'TiO_6' structural elements [119, 120]. Therefore, electrical resistivity measurements can be extended by the determination of photoluminescence signal, which can also be applied for target gas and VOC determination by titanium oxide-based sensors. The evaluation of photoluminescence-decay kinetics can be applied for the determination of the self-trapped exciton-based origin of photoluminescence, which, among titanium oxides, is the most characteristic for crystalline $TiO_{2(anatase)}$ [121], and during the formation of the sensing layer, it can be exploited as a confirmation of $TiO_{2(anatase)}$ presence in the composition of sensing layer [29] and for the determination of analytical signal. In addition to registration of conventional photoluminescence signal, the evaluation of photoluminescence-decay kinetics can provide new options for the evaluation of the quality of the sensing layer [29, 44] and the determination of analytical signal by sensors based on stoichiometric and non-stoichiometric titanium oxides.

It should be noted that the selectivity of gas and VOC sensors remains not very high, even if very good sensitivity has been achieved in a lot of research [4, 9, 29, 41, 75, 88, 89, 92, 111–116]. Therefore, approaches suitable for the evaluation of gas and/or VOC mixtures should be elaborated. In this context, it is very promising that the variation of sensing layer temperature significantly changes both the selectivity and sensitivity of gas and/or VOC sensors, which was well demonstrated by the gas- and VOC sensor based on TiO_{2-x}/TiO_2-layer [29], and this effect can be applied in the design of sensor arrays, where sensors with different selectivity and sensitivity can provide very different responses in the same gas and VOC mixture and these 'finger prints' registered by such a sensor array can be assessed and decoded by applying the corresponding methods of the multi-variation mathematical analysis.

2.1. MXenes: Description of Material and the Main Properties

MXenes have recently (in 2011) appeared as a new class of 2D materials with metallic conductivity [122, 123] and/or attractive some semiconducting properties, which can be well exploited in the design of sensors, biosensors, biofuel cells and in the development of some wearable bioelectronic devices. MXenes have some structural relation and even similarity of some physical properties with other 2D material – graphene [124, 125]. Most of MXenes are based on 2D transition metal carbides [123]. In addition to the carbides, 2D transition metal nitrides, carbonitrides are appointed to this MXene-materials class [126]. MXenes usually are prepared by etching of initial materials – called 'MAX phases', which can be presented by generalized formula $M_{n+1}AX_n$ in which 'M' is representing transition metal (that are Ti, Sc, Zr, Cr, V, Mn, Hf, Nb, Mo or Ta), 'A' is an element from periodic table [15, 127–130] 12,13,14,15 or 16 groups (that are Al, Cd, Si, S, P, Ga, As, Ge, In, Tl, Sn or Pb) and 'X' is either carbon (C), nitrogen (N) or a mixture both of them [131–134] and 'n' in this formula can be in the range of 1-3 [131, 132, 134–136].

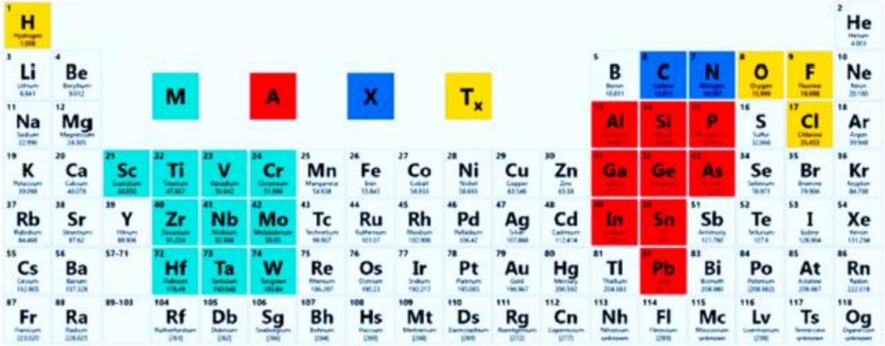

Figure 5. The composition of MXenes and MAX phases from the periodic table. Reprinted from [127]

In recent years, research of this class of materials expanded rapidly. In particular, $Ti_3C_2T_x$ (T_x here denotes the terminal functional group, usually -O, -OH or -F) type of MXenes obtained from Ti_3AlC_2 (MAX phase) are investigated the most [137–139]. Due to unique morphology and composition, these materials have the potential to be used as sensors [140, 141], for catalysis [142–144]; high absorbance in the UV-Vis-NIR range allows these materials to be used as an absorber in solar cells and other energy conversion devices

[145]. Moreover, intriguing metallic properties were observed for MXenes like conductivity and metal-like free electron density [3, 146, 147]. Such metallic behaviour can be altered by their surface termination groups leading to possible applications as supercapacitors [148, 149], resistive sensors [150–152] and other applications in electrochemistry [153], electronics [154]. Due to the presence of metal-like free chargers and plasmonic response to an incident electric field, some applications of Mxenes in spectroscopy can be considered as well. Similar to other plasmonic materials MXenes can have phenomena related to plasmon resonance.

The properties of MXenes can be well tailored through proper variation of M and X elements in MXene structure and by the introduction of various surface terminal groups [15, 128, 129]. Due to this option of applying very different surface "finishing", recent advances in surface chemistry enables the introduction of particular surface "terminal functional groups" [15, 128, 129], which can be suitable for the immobilization of enzymes and some other proteins. Hence, MXenes can be efficiently modified by particular biomolecules and many other compounds that are required for the action of biosensors. In addition, the above mentioned "terminal functional groups" can provide tailored electronic, electrochemical and optical properties to MXene-based biosensing structures [15, 128, 129]. The optical properties of MXenes are highly applicable for biosensing purposes [130], especially those which are based on fluorescence resonance energy transfer and induce changes in photoluminescence signal [157]. In some researches [13, 158–165] and reviews [166, 167] it is reported, that MXenes are compatible with enzymes and other protein molecules, which are used in the development of catalytic biosensors and affinity sensors. Biocompatibility of MXenes towards some microorganisms [168, 169] and even towards mammalian neural cells [170], was also determined. Catalytic activity has been reported for some MXenes, but immobilized enzymes and microorganisms can significantly extend the ability to utilize significantly broader ranges of substrates, which can provide chemical energy for biofuel cells. Bioelectronics devices dependent on the type of applied bio-recognition elements can be divided into several classes, such as: (i) catalytic sensors and biofuel cells based on enzymes [171] and non-enzymatic structures [172], (ii) whole-cell-based biosensors and biofuel cells [173], (iii) affinity sensors based on immobilized antibodies or antigens (immunosensors) [174], (iv) immobilized single-stranded DNA (ssDNA)-based sensors (DNA-sensors) [175], molecularly imprinted polymer-based sensors, [176] etc. The applicability of various nanomaterials in some of these classes of biosensors has been demonstrated [177]. Some researchers predicted that MXenes will form the basis for various MXene nanocomposites and the development of commercially available MXene-based biosensors [178].

2.2. MXenes Application in a Sensors based on SERS

Similar to other plasmonic materials MXenes can have phenomena related to plasmon resonance. For this reason, MXenes might be used as a substitute for metallic nanostructures with the ability to enhance the internal vibrations of molecules at near proximity [17, 155, 156]. Till now, only enhanced resonance Raman spectra of molecules adsorbed on MXene surface were obtained and the enhancement was explained via chemical enhancement mechanism (CEM) [17, 155, 156]. Due to the interband transition of MXenes to the vacant energy states, a charge transfer to the adsorbed dye molecule took place. Subsequently, a relaxation causes enhanced Raman scattering. This coupling between electronic levels of MXene and dye molecule can be considered as CEM of SERS [156, 179, 180]. Nevertheless, due to free electron oscillations and plasmonic response possible in MXene layers, the electromagnetic enhancement (EEM) mechanism of the SERS signal can not be neglected as well [181, 182].

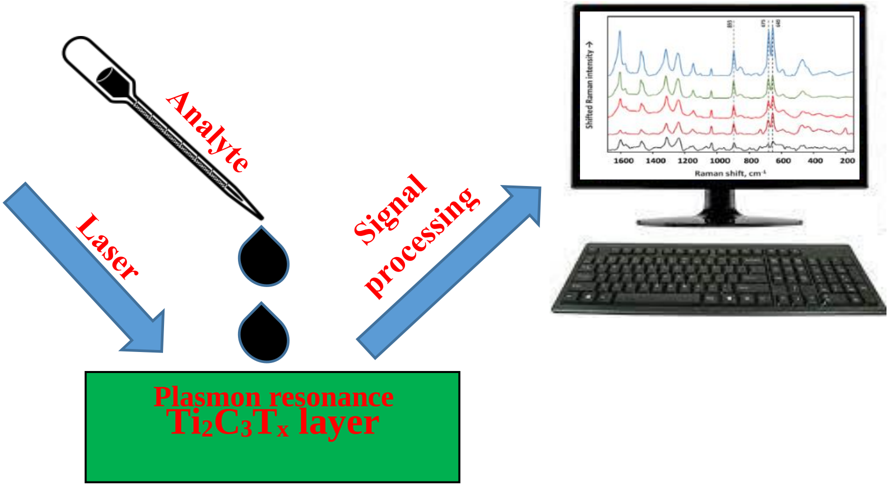

Figure 6. Schematic view and the main working principles of SERS sensors based on $Ti_2C_3T_x$ MXenes

2.3. Catalytic MXenes Sensors Based on Enzymes

Catalytic sensors based on enzymes and some other redox proteins have several advantages over other analytical systems because they can provide high selectivity. One of the most expanded areas of enzymatic sensors is related to the development of electrochemical sensors and the advantages of such sensors are based on low costs, simple operation and ability to be applied for the evaluation of optically badly transparent and turbid samples, e.g. blood. Moreover, recently implantable biosensors are appearing in the market and these require biocompatible materials for the design of electrodes and biofuel cells, which will supply power for these implantable devices. Therefore, efficient charge transfer between electrodes and immobilized enzymes is a very important issue [183, 184]. Moreover, sometimes it is possible to establish direct charge transfer (DCT), which is sometimes called direct electron transfer but this fact is not always correct, because our recent researches show that sometimes DCT is established between p-type semiconducting polymers and redox enzyme – glucose oxidase (GOx) [185, 186]. The determination of direct charge transfer (DCT) between redox enzymes enables to exploit the inherent thermodynamic potential of enzyme-catalysed reaction in the design of electrochemical-catalytic biosensors and all types of biofuel cells, which in the most optimal cases are free of soluble redox mediators [183, 184, 187–189]. Hence, application of MXenes in this respect is rather promising, the Nafion stabilized $Ti_3C_2T_x$-based MXene (where T_x were some transition metals) was applied for sensing of dopamine [190], and electrochemical characterization of Nafion/$Ti_3C_2T_x$/GCE revealed large surface area, large intrinsic conductivity and low charge transfer resistance. Therefore, it was predicted that MXenes can be well implemented into the construction of enzymatic sensors and biosensors and probably direct charge transfer between MXenes and some redox enzymes can be estimated. However, the determination of DCT between redox enzymes and solid electrodes is rarely possible, because the redox-active site of most enzymes is rather deeply encapsulated within ‘electrically insulating’ protein structure, which has low electric permittivity (ε) [191, 192]. Therefore, various soluble redox mediators are applied in the design of such biosensors [193] and biofuel cells [171]. However, soluble redox mediator based strategy is not very efficient, therefore, some conducting nanomaterials including carbon nanotubes [194], gold nanoparticles [187], conducting polymers [195] and very recently – MXenes can be applied for the purpose to establish direct charge transfer between redox enzyme and electrode surface and/or facilitate charge transfer from products formed during enzymatic reaction [196–199].

Even more complicated situation is with charge transfer from microorganisms because most of them are wrapped within an 'electrically insulating' layer of polysaccharides [200, 201], but recently we have found a way how the conductivity of cell-wall can be improved by the formation of conducting polymer nanoparticles [200, 202] and even some larger structures [201] within the cell wall of microorganisms and in such way conductivity of this initially not conducting structure can be remarkably improved. This formation of conducting polymers can be induced by a metabolic cycle of these microorganisms [203] and conducting polymer-based structures are well distributed within the cell wall and periplasm of microorganisms [202, 204].

Ti_3C_2-based MXene was used for the immobilization of tyrosinase within the pre-adsorbed chitosan layer and Tyr/MXene/CS/GCE was applied for the determination of phenol in water with a sensitivity of 414.4 mA/M, linear range between 0.05-15.5 mM and with LOD of 12 nM [159]. Drop-casting based dispersion was performed and electrostatic effects between MXene and tyrosinase enabled proper orientation of the enzyme during the immobilization and preserved catalytic activity of immobilized tyrosinase, therefore, very efficient direct charge transfer between tyrosinase and the electrode has been established [158, 205].

It should be noted that apart electrons the holes can be involved in direct charge transfer within the redox enzyme structure and at the interphase between enzyme and electrode [185, 186], therefore, MXenes in this charge-transfer related context are especially interesting; because they can act as metallic conductors with varied conductivity, which depends on the applied 'M' and 'X' elements in the structure of MXenes ($M_{n+1}X_nT_x$) and covalent surface modifications in their structure [206]. It is remarkable that covalent surface modifications in the structure of MXenes enable to achieve even superconductivity [206]. The redox-ability in addition to good conductivity enables MXenes to facilitate the electrochemical redox process [207]. Hence, some attempts to demonstrate the applicability of MXenes in the design of redox mediator free sensors were demonstrated [158, 170] and discussed [126, 208], which opens a great applicability of MXenes to be applied in various bioelectronics devices, including biosensors and biofuel cells. It was demonstrated that if some redox enzymes are trapped within MXene sheets, then a rather efficient charge transfer from the active site of the enzyme towards the electrode can be achieved due to the sufficient mobility of charge within MXene-based structure [209].

MXene and platinum nanoparticle (PtNPs) based nanocomposite was developed and deposited on GCE electrode (Ti_3C_2T/PtNPs/GCE) [165], PtNPs significantly enhanced the electro-catalytic activity of this MXene-based electrode, and it was sensitive to various compounds that are important during the development of biosensors and biofuel cells, including dopamine, ascorbic acid, uric acid, acetaminophen and H_2O_2. Such advantageous sensitivity of Ti_3C_2T/PtNPs/GCE electrode can be potentially adapted for the design of biofuel cell cathodes.

Electrochemical biosensor based on MXene/DNA/Pd/Pt/GCE electrode was developed and applied for amperometric determination of dopamine in the range between 0.2 and 1000 mM with LOD of 30 nM [210]. In this research, DNA was important for the dispersion of Ti_3C_2-based nano-sheets and facilitation of Pd and Pd/Pt formation structures, while Ti_3C_2-based MXene acted as conducting support. However, this MXene/DNA/Pd/Pt/GCE structure was highly sensitive to glucose, uric acid and ascorbic acid. Therefore, this structure probably is better suitable for the development of biofuel cells, which will be able to consume a much broader range of biological fuels.

In many researches were demonstrated that if the electrochemically active surface area of the electrode is not sufficient, the decoration by metal nanoparticles [192, 196, 198] or some other nanoparticles can be applied in order to increase catalytic activity and thus the currents registered by electrodes modified by enzymes. A similar strategy was applied during the development of some MXene-based catalytic sensors [170, 211]. Ti_3C_2-based MXene modified by AuNPs was applied for the Nafion-based immobilization of glucose oxidase (GOx) in order to design a biosensor for the determination of glucose, which was based on Nafion/GOx/AuNPs/Ti_3C_2/GCE structure [170]. It was predicted that in this structure AuNPs is involved in charge transfer between the catalytic site of the enzyme and electrode.

Amperometric biosensor based on acetylcholinesterase (AChE) immobilized on $Ti_3C_2T_x$ and chitosan (CS) modified glassy carbon electrode (AChE/CS/$Ti_3C_2T_x$/GCE) has been developed and applied for the determination of organophosphorus pesticide – malathion [164]. CS/$Ti_3C_2T_x$-based heterostructures provided a great environment for the immobilized AChE. A rather similar AChE/CS/$Ti_3C_2T_x$/GCE-hetero-structure was applied for determination of malathion in tap water [211], whereas acetylcholinesterase (AChE) immobilized on $Ti_3C_2T_x$ modified by silver nanoparticles (AgNPs) was developed and also applied for DPV-based determination of malathion [212]. In this sensor negatively charged acetylcholinesterase was electrostatically attracted to the surface of positively charged Ag/$Ti_3C_2T_x$-composite, which improved charge transfer from acetylcholinesterase.

Electrochemical biosensor based on acetylcholinesterase, MnO_2/Mn_3O_4 microcuboids, AuNPs, and MXenes (AChE/CS/Ti_3C_2/AuNPs/MnO_2/Mn_3O_4/GCE) was developed for the determination of some organophosphate – methamidophos, which has acted as inhibitors of immobilized enzyme – AchE [14]. Some researchers are reporting that anodic potentials, which are exceeding +200 mV leads to the oxidation of its outer surface of Ti_3C_2T -based MXenes and can be applied for the oxidation of NADH [13], this remarkable finding is eternally important for the development of enzyme- and microorganism-based biofuel cells because NAD/NADH system can served as a redox mediator for many enzymes and redox-proteins and in addition, NAD is a cofactor of NAD-dependent enzymes. The application of MXenes for the design of catalytic sensors based on enzymes seems rather effective due to the metallic conductivity of these compounds.

Ti_3C_2-based MXene, which was modified by Persian blue (PB), was applied in the design of ‘wearable’ electrochemical biosensors [213] showed good sensitivity to glucose and lactose. Applied MXene increased immobilization efficiency of an immobilized enzyme, the permeability of oxygen into biosensing structure, where it has taken part in the charge transfer from GOx. These sensors were integrated within a flexible polymeric structure and used as wearable biosensing devices for the determination of lactose and glucose in an actual concentration range of 1-20 mM with the sensitivity 11.4 $mA \times mM^{-1} \times 1cm^{-2}$ and 35.3 $mA \times mM^{-1}cm^{-2}$, respectively.

Two types of screen-printed-electrodes (i) Urease, methylene blue (MB), and $Ti_3C_2T_x$ based screen-printed-electrode (urease/MB/MXene/SPE), (ii) $Ti_3C_2T_x$ based screen-printed-electrode (MXene/SPE) were designed and applied in the microfluidic electrochemical system for continuous monitoring of urea and creatinine in whole blood [214]. During the development of this biosensor enzyme – urease was immobilized using glutaraldehyde as a cross-linking agent, which well binds enzymes on electrode surface [198]. The first electrode based on urease/MB-MXene deposited on the screen-printed electrode was used for determination of urea in the range of 0.1–3 mM and the second one MXene deposited on the screen-printed electrode was used for determination of creatinine in the range of 0.02–1.2 Mm; in this electrode, MXene was served as the electro-catalyst. These electrodes were incorporated within the microfluidic system and applied for the determination of urea and creatinine in whole blood. These electrodes are incorporated within a microfluidic system and applied for the determination of urea and creatinine in whole blood. It is very remarkable that some MXenes involved in composite structures are exhibiting peroxidase-like activity and have been applied in the design of biosensors, for example, MXene-Ti_3C_2/CuS nanocomposite based sensor dedicated to the colourimetric determination of cholesterol [215] and lactate dehydrogenase (LDH) based heterostructure of an MXene@NiFe-LDH for the detection of glutathione [216].

2.4. Direct charge transfer between redox proteins and MXenes

Direct charge transfer was observed in electrochemical biosensors based on Ti_3C_2 MXene deposited on glassy carbon electrode (GCE) and modified by immobilized haemoglobin (Hb) and Nafion in order to establish a Nafion/Hb/Ti_3C_2/MXene/GCE-based structure [160]. This sensor was suitable for the determination of nitrite in water samples. The catalytic activity of NO_2^- reduction in this sensor [158] was based on the proton-coupled reaction [217]. The other researches group designed a mediator-free enzymatic electrochemical biosensor based on Ti_3C_2 MXene and immobilized haemoglobin and reported the sensitivity of this sensor towards hydrogen peroxide (H_2O_2), with a linear range between 0.1 and 260 mM [160]; the authors speculated that this structure exhibits some ”organ-like” properties because it shows high efficiency towards reduction of hydrogen peroxide. This efficiency was achieved due to exfoliation of the MAX-phase, and it was determined that even layers that are thinner than 20 nm still show very high catalytic activity [160]. Exfoliation of separated sheets is observed each time when MXenes are formed [218, 219], and there are some evidence that MXenes are providing both compatible environments for immobilized proteins where they retain catalytic activity, very large surface area (Figure 7a) and some functional groups, which can be used for the immobilization of enzymes (Figure 7b) [213].

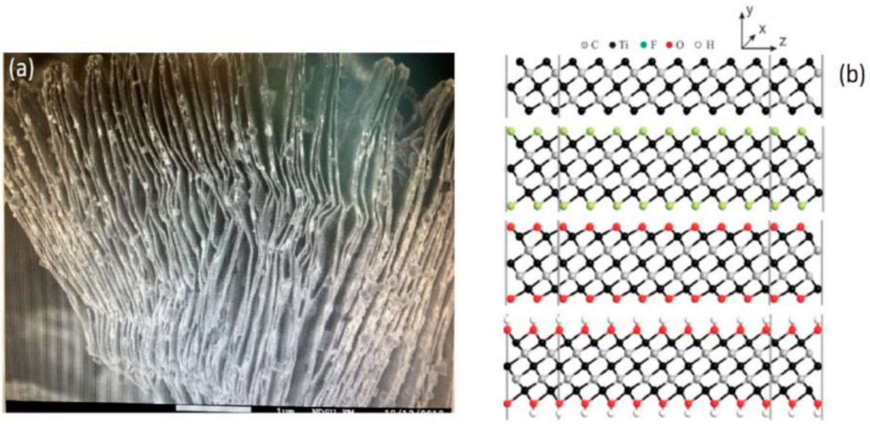

Figure 7. 2D multi-layered Ti_3C_2 MXene sheets: (**a**) scanning electron microscopy image; (**b**) pristine and surface-terminated Ti_3C_2 Mxene with different functional groups [220]

It should be noted that haemoglobin (Hb) is a very suitable candidate for the development of cathodes for biofuel cells [171]; therefore, this MXene/Hb based electrode seems very pertinent for the design of biofuel cells. It was demonstrated that even better current density can be achieved if, instead of bare Ti_3C_2, a heterostructure based on TiO_2-Ti_3C_2 nanocomposite is deposited on the GCE electrode and later it is modified by haemoglobin [160]. In this research, a designed Nafion/Hb/TiO_2-Ti_3C_2-structure based biosensor was characterized by good sensitivity (of 447.3 mA×mM^{-1}×cm^{-2}) towards H_2O_2 with a linear range of 0.1–380 mM, and LOD of 14 nM [160]. The Nafion/Hb/TiO_2-Ti_3C_2/GCE biosensor [160] showed much better long-term stability in comparison with previously described Nafion/Hb/Ti_3C_2/GCE biosensors [160]. It seems that TiO_2 significantly improves the biocompatibility and can enhance the conductivity of the formed structure, especially if the nonstoichiometric form of titanium oxide TiO_{2-x}/TiO_2 is formed, which increases both conductivity and catalytic activity of formed heterostructures [221]. This effect is based on the fact that the TiO_{2-x}/TiO_2-based structure has rather high concentrations of “oxygen vacancies”, which are responsible for n-type charge mobility in this semiconducting heterostructure [222]. Very recently, in one research conducted by our group, we predicted that such oxygen vacancies are providing increased sensitivity towards some reducing and oxidizing gases and VOCs [221]. These TiO_2-based structures can be reduced and can form nonstoichiometric titanium oxides (TiO_{2-x}), which can be partly based on Magnéli phases with a stoichiometry of Ti_nO_{2n-1} [223, 224]. It was determined that in the TiO_{2-x} structure, which has a rather low “x” value varying between 0 and 0.10, therefore, so-called “point defects” dominate in TiO_{2-x} crystal structure [225], and such structures possess high numbers of interstitials based on either Ti^{3+} and Ti^{4+}, great ability of oxygen vacancies, or both. The concentration of the above-mentioned defects in the crystal structure of TiO_{2-x} is increased by an increased “oxygen deficiency” rate. Some researches revealed that Magnéli phases having rather high “x” values between 0.10 and 0.34 crystallographic shear planes are significantly extended [226]. These TiO_{2-x} heterostructures are stable, therefore, they are finding many applications in catalytic decontamination of waste-water and the development of batteries and fuel cells [227, 228]. Hence, there are some expectations that these physical properties of TiO_{2-x}/TiO_2-based heterostructures will improve the performance of some MXene-based sensors and biosensors based on enzymes that are exhibiting direct charge transfer [183, 184]. There are some indications that tungsten-based MXenes [229] can be advanced by the incorporation of either stoichiometric, nonstoichiometric tungsten oxide, or both [230, 231], and will find some applications in the development of biofuel cells. The application of ink-jet printed MXene with graphene oxide heterocomposite (Ti_3C_2/GO) was also modified with Hb [161] and applied in biosensors for the determination of H_2O_2. The sensitivity of MXenes towards pH [232] can be well exploited in the design of some biosensors based on enzymes with pH that changes during catalytic action.

2.5. Affinity sensors based on antibodies and other affinity agents

Affinity sensors are analytical devices, which specifically recognize analytes and form stabile complexes with analytes. According to applied analyte-binding, affinity sensors are classified into immunosensors, DNA-sensors, RNA-sensors and molecularly imprinted polymer-based sensors. In some recent researches, it was demonstrated that MXenes can be applied in the design of various affinity sensors. A very promising direction here is to design artificial biological recognitions systems based on molecularly imprinted polymers (MIPs) which were developed for proteins [233], DNA-based structures [234], but MIP-based sensors work especially well for determination of small molecular weight analytes such as caffeine [235], theophylline [236], etc. In this research direction, a hierarchical porous MXene/amino carbon nanotubes-based molecular imprinting sensor for the determination of a low molecular mass analyte, fisetin, has also already been reported [237]. However, larger molecular mass analytes such as proteins were also determined by some MXene-based sensors based on immobilized receptors, for example, Ti_3C_2-based MXene was modified by biological receptor after the activation with 3-aminopropyl triethoxysilane (APTES) in order to perform covalent binding, and it was applied in the design of affinity sensor [238] for the determination of cancer biomarker, carcinoembryonic antigen [239]. In this research, it was reported that the carboxylic group of anti-carcinoembryonic-antibodies binds well to the amino group f-Ti_3C_2 MXene and forms a covalent bond. Hexaammineruthenium ($[Ru(NH_3)_6]^{3+}$) was applied as a redox-probe for potentiodynamic measurement-based determination of analytical signal. Authors declared an extremely long linear detection range of this sensor, which was in the range from 10^{-13} to 2 x 10^{-6} ng/mL with great sensitivity of 37.9 mA ng/mL x cm^{-2} per one decade of concentration with extremely low LOD of 0.000018 ng/mL. This sensor-operated well in human serum samples. Application of MXenes for the design of affinity sensors based on antibodies and some other affinity agents offers new avenues for the development of efficient affinity sensors. MXenes were applied for the design of chimeric DNA-functionalized sensors for mapping of some cancer biomarkers in living cells [240] and DNA-sensors suitable for the determination of label-free mismatches of DNA in real human samples [241]. RNA sensors based on the application of MXenes were also reported where a novel label-free electrochemical strategy for the determination of miRNA-182 detection based on MoS_2/Ti_3C_2 nanohybrids was applied [242]. Upon microRNA-155 detection based on AuNPs/Ti_3C_2 MXene three-dimensional nanocomposite for exonuclease III-aided cascade target recycling was designed [243] and the oncomiRs detection based on synergetic signal amplification of AuNPs/MXene was reported [244]. A very different application of DNA-based structures (such as DNA-aptamers) in the design of bio-recognition elements was applied in sensors dedicated to rapid electrochemical detection of thyroxine [245]. In another research, Ti_3C_2-based MXene was modified by DNA-aptamer applied in luminol-based chemo-luminescence based affinity sensor for the determination of MCF-7 exosomes [246], which established highly sensitive electro-generated chemo-luminescence. A glassy carbon electrode was modified by poly-N-isopropyl acrylamide/Au, which has provided a higher concentration of carboxyl available for covalent immobilization of DNA-aptamer, which has selectively recognized MCF-7 exosomes with LOD of 125 particles per mL^{-1}. Moreover, a label-free electrochemical biosensor for highly sensitive detection of gliotoxin based on DNA nanostructure/MXene nanocomplexes was also reported [247]. MXene-based structures are able to selectively adsorb different molecules through physical adsorption or electrostatic attraction, and lead to a measurable change in the conductivity of the material with a high signal-to-noise ratio and excellent sensitivity (Figure 8). Therefore, sensors based on 2-dimensional Ti_3C_2 MXene-based nanosheets were characterized by good sensitivity and selectivity towards PGE2 and 8-HOA, which are both present in A549 lung cancer cells [220].

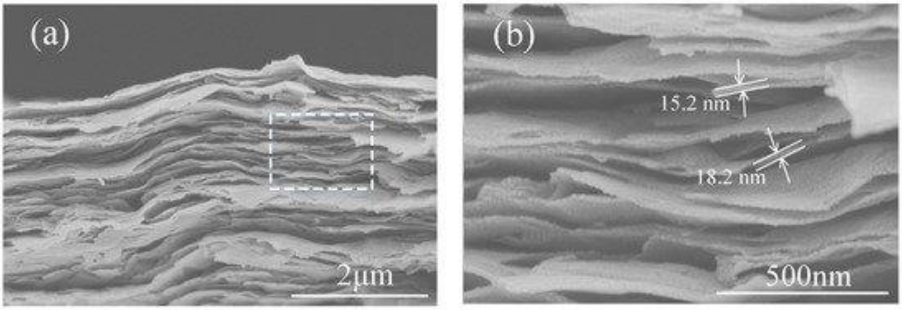

Figure 8. SEM images of (**a**) a cross-section of $Ti_3C_2T_x$ film and (**b**) an enlarged part with estimated flake thickness. Reprinted from [248].

2.6. Non-enzymatic biosensors cell electrodes

Non-enzymatic biosensors and biofuel cell electrodes are electrochemical systems that are suitable for the determination of biological compounds and catalyze spontaneous oxidation/reduction of various biological compounds by a generation of substantial potential (in the range of 50–1200 mV) and electrical current. Nonenzymatic glucose sensors based on the application of Ni-nanoparticle/polypyrrole composite was reported recently [172]. The application of MXenes in non-enzymatic glucose sensors also seems very promising as it was demonstrated by the application of three-dimensional porous MXene/NiCo-LDH composite in the design of high-performance non-enzymatic glucose sensors [249]. However, despite mentioned achievements, until recently most glucose oxidase (GOx) based sensors used are in this area [183–189], and during catalytic action of GOx as well as by the action of many other oxidases hydrogen peroxide (H_2O_2) is produced. Some recent reports in this area illustrate that hydrogen peroxide can be easily determined by non-enzymatic PB/Ti_3C_2 hybrid nanocomposite [250].

In order to design other non-enzymatic sensors, MXene was introduced into graphite composite paste in order to design (MXene/GCPE)-electrodes, which were sensitive to adrenaline by chronoamperometry with LOD of 9.5 nM [251]. Very efficient determination of adrenaline, serotonin and ascorbic acid was achieved by differential pulse voltammetry (DPV), which enabled separate characteristic DPV-peaks for adrenaline, serotonin and ascorbic acid.

Screen-printed electrodes modified by $Ti_3C_2T_x$ MXene modified (MXene/SPE) were applied for simultaneous detection of acetaminophen and isoniazid drugs [252]. DPV was applied as a detection method, which enabled distinguishing of characteristic DPV-peaks of acetaminophen and isoniazid with a linear range between 0.25 and 2000 mM and LOD of 0.048 mM for acetaminophen and linear range between 0.1 and 4.6 mM and LOD of 0.064 mM for isoniazid.

Several MXene-based NH_3 sensors were developed, where the remarkable properties of MXenes to adsorb gaseous materials were well exploited [253, 254]. Moreover, the catalytic properties of MXenes can be exploited for the catalytic determination of various chemical and biochemical compounds [208].

2.7. Immobilization of enzymes and affinity-agents on MXenes

Oriented immobilization is a very important issue in the design of enzymatic immunosensors and biofuel cells [171]. Well, oriented enzymes exhibit sufficient activity, because in such cases the substrate has good access into active sites with lower diffusional limitations in comparison when the enzyme's active center is oriented upside down and oriented towards the electrode. The only exception is when the direct charge transfer is observed between electrode and enzyme, then the orientation is playing a different role; therefore, the active redox center should be oriented towards the electrode [183, 184]. The advantage of MXenes in the application of biofuel cells would be useful for the adsorption of redox enzymes within 2D planes [255–257] because in such a system the orientation of enzymes would play a less critical role and in such a way MXene 2D planes will significantly increase the electrochemically active surface area of electrodes [124]. It is remarkable that MXenes are suitable to be applied for both anodic and cathodic potentials [259]. This property is highly appreciable for the development of biofuel cells because both electrodes can be based on very similar kinds of modifications and can be used for similar enzyme or cell immobilization procedures.

Rather unusual morphology and the ability of MXenes to be split into multiple one-dimensional planes [260] (Figures 7 and 8) during the preparation of these materials, enable "to load" MXene-based matrix by high concentrations of enzymes and microorganisms, which together with remarkable metallic conductivity of MXenes increases the applicability of these materials for the design of both enzymatic and microbial biofuel cells. It is remarkable that MXenes offer a good environment for immobilized enzymes or other proteins, which enables retaining sufficient catalytic activity [209, 212]. However, up to now, only rather small sheets of MXenes were developed (up to a maximum of 1 μm in length and width), therefore, they can just be treated as deposits on other substrates.

During the design of immunosensors and affinity sensors, the proper side of the affinity site of antibodies or other receptors should be oriented towards the solution with the analyte, which can be achieved by proper terminal groups of MXenes that are most suitable for covalent attachment [16, 129, 130]. Some affinity sensors have been designed by the immobilization of affinity agents by simple adsorption on the surface of a working electrode, which was modified by MXene-based sheets [171]. However, this strategy is not very efficient due to the random orientation of these affinity agents, therefore, improved strategies, which enable the orientation of antibodies should be adapted for the development of more efficient affinity sensors [261, 262]. A number of such strategies were reported in a targeted review dedicated to the development of immunosensors based on oriented antibodies [262] and in their experimental works, it was well demonstrated that whole antibodies [263], receptors [264] and some particular parts of antibodies, which were chemically split into two or four pieces [261, 262], can be immobilized in oriented-fashion on electrode surfaces. It should be noted that MXenes formed by chemical etching usually possess various surficial functional groups, mostly fluorine (−F) hydroxyl (−OH) or oxygen (−O) [265–267] (Figure 9). It is related to the chemical formula of MXenes, which is "Mn+1XnTx", where T indicates surficial functional groups. Ti_3C_2 MXene formed by chemical etching can be based on the following three structures: $Ti_3C_2(OH)_2$, $Ti_3C_2O_2$ and $Ti_3C_2F_2$ (Figure 9) [268]. The quantity and structure of terminal groups are mostly influenced by the synthesis protocol; therefore, the structure of terminal groups can be tailored, which is very important for the covalent immobilization of proteins (e.g., antigens or antibodies), which are used in immunosensor design as biological recognition parts [175].

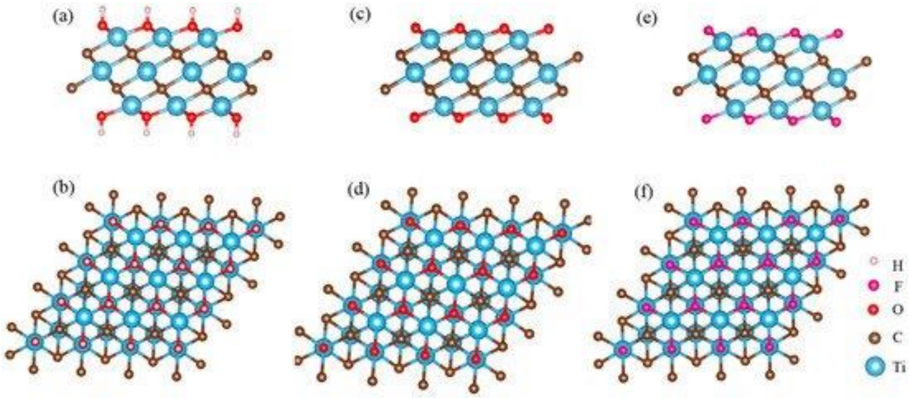

Figure 9. The structure of Ti_3C_2 nanosheets with different functional groups from side and top views: (**a**,**b**) $Ti_3C_2(OH)_2$; (**c**,**d**) $Ti_3C_2O_2$ and (**e**,**f**) $Ti_3C_2F_2$. Reprinted from [268].

Ti_3C_2-based MXene was applied in the design of biomimetic-sensors, which was based on adenosinetriphosphate(ATP) deposited on Mxene surface and then modified by $Mn_3(PO_4)_2$; this system was applied for amperometric determination of superoxide anions (O_2^-) [269], which were generated by HepG2 cells. In this chemical sensor, $Mn_3(PO_4)_2$ was sensing superoxide (O_2^-) in the range between 2.5 and 14 mM, the sensitivity of 7.86 mA $^\times$ mM^{-1} $^\times$ cm^{-2} and LOD of 0.5 nM. In addition to amperometric measurements, capacitance measurements can also be applied due to the high capacitance storage ability of MXenes; in this direction, Ti_3C_2 MXene nanosheet-based immunoassay with tyramine-enzyme repeating detection of prostate-specific antigens on interdigitated micro-comb electrodes was designed [270].

2. MATERIALS AND METHODS

2.1. Materials and Chemicals

In this project, all chemicals were of analytical grade and used as received without further purification unless otherwise stated. The main chemicals which were used in this research are given in table2:

Table 2. The list of chemical reagents used during PhD project and the suppliers where they were purchased.

Reagent	Source
Nitric acid (HNO_3), 70 % Sodium hydroxide (NaOH), 98.8 % Acetone ($(CH_3)_2CO$), 99.8 % Ammonium heptamolybdate ($(NH_4)_6Mo_7O_{24}\cdot 4H_2O$), ≥99,5 % Thiourea ($CH_4N_2S$), ≥99 %	Eurochemicals
Titanium foil, 0,127mm 99.7% Titanium foil, 0,25 mm 99.7% Concentrated hydrofluoric acid, HF	Sigma-Aldrich
Ethanol, 96 %	Vilniaus Degtinė
Pure Ti particles (<20 mm, 93% in water)	Alfa Aesar
Ti_3AlC_2 MAX phase	Drexel University, Nanomaterials institute
H_2SeO_3, the highest purity	Reachim

Milli-Q distilled water (DI, 18.2 MΩ·cm) was used for the preparation of all solutions, synthesis and rinsing of particles and structures surfaces.

2.2. Synthesis of materials

2.2.1. Formation of TiO_x-based Films

The surface of Ti foil was ultrasonically cleaned in acetone, ethanol, and water, for 6 min in each, then the native oxide layer from the surface was removed by etching in the solution containing H_2O, HNO_3 and HF (20%) (5: 4: 1 by volume) at room temperature for 10 s, washed with deionized water and transferred directly to the autoclave filled with the prepared reaction solution. Reaction solution contains from 0.05 to 0.5 mol L^{-1} of selenious acid dissolved in alkaline solution in a pH range from 9 to 12. All titanium electrodes were mounted vertically in the solution by means of a Teflon holder. The synthesis was conducted at the temperature range from 150 to 200 °C for 15 to 45 hours. The temperature ramp was 10°C/min. After synthesis, titanium suboxide electrodes were carefully rinsed with water. Finally, to form crystalline titanium suboxide structure the samples were annealed under an oxygen-free atmosphere at the temperature from 300 to 440°C.

2.2.2. Formation of TiO_x Particles

Submicrometer sized titanium suboxide particles were prepared in a similar way, as thin films. In this case, the same solution equipment and synthesis parameters were used. As substrate for titanium suboxide formation submicrometer sized titanium particles was used. After synthesis, particles were washed with distilled water followed by centrifugation. Finally, to form crystalline titanium suboxide structure the samples were annealed under an oxygen-free atmosphere at the temperature from 300 to 440°C.

2.2.3. Formation of MXenes (Ti_3C_2)

MXenes (Ti_3C_2) were synthesized by selective etching of its precursors Ti_3AlC_2 in a diluted (5 w%) HF solution for 24 hours. This selective etching was used for the removal of Al and the formation of literature described as „accordion-like“ structures. After the etching, the next procedure was washing Mxene structures from the residue of acid and it was done in a centrifuge at 9000 rcf, till the pH of MXenes solution became neutral.

2.3. Applications

2.3.1. Formation of TiO_x Based Gas Sensors

A Si wafer (1) was oxidized in an electric oven with an increased concentration of oxygen to form a few micrometres thick oxide (SiO_2) layer (2) over the Si wafer. After that, the metallic titanium (Ti) layer (3) of 100 nm thickness was sputtered by a magnetron. Amorphous non-stoichiometric titanium oxide (TiO_{2-x}) and titanium dioxide (TiO_2) based hetero-structure (TiO_{2-x}/TiO_2) was formed by hydrothermal oxidation of $Si/SiO_2/Ti$-based wafer in an aqueous alkaline solution. Finally, platinum (Pt) electrodes/(contact zones) (Figure 10, Section 3) were formed on the top of the crystalline TiO_2 by magnetron sputtering.

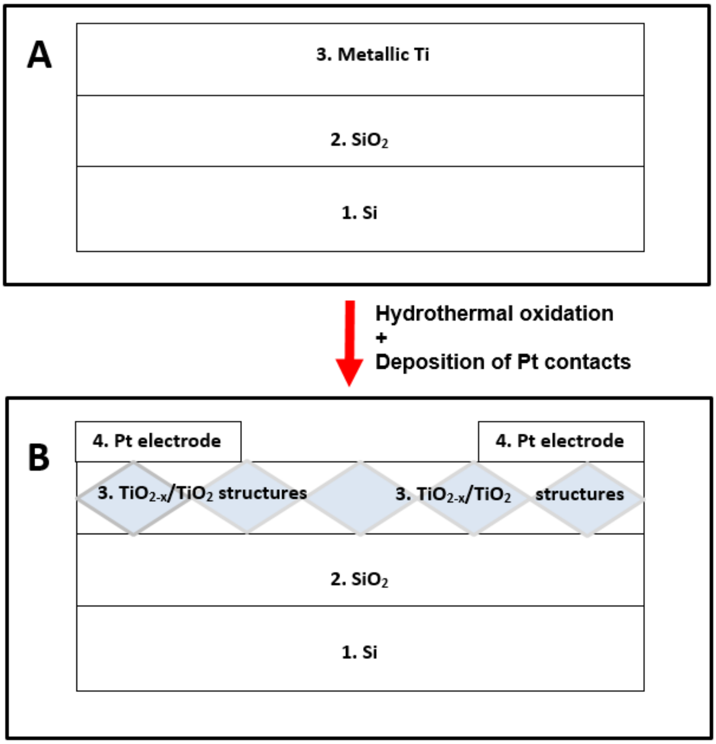

Figure 10. (**A**) Schematic view (layer-by-layer) of the initial structure, which was used for the design of sensor: 1—Si-based wafer; 2—thin layer (100 nm) of SiO_2; 3—thin layer (100 nm) of Ti deposited by magnetron sputtering. (**B**) Schematic view (layer-by-layer) of TiO_{2-x}/TiO_2-based sensor structure: 1—Si-based wafer; 2—thin layer (100 nm) of SiO_2; 3—nonstoichiometric TiO_{2-x}/TiO_2 layer formed by hydrothermal oxidation; 4—Pt electrodes/(contact zones) deposited by magnetron sputtering.

The next step in a sensor development procedure was based on annealing of Ti-based structures, which was performed at three different temperature regimes:

(i) 50 °C/1 h + 400 °C/2 h temperature for the formation of TiO_{2-x}/TiO_2 (400 °C) structure;

(ii) 50 °C/1 h + 600 °C/2 h temperature for the formation of TiO_{2-x}/TiO_2 (600 °C) structure;
(iii) 50 °C/1 h + 800 °C/2 h temperature for the formation of TiO_{2-x}/TiO_2 (800 °C) structure.

All the aforementioned procedures enabled to form of mixed crystal phase TiO_{2-x}/TiO_2-based heterostructures (Figure 10, layers 4 and 5) at over-layer containing a significant amount of TiO_2 in the form of anatase and/or rutile phases and TiO_{2-x}, which was formed in the deeper layers of the structure below fully oxidized stoichiometric TiO_2.

Finally, platinum-based electrodes were deposited on the formed TiO_{2-x}/TiO_2 (400 °C), TiO_{2-x}/TiO_2 (600 °C) and TiO_{2-x}/TiO_2 (800 °C) layers by magnetron sputtering. The dimensions of the structure were: 8 mm—length of the structure and 3 mm—the distance between platinum electrodes deposited over the TiO_{2-x}/TiO_2-based layer. The thickness of the formed titanium layer was 100 nm.

The measurements were performed at 25 °C (room temperature), 72 °C, 150 °C, 180 °C. The humidity of the supplied aforementioned gaseous materials containing airstream was constant during all parts of measurements with methanol, ethanol, n-propanol, and acetone vapour: partial pressure of water in the airstream was 3.170 kPa, which corresponds to 100% of relative humidity at 25 °C and 101.325 kPa pressure. During the measurement of signals towards the water, initially, a dry air stream was supplied and mixed with 1170 ppm of H_2O containing airstream at the corresponding ratio.

2.3.1.2. Determination of Analytical Signal Towards Reducing Gases by TiO_{2-x}/TiO_2-Structure-Based Sensor

The measurements were performed at 25 °C (room temperature), 72 °C, 150 °C, 180 °C. The humidity of the supplied aforementioned gaseous materials containing airstream was constant during all parts of measurements with methanol, ethanol, n-propanol, and acetone vapour: partial pressure of water in the airstream was 3.170 kPa, which corresponds to 100% of relative humidity at 25 °C and 101.325 kPa pressure. During the measurement of signals towards the water, initially, a dry air stream was supplied and mixed with 1170 ppm of H_2O containing airstream at the corresponding ratio. Measurements of current passing through the sensor structure were performed by potentiostat/galvanostat Autolab 30 Eco Chemie Gmbh (Utrecht, The Netherlands), which was controlled by NOVA software. The TiO_{2-x}/TiO_2 (400 °C) sample was investigated under different constant voltages on the platinum-based electrodes deposited on the TiO_{2-x}/TiO_2 (400 °C) layer using the potentiostat.

Evaluated gas concentrations were fixed at: 105 ppm for water, 118 ppm for methanol, 53 ppm for ethanol, 18 ppm for n-propanol, and 220 ppm for acetone. The electrical resistance of TiO_{2-x}/TiO_2 (400 °C)-based gas-sensitive structure decreased due to their increased conductivity, therefore, current passing through TiO_{2-x}/TiO_2 (400 °C)-based structure increased. These variations of measured current (I) (Figure 11) were converted into resistance (R) of TiO_{2-x}/TiO_2-based structure according to Ohms law:

$$R = V/I \quad (1)$$

where V is applied voltage.

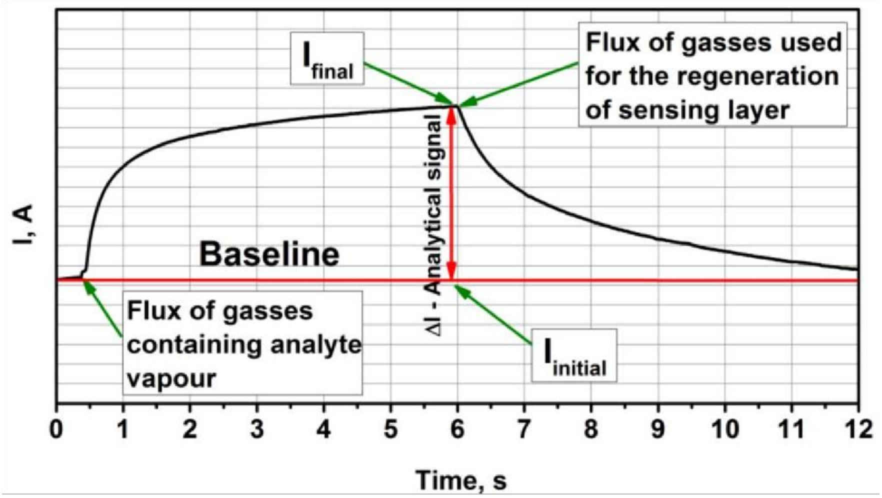

Figure 11. Representation of typical analytical signal registered by TiO_{2-x}/TiO_2 (400 °C)-based structure. It should be noted that ΔI, the duration of signal development and the regeneration of sensor after measurements were different for different gases and different concentrations of those gases.

Then relative response (ΔR, %) was calculated as:

$$\Delta R = 100 \times (R\text{final} - R\text{initial})/R\text{initial}\ (\%) \quad (2)$$

where R_{initial} is initial resistance of TiO_{2-x}/TiO_2 (400 °C)-based structure calculated from I_{initial} at baseline, R_{final}—final resistance calculated from I_{final} (Figure 11).

2.3.1.3 Determination of Electrical Resistance Variation with Temperature

Measurements of resistance vs. temperature were performed by system based on closed-cycle helium cryostat made by Sumitomo Heavy Industries (Tokyo, Japan) combined with RDK-408D 4K cold head and SRDK Series cryocooler and CSA-71A compressor unit. The temperature was controlled by Lakeshore 340 temperature controller (Lake Shore Cryotronics, Inc., Westerville, OH, USA). Resistance was measured by Tektronix DMM 4050 multimeter

(Tektronix UK Ltd., Bracknell, UK). This closed-cycle helium cryostat was used for measurement of resistance and was performed only after exact equilibration of temperature at each selected point in the temperature range from 4.2 K to 310 K, with 5 K intervals between measurement points. Measurements performed in vacuum 10^{-3} Torr.

2.3.2.1. Formation of Electrodes for HER Where Ti, TiO_x and TiO_2 Were Used as Substrates

For this investigation three kinds of Ti surface preparation were used, namely, pure Ti, Ti covered by nanotube-shaped anatase TiO_2 layer via anodizing and calcination, and Ti covered with nanostructured titanium suboxide by hydrothermal treatment under conditions described above. Ti surface anodizing was conducted in the thermostated Teflon cell containing 2.0 mol L^{-1} H_3PO_4 and 0.2 mol L^{-1} NH_4F at 17 ± 0.3 °C and 20 V dc for 1 h. In this setup, two platinum plates were used as cathodes. After anodizing, the specimens were thoroughly rinsed with water, air-dried, and calcined in air at 450 °C for 2 h using a 10 °C min^{-1} temperature ramp. For Ti surface coating with the nanostructured titanium suboxide (TiO_x) film, the specimens were hydrothermally treated in 0.2 mol L^{-1} H_2SeO_3 at 180 °C for 15 h, rinsed, and annealed in the deoxygenated atmosphere by heating together with Cu foil in a sealed glass tube at 300 °C for 10 h. Then on top of these substrates, flower-shaped MoS2 species were formed by the hydrothermal method. The typical solution comprised 5.0 $(NH_4)_6Mo_7O_{24}$, 90 thiourea, and 25 mmol/L aniline. The cleaned specimen was inserted vertically into the solution using a special holder made of Teflon. The synthesis reaction was carried out at 220 °C for 5 to 15 h in a programmable muffle furnace Czermack (Badia Polesine, Italy) using 10 °C /min temperature ramp.

2.3.2.2. Electrochemical Measurements of Catalysts Were Ti, TiO_x and TiO_2 Used as a Substrate Material

Electrochemical measurements were performed in a three-electrode glass cell equipped with the working, Ag/AgCl, KCl reference, and the glassy carbon electrode, as a counter. Prior to the measurements, Ar gas was bubbled through the electrolyte solution for at least 0.5 h to remove the dissolved air. The catalytic performance of prepared electrodes was studied in the solution containing 0.5 mol L^{-1} H_2SO_4 and 0.25 mol L^{-1} formic acid by the potential cycling within 0.05 to -0.35 V vs. reference hydrogen electrode RHE potentials range at the 10 mV s^{-1} scan rate using a workstation ZENNIUM Zahner-Electrik Gmb & Co, KG, Kronach, Germany). Formic acid was added to hinder the destruction of glassy carbon counter electrode in our prolonged HER tests. In the stability tests, up to 3000 cycles were used.

2.3.3.1. MXenes Based SERS Sensor For the Detection of Pharmaceuticals Traces

MXene films on a microscope glass slide were prepared. For this purpose, the glass slides were covered with 0.5 mL of aqueous MXene solution (0.01 g/mL) and dried under a nitrogen atmosphere. $Ti_3C_2T_x$-based MXene film and its interaction with salicylic acid (SA) were investigated by means of Raman spectroscopy. MonoVista CRS+ Raman microscope system (S & I GmbH, Warstein, Germany) equipped with four excitation lasers (457 nm, 532 nm, 633 nm and 785 nm) and a liquid-nitrogen-cooled CCD detector were used for acquiring the spectra. The diameter of the focused laser beam on the sample was ≈ 1 μm, and its power density on the sample was ≈20 kW/cm2 (for 633 nm excitation) and ≈45 kW/cm2 (for 785 nm excitation). Before the measurements, the spectrometer was calibrated to a fundamental vibrational band at 520.7 cm^{-1} of the silicon wafer. Fourier transform MultiRAM spectrometer (Bruker, Mannheim, Germany) equipped with liquid-nitrogen-cooled Ge diode detector was used for the calculations of enhancement factor for salicylic acid–MXene complex with 1064 nm excitation wavelength. Solution of salicylic acid in water with a concentration equal to 2 mM was prepared. Two drops (5 μL each) of the solution were dried on the glass substrate covered by the MXene film. To ensure the most homogenous distribution of salicylic acid molecules, the drying was performed in a confined space when the saturated vapour diminishes the surface tension in the air-water interface and a more uniform distribution can be achieved. The same volume of salicylic acid solution was dried on the aluminium foil as a reference. Salicylic acid solution spread to form a 2 mm spot on the film. After drying out, no crystallization occurred on the MXene film, while on the reference glass substrate, crystals of salicylic acid were formed. Presented SERS spectra of salicylic acid were recorded on 20 randomly chosen positions on the MXene surface and averaged. The standard deviation for the spectral intensity of salicylic acid on MXene substrate was calculated while applying 3 s acquisition time.

2.4. Characterization of Structures

Particles, coatings and other heterostructured materials were characterized using structural and analytical characterization techniques:

- **Scanning electron microscopy** (SEM). The surface morphology, cross-sections and elemental composition of as-synthesized coatings were carried out in a dual-beam system of a scanning electron microscope Helios Nanolab 650 (FEI Quanta 200 F) equipped with an EDX spectrometer X-Max (Oxford Instruments), field emission source and imbedded focus ion beam (FIB) system. It should be noticed that before cross-section analysis, a thin (~ 100 nm) platinum layer was deposited on top of the sample.
- **Raman spectroscopy**. Raman spectra were recorded using an inVia (Renishaw) spectrometer equipped with a thermoelectrically cooled (- 70 °C) CCD camera and microscope. The 532 nm solid-state diode laser beam was used as an excitation source. The laser power at the sample was restricted to 0.06 mW and 0.6 mW for TiNT/Cu_2O and bare Ti oxide, respectively. Raman spectra were taken using a 50× objective lens. The parameters of bands were determined by fitting the experimental spectra with Gaussian-Lorentzian shape components using GRAMS/A1 8.0 (Thermo Scientific) software.
- **X-ray diffraction** (XRD). Phase analysis of NPs and coatings were carried out using a diffractometer SmartLab (Rigaku) with a rotating Cu anode. CuKα radiation ($\alpha = 0.154183$ nm) was separated by a multilayer bent graphite monochromator. The XRD patterns were measured in Bragg-Brentano scan mode with a step 0.02º (in 2θ scale) and a counting time of 8 s per step. Phase identification was performed using the powder diffraction database PDF4+ (2015). The size of NPs was determined by the Halder-Wagner (H-W) approximation.
- **Diffuse reflectance spectra measurements.** Diffuse reflectance spectra of titania films were obtained by means of a Shimadzu UV-VIS-NIR spectrophotometer UV-3600 coupled with a MRC-3100 unit. Measurements were performed by mounting a sample holder onto the integrating sphere. The measurable range of wavelengths falls between 200 nm and 850 nm, covering the UV and visible light regions. In the integrating sphere, one beam strikes the sample normally to the surface while the other beam – aslant. The light absorbance was calculated from the diffuse reflection coefficient using the Kubelka–Munk function.
- **UV-VIS-NIR spectra measurements.** To investigate the optical properties of titania films, the reflectance spectra of the samples were recorded

in the wavelength range of 200–1700 nm using a Shimadzu UV-VIS-NIR spectrophotometer equipped with a MPC-3100 integrating sphere. The specular reflectance of the light from the film surface was calculated using an optical model of two layers. The Bruggeman Effective Medium Approximation (EMA) was applied to calculate the optical constants of the nanoplatelet titanium monoxide film formed on the Ti substrate and consisting of the naturally formed thin layer of TiO_2 and the nanoplatelet titanium monoxide layer with the empty voids. The porosity of films was calculated by fitting the model functions to the measured data using a CompleteEASE software program, as in our previous study of porous alumina.

➢ **X-ray photoelectron spectroscopy** (XPS). XPS measurements were carried out using the ESCALAB MKII spectrometer equipped with a new XR4 twin anode. The non-monochromatic MgKa, X-ray source was operated at hν = 1253.6 eV with 300 W power (20 mA/15 kV) and the pressure in the analysis chamber was lower than 5×10^{-7} Pa during spectral acquisition. The spectra were obtained using an electron analyzer with a pass energy of 20 eV for narrow scans and a resolution of 0.05 eV and with a pass energy of 100 eV for survey spectra. All spectra were recorded at a 90° take-off angle and calibrated using the C 1s peak at 284.6 eV. The spectra calibration, processing and fitting routines were done using the Advantage software (5.918) provided by Thermo VG Scientific. Core level peaks of Ti 2p, Se 3d, and O 1s were analyzed using the nonlinear Shirley-type background and the calculation of the elemental composition was performed on the basis of Scofield's relative sensitivity factors.

➢ **Electron paramagnetic resonance spectroscopy** (EPR). Continuous-wave electron paramagnetic resonance (CW EPR) experiments were performed using a Bruker X-band ELEXSYS E580 EPR spectrometer. The strength and frequency of the modulating field were 0.3 mT and 100 kHz, respectively. Simulations of the CW EPR spectra were performed using EasySpin 5.2.20.

➢ **Computational Methods.** In order to make a more detailed analysis of the interaction between salicylic acid and MXene, theoretical calculations of structure and vibrational spectra of monomeric salicylic acid and salicylic acid dimer were performed by means of quantum chemistry calculations implemented in the Gaussian 09W software package. The salicylic acid dimer was chosen to resemble the crystalline structure of solid-state salicylic acid. The density functional theory (DFT) calculations using B3LYP/6311G++ functional were performed. For the investigation of the salicylic acid–MXene complex, the 2 ×2 ×1 supercell expansion of

$Ti_3C_2(OH)_2$ MXene crystal structure (of 20 atoms) was built and optimized. Initially, geometry optimization was performed separately for salicylic acid (B3LYP/6311G++) and $Ti_3C_2(OH)_2$ cluster (B3LYP/LanL2DZ) and their complex afterwards (B3LYP/LanL2DZ). No virtual frequencies were present after the complex optimization. The excited-state calculations were performed to assess the redistribution of the electronic energy levels.

3. RESULTS AND DISCUSSION

3.1. Hydrothermal synthesis and characterization of titanium suboxides structures

Titanium oxide nanostructures were synthesized hydrothermally in alkaline solutions with the presence of selenious acid at temperatures 150-200°C and with a further calcination step in a range of 300-440°C under reduced oxygen atmosphere. The whole procedure was described in detail in the methodology part. The XRD analysis of synthesized products (Fig 12) shows that crystal phase structures depend and could be controlled by tuning formation parameters forming titanium suboxides structures with stoichiometry from $TiO_{0,84}$ to TiO.

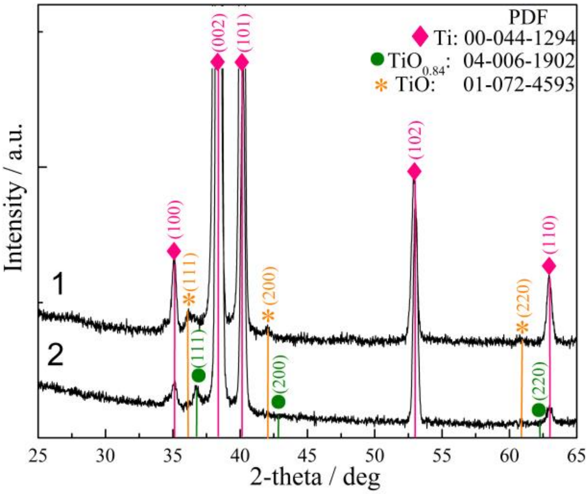

Figure 12. XRD patterns of the film formed at the Ti substrate by hydrothermal treatment in the solution of 0.2 mol L^{-1} H_2SeO_3 (pH = 9.0) at 150 °C for 15 h before (a) and after (b) annealing in the oxygen-free containing atmosphere at 350 °C for 2 h.

XRD data were supported by EPR measurements (Fig. 13) which proves Ti^{3+} existence in the structure. Also, it is a prove of titanium suboxide formation as Ti^{3+} does not exist in a regular TiO_2 (anatase, rutile, brookite).

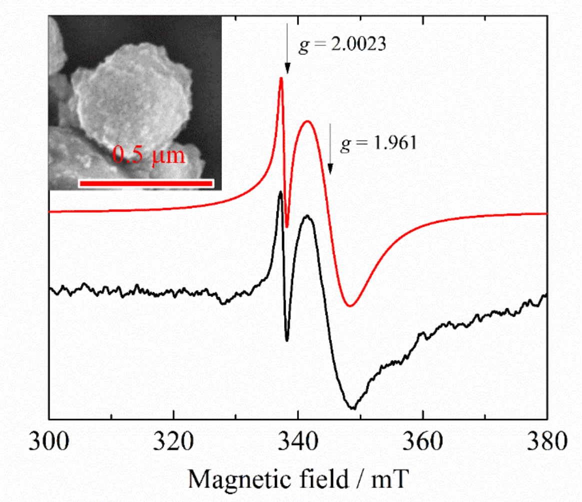

Figure 13. Experimental (black) and simulated (red) CW EPR spectrum of titanium particles hydrothermally treated in the solution of 0.2 mol L^{-1} selenious acid at 180 °C for 45 h. In the inset, SEM image of $TiO_{0.84}$ coated NP.

Calculation of formed titanium oxide thin films showed that the porosity of the structures are nearly 80% (fig 14) and it could be even called metal oxide foam as it has more voids in the structure than solid material. This is a favourable property for the application of such structures in gas sensing or as a substrate for various applications.

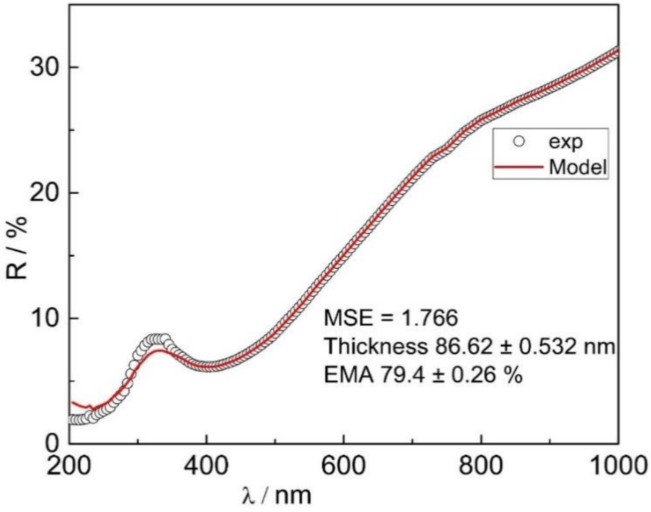

Figure 14. The reflection vs. wavenumber (l) plots for experimental 180 °C $TiO_{0.84}$ film (circles) and the calculated one (line) by the adapted nanoporous film model.

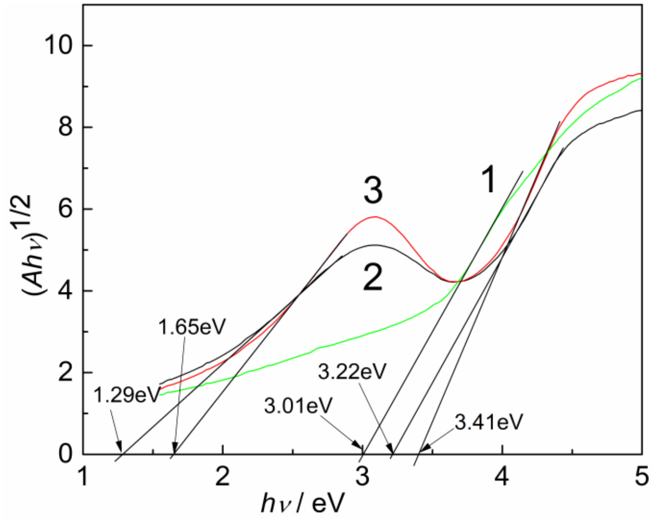

Figure 15. Tauc plots for indirect transitions of titanium monoxide nanoplatelet arrays formed by hydrothermal treatment in the 0.3 mol L^{-1} H_2SeO_3 solution (pH = 9.0) 180 °C for 15 h after calcination in air (1) and oxygen-free atmosphere at 400 °C (2) and 440 °C (3) for 2 h.

After the diffuse reflectance spectra of titania films were registered and bandgap values calculated it was observed that hydrothermally formed titanium suboxides possess significantly narrow bandgaps. As 1.29 – 1.65 eV are energies for the visible light spectrum it opens a variety of new possible application areas. It is important to note that regular titania in all its forms also has applications where activation of UV light is necessary and a significantly lower bandgap should make activation possible with visible light.

3.2. Application of titanium suboxides as substrates for HER catalysts

After hydrothermal formation of titanium suboxide thin films on top of these structures, MoS_2 were grown as well by hydrothermal method. Ti/TiO_x/MoS_2-based electrodes were formed and their performance as electrocatalyst was tested (Fig. 16). The catalytic performance of prepared electrodes was studied in the solution containing 0.5 mol L^{-1} H_2SO_4 and 0.25 mol L^{-1} formic acid by the potential cycling within 0.05 to -0.35 V vs. the reference hydrogen electrode RHE potentials range at the 10 mV s^{-1} scan rate.

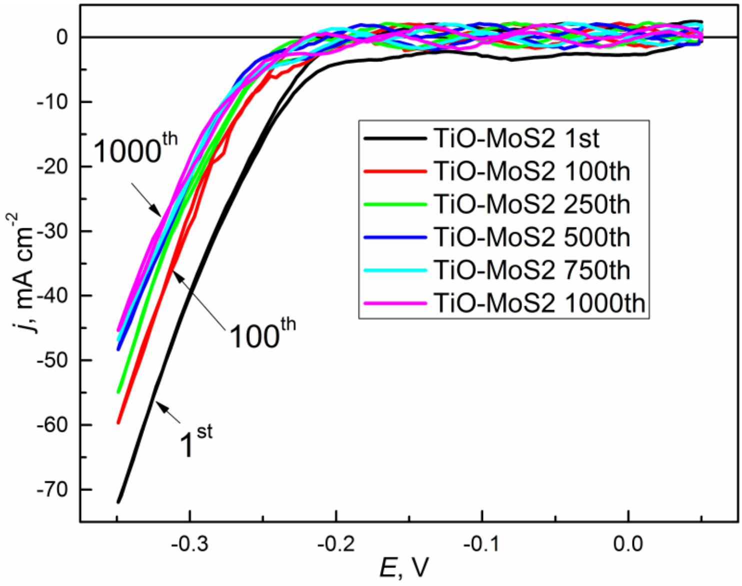

Figure 16. HER voltammograms at indicated potential scan number for the Ti/TiO_x/MoS_2-based electrode in the 0.5 H_2SO_4 and 0.25 mol L^{-1} COOH solution at 10 mV s^{-1} potential scan rate.

Electrochemical tests in the acidic solution showed that the H_2 evolution reaction at the surface of this film proceeds initially from the onset potential of ~170 mV vs. RHE (Figure 16) that can be linked with the higher electrical conductivity of titanium monoxides compared to TiO_2. However, the activity of this electrocatalyst decreases during prolonged potential cycling attaining 50–45 mA cm^{-2} after 1000 cycles. Moreover, the pulsation of j(E) plots that were not characteristic for other substrates, was determined (Figure 16).

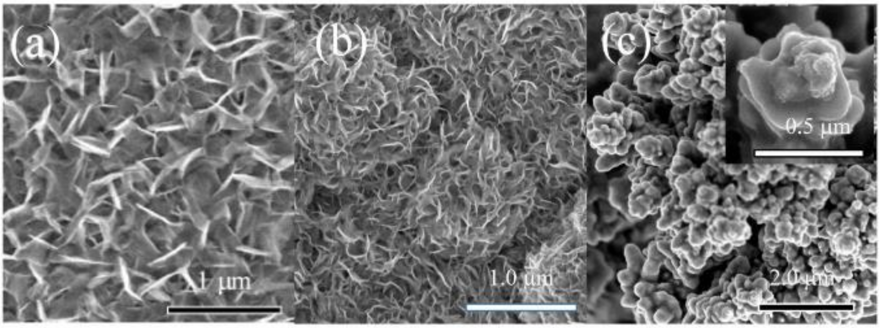

Figure 17. Top-side SEM views of TiO_x (a) and TiO_x/MoS_2 film (b) surfaces before (b) and after (c) potential cycling in the solution of 0.5 H_2SO_4 + 0.25 mol L^{-1} formic acid at 10 mV s^{-1} within -0.45 to 0.05 V potential range for a period of 1000 potential scans.

The effect of the pulsation of j(E) plots might be linked with the polymerization of aniline molecules entrapped during MoS_2 hydrothermal synthesis and unhooked during the intense HER processing, covering MoS_2 platelets as clearly evidenced by the top-side film SEM image presented in Figure 17c. Figure 17. Top-side SEM views of TiO_x (a) and TiO_x/MoS_2 film (b) surfaces before (b) and after (c) potential cycling in the solution of 0.5 mol L^{-1} H_2SO_4 and 0.25 mol L^{-1} formic acid at 10 mV s^{-1} within −0.45 to 0.05 V potential

3.3. Application of titanium suboxides as a sensing material for volatile organic compounds detection

Titanium suboxide based gas sensor was prepared in a way described in a methodology part. SEM images of the surface morphology of samples are depicted in figure 18. It is seen that surface of these samples were nanoplatelet and had a high surface area what is favourable for gas sensors.

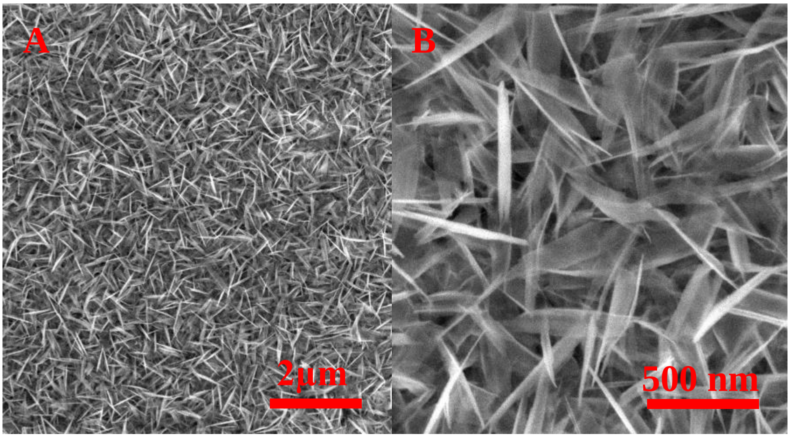

Figure 18. Scanning electron microscope (SEM) images of TiO_{2-x}/TiO_2 (400 °C)-based hetero-structure at different magnification.

Changes of electrical current passing through TiO_{2-x}/TiO_2-based hetero-structure at fixed potential were evaluated and recalculated into changes of resistance (ΔR %). ΔR was evaluated as an analytical signal of this sensor. Results presented in Figure 19 illustrate that already at room temperature (25 °C) the sensor shows some sensitivity towards humidity and to all tested gaseous materials (methanol, ethanol, n-propanol, acetone) evaluated here. But the signals determined amperometrically at constant 0.5 V potential, which was required for the achievement of 25 °C, temperature towards humidity and towards all the aforementioned gases were different. In the presence of water, the resistance decreased, while in the presence of methanol, ethanol, n-propanol and acetone the resistance of the sensor increased.

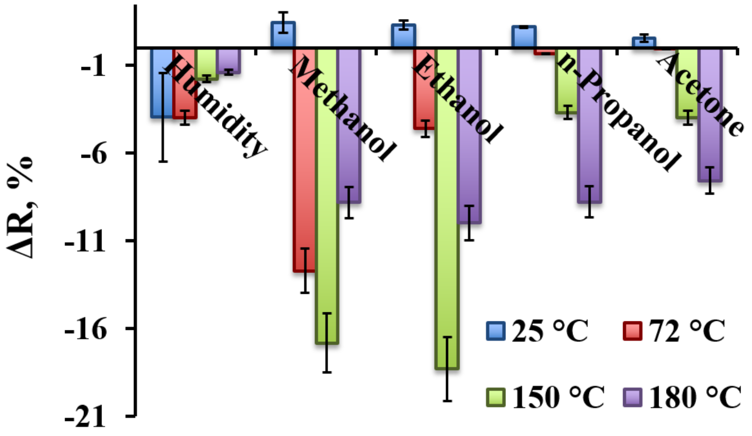

Figure 19. The response of TiO_{2-x}/TiO_2 (400 °C)-based hetero-structure towards humidity (H_2O), methanol, ethanol, n-propanol, and acetone at different temperatures (25–180 °C).

Different sensitivities towards various gaseous materials at different temperatures opens the avenue to apply the array based on similar TiO_{2-x}/TiO_2-based hetero-structures, where between Pt electrodes different constant potential will be applied and this will heat these structures up to different temperatures, where TiO_{2-x}/TiO_2-based structures will have different sensitivities. Therefore, the read-out signals from such arrays can be evaluated by analysis of variance (ANOVA)-based approaches and interpreted as analytical signals. With the applied ‘self-heating’ of the sensor, the best selectivity towards methanol was achieved at 72 °C, and for ethanol, the temperature was 150–180 °C. For n-propanol and acetone signals increase with heating and reaches their maximum at 180 °C. Thus TiO_2 thin films are the best for methanol detection at 72 °C, for ethanol at 150 °C and for acetone at 180 °C as the response to other gases are significantly lower. There are some indications that to all other gaseous materials investigated here, TiO_{2-x}/TiO_2-based hetero-structures were the most sensitive at even higher temperatures, but these temperatures were not available due to limitations of our experimental set up.

3.4. Synthesis of Ti_3C_2 MXenes and application for detection of salicylic acid

The structure and morphology of the MAX phase and synthesized MXene-based materials were evaluated using the scanning electron microscopy (SEM) imaging technique (Figure 20). Etching with 5 wt.% HF solution allows preparing $Ti_3C_2T_x$, for which the structure is quite similar to that of the MAX phase. However, MXene layers were slightly opened. The ‘accordion-like’ structure was not observed. A possible explanation may be found in low hydrofluoric acid concentration, which is insufficient for the formation of a sufficient amount of H_2 evolving during the exothermic reaction of hydrofluoric acid with aluminium atoms. Successful etching of aluminium atoms was confirmed by energy-dispersive X-ray spectroscopy (EDX) analysis (Table 3). It was revealed that the number of aluminium atoms in MXenes decreased by five times in comparison with the initial amount of these atoms in the MAX phase.

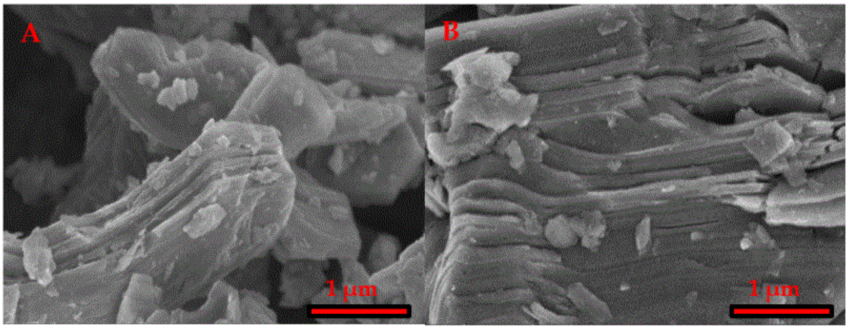

Figure 20. SEM images of (A) MAX phase (Ti_3AlC_2) and (B) MXenes ($Ti_3C_2T_x$).

Table 3. EDX analysis results for aluminium (Al) and titanium (Ti) atomic ratio in MAX phase and MXene samples.

Sample	Atomic Ratio, %	
	Aluminium (Al)	Titanium (Ti)
MAX Phase (Ti_3AlC_2)	39.39 ± 0.96	60.61 ± 0.96
MXenes ($Ti_3C_2T_x$)	6.33 ± 1,97	93,67 ± 1.97

Comparing resistivity of MAX phase and MXenes etched in 5 wt.% HF, it was measured that the resistivity of samples at room temperature decreased from 36 Ω to 20.5 Ω. A decrease in sample resistivity might be explained by a reduced amount of aluminium by etching and the formation of semi-metallic Ti_3C_2 MXene structures.

The synthesis of MXenes was confirmed using XRD analysis (Figure 21). A shift of the (002) peak of Ti_3AlC_2 at 9.5° to 7.3° for the $Ti_3C_2T_x$ was observed. Such sufficiently large shift is typical for wet multilayered MXene samples [39], whereas an intense and sharp (002) peak is characteristic for MXenes etched by hydrofluoric acid [40]. Such results, together with the absence of other MAX phase characteristic peaks in MXene spectra, coincide with EDX analysis results and confirm successful etching of Al out of Ti_3AlC_2.

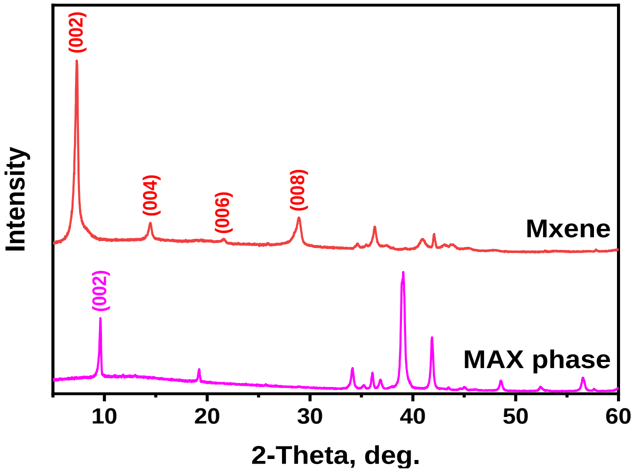

Figure 21. XRD patterns of MAX phase (Ti_3AlC_2) and MXene ($Ti_3C_2T_x$) powders.

An interesting effect was observed when salicylic acid (SA) solution was dried on the MXene thin film of 70 nm thickness. The measured Raman spectrum of salicylic acid on MXene film clearly differs from that of crystalline salicylic acid (Figure 22). The redshifts of the vibrational bands are evident and indicate an interaction between salicylic acid molecules and the $Ti_3C_2T_x$-based MXene film. The appearance of prominent Raman spectral bands at 896 cm^{-1} and a band doublet at 681 cm^{-1} and 654 cm^{-1} confirms the interaction between salicylic acid and the MXene. Based on our DFT calculations performed for monomeric salicylic acid molecule and salicylic acid dimer (as in crystalline salicylic acid form), these newly emerged bands can be assigned to out-of-plane vibrations of CH groups and out-of-plane ring deformation, respectively.

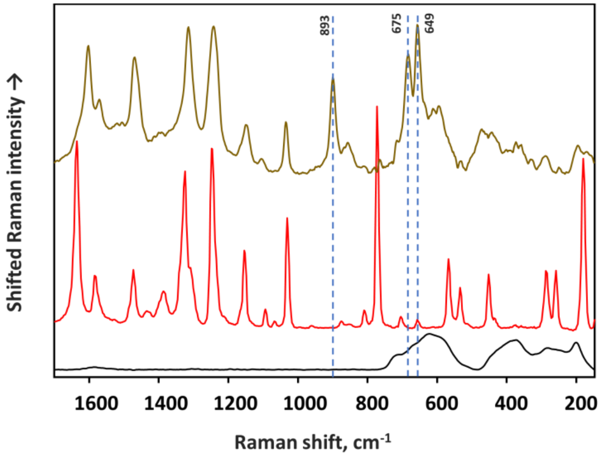

Figure 22. Raman spectra of MXene film (bottom) and salicylic acid: dried on MXene surface (middle) and on aluminium foil (top). Excitation wavelength—633 nm.

Comparing salicylic acid deposited directly on the aluminium surface and on the Mxene film, enhancement factor reached 125, 110 and 220 for the band at 896 cm^{-1} and band doublet at 681 cm^{-1} and 654 cm^{-1}, respectively (532 nm excitation).

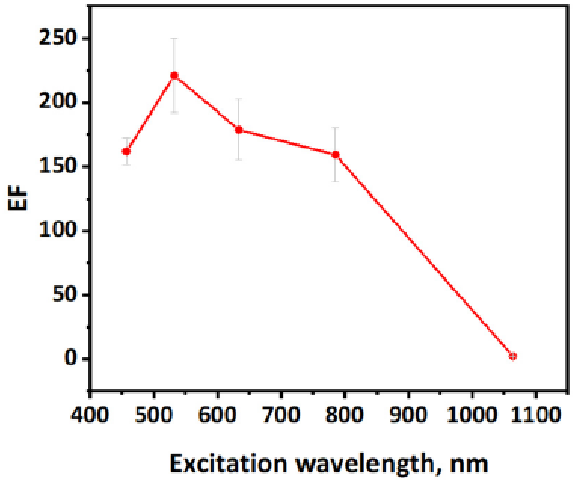

Figure 23. Calculated SERS enhancement factor (EF) for 2 mM salicylic acid dried on the MXene film with different excitation wavelengths.

Based on the spectra acquired at different excitations, the enhancement factor dependence on the excitation can be evaluated (Figure 23). To minimize the influence of spectrometer response to a different wavelength, the crystalline salicylic acid was acquired with each excitation, and the salicylic acid–MXene complex spectrum was compared to crystalline salicylic acid spectrum acquired at the same conditions.

CONCLUSIONS

1. For the first time it was determined that nanoplatelet shaped titanium suboxide structures could be formed on titanium substrates in an alkaline 0,05 - 0,5 mol L^{-1} selenious acid solutions by the hydrothermal synthesis performed for 0,5 - 2 days in a temperatures range of 150 - 200°C with subsequent calcination under oxygen-free atmosphere.
2. Hydrothermally formed non-stoichiometric titanium oxides porosity is as high as 80%, while bandgaps are as low as 1,29 eV. These characteristics are favourable for applications in sensorics and composite material formation.
3. Hydrothermally formed titanium suboxide thin films can be used as substrates for electrocatalyst and have a positive impact in comparison to metal substrates for $Ti/TiO_x/MoS_2$-based electrode stability used in hydrogen evolution reaction. The catalytic performance of prepared electrodes was studied by the potential cycling within 0,05 to -0,35 V vs. the reference hydrogen electrode RHE potentials range at the 10 mV s^{-1} scan rate.
4. Hydrothermally formed titanium suboxide thin films heterostructured with TiO_2 have an ability to heat itself under voltage of 0,5 to 5 V, while the resistivity of the sensing layer is changing being in contact with volatile organic compounds vapours such as methanol, ethanol, n-propanol and acetone. Sensitivity to these gases depends on the operating temperature and it makes TiO_x-based sensor selective to test gases under different temperatures.
5. MXenes ($Ti_3C_2T_x$) „accordion-like“ structures can be made from its precursor of Ti_3AlC_2 after selective etching in a 5% hydrofluoric acid solution for 24 hours at 25°C. MXenes substrates thickness of 70 nm can be used for the detection of salicylic acid by surface-enhanced Raman spectroscopy due to substantial enhancement of out-of-plane bending modes of salicylic acid at 896 cm^{-1}, 681 cm^{-1} and 654 cm^{-1}.
6. Due to values of calculated experimental enhancement factors, it was indicated that chemical enhancement mechanisms are dominant in SERS spectra of salicylic acid adsorbed on the MXene surface. For the deformation out-of-plane vibrational modes, this factor varies from 220 (at $\lambda = 532$ nm) to 60 (at $\lambda = 1064$ nm).

SANTRAUKA

Įvadas

Titano dioksidas yra detaliai ištirta medžiaga ir jau yra atlikta daug ir nuodugnių tyrimų susijusių su titano dioksido (TiO_2) sinteze ir pritaikymu. Titano dioksidas plačiai taikomas ir praktikoje, tačiau siekiant dar labiau išplėsti titano dioksido taikymo sritis, vienas iš didžiausių iššūkių yra praplėsti arba pagerinti titano dioksido savybes [1]. Siekiant praplėsti titano dioksido savybes, vienas iš galimų kelių yra formuoti nestecheometrinius titano oksidus (TiO_{2-x}) arba struktūras susidedančias iš Magnéli fazių (Ti_nO_{2n-1}) [2]. Taip pat, vis daugiau dirbama ties nauja medžiagų klase „Maksenais“, kurių struktūrinė formulė yra ($Ti_3C_2T_x$). Šios medžiagos pasižymi patraukliomis optinimėmis savybėmis, kurios kaip manoma yra nulemtos Ti^{3+} bei nestecheometrinių jo oksido susidarymu ant įvairių struktūrų paviršiaus [3]. Pagrindiniai iššūkiai kylantys formuojant šias medžiagas yra siejami su jų stabilumu įvairiose terpėse. Šiame darbe daug dėmesio skirta nanostruktūrizuotoms titano dioksido (TiO_2), nestechiometrinio titano oksido (TiO_{2-x}) bei Magnéli fazių (Ti_nO_{2n-1}) pagrindu suformuotoms struktūroms, kurios yra tinkamos naudoti kaip optiškai aktyvios, jutikliuose pritaikomos bei parankios auginti heterostruktūroms, medžiagos [2,4].

Stecheometrinis TiO_2 yra n-tipo puslaidininkis. Jis sutinkamas trijose skirtingose kristalinėse fazėse (anatazo, rutilo ir brukito). Siekiant pagerinti jutimines TiO_2 savybes, jautrus sluoksnis dažnai sudaromas iš skirtingų jo kristalinių fazių [5]. Be to, kuriant jutiklius pastaruoju metu vis daugiau dėmesio sulaukia nestecheometriniai titano oksidai, kurie literatūroje yra aprašomi struktūrinėmis formulėmis: TiO_n, TiO_{2-x} bei (Ti_nO_{2n-1}) įvardijamų Magnéli fazėmis [6].

Šiuo metu kuriamų ir taikomų dujų jutiklių jautrumas yra didelis, tačiau iššūkių kyla su jų atrankumu bei dideliu energijos kiekiu, reikalingu sensoriaus pašildymui iki darbinės temperatūros. Pastaroji dažnai siekia kelis šimtus laipsnių. Siekiant išspręsti šias problemas, pasitelkiami šie sprendimai: pirma, naudojami save kaitinantys jutikliai [7], antra, tobulinama jutiklio paviršiaus morfologija leidžianti pasiekti didesnį atrankumą [8], trečia, kuriamos šerdies-apvalkalo struktūros [9], pvz. kvatiniai taškai [10], kur šerdį sudaranti medžiaga yra apvelkama kita medžiaga, turinčia esminę įtaką hibridinės struktūros jutiminėms savybėmis.

Pastaruoju metu pasiektas proveržis ir optiškai aktyvių titano karbidų, dar kitaip vadinamų Maksenais ($Ti_3C_2T_x$), formavime. Šie tyrimai paskatino 2D medžiagų pritaikymo paieškas biojutikliuose, biokuro elementuose, bioelektronikoje. Nors Maksenai pasižymi savybėmis pritaikomomis biojutikliuose, tačiau tai nėra jų vienintelė panaudojimo sritis. Kadangi svarbi Maksenų savybė yra jų didelis ir artimas metaliniam laidumas sąlygotas paviršinių funkcinių grupių [12], kas leidžia tikėtis jų galimo pritaikymo ateities elektronikoje [16], superkondensatoriuose [13], jutikliuose [14] bei įvairiose kitose elektrochemijos srityse [15]. Didelė laisvų elektronų koncentracija ir plazmoninis efektas leidžia klasifikuoti maksenus kaip metalus, kuriuose plazmoninių virpesių dažnis priklauso nuo laisvų elektronų tankio [17]. Dėl šios priežasties Maksenai gali būti panaudotini kaip pakaitalai metalinėms nanostruktūroms gebančioms efektyviai sustiprinti vidines molekulių vibracijas artimu atstumu, kas yra pritaikoma paviršiaus susitiprintoje Ramano spektroskopijoje [18] ir valdyti šviesos srautus.

Darbo tikslas

Susintetinti siaura draustine juosta pasižyminčias titano nanodarinių struktūras, charakterizuoti ir rasti galimus taikymus.

Darbo uždaviniai

- ✓ Susintetinti siaura draustine juosta pasižyminčius titano suboksido plonus sluoksnius bei daleles naudojant hydroterminį sintezės metodą ir atkaitinimą bedeguonėje aplinkoje.
- ✓ Susintetinti (Ti_3C_2) maksenų struktūras iš Ti_3AlC_2 pirmtako naudojant praskiestus vandenilio fluorido rūgšties tirpalus.
- ✓ Charakterizuoti titano suboksido ir Maksenų (Ti_3C_2) struktūras.
- ✓ Rasti suformtuotoms TiO_x ir Maksenų struktūroms pritaikymus jutikliuose bei kataliziniuose procesuose.

Darbo naujumas

- ✓ Pirmą kartą nustatyta, kad hidroterminis formavimas bei vėliau sekantis atkaitinimas bedeguonėje aplinkoje, skirtingai nei kiti įvairių titano suboksidų formavimo būdai leidžia formuoti didelio pavišiaus ploto nanostruktūras ir valdyti šių struktūrų paviršiaus morfologiją, fazinę sudėtį bei draustinės juostos plotį.
- ✓ Pirmą kartą parodyta, kad dideliu poringumu ir paviršiaus plotu pasižyminčius hidroterminiu būdu suformuotus suboksidus panaudojant kaip pagrindus MoS_2 elektrokatalizatoriams vandenilio skyrimosi reakcijai

iš rūgštinių tirpalų inicijuoti, galima pasiekti žymiai didesnį stabilumą, nei formuojant MoS_2 katalizatorius ant metalinių paviršių.

- ✓ Pirmą kartą parodyta, kad titano suboksido pagrindu suformuoti dujų jutikliai pasižymi savybe ne tik detektuoti dujas, tačiau ir kaisti savaime, pasiekiant aukštas darbines temperatūras.

- ✓ Pirmą kartą iš Ti_3C_2 Maksenų buvo suformuoti paviršiai tinkami salicilo rūgšties aptikimui sustiprintos Ramano spektroskopijos pagalba.

Ginamieji teiginiai

- ✓ Hidroterminiu sintezės metodu selenitinės rūgšties šarminiuose tirpaluose galima formuoti nanolapelinės morfologijos titano suboksido nanostruktūras ant titano paviršiaus.
- ✓ Hidroterminiu sintezės metodu panaudojus selenitinę rūgštį suformuotos titano suboksido nanostruktūros yra itin poringos ir lyginant su stecheometriniais titano oksidais, pasižymi siaura draustine juosta.
- ✓ Titano pagrindų, dengtų nestechiometrinės sudėties oksidais, paviršiuje galima konstruoti MoS_2 struktūras elektrokataliziniam vandens molekulių skaldymui.
- ✓ Maksenų ($Ti_3C_2T_x$) struktūros gali būti susintetintos iš Ti_3AlC_2 atliekant selektyvų aliuminio išėsdinimą praskiestuose vandenilio fluorido rūgšties tirpaluose.
- ✓ Titano suboksido ir maksenų ($Ti_3C_2T_x$) struktūros panaudotinos jutiklių formavime.
- ✓ Pagrindai suformuoti iš maksenų ($Ti_3C_2T_x$) yra tinkami salicilo rūgšties detekcijai paviršiaus sustiprinta Ramano spektroskopija.

Autoriaus indėlis

Disertacijos autorius pats sintetino ir formavo disertaciniame darbe minėtas struktūras. Taip pat pats paruošė bandinius SEM, PEM, XPS, EPR ir Ramano spektroskopijos analizėms. Be to, autorius svariai prisidėjo analizuojant gautus eksperimentinius duomenis, kūrė grafines iliustracijas bei rengė mokslines publikacijas. Žodinius ir stendinius pranešimus tarptautinėse konferencijose pristatinėjo pats. Visi neorginalūs paveikslai teikiami šiame darbe yra cituojami.

4. LITERATŪROS APŽVALGA

4.1. Titano suboksidai: nauja medžiagų klasė

Titano dioksidas (TiO_2) priklauso medžiagų grupei, kuri pastaruosius tris dešimtmečius buvo aktyviai tyrinėjama dėl unikalių optinių, dielektrinių, katalizinių savybių, taip pat cheminio atsparumo, mechaninio stiprumo, biosuderinamumo bei lengvo ir pigaus apdirbimo. Yra žinomos trys kristalinės TiO_2 formos: anatazas, rutilas ir brukitas [1]. Tyrimų metų nustatyta, kad anatazo ir rutilo kristalinės fazės pasižymi 3,23 eV ir 3,02 eV draustinėmis juostomis, dėl ko šios medžiagos puikiai absorbuoja UV spinduliuotę [1]. Šios savybės sėkmingai panaudotos fotokatalizėje, saulės kolektoriuose [19], dujų sensoriuose [20], apsauginiuose kremuose ir daugiasluoksnėse dangose [1]. Siekiant kontroliuoti TiO_2 absorbcijos kraštą regimosios šviesos srityje, dažniausiai pasitelkiamos tokios technologijos kaip: (I) titano oksido dopavimas įvairiais elementais kristalinėje gardelėje užimančiais tiek Ti, tiek ir O pozicijas [21], (II) titano oksido hibridizacija su kvantiniais taškais bei nanodalelėmis pasižyminčiais siauresniu draustinės juostos tarpu [22], (III) defektinių titano suboksidų struktūrų formavimas, kuriose yra deguonies trūkumas [23].

Nestecheometrinių puslaidinikinėmis savybėmis pasižyminčių titano oksidų dar kitaip vadinamų titano suboksidų formavimas yra naujausia tyrimų kryptis siekiant formuoti siauros draustinės juostos titano oksidus. Šios medžiagos pasižymi vakancijomis, kurios gali būti pasiskirsčiusios tarp tiek titano, tiek ir deguonies atomų padėčių ir yra aprašomos bendra formule Ti_nO_{2n-1}, kur $n \geq 2$ [2].

4.2. Maksenai: medžiagos apibūdinimas ir pagrindinės savybės

Maksenai neseniai (2011) pasirodė kaip nauja 2D medžiagų klasė pasižyminti metaliniu laidumu [122,123] bei pasižyminti puslaidininkinėmis savybėmis, kurios gali būti pritaikomos kuriant jutiklius, biojutiklius, biokuro elementus bei nešiojamus bioelektronikos įrenginius. Maksenai turi struktūrinių panašumų bei panašių fizikinių savybių su kita 2D struktūra – grafenu [124,125]. Dauguma Maksenų yra 2D pereinamųjų metalų karbidai [123]. Kaip ir karbidai, 2D pereinamųjų metalų nitridai bei karbonitridai taip pat priklauso Maksenų medžiagų klasei [126]. Maksenai papratai yra formuojami ėsdininant medžiagas-pirmtakus vadinamąsias "MAX fazes", kurios aprašomos bendrine formule $M_{n+1}AX_n$, kurioje M – pereinamasis metalas (Ti, Sc, Zr, Cr, V, Mn, Hf, Nb, Mo, Ta), A – periodinės lentelės 12,13,14,15 ar 16 grupės elementai (Al, Cd, Si, S, P, Ga, As, Ge, In, Tl, Sn, Pb) [15, 127-130], o X – anglis (C), azotas (N) arba jų mišinys [131-134], o n – gali būti tarp 1 ir 3 [131, 132, 134-136].

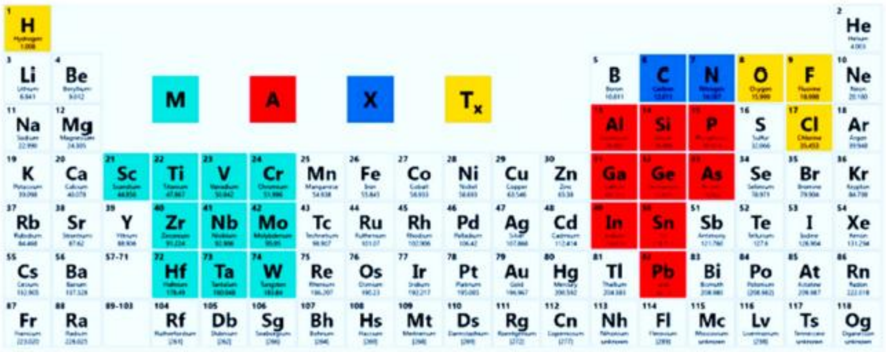

1 Pav. Galimos Maksenų ir MAX fazes kompozicijos pažymėtos periodinėje elementų lentelėje. Paimta iš [127]

Pastaraisiais metais šių medžiagų tyrimų sparčiai daugėjo. Tame tarpe, $Ti_3C_2T_x$ (T_x – čia žymi paviršines funkcines grupes, kurias paprastai sudaro -O, -OH or -F) Maksenai suformuoti iš Ti_3AlC_2 (MAX fazes) iki šiol buvo tyrinėjami daugiausia [137-139]. Unikali paviršiaus morfologija ir kompozicija skatina šių medžiagų taikymą jutikliuose [140-141], katalizėje [142-144], o tokios savybės kaip didelė absorbcija UV-Vis-NIR srityje – taikymus saulės šviesos absorberiuose ir kituose enegijos konvertavimo įrenginiuose [145]. Nustatyta, kad Maksenai pasižymi metalams būdingomis savybėmis,- turi artimą metaliniam laidumą ir artimą metalams elektronų tankį [3, 146, 147]. Manoma, kad šias metalams būdingas savybes lemia paviršiaus funkcinės grupės ir leidžia tikėtis Maksenų pritaikymo elektronikoje [154], superkondensatoriuose [148-149], jutikliuose [150-152] bei kitose elektrochemijos srityse [153]. Dėl artimos metalams laisvų elektronų koncentracijos bei plazmoninio atsako į kintantį elektrinį lauką, galima tikėtis, kad Maksenai ras taikymą ir spektroskopijoje. Panašiai kaip ir kitos plazmoninės medžiagos Maksenai pasižymi plazmonų rezonansu tad gali būti naudojami kaip pakaitalai metalų nanostruktūroms gebančių sustiprinti vidines molekulių vibracijas artimu atstumu ir panaudoti paviršiaus sustiprintoje Ramano spektroskopijoje (SERS) [17,155,156].

5. EKSPERMENTO METODIKA

5.1. TiO_x plonų sluoksnių sintezė

Prieš sintezę titano folijos paviršius buvo valomas ultragarsinėje vonelėje po 6 min iš eilės etanolyje, acetone ir galiausiai vandenyje. Tuomet natūralus oksido sluoksnis buvo pašalinamas ėsdinant 10 sekundžių kambario temperatūros tirpale susidedančiame iš H_2O, HNO_3 ir HF (20 %) (5: 4: 1 santykiu). Po ėsdinimo titano elektrodas buvo nuplaunamas distiliuotu vandeniu ir įmontuojamas į autoklavą su jau paruoštu reakcijos tirpalu. Reakcijos tirpalas: 0,05 – 0,5 mol L^{-1} selenitinės rūgšties vandeninis tirpalas, kurio pH nuo 9 iki 12, buvo sukurtas, optimizuotas ir naudojamas šiam darbui FTMC laboratorijoje. Titano elektrodai autoklave buvo įtvirtinami vertikaliai naudojant tefloninį laikiklį. Sintezės buvo atliekamos 15 – 45 valandas temperatūrą keliant tolygiai 10°C/min iki 150 – 200 °C. Po sintezės, titano suboksido elektrodai buvo nuplaunami distiliuotu vandeniu. Galiausiai, siekiant suformuoti kristalinę titano suboksidų struktūrą, pavyzdžiai buvo atkaitinami bedeguonėje atmosferoje 300 – 440 °C temperatūroje.

5.2. TiO_x dalelių sintezė

Submikrometrinio dydžio titano suboksido dalelės buvo sintetinamos panašiai kaip ir ploni sluoksniai. Sintezės metu naudota ta pati įranga bei tirpalai. Darbiniu paviršiumi tarnavo submikrometrinio dydžio gryno titano dalelės. Atlikus hidroterminę sintezę ir surinkus daleles centrifugavimo būdu bei jas kruopščiai išplovus vandeniu jos buvo atkaitinamos bedeguonėje atmosferoje 300 – 440 °C temperatūroje.

5.3. Maksenų (Ti_3C_2) sintezė

Maksenai (Ti_3C_2) buvo susintetinti atrankaus ėsdinimo būdu iš pirmtako Ti_3AlC_2 praskiestoje (5 w %) HF rūgštyje, ėsdinimą atliekant 24 valandas. Šis atrankus ėsdinimas panaudotas aliuminio pašalinimui iš struktūros bei į “okordeoną” panašios struktūros maksenų formavimui. Po ėsdinimo gauti Maksenai buvo išplaunami nuo rūgšties likučių cetentrifuguojant distiliuotame vandenyje prie 9000 rcf iki neutralaus pH.

6. TYRIMO REZULTATAI IR JŲ APTARIMAS

6.1. Titano suboksido sintezė hidroterminiu būdu ir savybių tyrimas

Titano oksido nanostruktūros buvo sintetinamos hidroterminiu būdu šiame darbe sukurtame šarminiame selenitinės rūgšties tirpale esant 150-200°C. Suformuotos hierarchinės TiO struktūros vėliau buvo atkaitinamos 300-440°C bedeguonėje atmosferoje. Visos formavimo procedūros detaliai aprašytos metodinėje dalyje. Iš rentgeno spindulių difraktogramos (2 Pav.) matyti, kad medžiagos kristalinė fazė priklausomai nuo formavimo sąlygų kontroliuojamai kinta tarp $TiO_{0,84}$ ir TiO.

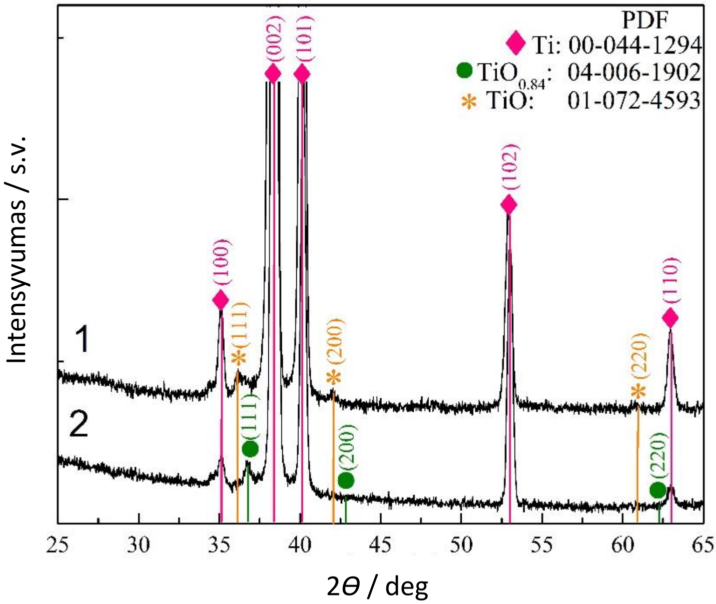

2 Pav. Plonų sluoksnių suformuotų ant metalinio titano pagrindo per 15 valandų trukmės hidroterminę sintezę 0.2 mol L^{-1} H_2SeO_3 (pH = 9.0) vandeniniame tirpale prie 150 °C prieš (2) ir po (1) 2 valandų trukmės atkaitinimo prie 350 °C rentgeno spindulių difraktogramos.

Rentgeno spindulių difraktogramų duomenys buvo papildyti elektronų paramagnetinio rezonanso spektroskopijos matavimais (3 Pav.), kurie įrodo Ti^{3+} egzistavimą struktūroje. Tuo pačiu, tai yra ir titano suboksido formavimosi įrodymas, kadangi Ti^{3+} nėra būdingas įprastam TiO_2 (anatazui, rutiliui ar brukitui)

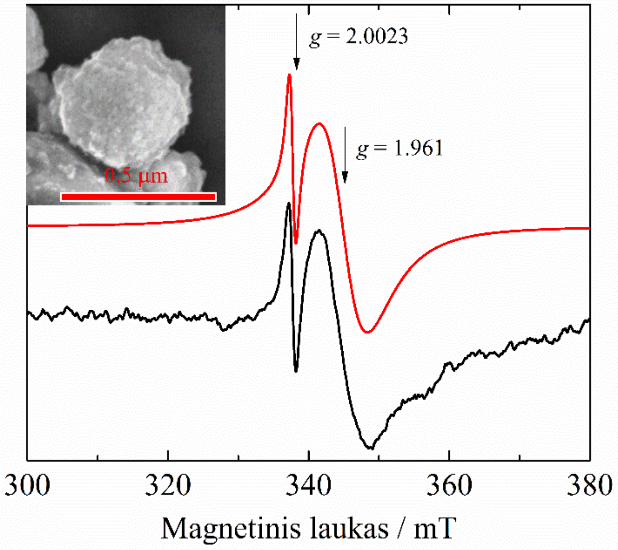

3 Pav. Hidrotermiškai suformuotų titano suboksido dalelių EPR spektrai: eksperimentiškai užrašytas (juoda) ir simuliuotas (raudona).

Atlikti skaičiavimai rodo, kad susintetintų titano suboksidų ploni sluoksniai pasižmi dideliu poringumu, kuris yra artimas 80% (4 Pav.). Dėl to šios struktūros gali būti laikomos metalo oksido putomis, nes struktūroje yra daugiau tuštumų, nei medžiagos (4 Pav. intarpas). Tai yra palanki savybė siekiant pritaikyti šiuos plonus sluoksnius dujų sensoriuose ar panaudoti kaip pagrindą įvairiems kitiems taikymams.

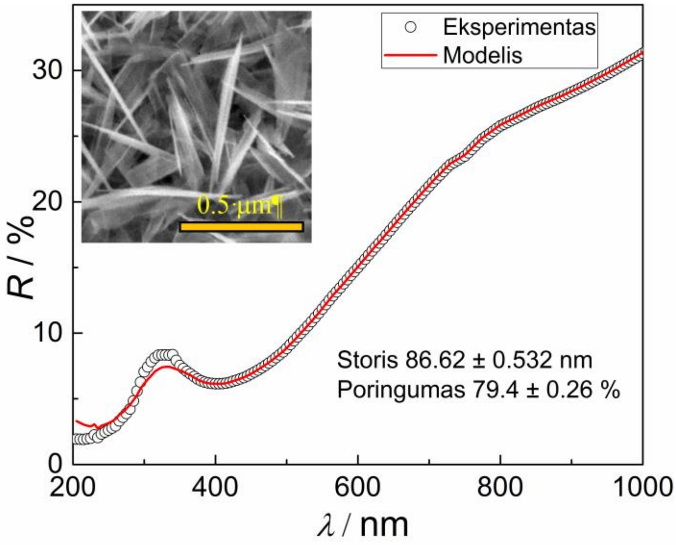

4 Pav. Atspindžio ir bangos ilgio eksperimentinė $TiO_{0.84}$ (apskritimai) ir sumodeliuota (raudona linija) priklausomybės pritaikius poringo sluoksnio modelį. Intarpe: dangos paviršiaus SEM vaizdas.

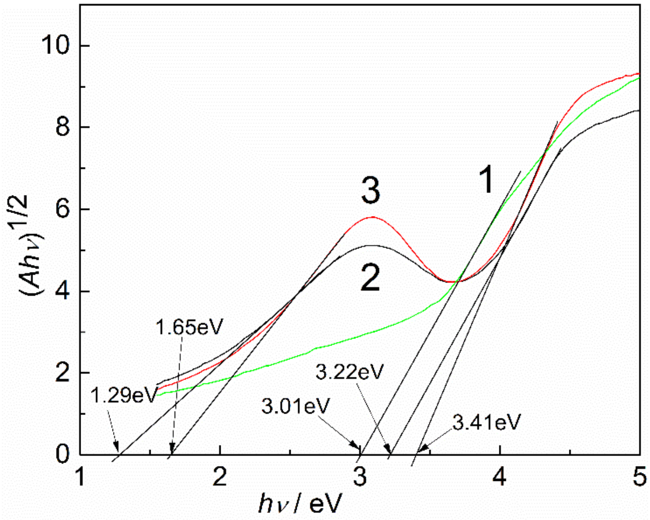

5 Pav. Tauk priklausomybės netiesiniams perėjimams titano suboksido sluoksniuose suformuotuose hidroterminiu būdu

Užregistravus difuzinio atspindžio spektrus ir suskaičiavus draustinių juostų pločius (5 Pav.) nustatyta, kad hidrotermiškai suformuoti titano suboksidai pasižymi ženkliai mažesniu draustinės juostos pločiu, E_g. Kadangi 1,29 – 1,65 eV patenka į regimosios šviesos spektrą titano suboksido nanodarinių E_g atveria galimybę naujiems taikymams. Svarbu paminėti, kad stecheometrinis TiO_2 turi pritaikymų, kuriems reikalinga aktyvacija UV šviesa, todėl TiO_x struktūroms su ženkliai siauresne draustine juosta aktyvacijai turėtų pakakti regimosios šviesos.

6.2. Titano suboksido taikymas pagrinduose skirtuose formuoti katalizatoriams inicijuojantiems vandenilio skyrimosi reakciją

Šiuo tikslu, ant hidrotermiškai suformuotų titano suboksidų plonų sluosnių hidrotermiškai buvo suformuotos MoS_2 nanostruktūros. Paruoštų $Ti/TiO_x/MoS_2$ elektrodų elektrokatalizinės savybės inicijuojant vandenilio skyrimosi reakciją iš rūgštaus vandens atvaizduotos 6 paveiksle. Tyrimai atlikti 0,5 mol L^{-1} H_2SO_4 ir 0,25 mol L^{-1} skruzdžių rūgšties elektrolite cikline voltamperometrija nuo 0,05 to -0,35 V standartinio vandenilio elektrodo atžvilgiu esant 10 mV s^{-1}potencialo skleidimo greičiui.

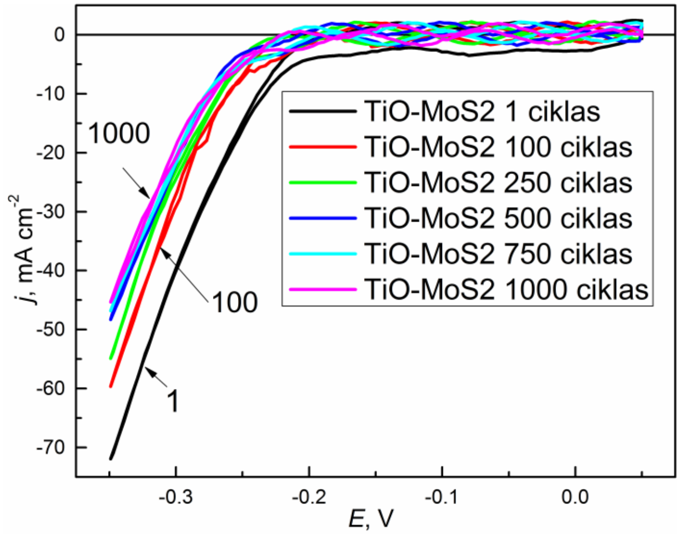

6 Pav. Ti/TiO_x/MoS_2 elektrodo ciklinto 0.5 H_2SO_4 ir 0.25 mol L^{-1} COOH elektrolite 10 mV s^{-1} potencialo skleidimo greičiui *j*(*E*) ciklinės voltamperogramos nurodytam ciklo skaičiui.

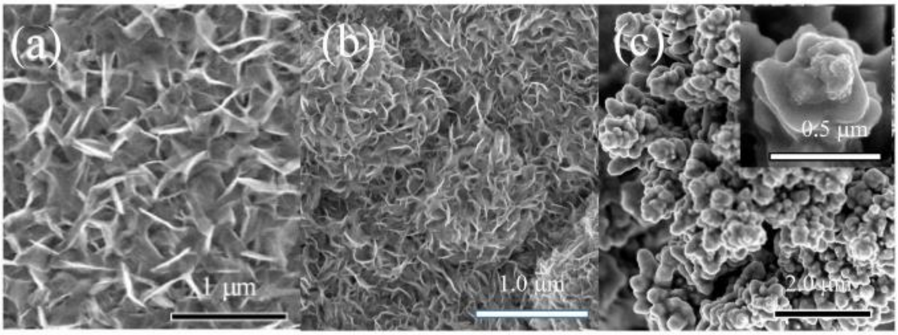

7 Pav. TiO_x (a) ir TiO_x/MoS_2 (b,c) paviršių SEM vaizdai prieš (b) ir po (c) 1000 ciklų 0.5 H_2SO_4 + 0.25 mol L^{-1} elektrolite esant skleidimo greičiui 10 mV s^{-1}.

Elektrocheminiai tyrimai rūgštiniame elektrolite parodė, kad H_2 išsiskyrimo reakcijos inicijavimui ant elektrodo paviršiaus padengto plonu TiO sluoksniu reikalinga ≈170 mV (vandenilio elektrodo atžvilgiu) viršįtampis. Tokį rezultatą galima paaiškinti didesniu TiO_x elektriniu laidumu lyginant su TiO_2. Nepaisant to, elektrokatalizatoriaus aktyvumas mažėja proceso bėgyje ir po 1000 ciklų siekia 50–45 mA cm^{-2}.

6.3. Titano suboksidų taikymas jutikliuose skirtuose lakiųjų organinių junginių nustatymui

Šiems tyrimams, titano suboksido pagrindu suformuoti dujų jutikliai buvo paruošti pagal metodinėje dalyje aprašytą procedūrą. SEM nuotraukose matyti nanolapelinės struktūros, kurios pasižymi dideliu paviršiaus plotu (8 pav.).

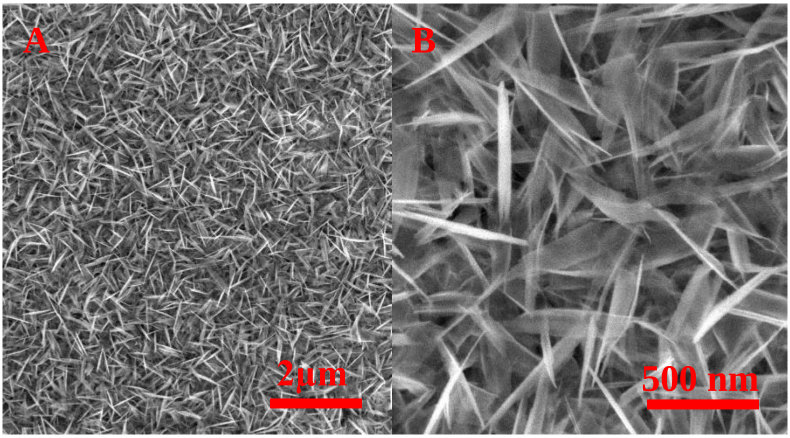

8 Pav. TiO_{2-x}/TiO_2 (400 °C) SEM nuotraukos esant skirtingiems didinimams.

Elektros srovė pratekanti per TiO_{2-x}/TiO_2 heterostruktūrą esant pastoviam potencialui buvo registruojama ir perskaičiuota į varžos pokytį (ΔR %). ΔR buvo įvertintas kaip analitinis jutiklio signalas. Matavimai temperatūrų intervale 25-180°C atlikti su skirtingais organiniais lakiaisiais junginiais ir apibendrinti 9 paveiksle. Jutiklis reagavo į drėmę bei organinius lakiuosius junginius: metanolį, etanolį, n-propanolį, acetoną.

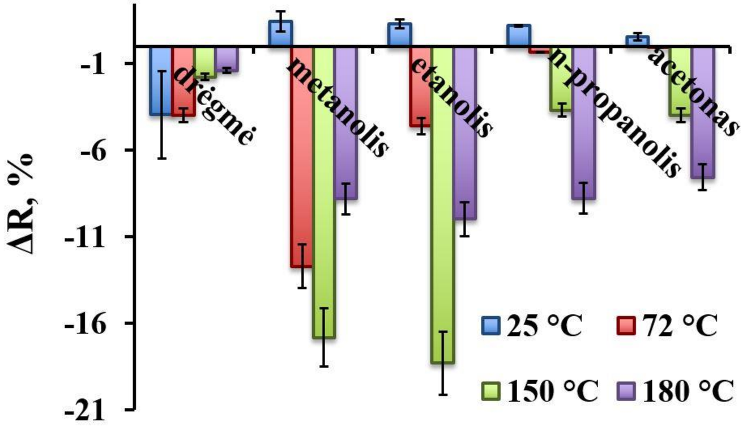

9 pav. TiO_{2-x}/TiO_2 (400 °C) dujų jutiklio atsakai į drėgmę, metanolį, etanolį, n-propanolį ir acetoną esant skirtingai temperatūrai (25–180 °C).

Skirtingas jautrumas įvairiems dujiniams organiniams junginiams esant skirtingoms temperatūroms buvo pastebėtas. Didžiausias jautrumas metanoliui pasiektas prie 72 °C, etanoliui prie 150–180 °C, o jautrumas n-propanoliui ir acetonui didėjo keliant temperatūrą bei pasiekė didžiausią vertę prie 180 °C.

6.4. Ti_3C_2 Maksenų sintezė ir taikymas salicilo rūgšties detekcijai

MAX fazės ir susintetintų maksenų struktūra ir morfologija buvo įvertinta skenuojančios elektroninės mikroskopijos pagalba. Ėsdinimas 5 wt.% HF tirpale leido suformuoti $Ti_3C_2T_x$ struktūras, kurios pasižymėjo panašia į „okordioną“ morfologija (10 pav.). Sėkmingas aliuminio išėsdinimas iš struktūros buvo įrodytas rentgeno spindulių fotoelektronų spektroskopijos pagalba (1 lentelė). Nustatyta, kad aliuminio kiekis Maksenų struktūroje sumažėjo 5 kartus lyginant su pradiniu kiekiu buvusiu prekursoriuje, MAX fazėje.

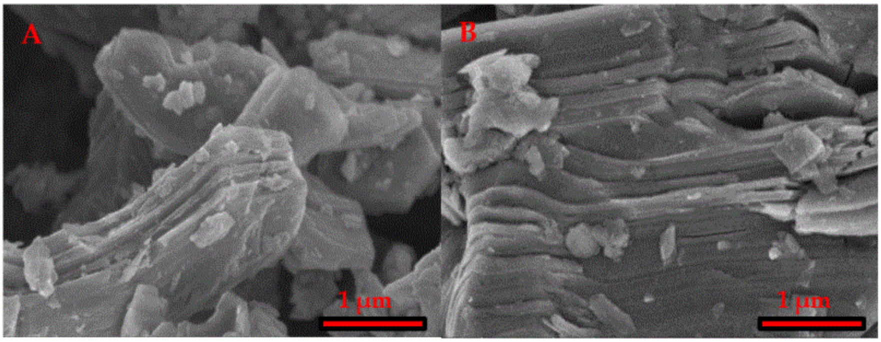

10 Pav. SEM nuotraukos: (A) MAX fazės (Ti_3AlC_2), (B) Maksenų ($Ti_3C_2T_x$).

1 Lentelė. EDX analizės rodančios aliuminio ir titano kiekį MAX fazės ir Maksenų sudėtyje.

Medžiaga	Atominė sudėtis, %	
	Aliuminis (Al)	Titanas (Ti)
MAX fazė (Ti_3AlC_2)	39.39 ± 0.96	60.61 ± 0.96
Maksenai ($Ti_3C_2T_x$)	6.33 ± 1,97	93,67 ± 1.97

Lyginant MAX fazės ir Maksenų suformuotų 5 wt.% HF tirpale laidumą kambario temperatūroje buvo pastebėtas varžos sumažėjimas nuo 36 Ω iki 20.5 Ω. Sumažėjusi varža gali būt paaiškinama sumažėjusiu aliumino kiekiu struktūroje dėl ėsdinimo HF bei Ti_3C_2 Maksenų struktūrų pasižyminčiu artimu metaliniam laidumui formavimuisi. Maksenų formavimasis buvo patvirtintas XRD analize (11 Pav.).

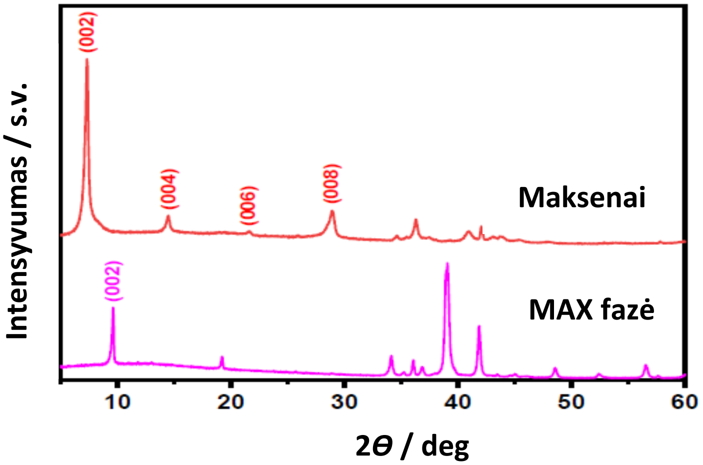

11 Pav. MAX fazės (Ti_3AlC_2) ir Maskenų ($Ti_3C_2T_x$) rentgeno spindulių difraktogramos.

Esant sąveikai tarp iš Maksenų suformuoto plono sluoksnio ir salicilo rūgšties Ramano spektroskopijos pagalba registruojamas spektras ryškiai skiriasi nuo grynos salicilo rūgšties (12 Pav.). Ryškių Ramano spektrinių juostų atsiradimas ties 896 cm_{-1} ir juostos dubletas ties 681 cm^{-1} ir 654 cm^{-1} patvirtina salicilo rūgšties ir Maksenų sąveiką.

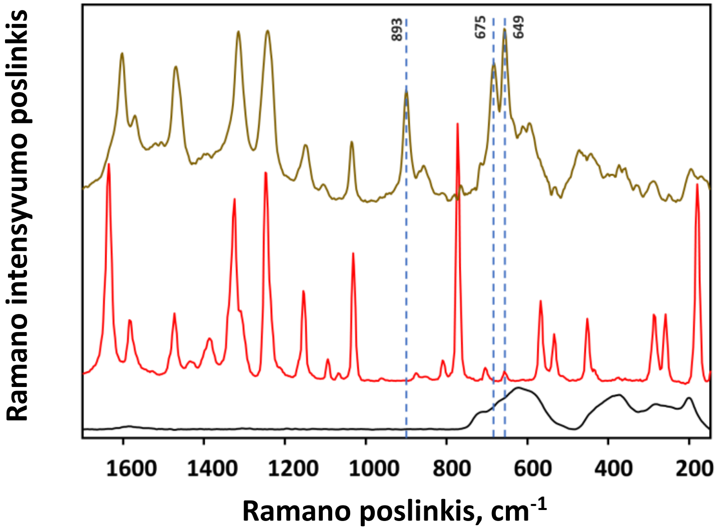

12 Pav. Maksenų sluoksnio ir salicilo rūgšties išdžiuvusios ant Maksenų sluoksnio (vidurinis) bei išdžiuvusios ant aliuminio folijos (viršutinis) Raman spektrai. Žadinimui naudoto šaltinio bangos ilgis - 633 nm.

Lyginant salicilo rūgšties nusodintos ant aliuminio paviršiaus ir ant Maksenų sluoksnio vibracijas, sustiprinimo koeficientas buvo 125, 110 and 220 juostoms ties 896 cm^{-1}, 681 cm^{-1} ir 654 cm^{-1} (532 nm sužadinimas).

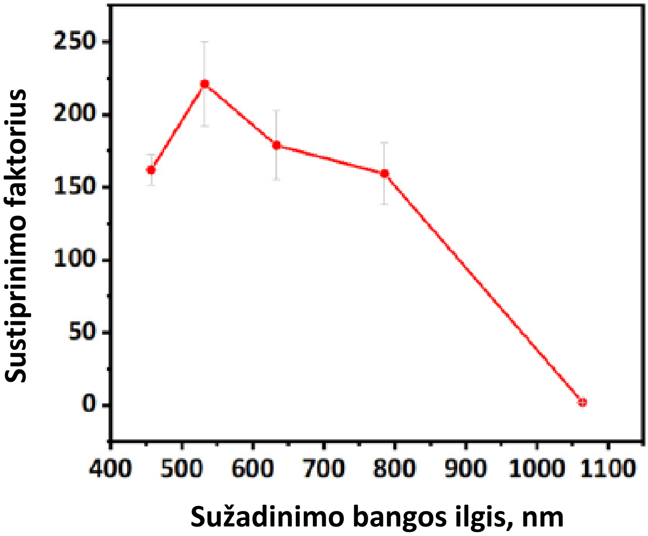

13 Pav. 2 mM salicilico rūgšties esančios sąveikoje su Maksenų sluoksniu SERS sustiprinimo koeficiento priklausomybė nuo žadinančio šaltinio bangos ilgio.

Remiantis spektrais registruotais esant skirtingiems žadinimams, sustiprinimo koeficiento priklausomybė nuo žadinančio šaltinio bangos ilgio buvo įvertinta (13 pav.). Siekiant sumažinti aparatūrines paklaidas, salicilo rūgšties ir Maksenų-salicilo rūgšties spektrai buvo užrašyti tomis pačiomis sąlygomis ir sulyginti.

Išvados

1. Pirmą kartą nustatyta, kad nanolapelines titano suboksido struktūras galima suformuoti ant titano paviršių 0,05 - 0,5 mol L^{-1} koncentracijos selenitinės rūgšties šarminiuose tirpaluose hidroterminiu keliu išlaikant pusę-dvi paras 150-200 °C temperatūroje, bei atkaitinant sintezės produktus bedeguonėje atmosferoje.
2. Hidroterminiu būdu susintetintų nestechiometrinės sudėties titano suboksidų poringumas sudaro 80% o draustinės juostos plotis gali siekti tik 1,29 eV,. Šios savybės leidžia titano suboksidus taikyti jutiklių konstravime bei kompozitinių medžiagų formavime.
3. Hidroterminiu būdu suformuoti titano suboksidų ploni sluoksniai gali būti pritaikyti kaip pagrindai formuojant $Ti/TiO_x/MoS_2$ elektrokatalizatorius vandenilio išsiskyrimo reakcijai inicijuoti. Cikline voltamperometrija nustatyta, kad titano suboksido pagrindu suformuoti vandens skaldymo elektrokatalizatoriai pasižymi didesniu stabilumu, nei suformuoti ant grynų metalų.
4. Hidroterminiu būdu susintetintų titano suboksidų plonų sluoksnių heterostruktūros su TiO_2 turi savybę kaisti esant užduotam potencialui 0,5 - 5 V ribose. Šios struktūros jautrios lakiųjų organinių junginių garams ir priklausomai nuo darbinės temperatūros yra jiems selektyvios.
5. Maksenų ($Ti_3C_2T_x$) į „akordeoną“ panašios struktūros gali būti suformuotos atrankaus ėsdinimo būdu su 5% vandenilio fluorido rūgštimi ėsdinant Ti_3AlC_2. Suformuoti maksenų 70 nm storio paviršiai gali būti panaudoti salicilo rūgšties detekcijai paviršiaus sustiprintos Ramano spektroskopijos pagalba dėl sustiprintų vibracijų ties 896 cm^{-1}, 681 cm^{-1} ir 654 cm^{-1}.
6. Nustatyta, kad salicilo rūgščiai adsorbavusis ant maksenų paviršiaus vibracijų sustiprinimo mechanizmas yra sietinas su jų chemine sąveika. Sustiprinimo faktorius kinta nuo 220 (λ = 532 nm) iki 60 (λ = 1064 nm).

REFERENCES

[1] Chen, X.; Mao, S. S. Titanium Dioxide Nanomaterials: Synthesis, Properties, Modifications, and Applications. *Chemical Reviews*, **2007**, *107* (7), 2891–2959. https://doi.org/10.1021/cr0500535.

[2] Jayashree, S.; Ashokkumar, M. Switchable Intrinsic Defect Chemistry of Titania for Catalytic Applications. *Catalysts*, **2018**, *8* (12). https://doi.org/10.3390/catal8120601.

[3] Seredych, M.; Shuck, C. E.; Pinto, D.; Alhabeb, M.; Precetti, E.; Deysher, G.; Anasori, B.; Kurra, N.; Gogotsi, Y. High-Temperature Behavior and Surface Chemistry of Carbide MXenes Studied by Thermal Analysis. *Chemistry of Materials*, **2019**, *31* (9), 3324–3332. https://doi.org/10.1021/acs.chemmater.9b00397.

[4] Enyashin, A. N.; Ivanovskii, A. L. Two-Dimensional Titanium Carbonitrides and Their Hydroxylated Derivatives: Structural, Electronic Properties and Stability of MXenes Ti3C2−xNx(OH)2 from DFTB Calculations. *Journal of Solid State Chemistry*, **2013**, *207*, 42–48. https://doi.org/10.1016/J.JSSC.2013.09.010.

[5] Bai, J.; Zhou, B. Titanium Dioxide Nanomaterials for Sensor Applications. *Chemical Reviews*, **2014**, *114* (19), 10131–10176. https://doi.org/10.1021/cr400625j.

[6] Wang, Y.; Wu, T.; Zhou, Y.; Meng, C.; Zhu, W.; Liu, L. TiO2-Based Nanoheterostructures for Promoting Gas Sensitivity Performance: Designs, Developments, and Prospects. *Sensors*, **2017**, *17* (9). https://doi.org/10.3390/s17091971.

[7] Prades, J. D.; Jimenez-Diaz, R.; Hernandez-Ramirez, F.; Barth, S.; Cirera, A.; Romano-Rodriguez, A.; Mathur, S.; Morante, J. R. Ultralow Power Consumption Gas Sensors Based on Self-Heated Individual Nanowires. *Applied Physics Letters*, **2008**, *93* (12), 123110.

[8] Smulko, J. M.; Trawka, M.; Granqvist, C. G.; Ionescu, R.; Annanouch, F.; Llobet, E.; Kish, L. B. New Approaches for Improving Selectivity and Sensitivity of Resistive Gas Sensors: A Review. *Sensor Review*, **2015**.

[9] Karnati, P.; Akbar, S.; Morris, P. A. Conduction Mechanisms in One Dimensional Core-Shell Nanostructures for Gas Sensing: A Review. *Sensors and Actuators B: Chemical*, **2019**, *295*, 127–143. https://doi.org/10.1016/J.SNB.2019.05.049.

[10] Mosadegh Sedghi, S.; Mortazavi, Y.; Khodadadi, A. Low Temperature CO and CH4 Dual Selective Gas Sensor Using SnO2 Quantum Dots Prepared by Sonochemical Method. *Sensors and Actuators B:*

Chemical, **2010**, *145* (1), 7–12. https://doi.org/10.1016/J.SNB.2009.11.002.

[11] Mirzaei, A.; Janghorban, K.; Hashemi, B.; Bonavita, A.; Bonyani, M.; Leonardi, S. G.; Neri, G. Synthesis, Characterization and Gas Sensing Properties of Ag@α-Fe2O3 Core–Shell Nanocomposites. *Nanomaterials*, **2015**, *5* (2), 737–749. https://doi.org/10.3390/nano5020737.

[12] Hart, J. L.; Hantanasirisakul, K.; Lang, A. C.; Anasori, B.; Pinto, D.; Pivak, Y.; van Omme, J. T.; May, S. J.; Gogotsi, Y.; Taheri, M. L. Control of MXenes' Electronic Properties through Termination and Intercalation. *Nature Communications*, **2019**, *10* (1), 522. https://doi.org/10.1038/s41467-018-08169-8.

[13] Melchior, S. A.; Raju, K.; Ike, I. S.; Erasmus, R. M.; Kabongo, G.; Sigalas, I.; Iyuke, S. E.; Ozoemena, K. I. High-Voltage Symmetric Supercapacitor Based on 2D Titanium Carbide (MXene, Ti2CTx)/Carbon Nanosphere Composites in a Neutral Aqueous Electrolyte. *Journal of The Electrochemical Society*, **2018**, *165* (3), A501–A511. https://doi.org/10.1149/2.0401803jes.

[14] Lorencova, L.; Bertok, T.; Dosekova, E.; Holazova, A.; Paprckova, D.; Vikartovska, A.; Sasinkova, V.; Filip, J.; Kasak, P.; Jerigova, M.; et al. Electrochemical Performance of Ti3C2Tx MXene in Aqueous Media: Towards Ultrasensitive H2O2 Sensing. *Electrochimica Acta*, **2017**, *235*, 471–479. https://doi.org/10.1016/J.ELECTACTA.2017.03.073.

[15] Song, D.; Jiang, X.; Li, Y.; Lu, X.; Luan, S.; Wang, Y.; Li, Y.; Gao, F. Metal−organic Frameworks-Derived MnO2/Mn3O4 Microcuboids with Hierarchically Ordered Nanosheets and Ti3C2 MXene/Au NPs Composites for Electrochemical Pesticide Detection. *Journal of Hazardous Materials*, **2019**, *373*, 367–376. https://doi.org/10.1016/J.JHAZMAT.2019.03.083.

[16] Kim, H.; Wang, Z.; Alshareef, H. N. MXetronics: Electronic and Photonic Applications of MXenes. *Nano Energy*, **2019**, *60*, 179–197. https://doi.org/10.1016/J.NANOEN.2019.03.020.

[17] Lee, K.-S.; El-Sayed, M. A. Gold and Silver Nanoparticles in Sensing and Imaging: Sensitivity of Plasmon Response to Size, Shape, and Metal Composition. *The Journal of Physical Chemistry B*, **2006**, *110* (39), 19220–19225. https://doi.org/10.1021/jp062536y.

[18] Velusamy, D. B.; El-Demellawi, J. K.; El-Zohry, A. M.; Giugni, A.; Lopatin, S.; Hedhili, M. N.; Mansour, A. E.; Fabrizio, E. di; Mohammed, O. F.; Alshareef, H. N. MXenes for Plasmonic

Photodetection. *Advanced Materials*, **2019**, *31* (32), 1807658. https://doi.org/https://doi.org/10.1002/adma.201807658.

[19] Lin, J.; Heo, Y.-U.; Nattestad, A.; Sun, Z.; Wang, L.; Kim, J. H.; Dou, S. X. 3D Hierarchical Rutile TiO2 and Metal-Free Organic Sensitizer Producing Dye-Sensitized Solar Cells 8.6% Conversion Efficiency. *Scientific Reports*, **2014**, *4* (1), 5769. https://doi.org/10.1038/srep05769.

[20] Maziarz, W.; Kusior, A.; Trenczek-Zajac, A. Nanostructured TiO2-Based Gas Sensors with Enhanced Sensitivity to Reducing Gases. *Beilstein Journal of Nanotechnology*, **2016**, *7*, 1718–1726. https://doi.org/10.3762/bjnano.7.164.

[21] Soni, P.; Murty, V. V. S.; Kushwaha, K. K. The Effect of Ni2+ Ions on Energy Band Gap of TiO2 Nanoparticles for Solar Cell Applications. *J. Nanosci. Nanoeng. Appl*, **2018**, *8*, 69–74.

[22] Zheng, Z.; Huang, B.; Meng, X.; Wang, J.; Wang, S.; Lou, Z.; Wang, Z.; Qin, X.; Zhang, X.; Dai, Y. Metallic Zinc- Assisted Synthesis of Ti3+ Self-Doped TiO2 with Tunable Phase Composition and Visible-Light Photocatalytic Activity. *Chem. Commun.*, **2013**, *49* (9), 868–870. https://doi.org/10.1039/C2CC37976G.

[23] Jayashree, S.; Ashokkumar, M. Switchable Intrinsic Defect Chemistry of Titania for Catalytic Applications. *Catalysts*, **2018**, *8* (12). https://doi.org/10.3390/catal8120601.

[24] Wang, G.; Wang, J.; An, Y.; Wang, C. Anodization Fabrication of 3D TiO2 Photonic Crystals and Their Application for Chemical Sensors. *Superlattices and Microstructures*, **2016**, *100*, 290–295. https://doi.org/10.1016/J.SPMI.2016.09.027.

[25] Qiu, J.; Zhang, S.; Zhao, H. Recent Applications of TiO2 Nanomaterials in Chemical Sensing in Aqueous Media. *Sensors and Actuators B: Chemical*, **2011**, *160* (1), 875–890. https://doi.org/10.1016/J.SNB.2011.08.077.

[26] Tereshchenko, A.; Smyntyna, V.; Ramanavicius, A. Interaction Mechanism between TiO2 Nanostructures and Bovine Leukemia Virus Proteins in Photoluminescence-Based Immunosensors. *RSC Adv.*, **2018**, *8* (66), 37740–37748. https://doi.org/10.1039/C8RA07347C.

[27] Tereshchenko, A.; Viter, R.; Konup, I.; Ivanitsa, V.; Geveliuk, S.; Ishkov, Y.; Smyntyna, V. TiO2 Optical Sensor for Amino Acid Detection. In *Biophotonics—Riga 2013*; International Society for Optics and Photonics, 2013; Vol. 9032, p 90320T.

[28] Yamazoe, N.; Sakai, G.; Shimanoe, K. Oxide Semiconductor Gas Sensors. *Catalysis Surveys from Asia*, **2003**, *7* (1), 63–75. https://doi.org/10.1023/A:1023436725457.

[29] Wunderlich, W.; Oekermann, T.; Miao, L.; Hue, N. T.; Tanemura, S.; Tanemura, M. ELECTRONIC PROPERTIES OF NANO-POROUS TiO 2- AND ZnO THIN FILMS- COMPARISON OF SIMULATIONS AND EXPERIMENTS. *Journal of Ceramic Processing & Research*, **2004**, *5* (4), 343–354.

[30] Ramanavicius, S.; Tereshchenko, A.; Karpicz, R.; Ratautaite, V.; Bubniene, U.; Maneikis, A.; Jagminas, A.; Ramanavicius, A. TiO2-x/TiO2-Structure Based 'Self-Heated' Sensor for the Determination of Some Reducing Gases. *Sensors*, **2020**, *20* (1). https://doi.org/10.3390/s20010074.

[31] Åsbrink, S.; Magnéli, A. Crystal Structure Studies on Trititanium Pentoxide, Ti3O5. *Acta Crystallographica*, **1959**, *12* (8), 575–581.

[32] Hong, S.-H.; Åsbrink, S. The Structure of γ-Ti3O5 at 297 K. *Acta Crystallographica Section B: Structural Crystallography and Crystal Chemistry*, **1982**, *38* (10), 2570–2576.

[33] Onoda, M. Phase Transitions of Ti3O5. *Journal of Solid State Chemistry*, **1998**, *136* (1), 67–73. https://doi.org/10.1006/JSSC.1997.7657.

[34] Ohkoshi, S.; Tsunobuchi, Y.; Matsuda, T.; Hashimoto, K.; Namai, A.; Hakoe, F.; Tokoro, H. Synthesis of a Metal Oxide with a Room-Temperature Photoreversible Phase Transition. *Nature Chemistry*, **2010**, *2* (7), 539–545. https://doi.org/10.1038/nchem.670.

[35] Tanaka, K.; Nasu, T.; Miyamoto, Y.; Ozaki, N.; Tanaka, S.; Nagata, T.; Hakoe, F.; Yoshikiyo, M.; Nakagawa, K.; Umeta, Y.; et al. Structural Phase Transition between γ-Ti3O5 and δ-Ti3O5 by Breaking of a One-Dimensionally Conducting Pathway. *Crystal Growth & Design*, **2015**, *15* (2), 653–657. https://doi.org/10.1021/cg5013439.

[36] Yoshimatsu, K.; Sakata, O.; Ohtomo, A. Superconductivity in Ti4O7 and γ-Ti3O5 Films. *Scientific Reports*, **2017**, *7* (1), 12544. https://doi.org/10.1038/s41598-017-12815-4.

[37] Marezio, M.; McWhan, D. B.; Dernier, P. D.; Remeika, J. P. Structural Aspects of the Metal-Insulator Transitions in Ti4O7. *Journal of Solid State Chemistry*, **1973**, *6* (2), 213–221. https://doi.org/10.1016/0022-4596(73)90184-9.

[38] Lakkis, S.; Schlenker, C.; Chakraverty, B. K.; Buder, R.; Marezio, M. Metal-Insulator Transitions in ${\mathrm{Ti}}_{4}$${\mathrm{O}}_{7}$ Single Crystals: Crystal Characterization, Specific Heat, and Electron Paramagnetic Resonance. *Physical Review B*, **1976**, *14* (4), 1429–1440. https://doi.org/10.1103/PhysRevB.14.1429.

[39] D'Angelo, A. M.; Webster, N. A. S. Evidence of Anatase Intergrowths Formed during Slow Cooling of Reduced Ilmenite. *Journal of Applied Crystallography*, **2018**, *51* (1), 185–192.

[40] Grey, I. E.; Cranswick, L. M. D.; Li, C.; White, T. J.; Bursill, L. A. New M3O5-Anatase Intergrowth Structures Formed during Low-Temperature Oxidation of Anosovite. *Journal of Solid State Chemistry*, **2000**, *150* (1), 128–138. https://doi.org/10.1006/JSSC.1999.8564.

[41] Linsebigler, A. L.; Lu, G.; Yates, J. T. Photocatalysis on TiO2 Surfaces: Principles, Mechanisms, and Selected Results. *Chemical Reviews*, **1995**, *95* (3), 735–758. https://doi.org/10.1021/cr00035a013.

[42] Kimura, M.; Sakai, R.; Sato, S.; Fukawa, T.; Ikehara, T.; Maeda, R.; Mihara, T. Sensing of Vaporous Organic Compounds by TiO2 Porous Films Covered with Polythiophene Layers. *Advanced Functional Materials*, **2012**, *22* (3), 469–476. https://doi.org/https://doi.org/10.1002/adfm.201101953.

[43] Wang, Y.; Du, G.; Liu, H.; Liu, D.; Qin, S.; Wang, N.; Hu, C.; Tao, X.; Jiao, J.; Wang, J.; et al. Nanostructured Sheets of Ti□O Nanobelts for Gas Sensing and Antibacterial Applications. *Advanced Functional Materials*, **2008**, *18* (7), 1131–1137. https://doi.org/https://doi.org/10.1002/adfm.200701120.

[44] Ramanavičius, S.; Petrulevičienė, M.; Juodkazytė, J.; Grigucevičienė, A.; Ramanavičius, A. Selectivity of Tungsten Oxide Synthesized by Sol-Gel Method Towards Some Volatile Organic Compounds and Gaseous Materials in a Broad Range of Temperatures. *Materials*, **2020**, *13* (3). https://doi.org/10.3390/ma13030523.

[45] Petruleviciene, M.; Juodkazyte, J.; Parvin, M.; Tereshchenko, A.; Ramanavicius, S.; Karpicz, R.; Samukaite-Bubniene, U.; Ramanavicius, A. Tuning the Photo-Luminescence Properties of WO3 Layers by the Adjustment of Layer Formation Conditions. *Materials*, **2020**, *13* (12). https://doi.org/10.3390/ma13122814.

[46] Haryński, Ł.; Grochowska, K.; Karczewski, J.; Ryl, J.; Siuzdak, K. Scalable Route toward Superior Photoresponse of UV-Laser-Treated

TiO2 Nanotubes. *ACS Applied Materials & Interfaces*, **2020**, *12* (2), 3225–3235. https://doi.org/10.1021/acsami.9b19206.

[47] Avansi, W.; Catto, A. C.; da Silva, L. F.; Fiorido, T.; Bernardini, S.; Mastelaro, V. R.; Aguir, K.; Arenal, R. One-Dimensional V2O5/TiO2 Heterostructures for Chemiresistive Ozone Sensors. *ACS Applied Nano Materials*, **2019**, *2* (8), 4756–4764. https://doi.org/10.1021/acsanm.9b00578.

[48] Hsu, K. C.; Fang, T. H.; Hsiao, Y. J.; Wu, P. C. Response and Characteristics of TiO2/Perovskite Heterojunctions for CO Gas Sensors. *Journal of Alloys and Compounds*, **2019**, *794*, 576–584. https://doi.org/10.1016/J.JALLCOM.2019.04.238.

[49] Seekaew, Y.; Wisitsoraat, A.; Phokharatkul, D.; Wongchoosuk, C. Room Temperature Toluene Gas Sensor Based on TiO2 Nanoparticles Decorated 3D Graphene-Carbon Nanotube Nanostructures. *Sensors and Actuators B: Chemical*, **2019**, *279*, 69–78. https://doi.org/10.1016/J.SNB.2018.09.095.

[50] Chen, K.; Chen, S.; Pi, M.; Zhang, D. SnO2 Nanoparticles/TiO2 Nanofibers Heterostructures: In Situ Fabrication and Enhanced Gas Sensing Performance. *Solid-State Electronics*, **2019**, *157*, 42–47. https://doi.org/10.1016/J.SSE.2019.03.024.

[51] Yu, Q.; Zhu, J.; Xu, Z.; Huang, X. Facile Synthesis of α-Fe2O3@SnO2 Core–Shell Heterostructure Nanotubes for High Performance Gas Sensors. *Sensors and Actuators B: Chemical*, **2015**, *213*, 27–34. https://doi.org/10.1016/J.SNB.2015.01.130.

[52] Lee, E.; Lee, D.; Yoon, J.; Yin, Y.; Lee, Y. N.; Uprety, S.; Yoon, Y. S.; Kim, D.-J. Enhanced Gas-Sensing Performance of GO/TiO2 Composite by Photocatalysis. *Sensors*, **2018**, *18* (10). https://doi.org/10.3390/s18103334.

[53] Stratakis, E.; Savva, K.; Konios, D.; Petridis, C.; Kymakis, E. Improving the Efficiency of Organic Photovoltaics by Tuning the Work Function of Graphene Oxide Hole Transporting Layers. *Nanoscale*, **2014**, *6* (12), 6925–6931. https://doi.org/10.1039/C4NR01539H.

[54] Chen, C.; Cai, W.; Long, M.; Zhou, B.; Wu, Y.; Wu, D.; Feng, Y. Synthesis of Visible-Light Responsive Graphene Oxide/TiO2 Composites with p/n Heterojunction. *ACS Nano*, **2010**, *4* (11), 6425–6432. https://doi.org/10.1021/nn102130m.

[55] Lightcap, I. v; Kosel, T. H.; Kamat, P. v. Anchoring Semiconductor and Metal Nanoparticles on a Two-Dimensional Catalyst Mat. Storing

and Shuttling Electrons with Reduced Graphene Oxide. *Nano Letters*, **2010**, *10* (2), 577–583. https://doi.org/10.1021/nl9035109.

[56] Ye, Z.; Tai, H.; Xie, T.; Yuan, Z.; Liu, C.; Jiang, Y. Room Temperature Formaldehyde Sensor with Enhanced Performance Based on Reduced Graphene Oxide/Titanium Dioxide. *Sensors and Actuators B: Chemical*, **2016**, *223*, 149–156. https://doi.org/10.1016/J.SNB.2015.09.102.

[57] Ammu, S.; Dua, V.; Agnihotra, S. R.; Surwade, S. P.; Phulgirkar, A.; Patel, S.; Manohar, S. K. Flexible, All-Organic Chemiresistor for Detecting Chemically Aggressive Vapors. *Journal of the American Chemical Society*, **2012**, *134* (10), 4553–4556. https://doi.org/10.1021/ja300420t.

[58] Lam, K. C.; Huang, B.; Shi, S.-Q. Room-Temperature Methane Gas Sensing Properties Based on in Situ Reduced Graphene Oxide Incorporated with Tin Dioxide. *J. Mater. Chem. A*, **2017**, *5* (22), 11131–11142. https://doi.org/10.1039/C7TA01293D.

[59] Buchsteiner, A.; Lerf, A.; Pieper, J. Water Dynamics in Graphite Oxide Investigated with Neutron Scattering. *The Journal of Physical Chemistry B*, **2006**, *110* (45), 22328–22338. https://doi.org/10.1021/jp0641132.

[60] Phan, D. T.; Chung, G. S. Effects of Rapid Thermal Annealing on Humidity Sensor Based on Graphene Oxide Thin Films. *Sensors and Actuators B: Chemical*, **2015**, *220*, 1050–1055. https://doi.org/10.1016/J.SNB.2015.06.055.

[61] Wang, P.; Zhai, Y.; Wang, D.; Dong, S. Synthesis of Reduced Graphene Oxide-Anatase TiO2 Nanocomposite and Its Improved Photo-Induced Charge Transfer Properties. *Nanoscale*, **2011**, *3* (4), 1640–1645. https://doi.org/10.1039/C0NR00714E.

[62] Cui, S.; Wen, Z.; Huang, X.; Chang, J.; Chen, J. Stabilizing MoS2 Nanosheets through SnO2 Nanocrystal Decoration for High-Performance Gas Sensing in Air. *Small*, **2015**, *11* (19), 2305–2313. https://doi.org/https://doi.org/10.1002/smll.201402923.

[63] Mirzaei, A.; Janghorban, K.; Hashemi, B.; Neri, G. Metal-Core@metal Oxide-Shell Nanomaterials for Gas-Sensing Applications: A Review. *Journal of Nanoparticle Research*, **2015**, *17* (9), 371. https://doi.org/10.1007/s11051-015-3164-5.

[64] Rieu, M.; Camara, M.; Tournier, G.; Viricelle, J. P.; Pijolat, C.; de Rooij, N. F.; Briand, D. Fully Inkjet Printed SnO2 Gas Sensor on

Plastic Substrate. *Sensors and Actuators B: Chemical*, **2016**, *236*, 1091–1097. https://doi.org/10.1016/J.SNB.2016.06.042.

[65] Chung, F. C.; Wu, R. J.; Cheng, F. C. Fabrication of a Au@SnO2 Core–Shell Structure for Gaseous Formaldehyde Sensing at Room Temperature. *Sensors and Actuators B: Chemical*, **2014**, *190*, 1–7. https://doi.org/10.1016/J.SNB.2013.08.037.

[66] Chen, G.; Ji, S.; Li, H.; Kang, X.; Chang, S.; Wang, Y.; Yu, G.; Lu, J.; Claverie, J.; Sang, Y.; et al. High-Energy Faceted SnO2-Coated TiO2 Nanobelt Heterostructure for Near-Ambient Temperature-Responsive Ethanol Sensor. *ACS Applied Materials & Interfaces*, **2015**, *7* (44), 24950–24956. https://doi.org/10.1021/acsami.5b08630.

[67] Li, F.; Gao, X.; Wang, R.; Zhang, T.; Lu, G. Study on TiO2-SnO2 Core-Shell Heterostructure Nanofibers with Different Work Function and Its Application in Gas Sensor. *Sensors and Actuators B: Chemical*, **2017**, *248*, 812–819. https://doi.org/10.1016/J.SNB.2016.12.009.

[68] Zeng, W.; Liu, T.; Wang, Z. UV Light Activation of TiO₂-Doped SnO₂ Thick Film for Sensing Ethanol at Room Temperature. *MATERIALS TRANSACTIONS*, **2010**, *51* (2), 243–245. https://doi.org/10.2320/matertrans.MC200904.

[69] Lee, H. C.; Hwang, W. S. Substrate Effects on the Oxygen Gas Sensing Properties of SnO2/TiO2 Thin Films. *Applied Surface Science*, **2006**, *253* (4), 1889–1897. https://doi.org/10.1016/J.APSUSC.2006.03.036.

[70] Lee, J. H.; Mirzaei, A.; Kim, J. H.; Kim, J. Y.; Nasriddinov, A. F.; Rumyantseva, M. N.; Kim, H. W.; Kim, S. S. Gas-Sensing Behaviors of TiO2-Layer-Modified SnO2 Quantum Dots in Self-Heating Mode and Effects of the TiO2 Layer. *Sensors and Actuators B: Chemical*, **2020**, *310*, 127870. https://doi.org/10.1016/J.SNB.2020.127870.

[71] Ng, S.; Prášek, J.; Zazpe, R.; Pytlíček, Z.; Spotz, Z.; Pereira, J. R.; Michalička, J.; Přikryl, J.; Krbal, M.; Sopha, H.; et al. Atomic Layer Deposition of SnO2-Coated Anodic One-Dimensional TiO2 Nanotube Layers for Low Concentration NO2 Sensing. *ACS Applied Materials & Interfaces*, **2020**, *12* (29), 33386–33396. https://doi.org/10.1021/acsami.0c07791.

[72] Song, Z.; Wei, Z.; Wang, B.; Luo, Z.; Xu, S.; Zhang, W.; Yu, H.; Li, M.; Huang, Z.; Zang, J.; et al. Sensitive Room-Temperature H2S Gas Sensors Employing SnO2 Quantum Wire/Reduced Graphene Oxide Nanocomposites. *Chemistry of Materials*, **2016**, *28* (4), 1205–1212. https://doi.org/10.1021/acs.chemmater.5b04850.

[73] Nasriddinov, A.; Rumyantseva, M.; Marikutsa, A.; Gaskov, A.; Lee, J.-H.; Kim, J.-H.; Kim, J.-Y.; Kim, S. S.; Kim, H. W. Sub-Ppm Formaldehyde Detection by n-n TiO2@SnO2 Nanocomposites. *Sensors*, **2019**, *19* (14). https://doi.org/10.3390/s19143182.

[74] Li, X.; Li, X.; Wang, J.; Lin, S. Highly Sensitive and Selective Room-Temperature Formaldehyde Sensors Using Hollow TiO2 Microspheres. *Sensors and Actuators B: Chemical*, **2015**, *219*, 158–163. https://doi.org/10.1016/J.SNB.2015.05.031.

[75] Tricoli, A.; Righettoni, M.; Pratsinis, S. E. Minimal Cross-Sensitivity to Humidity during Ethanol Detection by SnO2–TiO2solid Solutions. *Nanotechnology*, **2009**, *20* (31), 315502. https://doi.org/10.1088/0957-4484/20/31/315502.

[76] Li, Z.; Yao, Z. J.; Haidry, A. A.; Plecenik, T.; Xie, L. J.; Sun, L. C.; Fatima, Q. Resistive-Type Hydrogen Gas Sensor Based on TiO2: A Review. *International Journal of Hydrogen Energy*, **2018**, *43* (45), 21114–21132. https://doi.org/10.1016/J.IJHYDENE.2018.09.051.

[77] Shaposhnik, D.; Pavelko, R.; Llobet, E.; Gispert-Guirado, F.; Vilanova, X. Hydrogen Sensors on the Basis of SnO2-TiO2 Systems. *Procedia Engineering*, **2011**, *25*, 1133–1136. https://doi.org/10.1016/J.PROENG.2011.12.279.

[78] Plecenik, T.; Moško, M.; Haidry, A. A.; ɰurina, P.; Truchlý, M.; Grančič, B.; Gregor, M.; Roch, T.; Satrapinskyy, L.; Mošková, A.; et al. Fast Highly-Sensitive Room-Temperature Semiconductor Gas Sensor Based on the Nanoscale Pt–TiO2–Pt Sandwich. *Sensors and Actuators B: Chemical*, **2015**, *207* (PartA), 351–361. https://doi.org/10.1016/J.SNB.2014.10.003.

[79] Wang, C.; Yin, L.; Zhang, L.; Xiang, D.; Gao, R. Metal Oxide Gas Sensors: Sensitivity and Influencing Factors. *Sensors*, **2010**, *10* (3), 2088–2106. https://doi.org/10.3390/s100302088.

[80] Franke, M. E.; Koplin, T. J.; Simon, U. Metal and Metal Oxide Nanoparticles in Chemiresistors: Does the Nanoscale Matter? *Small*, **2006**, *2* (1), 36–50. https://doi.org/https://doi.org/10.1002/smll.200500261.

[81] Wang, C.; Yin, L.; Zhang, L.; Qi, Y.; Lun, N.; Liu, N. Large Scale Synthesis and Gas-Sensing Properties of Anatase TiO2 Three-Dimensional Hierarchical Nanostructures. *Langmuir*, **2010**, *26* (15), 12841–12848. https://doi.org/10.1021/la100910u.

[82] Barreca, D.; Comini, E.; Ferrucci, A. P.; Gasparotto, A.; Maccato, C.; Maragno, C.; Sberveglieri, G.; Tondello, E. First Example of

ZnO−TiO2 Nanocomposites by Chemical Vapor Deposition: Structure, Morphology, Composition, and Gas Sensing Performances. *Chemistry of Materials*, **2007**, *19* (23), 5642–5649. https://doi.org/10.1021/cm701990f.

[83] Galstyan, V.; Comini, E.; Faglia, G.; Sberveglieri, G. TiO2 Nanotubes: Recent Advances in Synthesis and Gas Sensing Properties. *Sensors*, **2013**, *13* (11), 14813–14838. https://doi.org/10.3390/s131114813.

[84] Zakrzewska, K. Gas Sensing Mechanism of TiO2-Based Thin Films. *Vacuum*, **2004**, *74* (2), 335–338. https://doi.org/10.1016/J.VACUUM.2003.12.152.

[85] Du, P.; Song, L.; Xiong, J.; Li, N.; Xi, Z.; Wang, L.; Jin, D.; Guo, S.; Yuan, Y. Coaxial Electrospun TiO2/ZnO Core–Sheath Nanofibers Film: Novel Structure for Photoanode of Dye-Sensitized Solar Cells. *Electrochimica Acta*, **2012**, *78*, 392–397. https://doi.org/10.1016/J.ELECTACTA.2012.06.034.

[86] Li, Z.; Ding, D.; Liu, Q.; Ning, C.; Wang, X. Ni-Doped TiO2 Nanotubes for Wide-Range Hydrogen Sensing. *Nanoscale Research Letters*, **2014**, *9* (1), 118. https://doi.org/10.1186/1556-276X-9-118.

[87] Ding, Y.; Wang, Y.; Zhang, L.; Zhang, H.; Li, C. M.; Lei, Y. Preparation of TiO2–Pt Hybrid Nanofibers and Their Application for Sensitive Hydrazine Detection. *Nanoscale*, **2011**, *3* (3), 1149–1157. https://doi.org/10.1039/C0NR00773K.

[88] Wu, Y.; Xing, S.; Fu, J. Examining the Use of TiO2 to Enhance the NH3 Sensitivity of Polypyrrole Films. *Journal of Applied Polymer Science*, **2010**, *118* (6), 3351–3356. https://doi.org/https://doi.org/10.1002/app.32382.

[89] Tai, H.; Jiang, Y.; Xie, G.; Yu, J.; Zhao, M. Self-Assembly of TiO2/Polypyrrole Nanocomposite Ultrathin Films and Application for an NH3 Gas Sensor. *International Journal of Environmental Analytical Chemistry*, **2007**, *87* (8), 539–551. https://doi.org/10.1080/03067310701272954.

[90] Bulakhe, R. N.; Patil, S. v.; Deshmukh, P. R.; Shinde, N. M.; Lokhande, C. D. Fabrication and Performance of Polypyrrole (Ppy)/TiO2 Heterojunction for Room Temperature Operated LPG Sensor. *Sensors and Actuators B: Chemical*, **2013**, *181*, 417–423. https://doi.org/10.1016/J.SNB.2013.01.056.

[91] Gong, J.; Li, Y.; Hu, Z.; Zhou, Z.; Deng, Y. Ultrasensitive NH3 Gas Sensor from Polyaniline Nanograin Enchased TiO2 Fibers. *The*

Journal of Physical Chemistry C, **2010**, *114* (21), 9970–9974. https://doi.org/10.1021/jp100685r.

[92] Pawar, S. G.; Chougule, M. A.; Sen, S.; Patil, V. B. Development of Nanostructured Polyaniline–Titanium Dioxide Gas Sensors for Ammonia Recognition. *Journal of Applied Polymer Science*, **2012**, *125* (2), 1418–1424. https://doi.org/https://doi.org/10.1002/app.35468.

[93] Wang, Q.; Dong, X.; Pang, Z.; Du, Y.; Xia, X.; Wei, Q.; Huang, F. Ammonia Sensing Behaviors of TiO2-PANI/PA6 Composite Nanofibers. *Sensors*, **2012**, *12* (12), 17046–17057. https://doi.org/10.3390/s121217046.

[94] Andersson, S.; Magnéli, A. Diskrete Titanoxydphasen Im Zusammensetzungsbereich TiO1,75-TiO1,90. *Naturwissenschaften*, **1956**, *43* (21), 495–496. https://doi.org/10.1007/BF00632520.

[95] Liborio, L.; Mallia, G.; Harrison, N. Electronic Structure of the ${\text{Ti}}_{4}{\text{O}}_{7}$ Magn\’eli Phase. *Physical Review B*, **2009**, *79* (24), 245133. https://doi.org/10.1103/PhysRevB.79.245133.

[96] Liborio, L.; Harrison, N. Thermodynamics of Oxygen Defective Magn\’eli Phases in Rutile: A First-Principles Study. *Physical Review B*, **2008**, *77* (10), 104104. https://doi.org/10.1103/PhysRevB.77.104104.

[97] Adamaki, V.; Clemens, F.; Ragulis, P.; Pennock, S. R.; Taylor, J.; Bowen, C. R. Manufacturing and Characterization of Magnéli Phase Conductive Fibres. *J. Mater. Chem. A*, **2014**, *2* (22), 8328–8333. https://doi.org/10.1039/C4TA00685B.

[98] Song, S. J.; Seok, J. Y.; Yoon, J. H.; Kim, K. M.; Kim, G. H.; Lee, M. H.; Hwang, C. S. Real-Time Identification of the Evolution of Conducting Nano-Filaments in TiO2 Thin Film ReRAM. *Scientific Reports*, **2013**, *3* (1), 3443. https://doi.org/10.1038/srep03443.

[99] Zhu, Q.; Peng, Y.; Lin, L.; Fan, C.-M.; Gao, G.-Q.; Wang, R.-X.; Xu, A.-W. Stable Blue TiO2−x Nanoparticles for Efficient Visible Light Photocatalysts. *J. Mater. Chem. A*, **2014**, *2* (12), 4429–4437. https://doi.org/10.1039/C3TA14484D.

[100] Seebauer, E. G.; Kratzer, M. C. Charged Point Defects in Semiconductors. *Materials Science and Engineering: R: Reports*, **2006**, *55* (3–6), 57–149. https://doi.org/10.1016/J.MSER.2006.01.002.

[101] Harada, S.; Tanaka, K.; Inui, H. Thermoelectric Properties and Crystallographic Shear Structures in Titanium Oxides of the Magneli Phases. *Journal of applied physics*, **2010**, *108* (8), 083703.

[102] Smith, J. R.; Walsh, F. C.; Clarke, R. L. Electrodes Based on Magnéli Phase Titanium Oxides: The Properties and Applications of Ebonex® Materials. *Journal of Applied Electrochemistry*, **1998**, *28* (10), 1021–1033. https://doi.org/10.1023/A:1003469427858.

[103] Walsh, F. C.; Wills, R. G. A. The Continuing Development of Magnéli Phase Titanium Sub-Oxides and Ebonex® Electrodes. *Electrochimica Acta*, **2010**, *55* (22), 6342–6351. https://doi.org/10.1016/J.ELECTACTA.2010.05.011.

[104] Kernazhitsky, L.; Shymanovska, V.; Gavrilko, T.; Naumov, V.; Fedorenko, L.; Kshnyakin, V.; Baran, J. Room Temperature Photoluminescence of Anatase and Rutile TiO2 Powders. *Journal of Luminescence*, **2014**, *146*, 199–204. https://doi.org/10.1016/J.JLUMIN.2013.09.068.

[105] Glinka, Y. D.; Lin, S.-H.; Hwang, L.-P.; Chen, Y.-T.; Tolk, N. H. Size Effect in Self-Trapped Exciton Photoluminescence from ${\mathrm{SiO}}_{2}$-Based Nanoscale Materials. *Physical Review B*, **2001**, *64* (8), 85421. https://doi.org/10.1103/PhysRevB.64.085421.

[106] Nakamura, I.; Negishi, N.; Kutsuna, S.; Ihara, T.; Sugihara, S.; Takeuchi, K. Role of Oxygen Vacancy in the Plasma-Treated TiO2 Photocatalyst with Visible Light Activity for NO Removal. *Journal of Molecular Catalysis A: Chemical*, **2000**, *161* (1–2), 205–212. https://doi.org/10.1016/S1381-1169(00)00362-9.

[107] le Mercier, T.; Mariot, J. M.; Parent, P.; Fontaine, M. F.; Hague, C. F.; Quarton, M. Formation of Ti3+ Ions at the Surface of Laser-Irradiated Rutile. *Applied Surface Science*, **1995**, *86* (1–4), 382–386. https://doi.org/10.1016/0169-4332(94)00421-8.

[108] Hashimoto, S.; Tanaka, A. Alteration of Ti 2p XPS Spectrum for Titanium Oxide by Low-Energy Ar Ion Bombardment. *Surface and Interface Analysis*, **2002**, *34* (1), 262–265. https://doi.org/https://doi.org/10.1002/sia.1296.

[109] Wang, W. K.; Gao, M.; Zhang, X.; Fujitsuka, M.; Majima, T.; Yu, H. Q. One-Step Synthesis of Nonstoichiometric TiO2 with Designed (101) Facets for Enhanced Photocatalytic H2 Evolution. *Applied Catalysis B: Environmental*, **2017**, *205*, 165–172. https://doi.org/10.1016/J.APCATB.2016.12.036.

[110] Fukushima, J.; Takizawa, H. Size Control of Ti4O7 Nanoparticles by Carbothermal Reduction Using a Multimode Microwave Furnace. *Crystals*, **2018**, *8* (12). https://doi.org/10.3390/cryst8120444.

[111] Hayfield, P. C. S. *Development of a New Material: Monolithic Ti4O7 Ebonex Ceramic*; Royal Society of Chemistry, 2007.

[112] Mirzaei, A.; Kim, S. S.; Kim, H. W. Resistance-Based H2S Gas Sensors Using Metal Oxide Nanostructures: A Review of Recent Advances. *Journal of Hazardous Materials*, **2018**, *357*, 314–331. https://doi.org/10.1016/J.JHAZMAT.2018.06.015.

[113] Mirzaei, A.; Leonardi, S. G.; Neri, G. Detection of Hazardous Volatile Organic Compounds (VOCs) by Metal Oxide Nanostructures-Based Gas Sensors: A Review. *Ceramics International*, **2016**, *42* (14), 15119–15141. https://doi.org/10.1016/J.CERAMINT.2016.06.145.

[114] Mirzaei, A.; Kim, J.-H.; Kim, H. W.; Kim, S. S. Resistive-Based Gas Sensors for Detection of Benzene, Toluene and Xylene (BTX) Gases: A Review. *J. Mater. Chem. C*, **2018**, *6* (16), 4342–4370. https://doi.org/10.1039/C8TC00245B.

[115] Simon, I.; Bârsan, N.; Bauer, M.; Weimar, U. Micromachined Metal Oxide Gas Sensors: Opportunities to Improve Sensor Performance. *Sensors and Actuators B: Chemical*, **2001**, *73* (1), 1–26. https://doi.org/10.1016/S0925-4005(00)00639-0.

[116] Kim, J. H.; Mirzaei, A.; Kim, H. W.; Kim, S. S. Low Power-Consumption CO Gas Sensors Based on Au-Functionalized SnO2-ZnO Core-Shell Nanowires. *Sensors and Actuators B: Chemical*, **2018**, *267*, 597–607. https://doi.org/10.1016/J.SNB.2018.04.079.

[117] Zeng, W.; Liu, T.; Wang, Z. Enhanced Gas Sensing Properties by SnO2 Nanosphere Functionalized TiO2 Nanobelts. *J. Mater. Chem.*, **2012**, *22* (8), 3544–3548. https://doi.org/10.1039/C2JM15017D.

[118] Gallart, M.; Cottineau, T.; Hönerlage, B.; Keller, V.; Keller, N.; Gilliot, P. Temperature Dependent Photoluminescence of Anatase and Rutile TiO2 Single Crystals: Polaron and Self-Trapped Exciton Formation. *Journal of Applied Physics*, **2018**, *124* (13), 133104.

[119] Serpone, N.; Lawless, D.; Khairutdinov, R. Size Effects on the Photophysical Properties of Colloidal Anatase TiO2 Particles: Size Quantization versus Direct Transitions in This Indirect Semiconductor? *The Journal of Physical Chemistry*, **1995**, *99* (45), 16646–16654. https://doi.org/10.1021/j100045a026.

[120] Saraf, L. v; Patil, S. I.; Ogale, S. B.; Sainkar, S. R.; Kshirsager, S. T. Synthesis of Nanophase TiO 2 by Ion Beam Sputtering and Cold

Condensation Technique. *International journal of modern physics B*, **1998**, *12* (25), 2635–2647.

[121] Zhang, Y.; Jiang, Z.; Huang, J.; Lim, L. Y.; Li, W.; Deng, J.; Gong, D.; Tang, Y.; Lai, Y.; Chen, Z. Titanate and Titania Nanostructured Materials for Environmental and Energy Applications: A Review. *RSC Adv.*, **2015**, *5* (97), 79479–79510. https://doi.org/10.1039/C5RA11298B.

[122] Fujihara, K.; Izumi, S.; Ohno, T.; Matsumura, M. Time-Resolved Photoluminescence of Particulate TiO2 Photocatalysts Suspended in Aqueous Solutions. *Journal of Photochemistry and Photobiology A: Chemistry*, **2000**, *132* (1–2), 99–104. https://doi.org/10.1016/S1010-6030(00)00204-5.

[123] Naguib, M.; Kurtoglu, M.; Presser, V.; Lu, J.; Niu, J.; Heon, M.; Hultman, L.; Gogotsi, Y.; Barsoum, M. W. Two-Dimensional Nanocrystals Produced by Exfoliation of Ti3AlC2. *Advanced Materials*, **2011**, *23* (37), 4248–4253. https://doi.org/https://doi.org/10.1002/adma.201102306.

[124] Naguib, M.; Mashtalir, O.; Carle, J.; Presser, V.; Lu, J.; Hultman, L.; Gogotsi, Y.; Barsoum, M. W. Two-Dimensional Transition Metal Carbides. *ACS Nano*, **2012**, *6* (2), 1322–1331. https://doi.org/10.1021/nn204153h.

[125] Naguib, M.; Mochalin, V. N.; Barsoum, M. W.; Gogotsi, Y. 25th Anniversary Article: MXenes: A New Family of Two-Dimensional Materials. *Advanced Materials*, **2014**, *26* (7), 992–1005. https://doi.org/https://doi.org/10.1002/adma.201304138.

[126] Naguib, M.; Gogotsi, Y. Synthesis of Two-Dimensional Materials by Selective Extraction. *Accounts of Chemical Research*, **2015**, *48* (1), 128–135. https://doi.org/10.1021/ar500346b.

[127] Deshmukh, K.; Kovářík, T.; Khadheer Pasha, S. K. State of the Art Recent Progress in Two Dimensional MXenes Based Gas Sensors and Biosensors: A Comprehensive Review. *Coordination Chemistry Reviews*, **2020**, *424*, 213514. https://doi.org/10.1016/J.CCR.2020.213514.

[128] Ibrahim, Y.; Mohamed, A.; Abdelgawad, A. M.; Eid, K.; Abdullah, A. M.; Elzatahry, A. The Recent Advances in the Mechanical Properties of Self-Standing Two-Dimensional MXene-Based Nanostructures: Deep Insights into the Supercapacitor. *Nanomaterials*, **2020**, *10* (10). https://doi.org/10.3390/nano10101916.

[129] Khazaei, M.; Arai, M.; Sasaki, T.; Ranjbar, A.; Liang, Y.; Yunoki, S. OH-Terminated Two-Dimensional Transition Metal Carbides and Nitrides as Ultralow Work Function Materials. *Physical Review B*, **2015**, *92* (7), 75411. https://doi.org/10.1103/PhysRevB.92.075411.

[130] Tahini, H. A.; Tan, X.; Smith, S. C. The Origin of Low Workfunctions in OH Terminated MXenes. *Nanoscale*, **2017**, *9* (21), 7016–7020. https://doi.org/10.1039/C7NR01601H.

[131] Liu, M.; He, Y.; Zhou, J.; Ge, Y.; Zhou, J.; Song, G. A ’’naked-Eye’’ Colorimetric and Ratiometric Fluorescence Probe for Uric Acid Based on Ti3C2 MXene Quantum Dots. *Analytica Chimica Acta*, **2020**, *1103*, 134–142. https://doi.org/10.1016/J.ACA.2019.12.069.

[132] Zhao, Y.; Watanabe, K.; Hashimoto, K. Self-Supporting Oxygen Reduction Electrocatalysts Made from a Nitrogen-Rich Network Polymer. *Journal of the American Chemical Society*, **2012**, *134* (48), 19528–19531. https://doi.org/10.1021/ja3085934.

[133] Ghidiu, M.; Lukatskaya, M. R.; Zhao, M.-Q.; Gogotsi, Y.; Barsoum, M. W. Conductive Two-Dimensional Titanium Carbide ‘Clay’ with High Volumetric Capacitance. *Nature*, **2014**, *516* (7529), 78–81. https://doi.org/10.1038/nature13970.

[134] Eklund, P.; Rosen, J.; Persson, P. O. Å. Layered Ternary Mn+1AXnphases and Their 2D Derivative MXene: An Overview from a Thin-Film Perspective. *Journal of Physics D: Applied Physics*, **2017**, *50* (11), 113001. https://doi.org/10.1088/1361-6463/aa57bc.

[135] Magnuson, M.; Mattesini, M. Chemical Bonding and Electronic-Structure in MAX Phases as Viewed by X-Ray Spectroscopy and Density Functional Theory. *Thin Solid Films*, **2017**, *621*, 108–130. https://doi.org/10.1016/J.TSF.2016.11.005.

[136] Ma, T. Y.; Cao, J. L.; Jaroniec, M.; Qiao, S. Z. Interacting Carbon Nitride and Titanium Carbide Nanosheets for High-Performance Oxygen Evolution. *Angewandte Chemie International Edition*, **2016**, *55* (3), 1138–1142. https://doi.org/https://doi.org/10.1002/anie.201509758.

[137] Seh, Z. W.; Fredrickson, K. D.; Anasori, B.; Kibsgaard, J.; Strickler, A. L.; Lukatskaya, M. R.; Gogotsi, Y.; Jaramillo, T. F.; Vojvodic, A. Two-Dimensional Molybdenum Carbide (MXene) as an Efficient Electrocatalyst for Hydrogen Evolution. *ACS Energy Letters*, **2016**, *1* (3), 589–594. https://doi.org/10.1021/acsenergylett.6b00247.

[138] Bhat, A.; Anwer, S.; Bhat, K. S.; Mohideen, M. I. H.; Liao, K.; Qurashi, A. Prospects Challenges and Stability of 2D MXenes for

Clean Energy Conversion and Storage Applications. *npj 2D Materials and Applications*, **2021**, *5* (1), 61. https://doi.org/10.1038/s41699-021-00239-8.

[139] Papadopoulou, K. A.; Chroneos, A.; Parfitt, D.; Christopoulos, S.-R. G. A Perspective on MXenes: Their Synthesis, Properties, and Recent Applications. *Journal of Applied Physics*, **2020**, *128* (17), 170902. https://doi.org/10.1063/5.0021485.

[140] Anasori, B.; Lukatskaya, M. R.; Gogotsi, Y. 2D Metal Carbides and Nitrides (MXenes) for Energy Storage. *Nature Reviews Materials*, **2017**, *2* (2), 16098. https://doi.org/10.1038/natrevmats.2016.98.

[141] Sinha, A.; Dhanjai; Zhao, H.; Huang, Y.; Lu, X.; Chen, J.; Jain, R. MXene: An Emerging Material for Sensing and Biosensing. *TrAC Trends in Analytical Chemistry*, **2018**, *105*, 424–435. https://doi.org/10.1016/J.TRAC.2018.05.021.

[142] Ramanavicius, S.; Ramanavicius, A. Progress and Insights in the Application of MXenes as New 2D Nano-Materials Suitable for Biosensors and Biofuel Cell Design. *International Journal of Molecular Sciences*, **2020**, *21* (23). https://doi.org/10.3390/ijms21239224.

[143] Xie, X.; Chen, S.; Ding, W.; Nie, Y.; Wei, Z. An Extraordinarily Stable Catalyst: Pt NPs Supported on Two-Dimensional Ti3C2X2 (X = OH, F) Nanosheets for Oxygen Reduction Reaction. *Chem. Commun.*, **2013**, *49* (86), 10112–10114. https://doi.org/10.1039/C3CC44428G.

[144] Zhang, J.; Zhao, Y.; Guo, X.; Chen, C.; Dong, C.-L.; Liu, R.-S.; Han, C.-P.; Li, Y.; Gogotsi, Y.; Wang, G. Single Platinum Atoms Immobilized on an MXene as an Efficient Catalyst for the Hydrogen Evolution Reaction. *Nature Catalysis*, **2018**, *1* (12), 985–992. https://doi.org/10.1038/s41929-018-0195-1.

[145] Ran, J.; Gao, G.; Li, F.-T.; Ma, T.-Y.; Du, A.; Qiao, S.-Z. Ti3C2 MXene Co-Catalyst on Metal Sulfide Photo-Absorbers for Enhanced Visible-Light Photocatalytic Hydrogen Production. *Nature Communications*, **2017**, *8* (1), 13907. https://doi.org/10.1038/ncomms13907.

[146] Yin, L.; Li, Y.; Yao, X.; Wang, Y.; Jia, L.; Liu, Q.; Li, J.; Li, Y.; He, D. MXenes for Solar Cells. *Nano-Micro Letters*, **2021**, *13* (1), 78. https://doi.org/10.1007/s40820-021-00604-8.

[147] Zhu, Z.; Zou, Y.; Hu, W.; Li, Y.; Gu, Y.; Cao, B.; Guo, N.; Wang, L.; Song, J.; Zhang, S.; et al. Near-Infrared Plasmonic 2D Semimetals for Applications in Communication and Biology. *Advanced Functional*

Materials, **2016**, *26* (11), 1793–1802. https://doi.org/https://doi.org/10.1002/adfm.201504884.

[148] Dillon, A. D.; Ghidiu, M. J.; Krick, A. L.; Griggs, J.; May, S. J.; Gogotsi, Y.; Barsoum, M. W.; Fafarman, A. T. Highly Conductive Optical Quality Solution-Processed Films of 2D Titanium Carbide. *Advanced Functional Materials*, **2016**, *26* (23), 4162–4168. https://doi.org/https://doi.org/10.1002/adfm.201600357.

[149] Mariano, M.; Mashtalir, O.; Antonio, F. Q.; Ryu, W.-H.; Deng, B.; Xia, F.; Gogotsi, Y.; Taylor, A. D. Solution-Processed Titanium Carbide MXene Films Examined as Highly Transparent Conductors. *Nanoscale*, **2016**, *8* (36), 16371–16378. https://doi.org/10.1039/C6NR03682A.

[150] Melchior, S. A.; Raju, K.; Ike, I. S.; Erasmus, R. M.; Kabongo, G.; Sigalas, I.; Iyuke, S. E.; Ozoemena, K. I. High-Voltage Symmetric Supercapacitor Based on 2D Titanium Carbide (MXene, Ti2CTx)/Carbon Nanosphere Composites in a Neutral Aqueous Electrolyte. *Journal of The Electrochemical Society*, **2018**, *165* (3), A501–A511. https://doi.org/10.1149/2.0401803jes.

[151] Echols, I. J.; An, H.; Zhao, X.; Prehn, E. M.; Tan, Z.; Radovic, M.; Green, M. J.; Lutkenhaus, J. L. PH-Response of Polycation/Ti3C2Tx MXene Layer-by-Layer Assemblies for Use as Resistive Sensors. *Mol. Syst. Des. Eng.*, **2020**, *5* (1), 366–375. https://doi.org/10.1039/C9ME00142E.

[152] Lorencova, L.; Bertok, T.; Dosekova, E.; Holazova, A.; Paprckova, D.; Vikartovska, A.; Sasinkova, V.; Filip, J.; Kasak, P.; Jerigova, M.; et al. Electrochemical Performance of Ti3C2Tx MXene in Aqueous Media: Towards Ultrasensitive H2O2 Sensing. *Electrochimica Acta*, **2017**, *235*, 471–479. https://doi.org/10.1016/J.ELECTACTA.2017.03.073.

[153] An, H.; Habib, T.; Shah, S.; Gao, H.; Patel, A.; Echols, I.; Zhao, X.; Radovic, M.; Green, M. J.; Lutkenhaus, J. L. Water Sorption in MXene/Polyelectrolyte Multilayers for Ultrafast Humidity Sensing. *ACS Applied Nano Materials*, **2019**, *2* (2), 948–955. https://doi.org/10.1021/acsanm.8b02265.

[154] Song, D.; Jiang, X.; Li, Y.; Lu, X.; Luan, S.; Wang, Y.; Li, Y.; Gao, F. Metal−organic Frameworks-Derived MnO2/Mn3O4 Microcuboids with Hierarchically Ordered Nanosheets and Ti3C2 MXene/Au NPs Composites for Electrochemical Pesticide Detection. *Journal of Hazardous Materials*, **2019**, *373*, 367–376. https://doi.org/10.1016/J.JHAZMAT.2019.03.083.

[155] Kim, H.; Wang, Z.; Alshareef, H. N. MXetronics: Electronic and Photonic Applications of MXenes. *Nano Energy*, **2019**, *60*, 179–197. https://doi.org/10.1016/J.NANOEN.2019.03.020.

[156] Zhu, X.; Liu, P.; Xue, T.; Ge, Y.; Ai, S.; Sheng, Y.; Wu, R.; Xu, L.; Tang, K.; Wen, Y. A Novel Graphene-like Titanium Carbide MXene/Au–Ag Nanoshuttles Bifunctional Nanosensor for Electrochemical and SERS Intelligent Analysis of Ultra-Trace Carbendazim Coupled with Machine Learning. *Ceramics International*, **2021**, *47* (1), 173–184. https://doi.org/10.1016/J.CERAMINT.2020.08.121.

[157] Hu, M.; Li, Z.; Hu, T.; Zhu, S.; Zhang, C.; Wang, X. High-Capacitance Mechanism for Ti3C2Tx MXene by in Situ Electrochemical Raman Spectroscopy Investigation. *ACS Nano*, **2016**, *10* (12), 11344–11350. https://doi.org/10.1021/acsnano.6b06597.

[158] Zhang, Q.; Wang, F.; Zhang, H.; Zhang, Y.; Liu, M.; Liu, Y. Universal Ti3C2 MXenes Based Self-Standard Ratiometric Fluorescence Resonance Energy Transfer Platform for Highly Sensitive Detection of Exosomes. *Analytical Chemistry*, **2018**, *90* (21), 12737–12744. https://doi.org/10.1021/acs.analchem.8b03083.

[159] Liu, H.; Duan, C.; Yang, C.; Shen, W.; Wang, F.; Zhu, Z. A Novel Nitrite Biosensor Based on the Direct Electrochemistry of Hemoglobin Immobilized on MXene-Ti3C2. *Sensors and Actuators B: Chemical*, **2015**, *218*, 60–66. https://doi.org/10.1016/J.SNB.2015.04.090.

[160] Wu, L.; Lu, X.; Dhanjai; Wu, Z. S.; Dong, Y.; Wang, X.; Zheng, S.; Chen, J. 2D Transition Metal Carbide MXene as a Robust Biosensing Platform for Enzyme Immobilization and Ultrasensitive Detection of Phenol. *Biosensors and Bioelectronics*, **2018**, *107*, 69–75. https://doi.org/10.1016/J.BIOS.2018.02.021.

[161] Wang, F.; Yang, C.; Duan, C.; Xiao, D.; Tang, Y.; Zhu, J. An Organ-Like Titanium Carbide Material (MXene) with Multilayer Structure Encapsulating Hemoglobin for a Mediator-Free Biosensor. *Journal of The Electrochemical Society*, **2014**, *162* (1), B16–B21. https://doi.org/10.1149/2.0371501jes.

[162] Zheng, J.; Diao, J.; Jin, Y.; Ding, A.; Wang, B.; Wu, L.; Weng, B.; Chen, J. An Inkjet Printed Ti3C2-GO Electrode for the Electrochemical Sensing of Hydrogen Peroxide. *Journal of The Electrochemical Society*, **2018**, *165* (5), B227–B231. https://doi.org/10.1149/2.0051807jes.

[163] Zhu, X.; Liu, B.; Hou, H.; Huang, Z.; Zeinu, K. M.; Huang, L.; Yuan, X.; Guo, D.; Hu, J.; Yang, J. Alkaline Intercalation of Ti3C2 MXene for Simultaneous Electrochemical Detection of Cd(II), Pb(II), Cu(II) and Hg(II). *Electrochimica Acta*, **2017**, *248*, 46–57. https://doi.org/10.1016/J.ELECTACTA.2017.07.084.

[164] Rasheed, P. A.; Pandey, R. P.; Rasool, K.; Mahmoud, K. A. Ultra-Sensitive Electrocatalytic Detection of Bromate in Drinking Water Based on Nafion/Ti3C2Tx (MXene) Modified Glassy Carbon Electrode. *Sensors and Actuators B: Chemical*, **2018**, *265*, 652–659. https://doi.org/10.1016/J.SNB.2018.03.103.

[165] Zhou, L.; Zhang, X.; Ma, L.; Gao, J.; Jiang, Y. Acetylcholinesterase/Chitosan-Transition Metal Carbides Nanocomposites-Based Biosensor for the Organophosphate Pesticides Detection. *Biochemical Engineering Journal*, **2017**, *128*, 243–249. https://doi.org/10.1016/J.BEJ.2017.10.008.

[166] Lorencova, L.; Bertok, T.; Filip, J.; Jerigova, M.; Velic, D.; Kasak, P.; Mahmoud, K. A.; Tkac, J. Highly Stable Ti3C2Tx (MXene)/Pt Nanoparticles-Modified Glassy Carbon Electrode for H2O2 and Small Molecules Sensing Applications. *Sensors and Actuators B: Chemical*, **2018**, *263*, 360–368. https://doi.org/10.1016/J.SNB.2018.02.124.

[167] Kalambate, P. K.; Gadhari, N. S.; Li, X.; Rao, Z.; Navale, S. T.; Shen, Y.; Patil, V. R.; Huang, Y. Recent Advances in MXene–Based Electrochemical Sensors and Biosensors. *TrAC Trends in Analytical Chemistry*, **2019**, *120*, 115643. https://doi.org/10.1016/J.TRAC.2019.115643.

[168] Zhu, X.; Zhang, Y.; Liu, M.; Liu, Y. 2D Titanium Carbide MXenes as Emerging Optical Biosensing Platforms. *Biosensors and Bioelectronics*, **2021**, *171*, 112730. https://doi.org/10.1016/J.BIOS.2020.112730.

[169] Rasool, K.; Mahmoud, K. A.; Johnson, D. J.; Helal, M.; Berdiyorov, G. R.; Gogotsi, Y. Efficient Antibacterial Membrane Based on Two-Dimensional Ti3C2Tx (MXene) Nanosheets. *Scientific Reports*, **2017**, *7* (1), 1598. https://doi.org/10.1038/s41598-017-01714-3.

[170] Lin, H.; Chen, Y.; Shi, J. Insights into 2D MXenes for Versatile Biomedical Applications: Current Advances and Challenges Ahead. *Advanced Science*, **2018**, *5* (10), 1800518. https://doi.org/https://doi.org/10.1002/advs.201800518.

[171] Rakhi, R. B.; Nayak, P.; Xia, C.; Alshareef, H. N. Novel Amperometric Glucose Biosensor Based on MXene Nanocomposite. *Scientific Reports*, **2016**, *6* (1), 36422. https://doi.org/10.1038/srep36422.

[172] Ramanavicius, A.; Ramanaviciene, A. Hemoproteins in Design of Biofuel Cells. *Fuel Cells,* **2009**, *9* (1), 25–36. https://doi.org/https://doi.org/10.1002/fuce.200800052.

[173] Emir, G.; Dilgin, Y.; Ramanaviciene, A.; Ramanavicius, A. Amperometric Nonenzymatic Glucose Biosensor Based on Graphite Rod Electrode Modified by Ni-Nanoparticle/Polypyrrole Composite. *Microchemical Journal*, **2021**, *161*, 105751. https://doi.org/10.1016/J.MICROC.2020.105751.

[174] Kisieliute, A.; Popov, A.; Apetrei, R. M.; Cârâc, G.; Morkvenaite-Vilkonciene, I.; Ramanaviciene, A.; Ramanavicius, A. Towards Microbial Biofuel Cells: Improvement of Charge Transfer by Self-Modification of Microoganisms with Conducting Polymer – Polypyrrole. *Chemical Engineering Journal*, **2019**, *356*, 1014–1021. https://doi.org/10.1016/J.CEJ.2018.09.026.

[175] Ramanavicius, A.; Oztekin, Y.; Ramanaviciene, A. Electrochemical Formation of Polypyrrole-Based Layer for Immunosensor Design. *Sensors and Actuators B: Chemical*, **2014**, *197*, 237–243. https://doi.org/10.1016/J.SNB.2014.02.072.

[176] Ramanaviciene, A.; Ramanavicius, A. Pulsed Amperometric Detection of DNA with an SsDNA/Polypyrrole-Modified Electrode. *Analytical and Bioanalytical Chemistry*, **2004**, *379* (2), 287–293. https://doi.org/10.1007/s00216-004-2573-6.

[177] Ratautaite, V.; Plausinaitis, D.; Baleviciute, I.; Mikoliunaite, L.; Ramanaviciene, A.; Ramanavicius, A. Characterization of Caffeine-Imprinted Polypyrrole by a Quartz Crystal Microbalance and Electrochemical Impedance Spectroscopy. *Sensors and Actuators B: Chemical*, **2015**, *212*, 63–71. https://doi.org/10.1016/J.SNB.2015.01.109.

[178] Fryxell, G. E.; Cao, G. *Environmental Applications of Nanomaterials: Synthesis, Sorbents and Sensors*; World Scientific, 2012.

[179] Yoon, J.; Shin, M.; Lim, J.; Lee, J.-Y.; Choi, J.-W. Recent Advances in MXene Nanocomposite-Based Biosensors. *Biosensors*, **2020**, *10* (11). https://doi.org/10.3390/bios10110185.

[180] Liu, R.; Jiang, L.; Lu, C.; Yu, Z.; Li, F.; Jing, X.; Xu, R.; Zhou, W.; Jin, S. Large-Scale Two-Dimensional Titanium Carbide MXene as SERS-Active Substrate for Reliable and Sensitive Detection of

Organic Pollutants. *Spectrochimica Acta Part A: Molecular and Biomolecular Spectroscopy*, **2020**, *236*, 118336. https://doi.org/10.1016/J.SAA.2020.118336.

[181] Elumalai, S.; Lombardi, J. R.; Yoshimura, M. The Surface-Enhanced Resonance Raman Scattering of Dye Molecules Adsorbed on Two-Dimensional Titanium Carbide Ti3C2Tx (MXene) Film. *Mater. Adv.*, **2020**, *1* (2), 146–152. https://doi.org/10.1039/D0MA00091D.

[182] Mauchamp, V.; Bugnet, M.; Bellido, E. P.; Botton, G. A.; Moreau, P.; Magne, D.; Naguib, M.; Cabioc'h, T.; Barsoum, M. W. Enhanced and Tunable Surface Plasmons in Two-Dimensional ${\mathrm{Ti}}_{3}{\mathrm{C}}_{2}$ Stacks: Electronic Structure versus Boundary Effects. *Physical Review B*, **2014**, *89* (23), 235428. https://doi.org/10.1103/PhysRevB.89.235428.

[183] Lashgari, H.; Abolhassani, M. R.; Boochani, A.; Elahi, S. M.; Khodadadi, J. Electronic and Optical Properties of 2D Graphene-like Compounds Titanium Carbides and Nitrides: DFT Calculations. *Solid State Communications*, **2014**, *195*, 61–69. https://doi.org/10.1016/J.SSC.2014.06.008.

[184] Oztekin, Y.; Ramanaviciene, A.; Yazicigil, Z.; Solak, A. O.; Ramanavicius, A. Direct Electron Transfer from Glucose Oxidase Immobilized on Polyphenanthroline-Modified Glassy Carbon Electrode. *Biosensors and Bioelectronics*, **2011**, *26* (5), 2541–2546. https://doi.org/10.1016/J.BIOS.2010.11.001.

[185] Kausaite-Minkstimiene, A.; Mazeiko, V.; Ramanaviciene, A.; Oztekin, Y.; Osman Solak, A.; Ramanavicius, A. Evaluation of Some Redox Mediators in the Design of Reagentless Amperometric Glucose Biosensor. *Electroanalysis*, **2014**, *26* (7), 1528–1535. https://doi.org/https://doi.org/10.1002/elan.201400023.

[186] Bagdžiūnas, G.; Ramanavičius, A. Towards Direct Enzyme Wiring: A Theoretical Investigation of Charge Carrier Transfer Mechanisms between Glucose Oxidase and Organic Semiconductors. *Phys. Chem. Chem. Phys.*, **2019**, *21* (6), 2968–2976. https://doi.org/10.1039/C8CP07233G.

[187] Bagdžiūnas, G.; Žukauskas, Š.; Ramanavičius, A. Insights into a Hole Transfer Mechanism between Glucose Oxidase and a P-Type Organic Semiconductor. *Biosensors and Bioelectronics*, **2018**, *102*, 449–455. https://doi.org/10.1016/J.BIOS.2017.11.053.

[188] Ramanaviciene, A.; Nastajute, G.; Snitka, V.; Kausaite, A.; German, N.; Barauskas-Memenas, D.; Ramanavicius, A. Spectrophotometric

Evaluation of Gold Nanoparticles as Red-Ox Mediator for Glucose Oxidase. *Sensors and Actuators B: Chemical*, **2009**, *137* (2), 483–489. https://doi.org/10.1016/J.SNB.2009.01.021.

[189] Ramanavicius, A.; Kausaite, A.; Ramanaviciene, A. Enzymatic Biofuel Cell Based on Anode and Cathode Powered by Ethanol. *Biosensors and Bioelectronics*, **2008**, *24* (4), 761–766. https://doi.org/10.1016/J.BIOS.2008.06.048.

[190] Ramanavicius, A.; Kausaite, A.; Ramanaviciene, A. Biofuel Cell Based on Direct Bioelectrocatalysis. *Biosensors and Bioelectronics*, **2005**, *20* (10), 1962–1967. https://doi.org/10.1016/J.BIOS.2004.08.032.

[191] Shahzad, F.; Iqbal, A.; Zaidi, S. A.; Hwang, S. W.; Koo, C. M. Nafion-Stabilized Two-Dimensional Transition Metal Carbide (Ti3C2Tx MXene) as a High-Performance Electrochemical Sensor for Neurotransmitter. *Journal of Industrial and Engineering Chemistry*, **2019**, *79*, 338–344. https://doi.org/10.1016/J.JIEC.2019.03.061.

[192] Lapenaite, I.; Ramanaviciene, A.; Ramanavicius, A. Current Trends in Enzymatic Determination of Glycerol. *Critical Reviews in Analytical Chemistry*, **2006**, *36* (1), 13–25. https://doi.org/10.1080/10408340500451973.

[193] German, N.; Ramanaviciene, A.; Ramanavicius, A. Formation of Polyaniline and Polypyrrole Nanocomposites with Embedded Glucose Oxidase and Gold Nanoparticles. *Polymers*, **2019**, *11* (2). https://doi.org/10.3390/polym11020377.

[194] Kausaite-Minkstimiene, A.; Glumbokaite, L.; Ramanaviciene, A.; Dauksaite, E.; Ramanavicius, A. An Amperometric Glucose Biosensor Based on Poly (Pyrrole-2-Carboxylic Acid)/Glucose Oxidase Biocomposite. *Electroanalysis*, **2018**, *30* (8), 1642–1652. https://doi.org/https://doi.org/10.1002/elan.201800044.

[195] Bruzaite, I.; Rozene, J.; Morkvenaite-Vilkonciene, I.; Ramanavicius, A. Towards Microorganism-Based Biofuel Cells: The Viability of Saccharomyces Cerevisiae Modified by Multiwalled Carbon Nanotubes. *Nanomaterials*, **2020**, *10* (5). https://doi.org/10.3390/nano10050954.

[196] Kausaite-Minkstimiene, A.; Glumbokaite, L.; Ramanaviciene, A.; Ramanavicius, A. Reagent-Less Amperometric Glucose Biosensor Based on Nanobiocomposite Consisting of Poly(1,10-Phenanthroline-5,6-Dione), Poly(Pyrrole-2-Carboxylic Acid), Gold Nanoparticles and

Glucose Oxidase. *Microchemical Journal*, **2020**, *154*, 104665. https://doi.org/10.1016/J.MICROC.2020.104665.

[197] German, N.; Ramanavicius, A.; Voronovic, J.; Oztekin, Y.; Ramanaviciene, A. The Effect of Colloidal Solutions of Gold Nanoparticles on the Performance of a Glucose Oxidase Modified Carbon Electrode. *Microchimica Acta*, **2011**, *172* (1), 185–191. https://doi.org/10.1007/s00604-010-0474-2.

[198] German, N.; Ramanavicius, A.; Voronovic, J.; Ramanaviciene, A. Glucose Biosensor Based on Glucose Oxidase and Gold Nanoparticles of Different Sizes Covered by Polypyrrole Layer. *Colloids and Surfaces A: Physicochemical and Engineering Aspects*, **2012**, *413*, 224–230. https://doi.org/10.1016/J.COLSURFA.2012.02.012.

[199] German, N.; Ramanavicius, A.; Ramanaviciene, A. Electrochemical Deposition of Gold Nanoparticles on Graphite Rod for Glucose Biosensing. *Sensors and Actuators B: Chemical*, **2014**, *203*, 25–34. https://doi.org/10.1016/J.SNB.2014.06.021.

[200] German, N.; Kausaite-Minkstimiene, A.; Ramanavicius, A.; Semashko, T.; Mikhailova, R.; Ramanaviciene, A. The Use of Different Glucose Oxidases for the Development of an Amperometric Reagentless Glucose Biosensor Based on Gold Nanoparticles Covered by Polypyrrole. *Electrochimica Acta*, **2015**, *169*, 326–333. https://doi.org/10.1016/J.ELECTACTA.2015.04.072.

[201] Apetrei, R. M.; Carac, G.; Bahrim, G.; Ramanaviciene, A.; Ramanavicius, A. Modification of Aspergillus Niger by Conducting Polymer, Polypyrrole, and the Evaluation of Electrochemical Properties of Modified Cells. *Bioelectrochemistry*, **2018**, *121*, 46–55. https://doi.org/10.1016/J.BIOELECHEM.2018.01.001.

[202] Stirke, A.; Apetrei, R. M.; Kirsnyte, M.; Dedelaite, L.; Bondarenka, V.; Jasulaitiene, V.; Pucetaite, M.; Selskis, A.; Carac, G.; Bahrim, G.; et al. Synthesis of Polypyrrole Microspheres by Streptomyces Spp. *Polymer*, **2016**, *84*, 99–106. https://doi.org/10.1016/J.POLYMER.2015.12.029.

[203] Andriukonis, E.; Stirke, A.; Garbaras, A.; Mikoliunaite, L.; Ramanaviciene, A.; Remeikis, V.; Thornton, B.; Ramanavicius, A. Yeast-Assisted Synthesis of Polypyrrole: Quantification and Influence on the Mechanical Properties of the Cell Wall. *Colloids and Surfaces B: Biointerfaces*, **2018**, *164*, 224–231. https://doi.org/10.1016/J.COLSURFB.2018.01.034.

[204] Ramanavicius, A.; Andriukonis, E.; Stirke, A.; Mikoliunaite, L.; Balevicius, Z.; Ramanaviciene, A. Synthesis of Polypyrrole within the Cell Wall of Yeast by Redox-Cycling of [Fe(CN)6]3−/[Fe(CN)6]4−. *Enzyme and Microbial Technology*, **2016**, *83*, 40–47. https://doi.org/10.1016/J.ENZMICTEC.2015.11.009.

[205] Garbaras, A.; Mikoliunaite, L.; Popov, A.; Ramanaviciene, A.; Remeikis, V.; Ramanavicius, A. The Isotope Method for the Determination of Stoichiometry between Compounds Forming the Polypyrrole and Glucose Oxidase Composite. *Phys. Chem. Chem. Phys.*, **2015**, *17* (3), 2252–2258. https://doi.org/10.1039/C4CP04885G.

[206] Wang, X.; Lu, X.; Wu, L.; Chen, J. Direct Electrochemical Tyrosinase Biosensor Based on Mesoporous Carbon and Co3O4 Nanorods for the Rapid Detection of Phenolic Pollutants. *ChemElectroChem*, **2014**, *1* (4), 808–816. https://doi.org/https://doi.org/10.1002/celc.201300208.

[207] Kamysbayev, V.; Filatov, A. S.; Hu, H.; Rui, X.; Lagunas, F.; Wang, D.; Klie, R. F.; Talapin, D. v. Covalent Surface Modifications and Superconductivity of Two-Dimensional Metal Carbide MXenes. *Science*, **2020**, *369* (6506), 979–983.

[208] Soomro, R. A.; Jawaid, S.; Zhu, Q.; Abbas, Z.; Xu, B. A Mini-Review on MXenes as Versatile Substrate for Advanced Sensors. *Chinese Chemical Letters*, **2020**, *31* (4), 922–930. https://doi.org/10.1016/J.CCLET.2019.12.005.

[209] Zhu, J.; Ha, E.; Zhao, G.; Zhou, Y.; Huang, D.; Yue, G.; Hu, L.; Sun, N.; Wang, Y.; Lee, L. Y. S.; et al. Recent Advance in MXenes: A Promising 2D Material for Catalysis, Sensor and Chemical Adsorption. *Coordination Chemistry Reviews*, **2017**, *352*, 306–327. https://doi.org/10.1016/J.CCR.2017.09.012.

[210] Yu, T.; Breslin, C. B. Review—Two-Dimensional Titanium Carbide MXenes and Their Emerging Applications as Electrochemical Sensors. *Journal of The Electrochemical Society*, **2020**, *167* (3), 037514. https://doi.org/10.1149/2.0142003jes.

[211] Zheng, J.; Wang, B.; Ding, A.; Weng, B.; Chen, J. Synthesis of MXene/DNA/Pd/Pt Nanocomposite for Sensitive Detection of Dopamine. *Journal of Electroanalytical Chemistry*, **2018**, *816*, 189–194. https://doi.org/10.1016/J.JELECHEM.2018.03.056.

[212] Sinha, A.; Dhanjai; Zhao, H.; Huang, Y.; Lu, X.; Chen, J.; Jain, R. MXene: An Emerging Material for Sensing and Biosensing. *TrAC*

Trends in Analytical Chemistry, **2018**, *105*, 424–435. https://doi.org/10.1016/J.TRAC.2018.05.021.

[213] Jiang, Y.; Zhang, X.; Pei, L.; Yue, S.; Ma, L.; Zhou, L.; Huang, Z.; He, Y.; Gao, J. Silver Nanoparticles Modified Two-Dimensional Transition Metal Carbides as Nanocarriers to Fabricate Acetycholinesterase-Based Electrochemical Biosensor. *Chemical Engineering Journal*, **2018**, *339*, 547–556. https://doi.org/10.1016/J.CEJ.2018.01.111.

[214] Lei, Y.; Zhao, W.; Zhang, Y.; Jiang, Q.; He, J.-H.; Baeumner, A. J.; Wolfbeis, O. S.; Wang, Z. L.; Salama, K. N.; Alshareef, H. N. A MXene-Based Wearable Biosensor System for High-Performance In Vitro Perspiration Analysis. *Small*, **2019**, *15* (19), 1901190. https://doi.org/https://doi.org/10.1002/smll.201901190.

[215] Liu, J.; Jiang, X.; Zhang, R.; Zhang, Y.; Wu, L.; Lu, W.; Li, J.; Li, Y.; Zhang, H. MXene-Enabled Electrochemical Microfluidic Biosensor: Applications toward Multicomponent Continuous Monitoring in Whole Blood. *Advanced Functional Materials*, **2019**, *29* (6), 1807326. https://doi.org/https://doi.org/10.1002/adfm.201807326.

[216] Li, Y.; Kang, Z.; Kong, L.; Shi, H.; Zhang, Y.; Cui, M.; Yang, D. P. MXene-Ti3C2/CuS Nanocomposites: Enhanced Peroxidase-like Activity and Sensitive Colorimetric Cholesterol Detection. *Materials Science and Engineering: C*, **2019**, *104*, 110000. https://doi.org/10.1016/J.MSEC.2019.110000.

[217] Li, H.; Wen, Y.; Zhu, X.; Wang, J.; Zhang, L.; Sun, B. Novel Heterostructure of a MXene@NiFe-LDH Nanohybrid with Superior Peroxidase-Like Activity for Sensitive Colorimetric Detection of Glutathione. *ACS Sustainable Chemistry & Engineering*, **2020**, *8* (1), 520–526. https://doi.org/10.1021/acssuschemeng.9b05987.

[218] Xu, Y.; Hu, C.; Hu, S. A Reagentless Nitric Oxide Biosensor Based on the Direct Electrochemistry of Hemoglobin Adsorbed on the Gold Colloids Modified Carbon Paste Electrode. *Sensors and Actuators B: Chemical*, **2010**, *148* (1), 253–258. https://doi.org/10.1016/J.SNB.2010.05.028.

[219] Srivastava, P.; Mishra, A.; Mizuseki, H.; Lee, K.-R.; Singh, A. K. Mechanistic Insight into the Chemical Exfoliation and Functionalization of Ti3C2 MXene. *ACS Applied Materials & Interfaces*, **2016**, *8* (36), 24256–24264. https://doi.org/10.1021/acsami.6b08413.

[220] Alhabeb, M.; Maleski, K.; Anasori, B.; Lelyukh, P.; Clark, L.; Sin, S.; Gogotsi, Y. Guidelines for Synthesis and Processing of Two-Dimensional Titanium Carbide (Ti3C2Tx MXene). *Chemistry of Materials*, **2017**, *29* (18), 7633–7644. https://doi.org/10.1021/acs.chemmater.7b02847.

[221] Sadiq, M.; Pang, L.; Johnson, M.; Sathish, V.; Zhang, Q.; Wang, D. 2D Nanomaterial, Ti3C2 MXene-Based Sensor to Guide Lung Cancer Therapy and Management. *Biosensors*, **2021**, *11* (2). https://doi.org/10.3390/bios11020040.

[222] Ramanavicius, S.; Tereshchenko, A.; Karpicz, R.; Ratautaite, V.; Bubniene, U.; Maneikis, A.; Jagminas, A.; Ramanavicius, A. TiO2-x/TiO2-Structure Based ‘Self-Heated’ Sensor for the Determination of Some Reducing Gases. *Sensors*, **2020**, *20* (1). https://doi.org/10.3390/s20010074.

[223] Zhu, Q.; Peng, Y.; Lin, L.; Fan, C.-M.; Gao, G.-Q.; Wang, R.-X.; Xu, A.-W. Stable Blue TiO2−x Nanoparticles for Efficient Visible Light Photocatalysts. *J. Mater. Chem. A*, **2014**, *2* (12), 4429–4437. https://doi.org/10.1039/C3TA14484D.

[224] Andersson, S.; Magnéli, A. Diskrete Titanoxydphasen Im Zusammensetzungsbereich TiO1,75-TiO1,90. *Naturwissenschaften*, **1956**, *43* (21), 495–496. https://doi.org/10.1007/BF00632520.

[225] Liborio, L.; Mallia, G.; Harrison, N. Electronic Structure of the ${\text{Ti}}_{4}{\text{O}}_{7}$ Magn\’eli Phase. *Physical Review B*, **2009**, *79* (24), 245133. https://doi.org/10.1103/PhysRevB.79.245133.

[226] Seebauer, E. G.; Kratzer, M. C. Charged Point Defects in Semiconductors. *Materials Science and Engineering: R: Reports*, **2006**, *55* (3–6), 57–149. https://doi.org/10.1016/J.MSER.2006.01.002.

[227] Harada, S.; Tanaka, K.; Inui, H. Thermoelectric Properties and Crystallographic Shear Structures in Titanium Oxides of the Magneli Phases. *Journal of applied physics*, **2010**, *108* (8), 083703.

[228] Smith, J. R.; Walsh, F. C.; Clarke, R. L. Electrodes Based on Magnéli Phase Titanium Oxides: The Properties and Applications of Ebonex® Materials. *Journal of Applied Electrochemistry*, **1998**, *28* (10), 1021–1033. https://doi.org/10.1023/A:1003469427858.

[229] Walsh, F. C.; Wills, R. G. A. The Continuing Development of Magnéli Phase Titanium Sub-Oxides and Ebonex® Electrodes. *Electrochimica Acta*, **2010**, *55* (22), 6342–6351. https://doi.org/10.1016/J.ELECTACTA.2010.05.011.

[230] Wu, D.; Wang, S.; Zhang, S.; Yuan, J.; Yang, B.; Chen, H. Highly Negative Poisson's Ratio in a Flexible Two-Dimensional Tungsten Carbide Monolayer. *Phys. Chem. Chem. Phys.*, **2018**, *20* (28), 18924–18930. https://doi.org/10.1039/C8CP01353E.

[231] Petruleviciene, M.; Juodkazyte, J.; Parvin, M.; Tereshchenko, A.; Ramanavicius, S.; Karpicz, R.; Samukaite-Bubniene, U.; Ramanavicius, A. Tuning the Photo-Luminescence Properties of WO3 Layers by the Adjustment of Layer Formation Conditions. *Materials*, **2020**, *13* (12). https://doi.org/10.3390/ma13122814.

[232] Ramanavičius, S.; Petrulevičienė, M.; Juodkazytė, J.; Grigucevičienė, A.; Ramanavičius, A. Selectivity of Tungsten Oxide Synthesized by Sol-Gel Method Towards Some Volatile Organic Compounds and Gaseous Materials in a Broad Range of Temperatures. *Materials*, **2020**, *13* (3). https://doi.org/10.3390/ma13030523.

[233] Chen, X.; Sun, X.; Xu, W.; Pan, G.; Zhou, D.; Zhu, J.; Wang, H.; Bai, X.; Dong, B.; Song, H. Ratiometric Photoluminescence Sensing Based on Ti3C2 MXene Quantum Dots as an Intracellular PH Sensor. *Nanoscale*, **2018**, *10* (3), 1111–1118. https://doi.org/10.1039/C7NR06958H.

[234] Ramanaviciene, A.; Ramanavicius, A. Molecularly Imprinted Polypyrrole-Based Synthetic Receptor for Direct Detection of Bovine Leukemia Virus Glycoproteins. *Biosensors and Bioelectronics*, **2004**, *20* (6), 1076–1082. https://doi.org/10.1016/J.BIOS.2004.05.014.

[235] Ratautaite, V.; Topkaya, S. N.; Mikoliunaite, L.; Ozsoz, M.; Oztekin, Y.; Ramanaviciene, A.; Ramanavicius, A. Molecularly Imprinted Polypyrrole for DNA Determination. *Electroanalysis*, **2013**, *25* (5), 1169–1177. https://doi.org/https://doi.org/10.1002/elan.201300063.

[236] Ramanaviciene, A.; Ramanavicius, A.; Finkelsteinas, A. Basic Electrochemistry Meets Nanotechnology: Electrochemical Preparation of Artificial Receptors Based on Nanostructured Conducting Polymer, Polypyrrole. *Journal of Chemical Education*, **2006**, *83* (8), 1212. https://doi.org/10.1021/ed083p1212.

[237] Ratautaite, V.; Janssens, S. D.; Haenen, K.; Nesládek, M.; Ramanaviciene, A.; Baleviciute, I.; Ramanavicius, A. Molecularly Imprinted Polypyrrole Based Impedimentric Sensor for Theophylline Determination. *Electrochimica Acta*, **2014**, *130*, 361–367. https://doi.org/10.1016/J.ELECTACTA.2014.03.035.

[238] Ma, X.; Tu, X.; Gao, F.; Xie, Y.; Huang, X.; Fernandez, C.; Qu, F.; Liu, G.; Lu, L.; Yu, Y. Hierarchical Porous MXene/Amino Carbon

Nanotubes-Based Molecular Imprinting Sensor for Highly Sensitive and Selective Sensing of Fisetin. *Sensors and Actuators B: Chemical*, **2020**, *309*, 127815. https://doi.org/10.1016/J.SNB.2020.127815.

[239] Kumar, S.; Lei, Y.; Alshareef, N. H.; Quevedo-Lopez, M. A.; Salama, K. N. Biofunctionalized Two-Dimensional Ti3C2 MXenes for Ultrasensitive Detection of Cancer Biomarker. *Biosensors and Bioelectronics*, **2018**, *121*, 243–249. https://doi.org/10.1016/J.BIOS.2018.08.076.

[240] Kulpa, J.; Wójcik, E.; Reinfuss, M.; Kołodziejski, L. Carcinoembryonic Antigen, Squamous Cell Carcinoma Antigen, CYFRA 21-1, and Neuron-Specific Enolase in Squamous Cell Lung Cancer Patients. *Clinical Chemistry*, **2002**, *48* (11), 1931–1937. https://doi.org/10.1093/clinchem/48.11.1931.

[241] Wang, S.; Wei, S.; Wang, S.; Zhu, X.; Lei, C.; Huang, Y.; Nie, Z.; Yao, S. Chimeric DNA-Functionalized Titanium Carbide MXenes for Simultaneous Mapping of Dual Cancer Biomarkers in Living Cells. *Analytical Chemistry*, **2019**, *91* (2), 1651–1658. https://doi.org/10.1021/acs.analchem.8b05343.

[242] Fang, Y.; Yang, X.; Chen, T.; Xu, G.; Liu, M.; Liu, J.; Xu, Y. Two-Dimensional Titanium Carbide (MXene)-Based Solid-State Electrochemiluminescent Sensor for Label-Free Single-Nucleotide Mismatch Discrimination in Human Urine. *Sensors and Actuators B: Chemical*, **2018**, *263*, 400–407. https://doi.org/10.1016/J.SNB.2018.02.102.

[243] Liu, L.; Wei, Y.; Jiao, S.; Zhu, S.; Liu, X. A Novel Label-Free Strategy for the Ultrasensitive MiRNA-182 Detection Based on MoS2/Ti3C2 Nanohybrids. *Biosensors and Bioelectronics*, **2019**, *137*, 45–51. https://doi.org/10.1016/J.BIOS.2019.04.059.

[244] Yang, X.; Feng, M.; Xia, J.; Zhang, F.; Wang, Z. An Electrochemical Biosensor Based on AuNPs/Ti3C2 MXene Three-Dimensional Nanocomposite for MicroRNA-155 Detection by Exonuclease III-Aided Cascade Target Recycling. *Journal of Electroanalytical Chemistry*, **2020**, *878*, 114669. https://doi.org/10.1016/J.JELECHEM.2020.114669.

[245] Mohammadniaei, M.; Koyappayil, A.; Sun, Y.; Min, J.; Lee, M. H. Gold Nanoparticle/MXene for Multiple and Sensitive Detection of OncomiRs Based on Synergetic Signal Amplification. *Biosensors and Bioelectronics*, **2020**, *159*, 112208. https://doi.org/10.1016/J.BIOS.2020.112208.

[246] Kashefi-Kheyrabadi, L.; Koyappayil, A.; Kim, T.; Cheon, Y. P.; Lee, M. H. A MoS2@Ti3C2Tx MXene Hybrid-Based Electrochemical Aptasensor (MEA) for Sensitive and Rapid Detection of Thyroxine. *Bioelectrochemistry*, **2021**, *137*, 107674. https://doi.org/10.1016/J.BIOELECHEM.2020.107674.

[247] Zhang, H.; Wang, Z.; Zhang, Q.; Wang, F.; Liu, Y. Ti3C2 MXenes Nanosheets Catalyzed Highly Efficient Electrogenerated Chemiluminescence Biosensor for the Detection of Exosomes. *Biosensors and Bioelectronics*, **2019**, *124–125*, 184–190. https://doi.org/10.1016/J.BIOS.2018.10.016.

[248] Wang, H.; Li, H.; Huang, Y.; Xiong, M.; Wang, F.; Li, C. A Label-Free Electrochemical Biosensor for Highly Sensitive Detection of Gliotoxin Based on DNA Nanostructure/MXene Nanocomplexes. *Biosensors and Bioelectronics*, **2019**, *142*, 111531. https://doi.org/10.1016/J.BIOS.2019.111531.

[249] Chen, L.; Shi, X.; Yu, N.; Zhang, X.; Du, X.; Lin, J. Measurement and Analysis of Thermal Conductivity of Ti3C2Tx MXene Films. *Materials*, **2018**, *11* (9). https://doi.org/10.3390/ma11091701.

[250] Li, M.; Fang, L.; Zhou, H.; Wu, F.; Lu, Y.; Luo, H.; Zhang, Y.; Hu, B. Three-Dimensional Porous MXene/NiCo-LDH Composite for High Performance Non-Enzymatic Glucose Sensor. *Applied Surface Science*, **2019**, *495*, 143554. https://doi.org/10.1016/J.APSUSC.2019.143554.

[251] Dang, Y.; Guan, X.; Zhou, Y.; Hao, C.; Zhang, Y.; Chen, S.; Ma, Y.; Bai, Y.; Gong, Y.; Gao, Y. Biocompatible PB/Ti3C2 Hybrid Nanocomposites for the Non-Enzymatic Electrochemical Detection of H2O2 Released from Living Cells. *Sensors and Actuators B: Chemical*, **2020**, *319*, 128259. https://doi.org/10.1016/J.SNB.2020.128259.

[252] Shankar, S. S.; Shereema, R. M.; Rakhi, R. B. Electrochemical Determination of Adrenaline Using MXene/Graphite Composite Paste Electrodes. *ACS Applied Materials & Interfaces*, **2018**, *10* (50), 43343–43351. https://doi.org/10.1021/acsami.8b11741.

[253] Zhang, Y.; Jiang, X.; Zhang, J.; Zhang, H.; Li, Y. Simultaneous Voltammetric Determination of Acetaminophen and Isoniazid Using MXene Modified Screen-Printed Electrode. *Biosensors and Bioelectronics*, **2019**, *130*, 315–321. https://doi.org/10.1016/J.BIOS.2019.01.043.

[254] Yu, X.; Li, Y.; Cheng, J.; Liu, Z.; Li, Q.; Li, W.; Yang, X.; Xiao, B. Monolayer Ti2CO2: A Promising Candidate for NH3 Sensor or Capturer with High Sensitivity and Selectivity. *ACS Applied Materials & Interfaces*, **2015**, *7* (24), 13707–13713. https://doi.org/10.1021/acsami.5b03737.

[255] Xiao, B.; Li, Y. C.; Yu, X. F.; Cheng, J. B. MXenes: Reusable Materials for NH3 Sensor or Capturer by Controlling the Charge Injection. *Sensors and Actuators B: Chemical*, **2016**, *235*, 103–109. https://doi.org/10.1016/J.SNB.2016.05.062.

[256] Lukatskaya, M. R.; Mashtalir, O.; Ren, C. E.; Dall'Agnese, Y.; Rozier, P.; Taberna, P. L.; Naguib, M.; Simon, P.; Barsoum, M. W.; Gogotsi, Y. Cation Intercalation and High Volumetric Capacitance of Two-Dimensional Titanium Carbide. *Science*, **2013**, *341* (6153), 1502–1505.

[257] Mashtalir, O.; Naguib, M.; Mochalin, V. N.; Dall'Agnese, Y.; Heon, M.; Barsoum, M. W.; Gogotsi, Y. Intercalation and Delamination of Layered Carbides and Carbonitrides. *Nature Communications*, **2013**, *4* (1), 1716. https://doi.org/10.1038/ncomms2664.

[258] Zhao, M.-Q.; Ren, C. E.; Ling, Z.; Lukatskaya, M. R.; Zhang, C.; van Aken, K. L.; Barsoum, M. W.; Gogotsi, Y. Flexible MXene/Carbon Nanotube Composite Paper with High Volumetric Capacitance. *Advanced Materials*, **2015**, *27* (2), 339–345. https://doi.org/https://doi.org/10.1002/adma.201404140.

[259] Chaudhari, N. K.; Jin, H.; Kim, B.; San Baek, D.; Joo, S. H.; Lee, K. MXene: An Emerging Two-Dimensional Material for Future Energy Conversion and Storage Applications. *J. Mater. Chem. A,* **2017**, *5* (47), 24564–24579. https://doi.org/10.1039/C7TA09094C.

[260] Ren, C. E.; Zhao, M.-Q.; Makaryan, T.; Halim, J.; Boota, M.; Kota, S.; Anasori, B.; Barsoum, M. W.; Gogotsi, Y. Porous Two-Dimensional Transition Metal Carbide (MXene) Flakes for High-Performance Li-Ion Storage. *ChemElectroChem*, **2016**, *3* (5), 689–693. https://doi.org/https://doi.org/10.1002/celc.201600059.

[261] Baniukevic, J.; Hakki Boyaci, I.; Goktug Bozkurt, A.; Tamer, U.; Ramanavicius, A.; Ramanaviciene, A. Magnetic Gold Nanoparticles in SERS-Based Sandwich Immunoassay for Antigen Detection by Well Oriented Antibodies. *Biosensors and Bioelectronics*, **2013**, *43* (1), 281–288. https://doi.org/10.1016/J.BIOS.2012.12.014.

[262] Makaraviciute, A.; Ramanaviciene, A. Site-Directed Antibody Immobilization Techniques for Immunosensors. *Biosensors and*

Bioelectronics, **2013**, *50*, 460–471. https://doi.org/10.1016/J.BIOS.2013.06.060.

[263] Morkvenaite-Vilkonciene, I.; Ramanaviciene, A.; Kisieliute, A.; Bucinskas, V.; Ramanavicius, A. Scanning Electrochemical Microscopy in the Development of Enzymatic Sensors and Immunosensors. *Biosensors and Bioelectronics*, **2019**, *141*, 111411. https://doi.org/10.1016/J.BIOS.2019.111411.

[264] Plikusiene, I.; Balevicius, Z.; Ramanaviciene, A.; Talbot, J.; Mickiene, G.; Balevicius, S.; Stirke, A.; Tereshchenko, A.; Tamosaitis, L.; Zvirblis, G.; et al. Evaluation of Affinity Sensor Response Kinetics towards Dimeric Ligands Linked with Spacers of Different Rigidity: Immobilized Recombinant Granulocyte Colony-Stimulating Factor Based Synthetic Receptor Binding with Genetically Engineered Dimeric Analyte Derivatives. *Biosensors and Bioelectronics*, **2020**, *156*, 112112. https://doi.org/10.1016/J.BIOS.2020.112112.

[265] Wang, X.; Garnero, C.; Rochard, G.; Magne, D.; Morisset, S.; Hurand, S.; Chartier, P.; Rousseau, J.; Cabioc'h, T.; Coutanceau, C.; et al. A New Etching Environment (FeF3/HCl) for the Synthesis of Two-Dimensional Titanium Carbide MXenes: A Route towards Selective Reactivity vs. Water. *J. Mater. Chem. A*, **2017**, *5* (41), 22012–22023. https://doi.org/10.1039/C7TA01082F.

[266] Wang, H.-W.; Naguib, M.; Page, K.; Wesolowski, D. J.; Gogotsi, Y. Resolving the Structure of Ti3C2Tx MXenes through Multilevel Structural Modeling of the Atomic Pair Distribution Function. *Chemistry of Materials*, **2016**, *28* (1), 349–359. https://doi.org/10.1021/acs.chemmater.5b04250.

[267] Hope, M. A.; Forse, A. C.; Griffith, K. J.; Lukatskaya, M. R.; Ghidiu, M.; Gogotsi, Y.; Grey, C. P. NMR Reveals the Surface Functionalisation of Ti3C2 MXene. *Phys. Chem. Chem. Phys.*, **2016**, *18* (7), 5099–5102. https://doi.org/10.1039/C6CP00330C.

[268] Zhang, Y.; Zhang, N.; Ge, C. First-Principles Studies of Adsorptive Remediation of Water and Air Pollutants Using Two-Dimensional MXene Materials. *Materials*, **2018**, *11* (11). https://doi.org/10.3390/ma11112281.

[269] Zheng, J.; Wang, B.; Jin, Y.; Weng, B.; Chen, J. Nanostructured MXene-Based Biomimetic Enzymes for Amperometric Detection of Superoxide Anions from HepG2 Cells. *Microchimica Acta*, **2019**, *186* (2), 95. https://doi.org/10.1007/s00604-018-3220-9.

[270] Chen, J.; Tong, P.; Huang, L.; Yu, Z.; Tang, D. Ti3C2 MXene Nanosheet-Based Capacitance Immunoassay with Tyramine-Enzyme Repeats to Detect Prostate-Specific Antigen on Interdigitated Micro-Comb Electrode. *Electrochimica Acta*, **2019**, *319*, 375–381. https://doi.org/10.1016/J.ELECTACTA.2019.07.010.

The main results of the doctoral thesis were published in 6 scientific publications (P: 1-6):

P1. Arunas Jagminas., **Simonas Ramanavicius**, Vitalija Jasulaitienė , Mantas Šimėnas, "Hydrothermal synthesis and characterization of nanostructured titanium monoxide films", RSC Advances, 2019, 9, 40727; https://doi.org/10.1039/C9RA08463K

P2. Arunas Jagminas, Arnas Naujokaitis, Paulius Gaigalas, **Simonas Ramanavicius**, Marija Kurtinaitiene, Romualdas Trusovas, Substrate Impact on the Structure and Electrocatalyst Properties of Molybdenum Disulfide for HER from Water, Metals 2020, 10, 1251; https://doi.org/10.3390/met10091251

P3. **Simonas Ramanavicius**, Alla Tereshchenko, Renata Karpicz, Vilma Ratautaite, Urte Bubniene, Andrius Maneikis, Arunas Jagminas, Arunas Ramanavicius A. "TiO_{2-x}/TiO_2-Structure Based 'Self-Heated' Sensor for the Determination of Some Reducing Gases", Sensors, 2020, 20, 74; https://doi.org/10.3390/s20010074

P4. **Simonas Ramanavičius**, Arūnas Ramanavičius, Insights in the Application of Stoichiometric and Non-Stoichiometric Titanium Oxides for the Design of Sensors for the determination of Gases and VOCs (TiO_{2-x} and Ti_nO_{2-n} vs. TiO_2), Sensors 2020, *20*(23), 6833; https://doi.org/10.3390/s20236833

P5. Sonata Adomavičiūtė-Grabusovė, **Simonas Ramanavičius**, Anton Popov, Valdas Šablinskas, Oleksiy Gogotsi, Arūnas Ramanavičius, Selective Enhancement of SERS Spectral Bands of Salicylic Acid Adsorbate on 2D $Ti_3C_2T_x$-Based MXene Film, Chemosensors 2021, 9(8), 223; https://doi.org/10.3390/chemosensors9080223

P6. **Simonas Ramanavičius**, Arūnas Ramanavičius, Progress and Insights in the Application of MXenes as New 2D Nano-Materials Suitable for Biosensors and Biofuel Cell Design, Int. J. Mol. Sci. 2020, 21(23), 9224; https://doi.org/10.3390/ijms21239224

The reprinted articles could be found on the following pages.

1st publication / 1 publikacija

Hydrothermal synthesis and characterization of nanostructured titanium monoxide films

Arunas Jagminas., **Simonas Ramanavicius**, Vitalija Jasulaitienė , Mantas Šimėnas

RSC Advances, 2019, 9, 40727
Reprinted by permission
The article could be find online at https://doi.org/10.1039/C9RA08463K

RSC Advances

PAPER

View Article Online
View Journal | View Issue

Check for updates

Cite this: *RSC Adv.*, 2019, **9**, 40727

Hydrothermal synthesis and characterization of nanostructured titanium monoxide films

Arūnas Jagminas, *[a] Simonas Ramanavičius,[a] Vitalija Jasulaitiene[a] and Mantas Šimėnas[b]

Received 16th October 2019
Accepted 2nd December 2019

DOI: 10.1039/c9ra08463k

rsc.li/rsc-advances

At the present time, the formation of titanium monoxide (TiO_x) two dimensional (2D) species with distinct composition, size, shape, and a significantly reduced bandgap (E_g) value compared to TiO_2 is of great scientific and practical importance. This paper describes our findings investigating Ti surface oxidation for the formation of TiO_x films possessing a densely-packed nanoplatelet morphology and a low bandgap value. This goal was herein achieved by the hydrothermal treatment of the Ti surface in selenious acid solution kept at a slightly alkaline pH. Furthermore, the nanoplatelet design not typical for TiO_2 porous films was created by this method for the first time. The formation of titanium monoxide, particularly $TiO_{0.84}$, as a major crystalline phase, was verified by XRD and confirmed by EPR investigations. It is worth noting that these nanoplatelet-shaped films with a thickness of 0.1–0.25 µm exhibited a very large shift of their light absorption threshold, down to 1.29 eV, compared to the E_g of anatase TiO_2 and a surprising 70% porosity determined *via* simulation of experimental reflection plots. It is anticipated that this unique TiO_x nanomaterial will pave the way for new investigations and applications.

Introduction

Titanium dioxide, TiO_2, belongs to the group of materials that were most intensely investigated during the past three decades due to their unique optical, dielectric, catalytic properties, chemical resistance, mechanical hardness, nontoxicity and simple processing at a low cost. The crystalline forms of TiO_2-anatase, TiO_2-rutile and TiO_2-brookite polymorphs are well documented. Nanostructured anatase and rutile crystallites possess excellent optical absorption performance under UV light illumination due to their bandgap values of 3.2 eV and 3.06 eV, respectively. They are successfully used in the modern photocatalysis, solar cell devices,[1–3] gas sensors,[4,5] and protective and multilayered coatings.[6] To tune the absorption edge of TiO_2 in the visible light region, the doping of titania with various elements both in the Ti and O sublattice positions has been proposed and discussed in numerous papers.[7–13] Besides, the hybridization of titania with lower bandgap semiconductor nanoparticles and quantum dots, such as Cu_2O,[14] $CuSe_x$,[15] CdSe,[16] *etc.* has been proposed.

Nonstoichiometric semiconducting titanium oxides, namely titanium suboxides, containing structural vacancies in both titanium and oxygen sublattices with a general formula Ti_nO_{2n-1}, where $n \geq 2$, represent a group of less known low band gap materials, well reviewed in the recent years by the Chen[17] and Xu[18] groups. The experimental results have shown that the n value usually varies between 3 and 10,[6] although significantly higher n values were also reported.[19–21] The excellent electric conductivity, and visible light absorption are also characteristic features of titanium monoxides, TiO_x ($x < 2$), making them very suitable for prospective applications in electronic and opto-electronic devices, photo catalysis, batteries, *etc.* For example, the presence of vacancies in $TiO_{1.0}$ results in an $E_g \cong 2.0$ eV, as reported by Gusev.[22] To date different precursors and synthesis methods have been reported for Ti_nO_{2n-1} and TiO_x fabrication.[23–28] From these reports, titanium monoxides can be synthesized from raw TiO_2 powders by high temperature reduction with hydrogen,[23,24] carbon[25,26] and active metals such as Ti, Na, Ca, Mg, Al, and Ca.[27,28] For example, well-mixed probes of TiO_2 and Ti powders can be converted to titanium monoxides *via* arc melting in an oxygen-free atmosphere at 2273 K, and in a tube furnace at 1173 K.[28] Various titanium monoxides have also been synthesized by heating of TiO_2 powders with $CaCl_2$ at 1373 K (ref. 25) and CaH_2 at 625 K.[26] Geng *et al.* established the nanotube-shaped Ti_nO_{2n-1} films by Ti anodizing in the H_2 atmosphere at 1323 K (ref. 29) whereas He *et al.* formed magneli phase Ti_8O_{15} nanowires with a diameter of 30 nm and a length of 2.5 µm on a cleaned Ti substrate by heating together with TiO_2 powders placed separately in a tube furnace under a N_2 stream at 1323 K.[30] However, it is commonly accepted that Ti_nO_{2n-1} is difficult to synthesize. Firstly, processing in the oxygen-free atmosphere at high temperature is required. Secondly, Ti_nO_{2n-1} is unstable even at 425–525 °C temperatures decomposing to various superstructures.[31] As a result, Ti_nO_{2n-1}

---

[a] State Research Institute Centre for Physical Sciences and Technology, Sauletekio Ave. 3, LT-10257 Vilnius, Lithuania. E-mail: arunas.jagminas@ftmc.lt

[b] Faculty of Physics, Vilnius University, Sauletekio Ave. 9, LT-10222 Vilnius, Lithuania

materials synthesized by heating a mixture of powdered Ti and TiO_2 at high temperature, usually comprised a two-phase composition. To overcome this problem, chemical,[32] electrochemical,[33] mechano-chemical,[34] and flame[35] synthesis methods of Ti_nO_{2n-1} compounds have been proposed.

Here we present a facile synthesis pathway of novel, nanoplatelet-shaped titanium monoxide film on a Ti substrate. It is worth noting that to date there are no reports of the direct formation of titanium monoxide nanoplatelet films well attached to a conductive substrate. The surprising result was obtained in this study *via* hydrothermal oxidation of a titanium substrate in a slightly alkaline selenious acid solution at a quite low temperature, *ca.* 150° to 180 °C. To explain the low bandgap value of titania films with a novel design, EPR investigations were performed.

Materials and methods

Materials

All of the materials were purchased from Sigma-Aldrich unless stated otherwise. Ti foil, 99.7 at% purity and 0.127 mm thick, purchased from Aldrich, was used to prepare specimens of 12 × 12 mm^2. For the EPR investigations, sub-micrometer-sized Ti particles (<20 μm, 93% in water) were purchased from Alfa Aesar.

Synthesis

The surface of Ti samples and particles was ultrasonically cleaned in acetone, ethanol, and water, for 6 min in each, etched in the solution containing H_2O, HNO_3 and HF (20%) (5 : 4 : 1 by volume) at room temperature (RT) for 10 s, well rinsed and air-dried. Nanoplatelet-shaped films on the Ti surface were synthesized as follows. At first, the pH of an aqueous solution containing 0.05 to 0.5 mol L^{-1} of selenious acid (the highest purity, purchased from Russia) was shifted to the alkaline region by dropwise addition of 0.1 mol L^{-1} NaOH solution and intense mixing. Then 15 mL of this solution was poured into a Teflon line stainless steel autoclave of 25 mL volume. Every Ti specimen was mounted vertically in the solution by means of a Teflon holder. For the EPR investigations, the sub-micrometer-sized Ti particles instead of Ti foil specimens were used. The synthesis was conducted at 180° for up to 48 h using a 10 °C min^{-1} ramp. Finally, the products were carefully rinsed with distilled water and dried in air naturally. The annealing of samples was carried out in air and oxygen-free (quartz ampule with Cu foil) atmospheres at 300, 400, and 440 °C for 2 h.

Characterization

The morphology and elemental composition of the obtained products were investigated using scanning electron microscopy FEI Quatra 200F and the Cross Beam Workstation Auriga equipped with the field emission gun and an EDX spectrometer.

X-ray powder diffraction experiments were performed with a D8 diffractometer (Bruker AXS, Germany), equipped with a Göbel mirror as a primary beam monochromator for CuK_α radiation. Diffuse reflectance spectra of titania films were obtained by means of a Shimadzu UV-VIS-NIR spectrophotometer UV-3600 coupled with a MRC-3100 unit. Measurements were performed by mounting a sample holder onto the integrating sphere. The measurable range of wavelengths falls between 200 nm and 850 nm, covering the UV and visible light regions. In the integrating sphere, one beam strikes the sample normally to the surface while the other beam – aslant. The light absorbance was calculated from the diffuse reflection coefficient using the Kubelka–Munk function. X-ray photo electron spectroscopy (XPS) measurements were carried out using the ESCALAB MKII spectrometer equipped with a new XR4 twin anode. The non-monochromatic MgK_α, X-ray source was operated at $h\nu = 1253.6$ eV with 300 W power (20 mA/15 kV) and the pressure in the analysis chamber was lower than 5×10^{-7} Pa during spectral acquisition. The spectra were obtained using an electron analyzer with a pass energy of 20 eV for narrow scans and a resolution of 0.05 eV and with a pass energy of 100 eV for survey spectra. All spectra were recorded at a 90° take-off angle and calibrated using the C 1s peak at 284.6 eV. The spectra calibration, processing and fitting routines were done using the Advantage software (5.918) provided by Thermo VG Scientific. Core level peaks of Ti 2p, Se 3d, and O 1s were analyzed using the nonlinear Shirley-type background and the calculation of the elemental composition was performed on the basis of Scofield's relative sensitivity factors. To investigate the optical properties of titania films, the reflectance spectra of the samples were recorded in the wavelength range of 200–1700 nm using a Shimadzu UV-VIS-NIR spectrophotometer equipped with a MPC-3100 integrating sphere. The specular reflectance of the light from the film surface was calculated using an optical model of two layers. The Bruggeman Effective Medium Approximation (EMA) was applied to calculate the optical constants of the nanoplatelet titanium monoxide film formed on the Ti substrate and consisting of the naturally formed thin layer of TiO_2 and the nanoplatelet titanium monoxide layer with the empty voids (see Scheme 1 in Fig. 6). The porosity of films was calculated by fitting the model functions to the measured data using a CompleteEASE software program, as in our previous study of porous alumina.[36]

EPR investigations

Continuous-wave electron paramagnetic resonance (CW EPR) experiments were performed using a Bruker X-band ELEXSYS E580 EPR spectrometer. The strength and frequency of the modulating field were 0.3 mT and 100 kHz, respectively. Simulations of the CW EPR spectra were performed using EasySpin 5.2.20.[37]

Results and discussion

Selenious acid (H_2SeO_3) aqueous solutions were selected herein due to their known oxidant reactivity[36] through the reaction: $H_2SeO_3 + H_2O + 4e \rightarrow Se^0 + 4OH^-$, resulting in the subsequent oxidation of titanium and the formation of a pale yellow colored film. The annealing in the air as well as in an oxygen free ampoule at temperatures from 300° to 450 °C for several hours resulted in an obviously darker yellow coloring. Moreover, after calcination of such films at up to 450 °C for 3 h, no obvious changes in the film morphology were detected by SEM.

Our initial investigations revealed that the expected oxidative behavior of the selenious acid towards the Ti substrate under hydrothermal conditions proceed in the 50 to 500 mmol L^{-1} concentration range at the pH of 8 to 11 and at 140–190 °C temperatures. However, uniformly designed nanostructured films were formed mainly in the 0.1–0.3 mol L^{-1} solutions at pH of 9. For evidence, Fig. 1 depicts the top-side SEM images of the Ti surface after autoclaving in 0.2 mol L^{-1} H_2SeO_3 solutions, kept at the pHs of 9.0 and 10.0 at 150° and 180 °C for 15 h. As seen, just at a pH close to 9.0 the films with a novel nanoplatelet-shaped design were formed (Fig. 1a–d). More detailed investigations of these films with a SEM revealed the formation of an array from densely packed nanoplatelets of the length of 80–100 nm and the thickness of 5–12 nm (see Fig. 1b and d), depending on the pH, synthesis temperature and the processing time. It was determined that apart from the pH, the crucial role on the titania film design and the film thickness is played the autoclaving temperature. By increasing the treatment temperature from 150° to 180 °C, the average thickness of the titania layer is increased from about 80–86 nm to 240–260 nm (see insets in Fig. 1).

Under the optimized synthesis conditions (150–180 °C, 15 h), most probably due to the small thickness, the elemental composition of these films cannot be determined by the EDX analysis. X-ray photoelectron spectroscopy (XPS) analysis indicated that the as-formed films on the surface side were mainly composed of titanium and oxygen. Just a small content of selenium was detected by XPS at the film surface. An increase in the concentration of selenious acid from 0.05 to 0.5 mol L^{-1} resulted in the incorporation of just somewhat larger amount of selenium. Noteworthy, at pH of 10.0 (Fig. 1f), there is an obvious difference of the as-formed film morphology because the somotoid-shaped species randomly distributing on the surface are formed. Fig. 2 depicts XRD patterns of the as-formed (a) and annealed (b) film formed on the Ti substrate by hydrothermal treatment in the H_2SeO_3 solution. It can be noted that the as-formed films in the low-concentrated solution, *e.g.* 0.05–0.1 mol L^{-1} for up to 30 h, were found to be composed mainly of amorphous components. In more concentrated H_2SeO_3 solutions, *e.g.* 0.2–0.5 mol L^{-1}, as-formed films were also found to be amorphous but containing titanium monoxide $TiO_{0.84}$ crystallites due to the clearly resolved peak at 2θ 36.92°, corresponding to the peak from the {111} plane. After annealing in the oxygen-containing atmosphere these nanoplatelet films seem to be composed of both crystalline TiO_2 and nonstoichiometric titania phases (see b pattern and inset in Fig. 2). It is reasonable to note that the shift of the main XRD peak ascribed to anatase and usually seen at $2\theta = 25.2°$ to the lower angles, namely 22.6°, could be related to the formation of nonstoichiometric titania. All other experiments, performed without H_2SeO_3 at the varying pH and temperature, have never shown such morphology and the TiO_x phase formation. Furthermore, no detectable peaks corresponding to Se–O or Ti–Se compounds were observed in the XRD patterns of nanoplatelet films formed in the solutions containing from 0.05 to 0.5 mol L^{-1} of H_2SeO_3 by the hydrothermal treatment at the temperatures from 150° to 180 °C for up to 48 h.

To further explore the composition of nanoplatelet-shaped films as-formed by the hydrothermal treatment under the optimized conditions of this study and after calcination at various temperatures, investigation were conducted using CW EPR of the sub-micrometer-sized titanium particles. It is worth noticing, that in this case the quite similar morphology films were formed. Note that EPR is a precise tool to reveal the existence of Ti^{3+} and oxygen vacancies in the titania materials.[38–40] Fig. 3 depicts the EPR spectrum recorded at 110 K for titanium species after hydrothermal treatments in the selenious acid solutions and subsequent calcination in the oxygen-free atmosphere. The spectrum consists of two slightly overlapping signals exhibiting different saturation behavior. The narrow line at $g = 2.0023 \pm 0.0001$ might be attributed to the conduction electrons as previously observed in anatase after thermal reduction at high temperature.[41] We also cannot rule out that the origin of this signal is some free radicals formed during the sample preparation. The second signal is much broader with an effective *g*-value of 1.961 ± 0.003, which is typical for Ti^{3+} ions in various environments and polymorphs of titania.[38,40,41]

X-ray photoelectron spectroscopy (XPS) investigations were carried out to determine the composition and valence states of elements involved in the nanoplatelets. In the survey spectrum (Fig. 4a), the elements of Ti, Se, and O are clearly identified. Besides the above elements, the C element was also observed most probably due to the adventitious hydrocarbon from the XPS spectrometer itself and was not further analyzed. The Ti $2p_{3/2}$ peak (Fig. 4b) can be decomposed into two components centered at 459.6 and 458.5 eV, attributable to different oxidation states of titanium.[42–45] The main component at 458.5 eV corresponds to the Ti^{4+} state.[43–45] The second component at 459.6 eV probably is due to the small or Ti–OH contribution.[43,44] The absence of clearly resolved Ti^{3+} $2p_{3/2}$ binding energy in a vicinity of 456.8–457.8 eV (ref. 46 and 47) most probably should be ascribed to the formation of titanium monoxide mainly in a lower part of film not capable analyze by XPS.

Fig. 4 panel c depicts the high-resolution scans of the Se 3d electrons for the sample obtained by the hydrothermal treatment in the same H_2SeO_3 solutions under the same synthesis conditions, *e.g.* 150 °C for 15 h. From the deconvoluted peak areas, Se is mainly present in the Se^0.[46,47] Furthermore, the incorporation of selenium was estimated to be just ~0.48, ~0.67 and ~1.1 at% for 0.1, 0.3, and 0.5 mol L^{-1} solutions. Besides, the quantity of Se^0 increased with the solution concentration increase from ~28% (at 0.1 mol L^{-1}) to ~33% (at 0.3 mol L^{-1}) and ~83% (at 0.5 mol L^{-1}). In addition, we have found that post-calcination of the nanoplatelet film in the oxygen-free ampoule at 350 °C results in the evaporation of elemental selenium from the titanium monoxide film sublimating onto the walls of the glass tube by drops, well confirming the incorporation of a-Se^0 species instead of formation the titanium selenides.

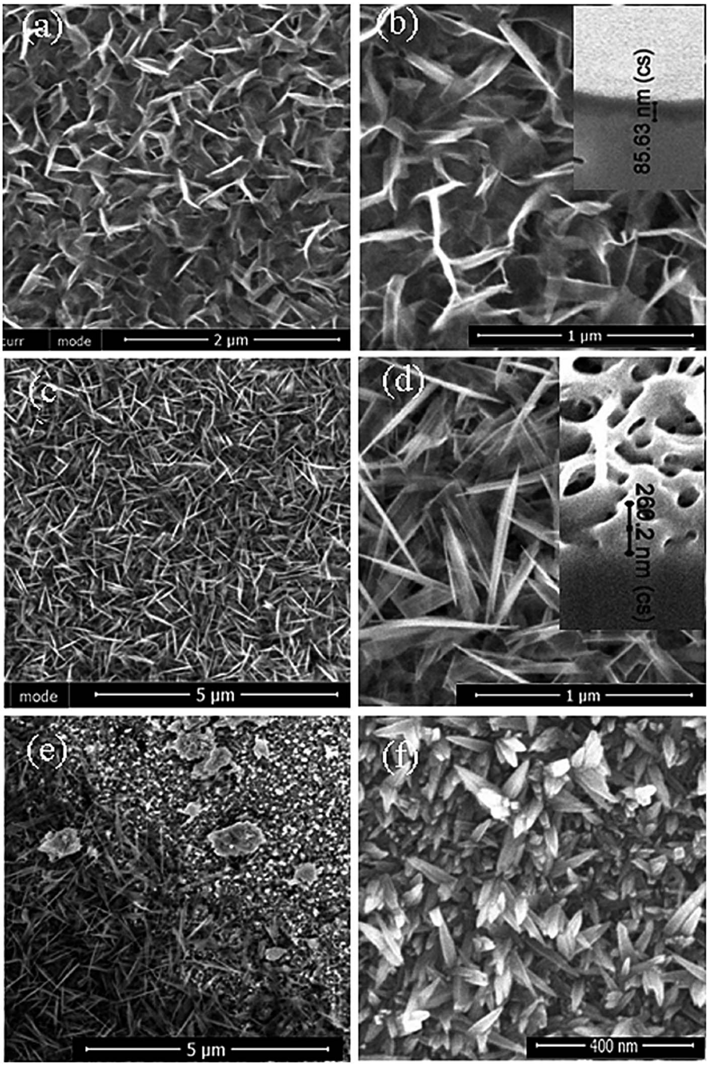

Fig. 1 Top-side FESEM images of the TiO_x film formed on the Ti surface by hydrothermal treatment in the solution containing 0.2 mol L^{-1} H_2SeO_3 and NaOH up to pH = 9.0 (a–e) or pH = 10.0 (f) at 150 °C (a, b and f), 180 °C (c and d) or 200 °C (e) for 15 h. In the insets, the cross-sectional fragments of the corresponding film are presented.

To determine the absorption coefficient and an indirect band gap characteristic of titania films, the diffuse reflectance spectra were further collected and analyzed. The absorption coefficient (A) was calculated by the formula: $A = (1 - R)^2/2R$,[48] where R is the reflectance. The Kubelka Munk function plots for possible indirect transitions $[(Ah\nu)^{1/2}$ *vs.* $h\nu]$ of selected nanoplatelet films fabricated under conditions of this study as a function of the subsequent annealing treatments are displayed in Fig. 5. As shown, the film synthesized at 150 °C and annealed in the oxygen-free atmosphere at 350°, 400°, and 440 °C exhibits the optical gap of 2.83, 1.74, and 2.32 eV, respectively. The strongest absorption in the visible range shows the film calcined at 400 °C. With the further T_{an} increase to 440 °C, the E_g value decreased to 2.32 eV, which is significantly lower than a typical E_g value of anatase TiO_2 equal to ~3.2 eV. This result can be ascribed to decomposition of titanium suboxides at $T_{an} \geq 450$ °C, as reported in ref. 49. It is worth noticing that in case of annealing the 180 °C film in the

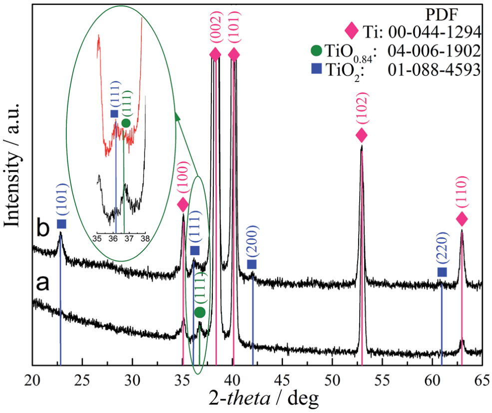

Fig. 2 XRD patterns of the film formed at the Ti substrate by hydrothermal treatment in the solution of 0.2 mol L^{-1} H_2SeO_3 (pH = 9.0) at 150 °C for 15 h before (a) and after (b) annealing in oxygen-containing atmosphere at 350 °C for 2 h.

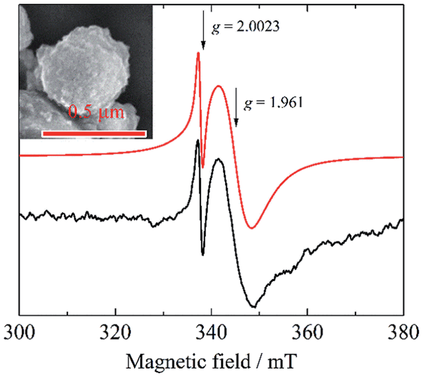

Fig. 3 Experimental (black) and simulated (red) CW EPR spectrum of titanium particles hydrothermally treated in the solution of 0.2 mol L^{-1} selenious acid at 180 °C for 45 h. In the inset, SEM image of $TiO_{0.84}$ coated NP.

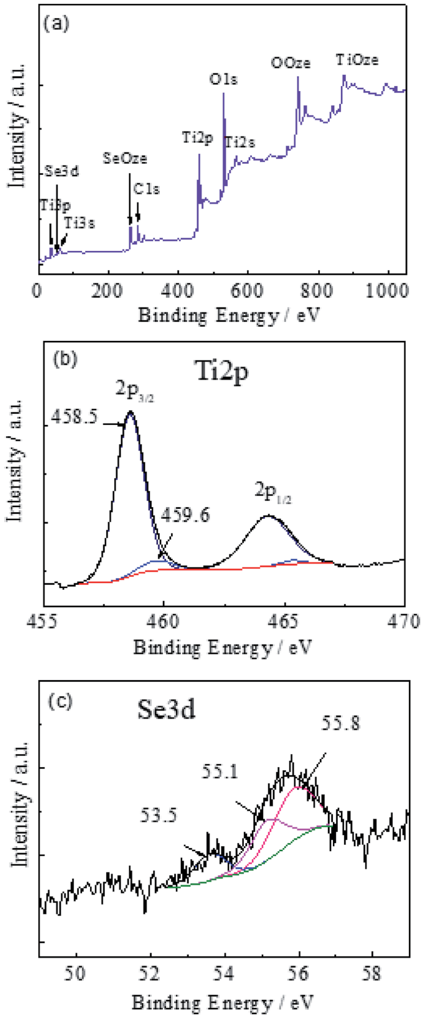

Fig. 4 Survey (a) and deconvoluted X-rays photoelectron spectra of Ti 2p (b) and Se 3d (c) elements encased at the surface side of the film formed on the Ti substrate by hydrothermal treatment in 0.3 mol L^{-1} H_2SeO_3 solution (pH = 9.0) at 150 °C for 15 h.

oxygen-free atmosphere at 400 °C the film possessing the smallest band gap value of 1.29 eV (Fig. 5b) was fabricated.

To determine the possible parameters of the nanoplatelet $TiO_{0.84}$ film formed in the adapted herein solution under the optimized hydrothermal treatment conditions, *e.g.* 180 °C, 15 h, before and after annealing at 400 °C in the air and in the oxygen-free atmosphere, the model of the nanoporous titania film as in ref. 50 and 51 was developed (Fig. 6a) and analyzed. For example, Fig. 6b depicts the experimental reflection *versus* wavelength, $R_p(\lambda)$, plot for the nanoplatelet film calcined in the oxygen-free atmosphere. The same plot was calculated on the basis of the film model and it is presented by a red line. In this way, it was determined that the shape of the theoretically calculated plot $R_p(\lambda)$ well resembled the experimental one if the film thickness approximated 86.6 nm and the surprising 79% porosity well complying with the film structure observation by SEM presented in Fig. 1d.

It can be inferred that an increase in the band gap reduction of nanoplatelet titania could be attributed to the doping with selenium. However, the selenium content in the film is very low, not detectable by XRD and Raman (the data are not presented) and it decreases further upon calcination in the ampoule due to evaporation and sublimation of Se^0 ruling out the possibility to

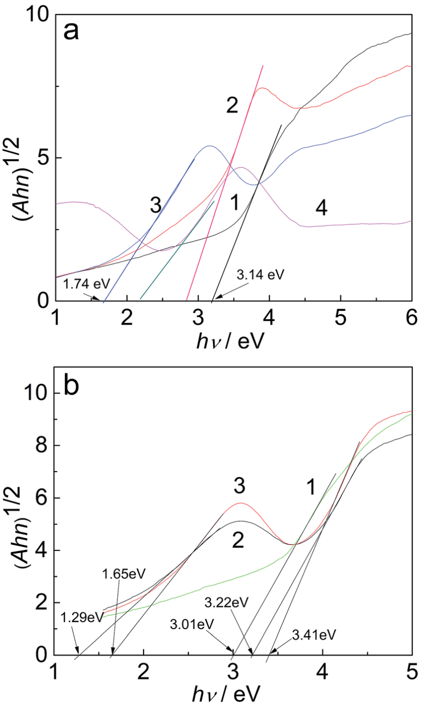

Fig. 5 (a) Tauc plots for indirect transitions of titanium monoxide nanoplatelet arrays formed by hydrothermal treatment in the 0.3 mol L^{-1} H_2SeO_3 solution (pH = 9.0) at 150 °C for 15 h after calcination in the air (1) and oxygen-free atmosphere at: 350 (2); 400 (3), and 440 °C (4) for 2 h. In (b), the same plots for the film grown at 180 °C for 15 h after calcination in air (1) and oxygen-free atmosphere at 400 °C (2) and 440 °C (3) for 2 h.

increase the band gap redshift. To check the influence of Se^0 incorporation, the nanotubed titania (TiNt) films decorated with Se^0 nanoparticles were further designed and their optical properties were investigated. For this purpose, Ti specimens were anodized in the ethylene glycol solution containing NH_4F and H_2O at 50 V for 30 min as previously reported[14] and calcined in the air at 450 °C for 2 h. In this way, the nanotube shaped (Fig. 7a) film of the 4.7 μm thickness with 120 nm tubes at the metal|film interface was formed. For crystallization, the samples were annealed at 450 °C in the air for 2 h ($\partial T/\partial t$ = 10 °C min^{-1}). The decoration of this film with Se^0 was carried out by electrodeposition from the 0.2 mol L^{-1} H_2SeO_3 solution as in the case of alumina.[52] As seen from the Se mapping image (Fig. 7b) and the Se distribution in the film cross-section (Fig. 7c), the adapted herein treatment conditions result in the rather uniform deposition of selenium species throught all the film thickness. Furthermore, the Raman spectra (Fig. 7d) revealed deposition of pure Se^0 species, whereas the XRD pattern (not shown herein) indicated their amorphous nature. Eventually, the diffuse reflectance spectra for several films with various Se^0 contents were investigated and characteristic plots (Fig. 7e) were analyzed. As can be seen, the heterostructuring of titania nanotubes with a-Se species only slightly redshifts the band gap of anatase TiO_2. These results well comply with the reported ones.[53] Therefore, a significant E_g redshift of our nanoplatelet films should be mainly ascribed to the formation of the low band gap titanium monoxide family member $TiO_{0.84}$ confirmed by XRD and EPR.

Conclusions

Herein we demonstrated a simple possibility of forming a low band gap nanoplatelet species array on a Ti substrate by hydrothermal synthesis and a subsequent calcination. For this purpose, selenious acid solutions kept at a pH close to 9.0 were successfully used for the first time. The current study shows that the nanoplatelet shaped film, of a thickness up to 250 nm formed under the optimized hydrothermal treatment conditions of this study, is mainly composed of semiconducting titanium monoxide $TiO_{0.84}$ with an indirect optical band gap value as low as 1.29 eV. The nanotube-shaped anatase TiO_2 film decorated with Se^0 species was

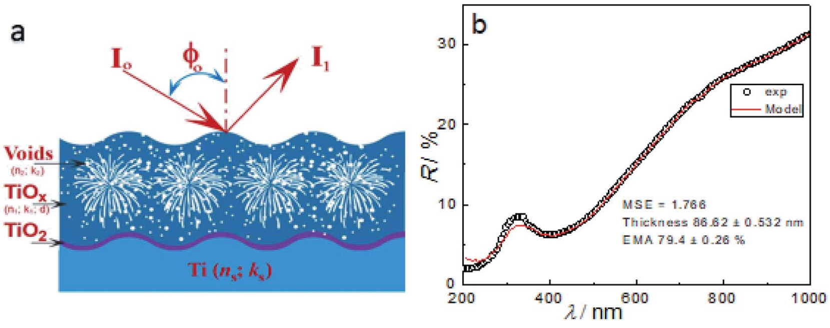

Fig. 6 (a) The scheme corresponding to the model used for the fitting of experimental $R(\lambda)$ dependency. In (b) the reflection vs. wavenumber (λ) plots for experimental 180 °C $TiO_{0.84}$ film (circles) and the calculated one (line) by the adapted nanoporous film model.

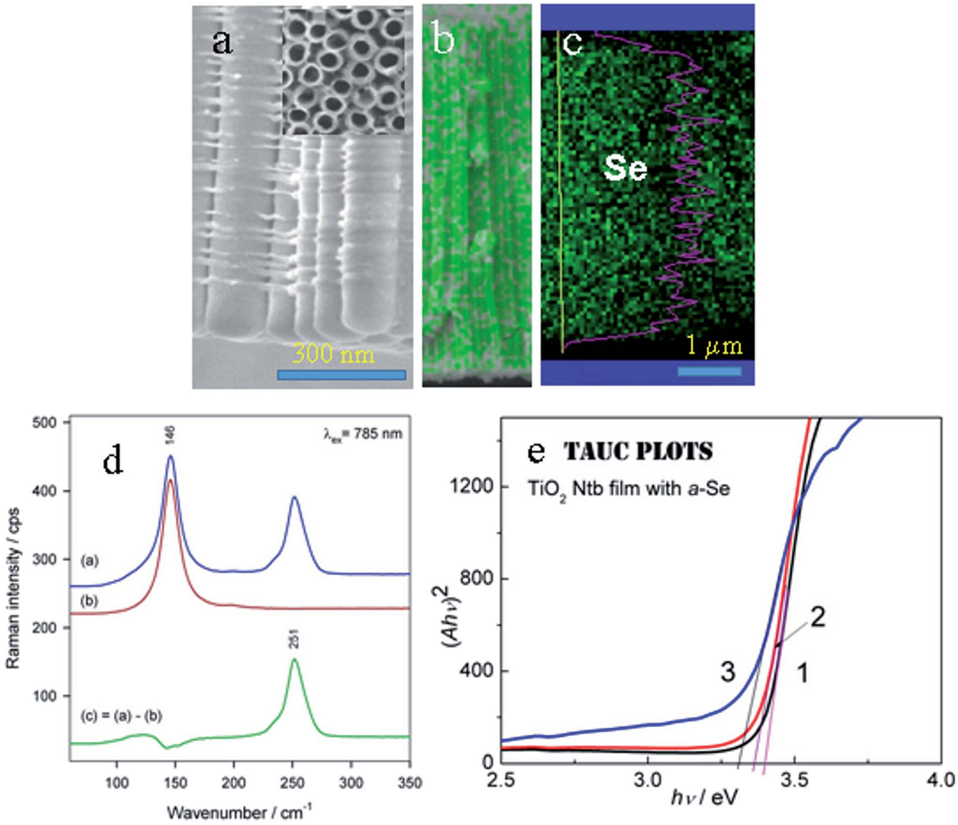

Fig. 7 Panoramic (a), top-side (inset), and cross-sectional (b) SEM views of anatase TiO_2 film fabricated by Ti anodizing in the ethylene glycol solution containing 0.25 NH_4F and 1.0 wt% H_2O at 50 V for 30 min followed by calcination at 450 °C for 2 h before (a) and after the Se DC deposition in 0.005 mol L^{-1} H_2SeO_3 solution at −2.0 V for 5 min (b). In (c) the element map and distribution profile of the Se species encased inside the film across all the TiO_2 film thickness *ca.* 4.75 μm. In (d) the Raman spectra of TiNt/Se (a), pure TiNt (b) and difference (c). In (e) the Tauc plots of TiNt film before (1) and after DC deposition of a-Se at 1.5 V for 2 (2) and 7 (3) min.

also designed and studied herein. The comparison of its optical properties with the those of our film implied that the significant E_g redshift of our nanoplatelet films should be ascribed to the formation of the low band gap titanium monoxide family member $TiO_{0.84}$ confirmed by XRD and EPR. We suppose that these nanotechnology-driven titania films could have an indispensable potential to discover novel sensor devices in the future.

Author contributions

A. J. designed, supervised and managed the study. S. R. performed syntheses and morphological characterization of the products. The XPS, and EPR investigations were carried out by V. J. and M. Š., respectively. All authors have given approval to final version of the manuscript.

Conflicts of interest

The authors declare no competing financial interest and any unpaid roles or relationships that might have a bearing on the publication process.

Acknowledgements

We acknowledge the help of Dr V. Pakštas for collection of XRD patterns, and Mr Arnas Naujokaitis for SEM observations.

References

1 M. Grätzel, Photoelectrochemical cells, *Nature*, 2001, **414**, 338–344.

2 B. O'Regan and M. Grätzel, A low-cost, high-efficiency solar cell based on dye-sensitized colloidal TiO$_2$ films, *Nature*, 1991, **353**, 737–740.

3 B. S. Richards, S. F. Rowlands, A. Ueranatasun, J. E. Cotter and C. B. Honsberg, Potential cost reduction of buried-contact solar cells through the use of titanium dioxide thin films, *Sol. Energy*, 2004, **76**, 269–276.

4 H. Tang, K. Prasad, R. Sanjinés and F. Lévy, TiO$_2$ anatase thin films as gas sensors, *Sens. Actuators, B*, 1995, **26**, 71–75.

5 O. K. Varghese, G. K. Mor, C. A. Grimes, M. Paulose and N. Mukherjee, A Titania Nanotube-Array Room-Temperature Sensor for Selective Detection of Hydrogen at Low Concentrations, *J. Nanosci. Nanotechnol.*, 2004, **4**, 733–737.

6 Y. Sawada and Y. Taga, TiO$_2$/(indium tin oxide) multilayer film: a transparent IR reflector, *Thin Solid Films*, 1984, **116**, L55–L57.

7 K. S. Yeung and Y. W. Lam, A simple chemical vapour deposition method for depositing thin TiO$_2$ films, *Thin Solid Films*, 1983, **109**, 169–178.

8 M. K. Nazeeruddin, A. Kay, I. Rodicio, R. Humphry-Baker, E. Mueller, P. Liska, N. Vlachopoulos and M. Graetzel, Conversion of light to electricity by cis-X2bis(2,2'-bipyridyl-4,4'-dicarboxylate)ruthenium(II) charge-transfer sensitizers (X = Cl-, Br-, I-, CN-, and SCN-) on nanocrystalline titanium dioxide electrodes, *J. Am. Chem. Soc.*, 1993, **115**, 6382–6390.

9 D. C. Gilmer, D. G. Colombo, C. J. Taylor, J. Roberts, G. Haugstad, S. A. Campbell, H. S. Kim, G. D. Wilk, M. A. Gribelyuk and W. L. Gladfelter, Low temperature CVD of crystalline titanium dioxide films using tetranitratotitanium(IV), *Adv. Mater.*, 1998, **10**, 9–11.

10 K. L. Siefering and G. L. Griffin, Growth Kinetics of CVD TiO$_2$: Influence of Carrier Gas, *J. Electrochem. Soc.*, 1990, **137**, 1206–1208.

11 J. C. Yu, J. Yu and J. Zhao, Enhanced photocatalytic activity of mesoporous and ordinary TiO$_2$ thin films by sulfuric acid treatment, *Appl. Catal., B*, 2002, **36**, 31–43.

12 F. Tian and C. Liu, DFT description on electronic structure and optical properties of anionic S-doped anatase-TiO$_2$, *J. Phys. Chem. B*, 2006, **110**, 17866–17871.

13 C. Burda, Y. B. Lou, X. B. Chen, A. C. S. Samia, J. Stout and J. L. Gole, Enhanced nitrogen doping in TiO$_2$ nano particles, *Nano Lett.*, 2003, **3**, 1049–1051.

14 A. Jagminas, J. Kovger, A. Rėza, G. Niaura, J. Juodkazyte, A. Selskis, R. Kondrotas, B. Šebeka and J. Vaičiūnienė, Decoration of the TiO$_2$ nanotube arays with copper suboxide by AC treatment, *Electrochim. Acta*, 2014, **125**, 516–523.

15 A. Jagminas, J. Kovger, A. Selskis and A. Rėza, Effect of hydrogen doping on the loading of titania nanotube films with copper selenide species via alternating current deposition, *J. Appl. Electrochem.*, 2015, **45**, 1141–1151.

16 I. Zerazua, E. De la Rosa, T. Lopez-Luke, J. Reyes-Gomez, S. Ruiz, C. Ageles Chavez and J. Z. Zhang, Photovoltaic Conversion Enhancement of CdSe Quantum Dot-Sensitized TiO$_2$ Decorated with Au Nanoparticles and P3OT, *J. Phys. Chem. C*, 2013, **115**, 23209–23220.

17 X. Chen, L. Liu and F. Huang, Black titanium dioxide (TiO$_2$) nanomaterials, *Chem. Soc. Rev.*, 2015, **44**, 1861–1885.

18 B. Xu, H. Y. Sohn and Y. Mahassab, Structures, preparation and applications of titanium suboxides, *RSC Adv.*, 2016, **6**, 79706–79722.

19 P. Waldner and G. Ericson, Thermodynamic modelling of the system titanium-oxygen, *Calphad*, 1999, **23**, 189–218.

20 P. Waldner, Modelling of oxygen solubility in titanium, *Scr. Mater.*, 1999, **40**, 969–974.

21 G. Ericson and A. D. Pelton, Critical evaluation and optimization of the thermodynamic properties and phase diagrams of the MnO-TiO$_2$, MgO-TiO$_2$, FeO-TiO$_2$, Ti$_2$O$_3$-TiO$_2$, Na$_2$O-TiO$_2$, and K$_2$O-TiO$_2$ systems, *Metall. Mater. Trans. B*, 1993, **24**, 795–805.

22 A. I. Gusev, *Physical Chemistry of Nonstoichiometric Refractory Compounds*, Nauka, Moscow, 1991.

23 M. Radecka, A. Trenczek-Zajac, K. Zakrzewska and M. Rekas, Effect of oxygen nonstoichiometry on photo-electrochemical properties of TiO$_{2-x}$, *J. Power Sources*, 2007, **173**, 816–821.

24 Y.-W. Lee, H.-D. Kwak, A.-R. Park, B. Roh, I. Hwang, G. Cao and K.-W. Park, Facile and Catalytic Synthesis of Conductive Titanium Suboxides for Enhanced Oxygen Reduction Activity and Stability in Proton Exchange Membrane Fuel Cells, *Int. J. Electrochem. Sci.*, 2013, **8**, 9499–9507.

25 Z. Cao, W. Xie, I.-H. Jung, G. Du and Z. Qiao, Critical Evaluation and Thermodynamic Optimization of the Ti-C-O System and Its Applications to Carbothermic TiO$_2$ Reduction Process, *Metall. Mater. Trans. B*, 2015, **46**, 1782–1801.

26 M. Toyoda, T. Yano, B. Tryba, S. Mozia, T. Tsumura and M. Inagaki, Preparation of carbon-coated Magneli phases Ti$_n$O$_{2n-1}$ and their photocatalytic activity under visible light, *Appl. Catal., B*, 2009, **88**, 160–164.

27 C. Hauf, R. Kniep and G. Pfaff, Preparation of Various Titanium Suboxide Powders by Reduction of TiO$_2$ with Silicon, *J. Mater. Sci.*, 1999, **34**, 1287–1292.

28 A. S. Bolokang, D. E. Motaung, C. J. Arendse and T. F. G. Muller, Morphology and structural development of reduced anatase-TiO$_2$ by pure Ti powder upon annealing and nitridation: synthesis of TiO$_x$ and TiO$_x$N$_y$ powders, *Mater. Charact.*, 2015, **100**, 41–49.

29 P. Geng, J. Su, C. Miles, C. Comninellis and G. Chen, *Electrochim. Acta*, 2015, **153**, 316–324.

30 C. He, X. Chang, X. Huang, Q. Wang, A. Mei and P. K. Shen, Direct synthesis of pure single-crystalline magnéli phase Ti$_8$O$_{15}$ nanowires as conductive carbon-free materials for electrocatalysis, *Nanoscale*, 2015, **7**, 2856–2861.

31 J. L. Murray and H. A. Wriedt, The O-Ti (Oxygen Titanium) System, *Bull. Alloy Phase Diagrams*, 1987, **8**, 148–165.

32 D. S. Shibuta, S. Koboyashi, M. Yoshizumi and H. Arai, *US Pat.* 4668501, 1987.

33 E. Wainer and M. E. Sibert, *US Pat.* 2707168, 1950.

34 I. Velkovic, D. Poleti, M. Zdujic, L. Karavic and C. Jovalekoc, Mechanochemical synthesis of nanocrystalline titanium monoxide, *Mater. Lett.*, 2008, **62**, 2769–2771.

35 A. Teleki and S. E. Pratsinis, Blue nano titania made in diffusion flames, *Phys. Chem. Chem. Phys.*, 2009, **11**, 3742–3747.

36 A. Jagminas, R. Žalnėravičius, A. Rėza, A. Paškevičius and A. Selskienė, Design, optical and antimicrobial properties of extremely thin alumina films colored with silver nanospecies, *Dalton Trans.*, 2015, **44**, 4512–4519.

37 S. Stoll, EasySpin, a comprehensive software package for spectral simulation and analysis in EPR, *J. Magn. Reson.*, 2006, **178**, 42–55.

38 J. M. Coronado, A. J. Maira, J. C. Conesa, K. L. Yeung, V. Augugliaro and J. Soria, EPR study of the surface characteristics of nanostructured TiO_2 under UV irradiation, *Langmuir*, 2001, **17**, 5368–5374.

39 R. F. Howe and M. Grätzel, EPR observation of trapped electrons in colloidal TiO_2, *J. Phys. Chem.*, 1985, **89**, 4495–4499.

40 M. Kus, T. Altantzin, S. Vercauteren, J. Caretti, O. Leenaerts, K. Batenburg, M. Mertens, V. Meynen, B. Partoens, S. V. Doorslaer, S. Bals and P. Cool, Mechanistic Insight into the Photocatalytic Working of Fluorinated Anatase {001} Nanosheets, *J. Phys. Chem.*, 2017, **121**, 26275–26286.

41 A. L. Attwood, D. M. Murphy, J. L. Edwards, T. A. Egerton and R. W. Harrison, An EPR study of thermally and photochemically generated oxygen radicals on hydrated and dehydrated titania surfaces, *Res. Chem. Intermed.*, 2003, **29**, 449–465.

42 V. Jandova, Z. Bastl, J. Šubrt and J. Pola, Infrared laser-produced carbon-phase shield to oxidation of nanosized titanium monoxide, *J. Anal. Appl. Pyrolysis*, 2011, **92**, 287–291.

43 F. Peng, L. Cai, L. Huang, H. Yu and H. Wang, Preparation of nitrogen-doped titanium dioxide with visible-light photocatalytic activity using a facile hydrothermal method, *J. Phys. Chem. Solids*, 2008, **69**, 1657–1664.

44 G. Shu, H. Wang, H.-X. Zhao and X. Zhang, Microwave-assisted synthesis of black titanium monoxide for synergistic tumor phototherapy, *ACS Appl. Mater. Interfaces*, 2019, **11**, 3323–3333.

45 W. Ni, M. Li, J. Cui, Z. Xing, Z. Li, X. Wu, E. Song, M. Gong and W. Zhou, 808 nm light triggered black TiO_2 nanoparticles for killing of bladder cancer cells, *Mater. Sci. Eng., C*, 2017, **81**, 252–260.

46 Y. Cong, J. Zhang, F. Chen and M. Anpo, Synthesis and characterization of nitrogen-doped TiO_2 nanophotocatalyst with high visible light activity, *J. Phys. Chem. C*, 2007, **111**, 6976.

47 N. Gopal, G. Rocker and R. Feierabend, Intrinsic defects of TiO_2 (110): Interaction with chemisorbed O_2, H_2, CO and CO_2, *Phys. Rev. B: Condens. Matter Mater. Phys.*, 1983, **28**, 3427.

48 V. Štengl, S. Bakardjieva and J. Bludska, Se and Te-modified titania for photocatalytic applications, *J. Mater. Sci.*, 2011, **46**, 3523–3536.

49 S. Lee and C. Jeon, Fabrication of TiO_2 tubules by template synthesis and hydrolysis with water vapor, *Chem. Mater.*, 2004, **16**, 4292–4297.

50 P. Simon, B. Pignon, B. Miao, S. Coste-Leconte, S. Leconte, Y. Marguet, P. Jegou, B. Bouchet-Fabre, C. Reynaud and N. Herlin-Boime, N-doped titanium monoxide nanoparticles with TiO rock-salt structure, low energy band gap, and visible light activity, *Chem. Mater.*, 2010, **22**, 3704–3711.

51 N. Ghrairi and M. Bouaicha, Structural, morphological and optical properties of TiO_2 films by the electrophoretic deposition technique, *Nanoscale Res. Lett.*, 2012, **7**, 357.

52 A. Jagminas, R. Żalnėravičius, R. Rėza, A. Paškevičius and A. Sielskienė, Design, optical and antimicrobial properties of extremely thin alumina films colored with silver nanospecies, *Dalton Trans.*, 2015, **44**, 4512–4519.

53 A. Jagminas, I. Gailiūtė, G. Niaura and R. Giraitis, Template-assisted fabrication of pure Se nanocrystals in controllable dimensions, *Chemija*, 2005, **16**, 15–20.

2nd publication / 2 publikacija

Substrate Impact on the Structure and Electrocatalyst Properties of Molybdenum Disulfide for HER from Water

Arunas Jagminas, Arnas Naujokaitis, Paulius Gaigalas, **Simonas Ramanavicius**, Marija Kurtinaitiene, Romualdas Trusovas

Metals 2020, 10, 1251

Reprinted by permission

The article could be find online at https://doi.org/10.3390/met10091251

metals

MDPI

Article

Substrate Impact on the Structure and Electrocatalyst Properties of Molybdenum Disulfide for HER from Water

Arūnas Jagminas *, Arnas Naujokaitis, Paulius Gaigalas, Simonas Ramanavičius, Marija Kurtinaitienė and Romualdas Trusovas

State Research Institute Center for Physical Sciences and Technology, Sauletekio ave. 3, LT-10257 Vilnius, Lithuania; arnas.naujokaitis@ftmc.lt (A.N.); paulius.gaigalas@ftmc.lt (P.G.); simonas.ramanavicius@ftmc.lt (S.R.); marija.kurtinaitiene@ftmc.lt (M.K.); romualdas.trusovas@ar.fi.lt (R.T.)

* Correspondence: arunas.jagminas@ftmc.lt; Tel.:+370-5264-8891

Received: 21 August 2020; Accepted: 15 September 2020; Published: 17 September 2020

Abstract: It is expected that utilization of molybdenum disulfide (MoS_2)-based nanostructured electrocatalysts might replace the Pt-group electrodes most effectively applied for hydrogen evolution reaction from water. Therefore, in the past two decades, various approaches have been reported for fabrication of nanostructured MoS_2-based catalysts, but their applications in practice are still missing due to lower activity and stability. We envisaged that the knowledge about the peculiarities of MoS_2 nanoplatelets attachment to various conductive substrates by hydrothermal processing could be helpful for fabrication of more active and stable working electrodes. Therefore, in this study, the hydrothermal syntheses at the Mo, Ti, Al, anodized Ti, and hydrothermally designed titanium suboxide substrates were performed; the electrodes obtained were characterized; and hydrogen evolution reaction (HER) activity was tested. In this way, MoS_2-based HER catalyst possessing a surprising stability and a low Tafel slope was designed via attachment of nanoplatelet-shaped MoS_2 species to the nanotube-shaped anatase-TiO_2 surface.

Keywords: electrocatalyst supports; hydrothermal synthesis; molybdenum disulfide; microstructure; hydrogen evolution

1. Introduction

Water splitting is the most promising way for hydrogen gas production attracting still growing attention in the past decade [1]. For this, besides bulk platinum and Pt alloys, as the most effective electrocatalysts for hydrogen evolution reaction (HER) from aqueous acidic solutions, application of various new nanostructured materials is currently of high interest [2–4]. Consequently, fabrication of new, cost-effective, and prospective electrocatalysts on the basis of nanostructured transition metal chalcogenides, molybdenum oxide [5], nitride [6], carbide [7], and phosphide [8] has been reported in the past decade. Noteworthy, if compared with platinum electrocatalysts, MoS_2-based ones were less effective and stable, but recently, they were classified as more extensively studied [9–11]. Gold [12], titanium [13], carbon paper [14], graphite [15], nickel foam [16], and graphene-based sheets [17,18] have been proposed as the supports for attachment of MoS_2-based nanostructures. However, the stability of reported nanostructured MoS_2 electrodes is not high enough to replace Pt group metals in the HER processes. Therefore, recent efforts have been focused on the developing more advanced MoS_2-based nanometer-scaled hybrid assembles using various approaches, including composition and morphology control [19], alloying [20], and support promotion [21]. A variety of conducting substrates such as reduced graphene oxide [22], carbon nanotubes [23], mesoporous graphene [24], and carbon fibers [25] have been also reported seeking to enhance HER activity. For example, the design of film from metallic 1T-MoS_2 and semiconducting 2H-MoS_2 phases rendered the catalyst possessing a high HER activity [19,26] and an initial overvoltage as small as 40 mV [27]. Meanwhile, various synthesis approaches have been reported in the past years, including laser ablation [28], thermal decomposition [29], gas-phase reaction [30], magnetron sputtering [31], hydrothermal [24,32–34], and sonochemical [35]. However, the design of stably working MoS_2-based electrocatalysts for hydrogen evolution at the conductive substrates is still challenging. Therefore, the creation of 2D-shaped MoS_2-based electrocatalyst well attached to conductive substrate is one of the fundamental problems that needs to be resolved.

This paper attempts to show the influence of how various substrates can be applied for the successive formation of nanoplatelet MoS_2 electrocatalysts by one-pot hydrothermal approach. To study the HER efficiency and stability, MoS_2-nanostructured films were designed onto the molybdenum, titanium, Si/SiO_2, and aluminum substrates. In addition, the influence of thin nanoporous anodic oxide films formed onto the titanium surface, underlying MoS_2, was investigated and discussed. In this way, the influence of the substrate nature on the HER activity stemmed from the quantity of exposed sulfur edges in the MoS_2-based film [12,36] was estimated.

2. Materials and Methods

2.1. Materials

For preparation of the synthesis solution, the ammonium heptamolybdate, $(NH_4)_6Mo_7O_{24}$ $4H_2O$, was purchased from REACHEM (Petržalka, Slovakia), whereas thiourea and aniline were obtained from Sigma-Aldrich (St. Louis, Missouri, USA). All reagents were of analytical grade and used without further treatment. Deionized water purified in a Milli-Q system was used throughout. Mo (99.9 at%, 0.1 mm thick) and Ti (99.7 at%, 0.127 mm thick) foils, purchased from Sigma-Aldrich, were used to cut rectangular specimens with working surface of 1.0 cm^2 (7 × 7 mm^2) and tagged (1 × 30 mm^2). Al foil (99.99 at%, 0.13 mm thick) was purchased from Sigma-Aldrich. To clean sample surfaces, high purity acetone and ethanol were applied. For the preparation of anodizing solutions, chemically green H_3PO_4 and H_2SO_4 acids were purchased from Reachim (Moscow, Russia). For titanium suboxide, TiO_x, synthesis at the Ti substrate, selenious acid, H_2SeO_3, (the highest purity, purchased from Reachim) (Moscow, Russia) was applied.

2.2. Hydrothermal Synthesis of MoS_2 Species

For fabrication of flower-shaped MoS_2 species in the solution bulk and on various substrates, hydrothermal synthesis in the solution containing thiourea, $(NH_2)_2CS$, ammonium heptamolybdate and aniline, $C_6H_5NH_2$, was used. In these investigations, a Teflon-lined stainless-steel autoclave of 20 mL capacity was filled with the working solution to 60% and then sealed. The typical solution comprised 5.0 $(NH_4)_6Mo_7O_{24}$, 90 thiourea, and 25 mmol L^{-1} aniline. The cleaned specimen was inserted vertically into the solution using a special holder made of Teflon. The synthesis reaction was carried out at 220 ± 2 °C for 5 to 15 h in a programmable muffle furnace Czermack (Badia Polesine, Italy) using 10 °C /min temperature ramp. As-formed products were cooled to room temperature, washed several times with distilled water, collected by centrifugation, and dried at 60 °C.

2.3. Ti Surface Pretreatment, Anodizing, and Oxidation

The surface of titanium samples was ultrasonically cleaned in acetone, ethanol, and water, 6 min in each, and air dried. Three kinds of Ti surface preparation were used in our subsequent study, namely, pure Ti, Ti covered by nanotube-shaped anatase TiO_2 layer via anodizing and calcination, and Ti covered with nanostructured titanium suboxide by hydrothermal treatment under conditions evaluated by us earlier [37]. Ti surface anodizing was conducted in the thermostated Teflon cell containing 2.0 mol L^{-1} H_3PO_4 and 0.2 mol L^{-1} NH_4F at 17 ± 0.3 °C and 20 V dc for 1 h. In this setup, two platinum plates were used as cathodes. After anodizing, the specimens were thoroughly rinsed with water, air-dried, and calcined in air at 450 °C for 2 h using 10 °C min^{-1} temperature ramp.

For Ti surface coating with the nanostructured titanium suboxide (TiO_x) film, the specimens were hydrothermally treated in 0.2 mol L^{-1} H_2SeO_3 at 180 °C for 15 h, rinsed, and annealed in deoxygenated atmosphere by heating together with Cu foil in a sealed glass tube at 300 °C for 10 h, as reported earlier [37].

2.4. Characterization Tests

The morphology and elemental composition of the products obtained was investigated using a scanning electron microscope (FEI Helios Nanolab 650, Eindhoven, Niderland) and Cross Beam Workstation Auriga (Eindhoven, Nederland) equipped with a field emission gun and EDX spectrometer. A FEI TECNAI F20 (Eindhoven, Nederland) electron transmission microscope equipped with a field emission electron gun was also applied. Accelerating voltage was 200 kV. X-ray powder and glancing angle diffraction experiments were performed on a D8 diffractometer (Bruker AXS, Germany), equipped with a Göbel mirror as a primary beam monochromator for CuK_α radiation.

Raman spectra were recorded using inVia (Renishaw) spectrometer equipped with thermoelectrically cooled (−70 °C) CCD camera and microscope (New Mills, UK). The 532 nm beam of the solid-state laser was used as an excitation source. Raman scattering wavenumber axis was calibrated by the silicon peak at 520.7 nm. The 50× objective was used during the measurements of TiNT/MoS_2 and TiNT samples, while 20 × objective was employed for the analysis of MoS_2 in powder form. To avoid damage of the samples, the laser power was limited to 0.3 mW. Parameters of the bands were determined by fitting the experimental spectra with Gaussian–Lorentzian shape components using GRAMS/A1 (Thermo Scientific) software (version 8.0, Thermo Electron Corp.).

Electrochemical measurements were performed in a three-electrode glass cell equipped with the working, Ag/AgCl, KCl reference, and the glassy carbon electrode, as a counter. Prior to the measurements, Ar gas was bubbled through the electrolyte solution for at least 0.5 h to remove the dissolved air. The catalytic performance of prepared electrodes was studied in the solution containing 0.5 mol L^{-1} H_2SO_4 and 0.25 mol L^{-1} formic acid by the potential cycling within 0.05 to −0.35 V vs. reference hydrogen electrode RHE potentials range at the 10 mV s^{-1} scan rate using a workstation ZENNIUM Zahner-Electrik Gmb & Co, KG, Kronach, Germany). Formic acid was added to hinder the destruction of glassy carbon counter electrode in our prolonged HER tests. In the stability tests, up to 3000 cycles were used. All potentials in the text refer to RHE.

3. Results

Structurally, the products, synthesized hydrothermally in the bulk solution containing ammonium heptamolybdate, thiourea, and aniline at 220 °C, are nanoplatelet-shaped flowers (Figure 1a). At the same time, densely packed nanoplatelet arrays usually covered various substrates inserted into the synthesis reactor (Figure 1b).

The thickness of individual nanoplatelet at the surface side varied between 3 and 7 nm (inset in Figure 1a) implying on the formation of 5–12 sandwiched S-Mo-S layers [19,38]. The thickness of films for the given solution was found to be dependent on the process duration varying from 700 to 800 nm and from 1.7 to 2.1 µm for 5 and 15 h, respectively. Note that the reaction times shorter than 3 h led to the formation of incompletely swelled coatings at the most tested substrates. When synthesis time lasted over 10 h, a substantial decrease in the working stability of such MoS_2-nanostructured electrocatalysts was observed under the intense HER. From the TEM observations, the high degree ordering in our MoS_2-based nanoplatelets is absent (Figure 2).

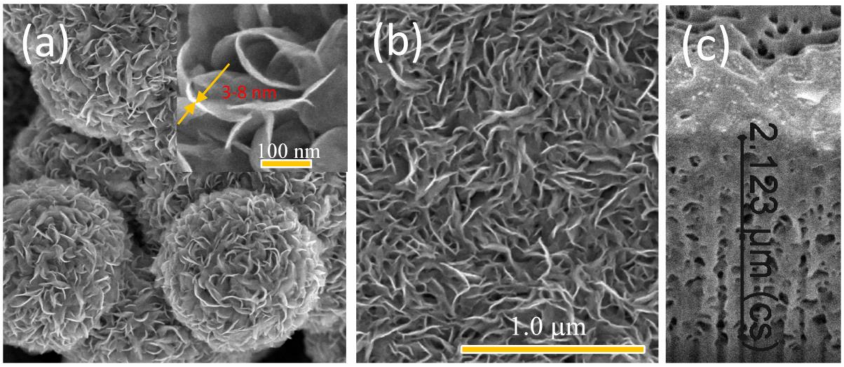

Figure 1. Typical top-side (**a**,**b**) and cross-sectional (**c**) SEM images of MoS_2 formed hydrothermally at 220 °C for 10 h in the solution containing (in mmol L^{-1}): 5 $(NH_4)_6Mo_7O_{24}$, 90 thiourea, and 25 aniline in bulk (**a**) and on the conducting substrate (**b**,**c**).

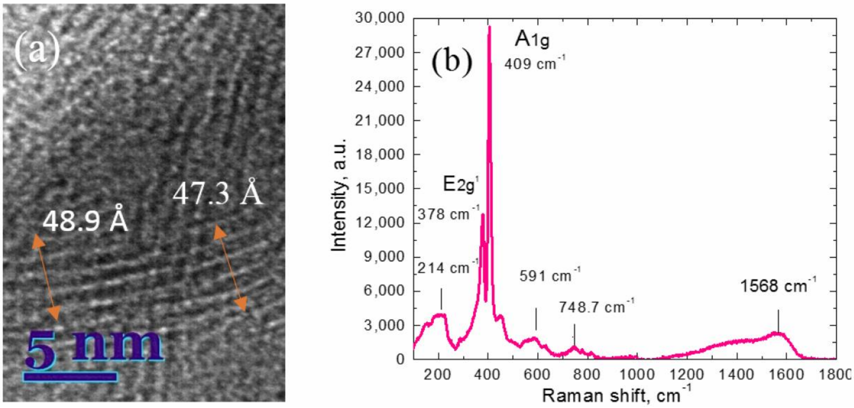

Figure 2. (**a**) HRTEM image and (**b**) Raman spectra of MoS_2 products synthesized in a solution containing 5 $(NH_4)_6Mo_7O_{24}$, 90 thiourea, and 25 mmol L^{-1} of aniline at 220 °C for 10 h.

Apart from typical interlayer spacing of ~0.62 nm for pure MoS_2 [39], significantly larger interlayer spacing up to 0.98 nm, can be viewed. This, probably, occurred due to nonuniform intercalation of aniline molecules between S-Mo-S layers resulting in the nonuniform interlayer expansion. The addition of aniline to the synthesis solution was grounded on our recent findings that aniline affected on the activity of nanoplatelet-shaped MoS_2 hybrid electrocatalysts. As a result, twice more efficient and significantly stable catalysts for HER were designed upon hybridization with aniline. This effect was verified herein by a continuous potential cycling in the acidic solution within a range of −0.35 to 0.05 V vs. RHE potential containing 5 $(NH_4)_6Mo_7O_{24}$, 90 thiourea, and 25 mmol L^{-1} of aniline at 220 °C for 10 h. We attributed this performance to a strong chemical coupling between the inserted aniline molecules and MoS_2 sheets, endowing them with more exposed active sites due to the lattice distortion and numerous defects viewed from the TEM observations (Figure 2a). Note that intercalation strategy of aniline and poly(aniline) molecules has been previously demonstrated for other HER catalysts with the lamellar structure allowing to enhance its activity [40,41]. The distorted MoS_2 lattice arrangements and defect-rich composition of the as-grown nanoplatelets at 220 °C for 10 h were also verified by Raman spectroscopy (Figure 2b) demonstrating clearly resolved A_{1g} and $E_{2g}{}^1$ modes, centered at 409 and 378 cm^{-1}, respectively, of the predominant MoS_2 phases. The difference between the $E_{2g}{}^1$ and

A_{1g} modes (31 cm^{-1}) implies that the structure of the MoS_2 in the nanocomposite consists of multiple layers [42]. Moreover, several additional modes, particularly a broad shoulder in a range from 1200 to 1650 cm^{-1}, centered at the 1568 cm^{-1}, implies that this mode should be ascribed to the vibration of intercalated aniline fragments [43]. Note, this band is absent in the Raman spectrum of the same MoS_2 synthesized without aniline (not showed here). At the same time, other less intense Raman signals, namely, at 214, 591, and 749 cm^{-1} are observed, that cannot be attributed to molybdenum oxides.

As illustrated in Figure 3a–c, the morphology of products hydrothermally synthesized in the adapted herein solution at 220 °C for 5 h depends on the substrate material. Brussel cabbage-shaped balls comprised from the thin nanoplatelets were formed in the solution bulk and at the silica wafer substrate (Figure 3a), meanwhile, nanoplatelet of "grass" shape usually coated the metals, metal oxides, and even Teflon substrate (Figure 3b). Furthermore, in this study, the surprising effect was determined for hydrothermal formation of MoS_2 films onto the aluminum substrate. In this case, the formation of region at the metal substrate in an average thickness of ~0.42 μm composed of aluminum oxide nanowire arrays has been observed for the first time (Figure 3c).

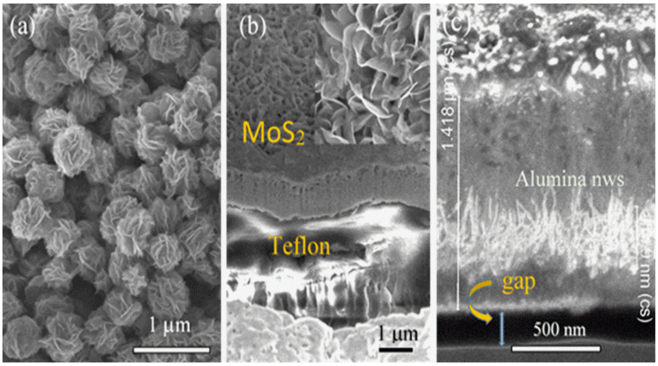

Figure 3. Top-side (**a**) and cross-sectional (**b**,**c**) SEM views of MoS_2 films fabricated onto the Si/SiO_2 (**a**), Teflon (**b**), and Al (**c**) substrates via hydrothermal synthesis in the solution containing (in mmol L^{-1}): 5 ammonium heptamolybdate, 90 thiourea, and 25 aniline at 220 °C for 10 h.

Figure 4 displays the Raman spectra of molybdenite films fabricated under the same autoclaving conditions on the molybdenum and titanium substrates as well as in the solution bulk clearly demonstrating an obvious compositional difference of the products formed. From these spectra, considerably pure MoS_2 species with clearly resolved characteristic phonon modes A_{1g} at 409 cm^{-1} and E'_{2g} at 385 cm^{-1} are formed in the solution bulk (Figure 4c) compared with the films grown at the substrates (Figure 4a,b). Furthermore, in accordance with the literature [42,44], the difference between E'_{2g} and A_{1g} peaks (24 cm^{-1}) strongly supports that MoS_2 cabbage-shape species are just few layered. In contrast, the shape of A_{1g} and E'_{2g} phonon modes as well as the large difference between E'_{2g} and A_{1g} peaks (>90 cm^{-1}) indicated on the significant degradation of the MoS_2 nanoplatelet material.

Figure 5 depicts the top-side (a) and cross-sectional (b) SEM images of MoS_2-based film fabricated onto the Ti substrate. These images outline that as-grown films are of nanosheet morphology with lateral size in the range of 100–200 nm. From the cross-sectional image (Figure 5b), an obvious gap between the film and substrate was, however, observed, which, of the most time, disfavors the charge transfer at the interface as well as a considerable decrease in the HER activity and durability even during a short HER processing (Figure 5c). In addition, the hydrogen evolution reaction at this electrode proceeds with trice larger Tafel slope compared with that at Pt electrode (Inset in Figure 5c). Better adhesion of MoS_2 film to substrate was not achieved by modulating the synthesis time within 2–15 h range. Upon an intense hydrogen gas evolution in an acidic solution, this film was destroyed quickly due to film sputtering from the Ti substrate resulting in the catalytic activity decrease (Figure 5c).

The gap between the Ti and MoS_2 film cannot be explained by a work function value of this metal (4.3 eV) [45]. We suspect that this effect could be ascribed to the formation of sublayer from $Ti(OH)_x$ due to the hydrothermal synthesis at 220 °C creating 23 bar pressure in the reactor and protecting a good adhesion of MoS_2 nanoplatelets.

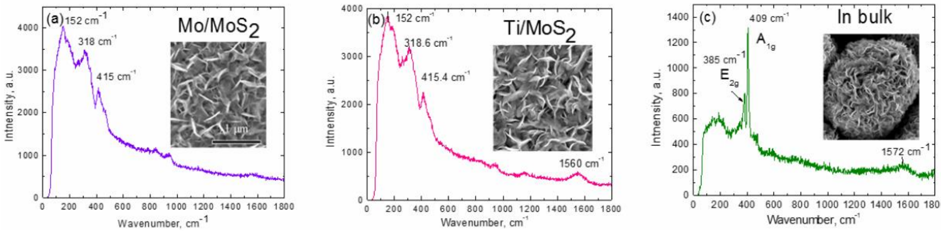

Figure 4. Raman spectra of the synthesized products on the Mo (**a**) and Ti (**b**) substrates, and in the solution bulk (**c**) by autoclaving in the solution containing 5 ammonium heptamolybdate, 90 thiourea and 25 mmol L^{-1} aniline at 220 °C for 5 h. λ_{exc} = 532 nm. In the insets, the corresponding SEM views of the resulted products.

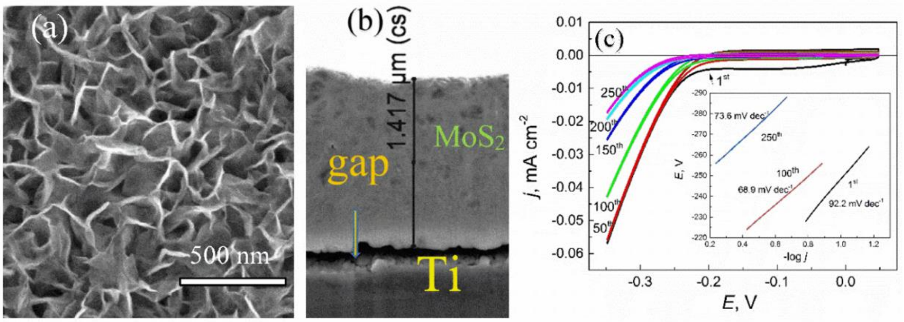

Figure 5. Top-side (**a**) and cross-sectional (**b**) SEM images of MoS_2 film formed onto the Ti substrate by hydrothermal treatment in the solution containing 5 ammonium heptamolybdate, 90 thiourea, and 25 mmol L^{-1} aniline. In (**c**), the cycling voltammograms of this catalyst in the acidic solution at 10 mV s^{-1} potential scan rate for indicated potential scan cycle are outlined. The inset outlined the Tafel slopes calculated for indicated potential scan.

From the SEM observations, the morphology of hybrid-type MoS_2 film formed on the molybdenum substrate under conditions of this study is quite similar to the one at the Ti substrate (Figure 6a,b). In sharp contrast, the nanoplatelets of this film are well attached to the Mo substrate (Figure 6c). The good adhesion of MoS_2 film to the Mo substrate can be attributed to a low work function (WF) of Mo (4.5 eV) because according to the Schottky Mott model, metal–semiconductor contacts would be based on the WF of metal [45]. To assess durability of this catalyst, we cycled them for 2000 HER cycles. A set of polarization curves obtained is shown in Figure 6d. From these curves, however, quite high activity for this electrocatalyst was determined only at the initial cycling. Upon 500–600 potential scans within 0.05 to −0.35 V range the catalytic activity of such electrocatalyst decreased in times, although the Tafel slope of electrochemical reaction changed insignificantly. For comparison, the HER activity at the Pt electrode under the same conditions attained ~100 mA cm^{-2} at 0.2 V and proceeded with the Tafel slope of about 31 mV dec^{-1} as is typical [46].

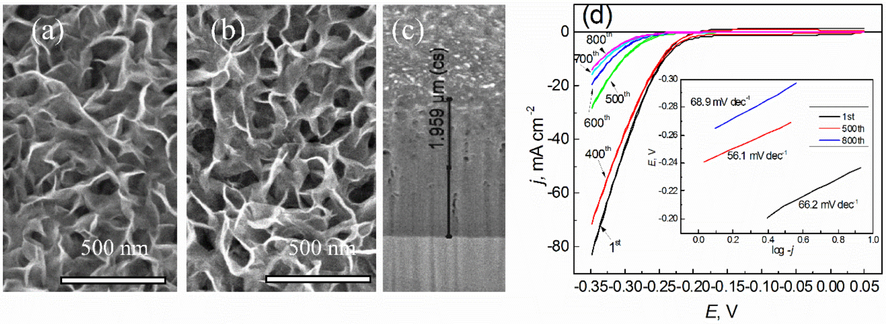

Figure 6. Top-side (**a**,**b**) and cross-sectional (**c**) SEM images of MoS_2 film formed onto the Mo substrate by hydrothermal treatment in the solution containing 5 ammonium heptamolybdate, 90 thiourea and 25 mmol L^{-1} aniline at 220 °C for 5 h before (**a**) and after (**b**) 1000 potential cycling within −0.35 to 0.05 V potential range at 10 mV s^{-1} rate. In (**d**), the set of HER voltammograms and the Tafel slopes calculated for indicated potential scan are outlined.

As the MoS_2-based films at the Ti substrate were unstable over a long period of the HER processing, we followed their stabilities after deposition onto the anodized Ti substrate. In this way, well-known Ti anodizing process [47] in the acidic aqueous solution containing 2.0 mol L^{-1} H_3PO_4 and 0.2 mol L^{-1} NH_4F at 20 V was chosen to design the typical nanotube-shaped film (Figure 7a).

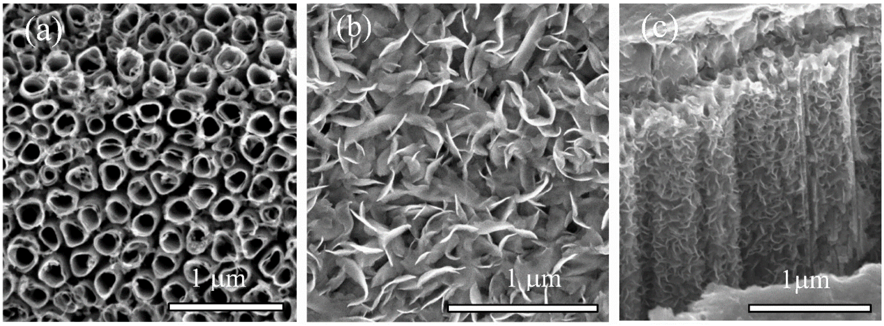

Figure 7. Top-side (**a**,**b**) and cross-sectional (**c**) SEM images of anodized Ti specimen before (**a**) and after (**b**,**c**) covering with MoS_2 film as in Figure 1.

Considering surprisingly low electrical resistance of the crystalline anatase-TiO_2 in the hydrogen gas environments [48], the anodized specimens were annealed and just then subjected to the hydrothermal treatment in the adapted herein solution under the identical conditions. The resulting film also demonstrated nanoplatelet's morphology (Figure 7b) and nice adhesion to the titania nanotubes (Figure 7c). Worth noticing that apart deposition onto the surface, MoS_2 species tightly filled titania tubes, cracks, and intertube gaps (Figure 7c), likely due to a strong chemical attachment to the TiO_2 surface [49]. As such, this electrode exhibited a high HER activity in the acidic solution (Figure 8a). Besides, this catalyst possessed exceptionally high HER stability even at 50–60 mA cm^{-2} current density and a small Tafel slope decreasing from 79 to 66 mV dec^{-1} during long period of exploitation (Figure 8a, inset). Note that for HER in acidic electrolyte, the theoretical Tafel slopes are 120, 40, and 30 mV dec^{-1}, corresponding to the Volmer, Heyrovsky, and Tafel step, respectively. A Tafel slope of 66 mV dec^{-1} indicated that hydrogen evolution occurred via a fast discharge reaction ($H_3O^+ + e^- + cat = cat\text{-}H + H_2O$) and thereafter, a rate determining (ion + atom) reaction ($H_3O^+ + e^- + cat\text{-}H = cat + H_2 + H_2O$), that is, the Volmer–Heyrovsky mechanism [50]. Electrolytic property robustness was confirmed by more than 15 h continuous HER processing in an acidic solution. The good catalytic activity and stability of MoS_2 films hybridized with aniline at the Ti/TiO_2 substrate was also confirmed by invariable values of the A_{1g} (410 cm^{-1}) and $E_{2g}{}^1$ (383 cm^{-1}) vibrational modes characteristic to MoS_2 Raman spectra [51] (Figure 8b) and could be explained not only by the nanotubed morphology and chemical affinity of MoS_2 to titania surface as has been reported [48,51] but also by the low Ti/TiO_2 interface resistance occurring via hydrogen spilt over effect [52,53].

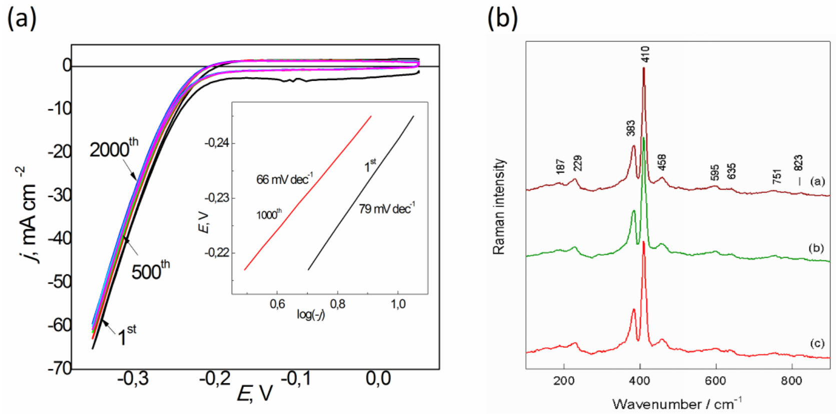

Figure 8. (**a**): HER voltammograms at the indicated potential scan number. (**b**) The Raman spectra of the samples after 1st (**a**), 500th (**b**), and 2000th potential scans. In the inset, the Tafel plots for the samples after 1st and 1000th potential scans are shown.

Titanium substrates covered with nanostructured titanium monoxide, particularly TiO_x nanofeatures, were also tested. These nanostructured films (Figure 9a) were fabricated hydrothermally in the selenious acid solution as reported recently [37]. The quality of MoS_2 nanoplatelet array formed onto the Ti/TiO_x substrate was dependent on the MoS_2 synthesis conditions. Thus, when Ti/TiO_x electrode was hydrothermally treated in the heptamolybdate-thiourea solution at 220 °C for 2 h, just random depositions of MoS_2 species were obtained, whereas if syntheses were conducted for 5 h or longer, Ti/TiO_x electrode were entirely covered with the nanoplatelet-shaped species (Figure 9b).

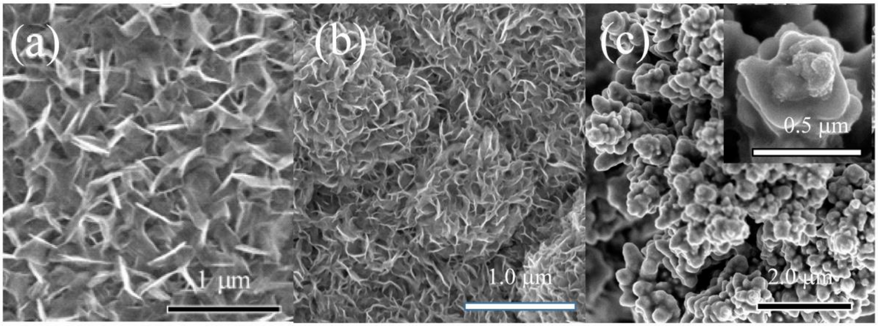

Figure 9. Top-side SEM views of TiO_x (**a**) and TiO_x/MoS_2 film (**b**) surfaces before (**b**) and after (**c**) potential cycling in the solution of 0.5 H_2SO_4 + 0.25 mol L^{-1} formic acid at 10 mV s^{-1} within −0.45 to 0.05 V potential range for a period of 1000 potential scans. MoS_2 film was synthesized as in Figure 6.

Electrochemical tests in the acidic solution showed that H_2 evolution reaction at the surface of this film proceeds initially from the onset potential of ~170 mV vs. RHE (Figure 10) that can be linked with the higher electrical conductivity of titanium monoxides comparing to TiO_2. However, the activity of this electrocatalyst decreases during prolonged potential cycling attaining 50–45 mA cm^{-2} after 1000 cycles. Moreover, the pulsation of j(E) plots that was not characteristic for other substrates, was determined (Figure 10). We linked this effect with the polymerization of aniline molecules entrapped during MoS_2 hydrothermal synthesis and unhooked during the intense HER processing, covering MoS_2 platelets as clearly evidenced by the top-side film SEM image presented in Figure 9c.

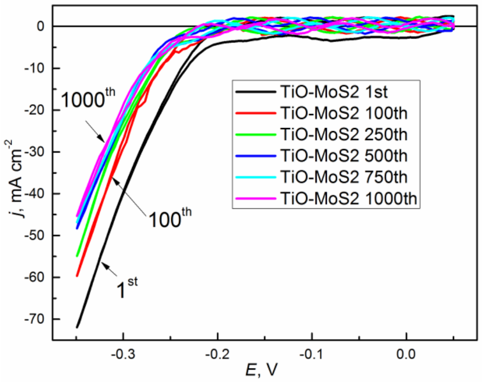

Figure 10. HER voltammograms at indicated potential scan number for the $Ti/TiO_x/MoS_2$-based electrode in the 0.5 H_2SO_4 and 0.25 mol L^{-1} COOH solution at 10 mV s^{-1} potential scan rate.

4. Conclusions

The influence of substrate material on the morphology, composition, and catalytic properties of the MoS_2 nanoplatelet-shaped films for hydrogen evolution reaction from the acidic solution was studied. One-pot hydrothermal synthesis approach was adapted as a simple and cost-effective way for the design of nanostructured catalyst films. To increase the HER activity of the synthesized material, aniline additives were successfully used for the first time. The compositional and processing optimization tests resulted in the formation of HER active 1–2 µm thick nanoplatelet MoS_2 film hybridized with aniline molecules as elucidated from the SEM view (Figure 7c) and Raman spectrum (Figure 2b), respectively. Via a long-term HER processing, it is determined that among various tested substrates, titanium covered by a thin nanotubed titania film is the most suitable for the preparation of well adherent to the substrate, efficient, and stably working catalyst.

Author Contributions: Data curation, S.R.; electrochemical investigations P.G.; structural analysis A.N. and M.K.; Raman analysis R.T.; writing—review and editing A.J. All authors have read and agreed to the published version of the manuscript.

Funding: P.G. acknowledged funds provided by the Lithuania Science Council via project no. 09.3.3-LMT-K-712-10-0039.

Conflicts of Interest: The authors declare no competing financial interest and any unpaid roles or relationships that might have a bearing on the publication process.

References

1. Yang, L.; Zhou, W.; Hou, D.; Zhai, K.; Li, G.; Tang, Z.; Li, L.; Chen, S. Porous metallic MoO_2-supported MoS_2 nanosheets for enhanced electrocatalytic activity in the hydrogen evolution reaction. *Nanoscale* **2015**, *7*, 5203–5208. [CrossRef]
2. Kong, D.; Wang, H.; Cha, J.J.; Pasta, M.; Koski, J.; Yao, J.; Cui, Y. Synthesis of MoS_2 and $MoSe_2$ films with vertically aligned layers. *Nano Lett.* **2013**, *13*, 1341–1347. [CrossRef]
3. Tang, C.; Sun, A.; Xu, Y.; Wang, D. High specific surface area Mo_2C nanoparticles as an efficient electrocatalyst for hydrogen evolution. *J. Power Sources* **2015**, *296*, 18–22. [CrossRef]

4. Zhou, Y.; Zhou, W.; Li, G.; Tang, Z.; Li, L.; Chen, S. MoS_2 nanosheet-coated CoS_2 nanowire arrays on carbon cloth as three-dimensional electrodes for efficient electrocatalytic hydrogen evolution. *J. Mater. Chem. A* **2015**, *3*, 22886–22891.
5. Liu, Y.-R.; Hu, W.-H.; Han, G.-Q.; Dong, B.; Chai, Y.-M.; Liu, Y.-Q.; Liu, C.-G. Facile synthesis of one-dimensional MoOx-based nanostructure for electrocatalytic hydrogen evolution. *ECS Electrochem. Lett.* **2015**, *4*, H5–H9. [CrossRef]
6. McKone, J.R.; Marinescu, S.C.; Brunschwig, B.S.; Winkler, J.R.; Gray, H.B. Earth-abundant hydrogen evolution electrocatalysts. *Chem. Sci.* **2014**, *5*, 865–878. [CrossRef]
7. Xiao, P.; Yan, Y.; Ge, X.; Liu, Z.; Wang, J.Y.; Wang, X. Investigation of molybdenum carbide nano-rod as an efficient and durable electrocatalyst for hydrogen evolution in acidic and alkaline media. *Appl. Catal. B Environ.* **2014**, *154–155*, 232–237. [CrossRef]
8. McEnaney, J.M.; Crompton, J.C.; Callejas, J.F.; Popczun, E.J.; Biacchi, A.J.; Lewis, N.S.; Schaak, R.E. Amorphous molybdenum phosphide nanoparticles for electrocatalytic hydrogen evolution. *Chem. Mater.* **2014**, *26*, 4826–4831. [CrossRef]
9. Kong, D.; Cha, J.J.; Wang, H.; Lee, H.R.; Cui, Y. First-row transition metal dichalcogenide catalysts forhydrogen evolution reaction. *Energy Environ. Sci.* **2013**, *6*, 3553–3558. [CrossRef]
10. Wu, Z.; Fang, B.; Wang, Z.; Wang, C.; Liu, Z.; Liu, F.; Wang, W.; Alfantazi, A.; Wang, D.; Wilkinson, D.P. MoS_2 nanosheets: A designed structure with high active site density for the hydrogen evolution reaction. *ACS Catal.* **2013**, *3*, 2101–2107. [CrossRef]
11. Bian, X.; Zhu, J.; Liao, L.; Scanlon, M.D.; Ge, P.; Ji, C.; Girault, H.H.; Liu, B. Nanocomposite of MoS_2 on ordered mesoporous carbon nanospheres: A highly active catalyst for electrochemical hydrogen evolution. *Electrochem. Commun.* **2012**, *22*, 128–132. [CrossRef]
12. Jaramillo, T.F.; Jorgensen, K.P.; Bonde, J.; Nielsen, J.H.; Horch, S.; Chorkendorff, I. Identification of Active Edge Sites for Electrochemical H_2 Evolution from MoS_2 Nanocatalysts. *Science* **2007**, *317*, 100–102. [CrossRef] [PubMed]
13. Jagminas, A.; Niaura, G.; Žalnėravičius, R.; Trusovas, R.; Račiukaitis, G.; Jasulaitienė, V. Laser light-induced transformation of molybdenum disulfide-based nanoplatelet arrays. *Sci. Rep.* **2016**, *6*, 37514. [CrossRef] [PubMed]
14. Bonde, J.; Moses, P.G.; Jaramillo, T.F.; Norskov, J.K.; Chorkendorff, J. Hydrogen evolution on nano-particulate transition metal sulfides. *Faraday Discuss.* **2008**, *140*, 219–231. [CrossRef] [PubMed]
15. Jaramillo, T.F.; Bonde, J.; Zhang, J.; Ooi, B.-L.; Andersson, K.; Ulstrup, J.; Chorkendorff, I. Hydrogen Evolution on Supported Incomplete Cubane-type $[Mo_3S_4]^{4+}$ Electrocatalysts. *J. Phys. Chem. C* **2008**, *112*, 17492–17498. [CrossRef]
16. Li, Y.; Wang, H.; Xie, L.; Liang, Y.; Hong, G.; Dai, H. MoS_2 Nanoparticles Grown on Graphene: An Advanced Catalyst for the Hydrogen Evolution Reaction. *J. Am. Chem. Soc.* **2011**, *133*, 7296–7299. [CrossRef] [PubMed]
17. Wang, H.; Robinson, J.T.; Diankov, G.; Dai, H. Nanocrystal Growth on Graphene with Various Degrees of Oxidation. *J. Am. Chem. Soc.* **2010**, *132*, 3270–3271. [CrossRef]
18. Liang, Y.Y.; Wang, H.J.; Casalongue, H.S.; Chen, Z.; Dai, H.J. TiO_2 Nanocrystals Grown on Graphene as Advanced Photocatalytic Hybrid Materials. *Nano Res.* **2010**, *3*, 701–705. [CrossRef]
19. Wang, D.; Zhang, X.; Bar, S.; Zhang, Z.; Fei, H.; Wu, Z. Phase engineering of a multiphasic 1T/2H MoS_2 catalyst for highly efficient hydrogen evolution. *J. Mater. Chem. A* **2017**, *5*, 2681–2688. [CrossRef]
20. Lu, X.J.; She, G.W.; Zhou, S.X.; Li, Y.M. Highly efficient electrocatalytic hydrogen production by nickel promoted molybdenum sulfide microspheres catalysts. *RSC Adv.* **2013**, *3*, 21231–21236.
21. Chen, Z.B.; Cummins, D.; Reinecke, B.N.; Clark, E.; Sunkara, M.K.; Jaramillo, T.F. Core-shell MoO_3-MoS_2 nanowires for hydrogen evolution: A functional design for electrocatalytic materials. *Nano Lett.* **2011**, *11*, 4168–4175. [CrossRef] [PubMed]
22. Aditya, T.; Nayak, A.K.; Pradhan, D.; Pal, A.; Pal, T. Fabrication of MoS_2 decorated reduced graphene oxide sheets from solid Mo-precursor for electrolytic hydrogen evolution reaction. *Electrochimica Acta* **2019**, *313*, 341–351. [CrossRef]
23. Yan, Y.; Ge, X.M.; Liu, Z.L.; Wang, J.Y.; Lee, J.M.; Wang, X. Facile synthesis of low crystalline MoS_2 nanosheet-coated CNTs for enhanced hydrogen evolution reaction. *Nanoscale* **2013**, *5*, 7768–7771. [CrossRef]
24. Liao, L.; Zhu, J.; Bian, X.; Zhu, L.; Scanlon, M.D.; Girault, H.H.; Liu, B. MoS_2 formed on mesoporous graphene as a highly active catalyst for hydrogen evolution. *Adv. Func. Mater.* **2013**, *23*, 5326–5333. [CrossRef]

25. Park, S.; Chun, D.; Ko, D.; Sung, Y.; Piao, Y. Three-dimensional carbon foam/N-doped graphene@MoS_2 hybrid nanostructures as effective electrocatalysts for the hydrogen evolution reaction. *J. Mater. Chem. A* **2016**, *4*, 12720–12725. [CrossRef]
26. Geng, X.; Sun, W.; Wu, W.; Chen, B.; Hilo, A.A.; Benamara, M.; Zhu, H.; Watanabe, F.; Cui, J.; Chen, T.P. Pure and stable metallic phase molybdenum disulphide nanosheets for hydrogen evolution reaction. *Nat. Commun.* **2016**, *7*, 10672. [CrossRef]
27. Liu, Q.; Fang, Q.; Chu, W.; Wan, Y.; Li, X.; Xu, W.; Habib, M.; Tao, S. Electron-doped 1T-MoS_2 via interface engineering for enhanced electrocatalytic hydrogen evolution. *Chem. Mater.* **2017**, *29*, 4738–4744. [CrossRef]
28. Hu, J.J.; Zabinski, J.S.; Sanders, J.H.; Bultman, J.E.; Vacvodin, A.A. Pulsed Laser Syntheses of Layer-Structured WS_2 Nanomaterials in Water. *J. Phys. Chem. B* **2006**, *110*, 8914–8916. [CrossRef]
29. Zelenski, C.M.; Dorhout, R.K. Template Synthesis of Near-Monodisperse^1 Microscale Nanofibers and Nanotubules of MoS_2. *J. Am. Chem. Soc.* **1998**, *120*, 734–742. [CrossRef]
30. Feldman, Y.; Wassermann, E.; Srolovitz, D.J.; Tenne, R. High-Rate, Gas-Phase Growth of MoS_2 Nested Inorganic Fullerenes and Nanotubes. *Science* **1995**, *267*, 222–225. [CrossRef]
31. Ellmer, K.; Mientus, R.; Seeger, S.; Weiβ, V. Highly (001)-textured WS_{2-x} films prepared by reactive radio frequency magnetron sputtering. *Phys. Status Solidi A* **2004**, *201*, R97–R100. [CrossRef]
32. Wu, Z.; Tang, C.; Zhou, P.; Liu, Z.; Xu, Y.; Wang, D.; Fang, B. Enhanced hydrogen evolution catalysis from osmotically swollen ammoniated MoS_2. *J. Mater. Chem. A* **2015**, *3*, 13050–13056. [CrossRef]
33. Ma, L.; Chen, W.X.; Li, H.; Xu, Z.D. Synthesis and characterization of MoS_2 nanostructures with different morphologies via an ionic liquid-assisted hydrothermal route. *Mater. Chem. Phys.* **2009**, *116*, 400–405. [CrossRef]
34. Zhang, H.; Lin, H.; Zheng, Y.; Hu, Y.; MacLennan, A. Understanding the effect of synthesis temperature on the crystallization and activity of nano-MoS_2 catalyst. *Appl. Catal. B Environ.* **2015**, *165*, 537–546. [CrossRef]
35. Dhas, N.A.; Suslikk, K.S. Sonochemical Preparation of Hollow Nanospheres and Hollow Nanocrystals. *J. Am. Chem. Soc.* **2005**, *127*, 2368–2369. [CrossRef]
36. Merki, D.; Vrubel, H.; Rovelli, L.; Fierro, S.; Hu, X. Fe, Co, and Ni ions promote the catalytic activity of amorphous molybdenum sulfide films for hydrogen evolution. *Chem. Sci.* **2012**, *3*, 2515–2525. [CrossRef]
37. Jagminas, A.; Ramanavicius, S.; Jasulaitienė, V.; Šimėnas, M. Hydrothermal synthesis and characterization of nanostructured titanium monoxide films. *RSC Adv.* **2019**, *9*, 40727–40735. [CrossRef]
38. Wu, Z.; Wang, D.; Sun, A. Preparation of MoS_2 nanoflakes by a novel mechanical activation method. *J. Cryst. Growth* **2010**, *312*, 340–343. [CrossRef]
39. Xiong, X.Q.; Luo, W.; Hu, X.L.; Chen, C.J.; Qie, L.; Hou, D.F.; Huang, Y.H. Flexible Membranes of MoS_2/C Nanofibers by Electrospinning as Binder-Free Anodes for High-Performance Sodium-Ion Batteries. *Sci. Rep.* **2015**, *5*, 9254.
40. Kerr, T.A.; Wu, H.; Nazar, L.F. Concurrent polymerization and insertion of aniline in molybdenum trioxide: Formation and properties of a $[Poly(aniline)]_{0.24}MoO_3$ nanocomposite. *Chem. Mater.* **1996**, *8*, 2005–2015. [CrossRef]
41. Kanatzidis, G.; Bissessur, R.; deGroot, D.C.; Schindler, J.L.; Kannewurf, C.R. New intercalation compounds of conjugated polymers. Encapsulation of polyaniline in MoS_2. *Chem. Mater.* **1993**, *5*, 595–596. [CrossRef]
42. Seguin, L.; Figlarz, M.; Cavagnat, R.; Lassegues, J.-C. Infrared and Raman spectra of MoO_3 molybdenum trioxides and MoO_3 xH_2O molybdenum trioxide hydrates. *Spectrochim. Acta Part A* **1995**, *51*, 1323–1344. [CrossRef]
43. Li, S.L. Qantitative Raman spectrum and reliable thickness identification for atomic layers on insulating substrates. *ACS. Nano.* **2012**, *6*, 7381–7388. [CrossRef] [PubMed]
44. Ji, Q.; Zhang, Y.; Gao, T.; Zhang, Y.; Ma, D.; Liu, M.; Chen, Y.; Qiao, X.; Tan, P.H.; Kan, M. Epitaxial Monolayer MoS_2 on Mica with Novel Photoluminescence. *Nano Lett.* **2013**, *13*, 3870–3877. [CrossRef]
45. Das, S.; Chen, H.-Y.; Penumatch, A.V.; Appenzeller, J. High performance multilayer MoS_2 transistors with scandium contacts. *Nano. Lett.* **2013**, *13*, 100–105. [CrossRef]
46. He, Z.; Que, W. Molybdenum disulfide nanomaterials: Structure, properties, synthesis and recent progress on hydrogen evolution reaction. *Appl. Mater. Today* **2016**, *3*, 23–56. [CrossRef]
47. Li, G.; Liu, Z.-Q.; Lu, J.; Wang, L.; Zhang, Z. Effect of calcination temperature on the morphology and surface properties of TiO_2 nanotube array. *Appl. Surf. Sci.* **2009**, *255*, 7323–7328. [CrossRef]

48. Paulose, M.; Varghese, O.K.; Mor, G.K.; Grimes, C.A.; Ong, K.G. Unprecedented ultra-high hydrogen gas sensitivity in undopted titania nanotubes. *Nanotechnology* **2005**, *17*, 398–402. [CrossRef]
49. Chen, G.; Song, X.; Guan, L.; Chai, J.; Zhang, H.; Wang, S.; Pan, J.; Tao, J. Defect assisted coupling of a MoS_2/TiO_2 interface and tuning of its electronic structure. *Nanotechnology* **2016**, *27*, 355203. [CrossRef]
50. Zou, X.; Zhang, Y. Noble metal-free hydrogen evolution catalysts for water splitting. *Chem. Soc. Rev.* **2015**, *44*, 5148–5180. [CrossRef]
51. Zhang, J.; Wu, J.; Guo, H.; Chen, W.; Yuan, J.; Martinez, U.; Gupta, G.; Mohite, A.; Ajayan, P.M.; Lou, J. Unveiling Active Sites for the Hydrogen Evolution Reaction of Monolayer MoS_2. *Adv. Mater.* **2017**, *29*, 1701955. [CrossRef] [PubMed]
52. Roland, U.; Braunscheig, T.; Roessner, F. On the nature of spilt-over hydrogen. *J. Mol. Catal. A* **1997**, *127*, 61–84. [CrossRef]
53. Jagminas, A.; Kovger, J.; Selskis, A.; Reza, A. Effect of hydrogen doping on the loading of titania nanotube films with copper selenide species via alternating current deposition. *J. Appl. Electrochem.* **2015**, *45*, 1141–1151. [CrossRef]

3rd publication / 3 publikacija

TiO_{2-x}/TiO_2-Structure Based ‘Self-Heated’ Sensor for the Determination of Some Reducing Gases

Simonas Ramanavicius, Alla Tereshchenko, Renata Karpicz, Vilma Ratautaite, Urte Bubniene, Andrius Maneikis, Arunas Jagminas, Arunas Ramanavicius

Sensors, 2020, 20, 74
Reprinted by permission
The article could be find online at https://doi.org/10.3390/s20236833

sensors

MDPI

Article

$TiO_{2\text{-}x}/TiO_2$-Structure Based 'Self-Heated' Sensor for the Determination of Some Reducing Gases

Simonas Ramanavicius [1], Alla Tereshchenko [2,3], Renata Karpicz [1], Vilma Ratautaite [1,3], Urte Bubniene [1,3], Audrius Maneikis [1], Arunas Jagminas [1] and Arunas Ramanavicius [1,3,*]

[1] Center for Physical Sciences and Technology, Sauletekio av. 3, LT-10257 Vilnius, Lithuania;
simonas.ramanavicius@gmail.com (S.R.); renata.karpicz@ftmc.lt (R.K.); vilma.ratautaite@gmail.com (V.R.);
urte.bubniene@gmail.com (U.B.); andrius.maneikis@ftmc.lt (A.M.); arunas.jagminas@ftmc.lt (A.J.)
[2] Department of Experimental Physics, Faculty of Mathematics, Physics and Information Technologies,
Odesa National I.I. Mechnikov University, Pastera 42, 65023 Odesa, Ukraine; alla_teresc@onu.edu.ua
[3] Department of Physical Chemistry, Institute of Chemistry, Faculty of Chemistry and Geosciences,
Vilnius University, Naugarduko 24, LT-03225 Vilnius, Lithuania
* Correspondence: Arunas.Ramanavicius@chf.vu.lt

Received: 12 November 2019; Accepted: 17 December 2019; Published: 21 December 2019

Abstract: In this research we report the gas-sensing properties of $TiO_{2\text{-}x}/TiO_2$-based hetero-structure, which was 'self-heated' by current that at constant potential passed through the structure. Amperometric measurements were applied for the evaluation of sensor response towards ethanol, methanol, n-propanol and acetone gases/vapours. The sensitivity towards these gases was based on electrical resistance changes, which were determined by amperometric measurements of current at fixed voltage applied between Pt-based contacts/electrodes deposited on the $TiO_{2\text{-}x}/TiO_2$-based layer. X-ray diffraction (XRD) analysis revealed the formation of $TiO_{2\text{-}x}/TiO_2$-based hetero-structure, which is mainly based on Ti_3O_5/TiO_2 formed during the hydro-thermal oxidation-based sensing-layer preparation process. Additionally, photoluminescence and time-resolved photoluminescence decay kinetics-based signals of this sensing structure revealed the presence of TiO_2 mainly in the anatase phase in the $TiO_{2\text{-}x}/TiO_2$-based hetero-structure, which was formed at 400 °C annealing temperature. The evaluation of $TiO_{2\text{-}x}/TiO_2$-based gas-sensing layer was performed at several different temperatures (25 °C, 72 °C, 150 °C, 180 °C) and at these temperatures different sensitivity to the aforementioned gaseous materials was determined.

Keywords: nonstoichiometric titanium oxides; $TiO_{2\text{-}x}/TiO_2$; Ti_3O_5/TiO_2; photoluminescence; anatase; rutile; sensor for reducing gases

1. Introduction

Among many other inorganic semiconductor-based structures, TiO_2-based structures are often used for the development of gas-sensing devices due to their sensing properties [1]. Titanium dioxide (TiO_2) is an n-type semiconductor, which exists in three main phases (i) anatase, (ii) rutile and (iii) brookite with bandgaps of 3.02, 3.23, and 2.96 eV, respectively [2]. All phases of TiO_2 can be relatively easily synthesized and/or converted from each to another by relatively simple thermal treatment (annealing).

The attractiveness of TiO_2 has significantly increased since its water-splitting ability under ultraviolet (UV) light irradiation was discovered [3]. The discovery of the latter effect facilitated the exploitation of catalytic TiO_2 properties in the design of sensors for gases and gaseous materials. Due to remarkable properties, many different TiO_2-based structures have found applications in various technological areas including biosensors [4,5] and chemical sensors [6–10].

TiO_2-based gas sensors are not expensive. They mostly require simple analytical signal detection and evaluation systems and offer good sensitivity towards many gases and gaseous materials, including both major types of gases: (i) reducing gases such as H_2S, H_2, CO, NH_3, CH_3OH, C_2H_5OH, and many others volatile organic compounds (VOCs), and (ii) oxidizing gases such as O_2, NO_2, CO_2 [11–13]. When TiO_2-based sensors are affected by different types of gases (reducing or oxidizing) such sensors generate opposite (positive or negative) current/(electrical resistance)-based response, which depends on the type of the gas. Electrical resistance measurement-based registration is one of the simplest analytical signal-registration method in comparison to many other analytical techniques, e.g., (i) the determination based on photoluminescence (PL) measurements [14] or (ii) based on more sophisticated potentiodynamic electrical/electrochemical techniques such as impedance spectroscopy [15], etc., which can be applied for analytical signal registration in the case of TiO_2-based sensors.

The sensing mechanism of TiO_2-based gas sensors is complex and it can be described by the superposition of several multi-step processes: (i) a gas adsorption/desorption on TiO_2 surface, which dependent on the nature of the gas is followed by enrichment or depletion of upper layer of TiO_2-based structure by electrons, which significantly (ii) changes the conductivity of TiO_2-based grains and (iii) the charge transfer between the grains. In these aforementioned processes the surface-to-volume ratio of grains, the grain size and the Debay length are playing a crucial role in the charge transfer ability of TiO_2-based layers. Therefore, the formation of nanostructured TiO_2 with a very high number of grains, i.e., a high number of boundaries between grains and increased surface on which gases of interest can be adsorbed, are advantageous for the development of gas sensors [12,16–20]. Even the sorption of gases on the surface of TiO_2-based structures is not a very simple phenomenon, which is mostly based on several different phases, particularly physical-adsorption and chemisorption [21]. During the physical adsorption phase gas molecules (mostly oxygen), which are initially adsorbed on the surface of TiO_2 from air, are replaced by molecules of other gases, which are present in gaseous specimen. This process is mainly determined by Van der Waals and electrostatic interactions between TiO_2 and the adsorbed gas molecules. During the next phase, adsorbed molecules dependently on their structure and/or orientation on the surface are either attracting or donating electrons to the TiO_2 surface layer, which induces the variation of conductivity by the aforementioned mechanism.

Despite some recent developments in TiO_2-based hetero-structure based sensors, n-type pure TiO_2-based gas sensors are characterized by relatively high resistance and relatively poor sensing activity, therefore, various TiO_2-based hetero-structures are used instead of pure TiO_2. Coupling of TiO_2 with various materials can result in increased sensing-ability. The most promising structures are based on coupling of TiO_2 with other semiconducting materials, which can increase sensitivity, alternate selectivity, reduce response time, lower operational temperatures in comparison to pure TiO_2-based sensors [17–25].

One option of modification and/or formation of hetero-structures, which are sensitive to various gaseous materials, is related to the application of conducting polymers such as polypyrrole (Ppy), which is used in order to form TiO_2/Ppy-based hetero-structures suitable for the determination of liquefied petroleum gases (LPG) such as propane and butane [26]. TiO_2/Ppy-based sensors operated at relatively low temperatures, which are close to the room temperature. Some other authors have demonstrated the sensitivity of ultra-thin TiO_2/Ppy-based hetero-structures towards NH_3 gas [27], which was advanced towards much higher sensitivity by another research team [28]. Advancement in the application of TiO_2/Ppy hetero-structures is attributed to the formation of n-p hetero-junctions between TiO_2 and Ppy layers. Similar hetero-junctions were reported for TiO_2 and another conducting polymer polyaniline (PANI) based hetero-structures TiO_2/PANI, which were sensitive towards NH_3 [27,29–31].

The primary aim of this research is to demonstrate the ability to form layer of $TiO_{2\text{-x}}$/TiO_2-based hetero-structures, which will be suitable for the design of gas sensor operating at relatively low temperatures. The next aim was to demonstrate that relatively low resistance of formed $TiO_{2\text{-x}}$/TiO_2 layer can be applied for 'self-heating' of the sensing structure and to evaluate how the selectivity and sensitivity of the here designed gas sensor depends on the temperature of $TiO_{2\text{-x}}$/TiO_2-based sensing-structure.

1. Experimental

1.1. Formation of TiO_2 Sample

A Si wafer (1) was oxidized in electric oven with increased concentration of oxygen to form a few micrometers thick oxide (SiO_2) layer (2) over the Si wafer. After that the metallic titanium (Ti) layer (3) of 100 nm thickness was sputtered by a magnetron. Amorphous non-stoichiometric titanium oxide (TiO_{2-x}) and titanium dioxide (TiO_2) based hetero-structure (TiO_{2-x}/TiO_2) was formed by hydrothermal oxidation of Si/SiO_2/Ti-based wafer in aqueous alkaline solution. Finally, platinum (Pt) electrodes/(contact zones) (Figure 1, Section 3) were formed on the top of the crystalline TiO_2 by magnetron sputtering.

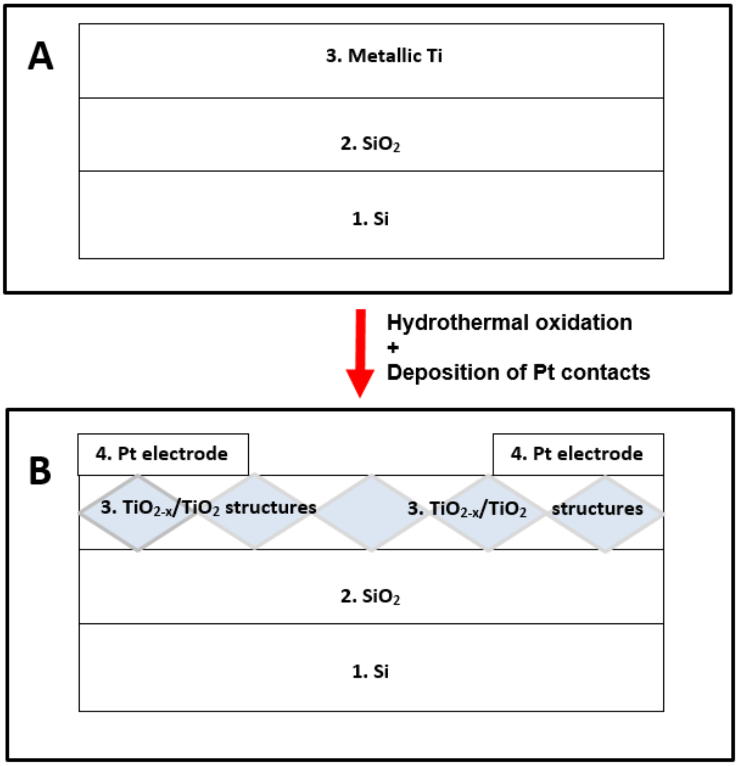

Figure 1. (**A**) Schematic view (layer-by-layer) of initial structure, which was used for the design of sensor: 1—Si-based wafer; 2—thin layer (100 nm) of SiO_2; 3—thin layer (100 nm) of Ti deposited by magnetron sputtering. (**B**) Schematic view (layer-by-layer) of TiO_{2-x}/TiO_2-based sensor structure: 1—Si-based wafer; 2—thin layer (100 nm) of SiO_2; 3—nonstoichiometric TiO_{2-x}/TiO_2 layer formed by hydrothermal oxidation; 4—Pt electrodes/(contact zones) deposited by magnetron sputtering.

The next step in sensor development procedure was based on annealing of Ti-based structures, which was performed at three different temperature regimes:

(i) 50 °C/1 h + 400 °C/2 h temperature for the formation of TiO_{2-x}/TiO_2 (400 °C) structure;
(ii) 50 °C/1 h + 600 °C/2 h temperature for the formation of TiO_{2-x}/TiO_2 (600 °C) structure;
(iii) 50 °C/1 h + 800 °C/2 h temperature for the formation of TiO_{2-x}/TiO_2 (800 °C) structure.

All the aforementioned procedures enabled us to form mixed crystal phase TiO_{2-x}/TiO_2-based hetero-structures (Figure 1, layers 4 and 5) at over-layer containing significant amount of TiO_2 in the form of anatase and/or rutile phases and TiO_{2-x}, which was formed in the deeper layers of the structure below fully oxidized stoichiometric TiO_2.

Finally, platinum-based electrodes were deposited on the formed TiO_{2-x}/TiO_2 (400 °C), TiO_{2-x}/TiO_2 (600 °C) and TiO_{2-x}/TiO_2 (800 °C) layers by magnetron sputtering. The dimensions of the structure were: 8 mm—length of the structure and 3 mm—distance between platinum electrodes deposited over the TiO_{2-x}/TiO_2-based layer. The thickness of formed titanium layer was 100 nm, the measurements were performed at 25 °C (room temperature), 72 °C, 150 °C, 180 °C. The humidity of the supplied aforementioned gaseous materials containing air stream was constant during all parts of measurements with methanol, ethanol, n-propanol, and acetone vapour: partial pressure of water in the air stream was 3.170 kPa, which corresponds to 100% of relative humidity at 25 °C and at 101.325 kPa pressure. During the measurement of signals towards water, initially a dry air stream was supplied and mixed with 1170 ppm of H_2O containing air stream at corresponding ratio.

Platinum (Pt) contacts were formed by magnetron sputtering using sputter from VSTSER (Tel-Aviv, Israel) in direct current (DC) regime under Argon (Ar) atmosphere (20 mTorr pressure) using 1″ diameter and 99.99% purity Pt target. Contacts geometry was determined by a mask. In order to improve adhesion between TiO_{2-x}/TiO_2-based layer and platinum at first a thin (20 nm) titanium (Ti) layer was sputtered on which Pt contacts were formed. Sputtering power for Ti layer formation was 2.55 W/cm^2 with the growth of 0.13 nm/s. During the formation of the Pt procedure, magnetron power was 3.06 W/cm^2, with layer growth of 0.08 nm/s.

1.2. Scanning Electron Microscopy (SEM)-Based Characterization of Formed TiO_{2-x}/TiO_2-Based Hetero-Structure

The structural properties of the obtained TiO_2 samples on silicon substrates were determined using a scanning electron microscope (SEM) Helios NanoLab 650 from FEI (Eindhoven, The Netherlands).

1.3. X-ray Diffraction (XRD) Characterization of TiO_{2-x}/TiO_2-Structure

The phase composition of thin films was determined by X-ray diffractometer D8 Advanced from Bruker (USA) with grazing-incident X-ray diffraction (XRD) over a 2θ range of 22°–65° using Cu Kα (= 1.5046). Films for XRD investigations were based on: (i) metallic Ti (100 nm) layer deposited over Si substrate covered by 300 nm SiO_2 layer (ii) TiO_{2-x}/TiO_2 (400 °C) hetero-structure, which was formed by the oxidation of the same metallic Ti layer (mentioned in part 'i') according to the aforementioned protocol of hydrothermal oxidation at 400 °C.

The diffraction pattern was generated by X-ray beam at grazing incidence angle of 2°. XRD data library 'CDD Database PDF2010-PDF-2/Release 2010 RDB' was applied for the analysis of XRD patterns.

TiO_2-powder, which by producer was declared as TiO_2 anatase ($TiO_{2(anatase)}$) phase, was received from Sigma-Aldrich (St. Louis, United States) and was used as XRD control while was investigated at the same grazing incidence angle of 2° over similar 2θ range of 22°–65°.

1.4. Photoluminescence (PL)-Based Characterization of TiO_{2-x}/TiO_2-Structure

Optical properties of TiO_{2-x}/TiO_2-based hetero-structures deposited on oxidized silicon substrates were investigated by photoluminescence (PL) studies using Edinburgh-F900 spectrophotometer (Edinburg Instruments Ltd., Livingston, UK). The photoluminescence spectra of TiO_{2-x}/TiO_2-based hetero-structures were excited by solid-state laser with an excitation wavelength of 375 nm (the average pulse power was about 0.15 mW/mm^2, the pulse duration 70 ps) and photoluminescence was measured in the range of 400–700 nm. For comparison, the photoluminescence spectra of similar oxidized silicon substrates were also registered. All fluorescence spectra were corrected accounting the sensitivity of the instrument.

Photoluminescence measurements of 'self-heated' structure were performed at different voltages that heated the sensor up to particular temperatures. The exact temperature was followed with a thermocouple attached to the TiO_{2-x}/TiO_2 hetero-structure.

The position and intensity of the photoluminescence maximum was determined as corresponding characteristics of a Gauss function using the Origin program.

1.5. Determination of Analytical Signal towards Reducing Gases by TiO_{2-x}/TiO_2-Structure Based Sensor

Measurements of current passing through the sensor structure were performed by potentiostat/galvanostat Autolab 30 Eco Chemie Gmbh (Utrecht, The Netherlands), which was controlled by NOVA software. The TiO_{2-x}/TiO_2 (400 °C) sample was investigated under different constant voltages, which were applied by potentiostat on platinum-based electrodes deposited on the TiO_{2-x}/TiO_2 (400 °C) layer.

Evaluated gas concentrations were fixed at: 105 ppm for water, 118 ppm for methanol, 53 ppm for ethanol, 18 ppm for n-propanol, 220 ppm for acetone.

Electrical resistance of TiO_{2-x}/TiO_2 (400 °C)-based gas-sensitive structure decreased due to their increased conductivity, therefore, current passing through TiO_{2-x}/TiO_2 (400 °C)-based structure increased. In present research we have registered a variation of current (ΔI) at constant potential. These variations of measured current (I) (Figure 2) were converted into resistance (R) of TiO_{2-x}/TiO_2-based structure according to Ohms law:

$$R = V/I \tag{1}$$

where V is applied voltage.

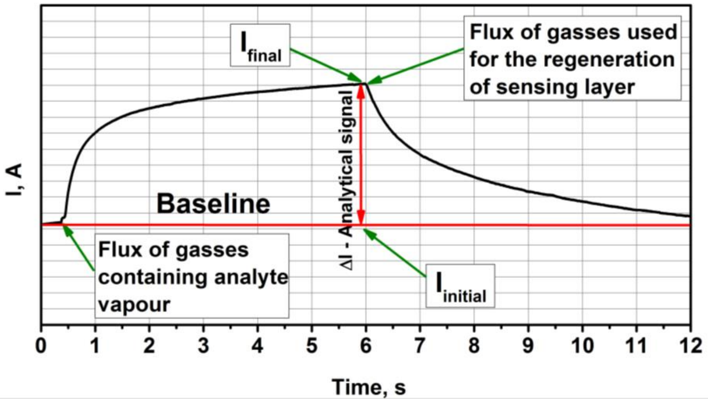

Figure 2. Representation of typical analytical signal registered by TiO_{2-x}/TiO_2 (400 °C)-based structure. It should be noted that ΔI, the duration of signal development and the regeneration of sensor after measurements were different for different gases and different concentrations of those gases.

Then relative response (ΔR, %) was calculated as:

$$\Delta R = 100 \times (R_{\text{final}} - R_{\text{initial}})/R_{\text{initial}}\ (\%) \tag{2}$$

where R_{initial} is initial resistance of TiO_{2-x}/TiO_2 (400 °C)-based structure calculated from I_{initial} at baseline, R_{final}—final resistance calculated from I_{final} (Figure 2).

1.6. Determination of Electrical Resistance Variation with Temperature

Measurements of resistance vs. temperature, were performed by system based on closed cycle helium cryostat made by Sumitomo Heavy Industries (Tokyo, Japan) combined with RDK-408D 4K cold head and SRDK Series cryocooler and CSA-71A compressor unit. Temperature was controlled by Lakeshore 340 temperature controller (Lake Shore Cryotronics, Inc., Westerville, OH, USA). Resistance was measured by Tektronix DMM 4050 multimeter (Tektronix UK Ltd., Bracknell, UK). This closed-cycle helium cryostat was used for measurement of resistance and was performed only after exact equilibration of temperature at each selected point in the temperature range from 4.2 K to 310 K, with 5 K intervals between measurement points. Temperature was changed in cyclic manner in two ways: black cycles shows points measured by cooling down, red squares shows points by increasing temperature. Measured performed in vacuum 10^{-3} Torr.

2. Results and Discussion

2.1. SEM-Based Structural Characterization of TiO_{2-x}/TiO_2-Based Layer

SEM images of TiO_{2-x}/TiO_2 (400 °C)-based hetero-structure at different at some extent s (Figure 3A,B) illustrate that the sample has a highly porous surface with nanostructures in the form of nano-plates and nano-sponges, which significantly enhanced both (i) surface area and (ii) surface to volume ratio of the gas-sensitive area of sensor. Therefore, such formations are very beneficial in order to obtain increased surface area, which is available for gas adsorption and enhances the sensitivity of such a structure.

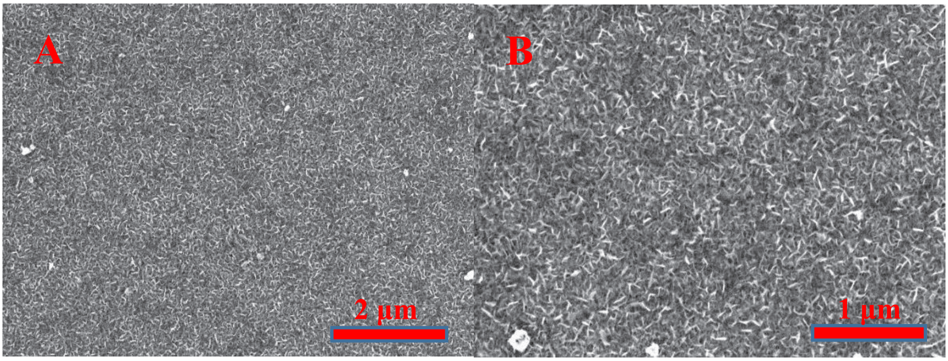

Figure 3. Scanning electron microscope (SEM) images of TiO_{2-x}/TiO_2 (400 °C)-based hetero-structure at different magnification: (**A**)—at ×25000; (**B**)—at ×50000.

2.2. XRD Characterization of TiO_{2-x}/TiO_2-Structure

The XRD pattern of metallic Ti (Figure 4, $A_{(\text{metallic Ti})}$), which was observed for initial metallic Ti layer of 100 nm thickness that was formed by magnetron sputtering and was used for further hydrothermal oxidation at 400 °C into a TiO_{2-x}/TiO_2 (400 °C)-based hetero-structure, represents all characteristic peaks of metallic Ti well (according to PDF '00-044-1294 for metallic Ti').

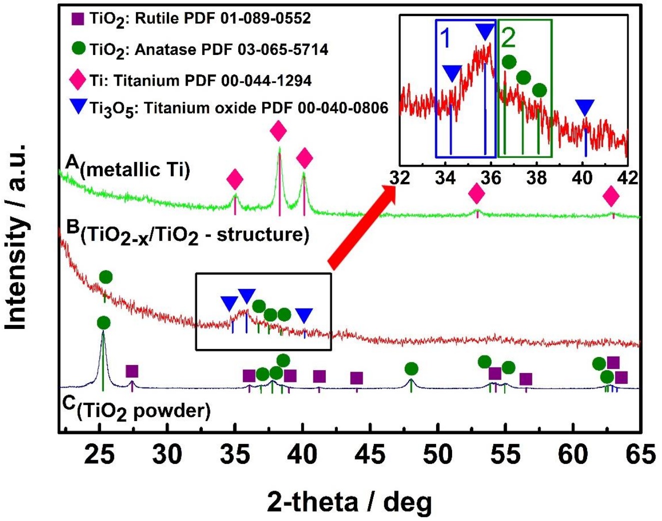

Figure 4. X-ray diffraction (XRD) patterns of: $A_{(metallic\ Ti)}$—metallic Ti layer of 100 nm thickness, which was formed by magnetron sputtering; $B_{(TiO2-x/TiO2-structure)}$— TiO_{2-x}/TiO_2 (400 °C)-based hetero-structure, which was formed from above mentioned metallic 100 nm thick Ti layer; $C_{(TiO2\ powder)}$—TiO_2-powder, which was used as 'control sample' and by supplier (Sigma-Aldrich) was declared as 99.3% TiO_2 in the anatase phase.

The XRD pattern of TiO_{2-x}/TiO_2 (400 °C) (Figure 4, $B_{(TiO2-x/TiO2-structure)}$) represents relatively high dispersion in TiO_{2-x}/TiO_2 (400 °C)-based hetero-structure, but according to Fukushima et al. [32] even the presence of broad 'peak area' in titanium oxide based pattern between 27° and 37° can be assigned to the presence of Ti_3O_5, Ti_4O_7 and/or Ti_8O_{15}. Thus, in our research we have observed a much better expressed XRD peak between 34° and 37° (Figure 4, Inset, area 1), which is in good agreement with γ-Ti_3O_5 reported in the PDF '00-040-0806 for γ-Ti_3O_5' and also in relatively good agreement with the XRD pattern presented by Yoshimatsu et al. [33] for γ-Ti_3O_5 formed by pulsed laser deposition. Results obtained by Yoshimatsu et al. [33] showed low-temperature superconductivity in both Ti_4O_7 and γ-Ti_3O_5 films. In addition, these authors reported relatively broad XRD peaks at 36–38° for γ-Ti_3O_5 and at 42–43° for Ti_4O_7. The peak observed in our research (Figure 4, $B_{(TiO2-x/TiO2-structure)}$ and Inset, area -1) according to the shape-like-features and signal to noise ratio is very similar to that at 36–38° for γ-Ti_3O_5, but just some shift is observed because preparation procedures of both films were very different, therefore, the composition and stoichiometry of both TiO_{2-x}-based structures discussed here can be different at some extent. Another broad peak area (Figure 4, Inset, area 2) between 36° and 39° is assigned to $TiO_{2(anatase)}$ according to PDF '01-075-2545 for $TiO_{2(anatase)}$' and control XRD pattern (Figure 4, $C_{(TiO2\ powder)}$) registered at the same experimental conditions for $TiO_{2(anatase)}$ powder purchased from Sigma Aldrich, where according to match between XRD patterns (Figure 4. $C_{(TiO2\ powder)}$) with PDF '01-089-0552 for $TiO_{2(rutile)}$' we have detected the presence of some $TiO_{2(rutile)}$ phase.

Titanium pentoxide (Ti_3O_5) with polymorphisms (α-, β-, γ-, δ-, and λ-phases) is 'a close neighbour' of the Magnéli phase [34–38], and sometimes it is designated as the first member of the Magnéli phase, because their chemical formula is consistent with that of the Magnéli phase ($TinO_{2n-1}$ at n = 3). According to PDF '00-040-0806 for γ-Ti_3O_5', Ti_3O_5 possesses a monoclinic cell (a = 9.9701 Å, b = 5.0747 Å, c = 7.1810 Å, β = 109.865°), which is superconducting at low temperatures (below 3 K) similarly to Ti_4O_7-based Magnéli phase [33]. Differently from the 'most respectful' member of Magneli phase—Ti_4O_7, which in crystal structure is having $TiO_{2(rutile)}$-based shear planes [39,40], in Ti_3O_5 there are no such TiO_2-rutile based shear planes [33]. Therefore, in our XRD patterns we are observing only signs of M_3O_5 and $TiO_{2(anatase)}$ without any presence of rutile. Such a composition was formed because for the formation of TiO_{2-x}/TiO_2-based hetero-structures we have applied 400 °C temperature at which the formation of M_3O_5-$TiO_{2(anatase)}$ 'intergrowths' is observed, as it has been reported and investigated by other research teams [41] and very recently has been confirmed by some other research group in different conditions [42]. The formation of above mentioned M_3O_5-$TiO_{2(anatase)}$ 'intergrowths' is in well agreement with our results based on photoluminescence (Figure 5A) and photoluminescence decay (Figure 5D) measurements, which are discussed in the next chapter, where we are clearly observing effects induced by the presence of $TiO_{2(anatase)}$.

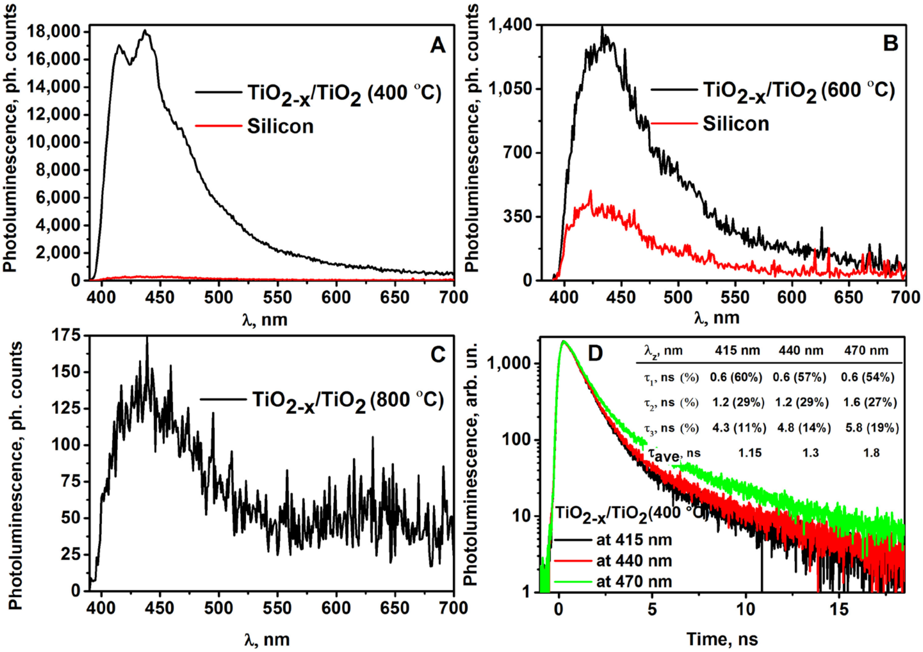

λ_z, nm	415 nm	440 nm	470 nm
τ_1, ns (%)	0.6 (60%)	0.6 (57%)	0.6 (54%)
τ_2, ns (%)	1.2 (29%)	1.2 (29%)	1.6 (27%)
τ_3, ns (%)	4.3 (11%)	4.8 (14%)	5.8 (19%)
τ_{ave}, ns	1.15	1.3	1.8

Figure 5. (**A**) Photoluminescence spectra of TiO_{2-x}/TiO_2 (400 °C) sample (1), and silicon substrate (2); (**B**) Photoluminescence spectra of TiO_{2-x}/TiO_2 (600 °C) sample (1), and silicon substrate (2); (**C**) Photoluminescence spectra of TiO_{2-x}/TiO_2 (800 °C) sample; (**D**) Photoluminescence decays of TiO_{2-x}/TiO_2 (400 °C) sample at different photoluminescence emissions bands under 375 nm excitation.

2.3. Photoluminescence Properties of Hybrid TiO_{2-x}/TiO_2-Based Structures

All photoluminescence spectra of the evaluated TiO_{2-x}/TiO_2-based structures were characterized by a wide photoluminescence maximum in the region of wavelengths between 415–500 nm. However, the quality of the photoluminescence signals of all three TiO_{2-x}/TiO_2-based structures were very different. As it is demonstrated in the Figure 5, this depends on the temperature that is applied for the annealing of TiO_{2-x}/TiO_2-based structures, because at different temperatures different phases of TiO_2 on the surface of TiO_{2-x}/TiO_2-based structures were formed. TiO_{2-x}/TiO_2(400 °C) structure, which was formed by annealing at 400 °C, generated the most intense photoluminescence signal (Figure 5A). The upper layer generates the strongest photoluminescence signal and the spectrum of TiO_{2-x}/TiO_2 (400 °C) is characterized by photoluminescence peaks, which are observed at 415, 440, 470 nm of the main photoluminescence band (Figure 5A). These photoluminescence peaks reveal the presence of $TiO_{2(anatase)}$ in TiO_{2-x}/TiO_2 (400 °C) hybrid-structure. TiO_{2-x}/TiO_2 (600 °C) structure, which was formed by annealing at 600 °C, also has demonstrated some photoluminescent properties but the photoluminescence signal was about 10 times lower (Figure 5B) and revealed presence of mixed $TiO_{2(anatase)}$ and $TiO_{2(rutile)}$ structures of TiO_{2-x}/TiO_2 (600 °C) sample.

TiO_{2-x}/TiO_2 (800 °C) structure, which was formed by annealing at 800 °C, was characterized by very weak, about 100 times lower photoluminescence signal, than that was observed for TiO_{2-x}/TiO_2 (400 °C) sample (Figure 5C). Thus $TiO_{2-x}TiO_2$ (800 °C) structure is not suitable for further investigations required for optoelectronic sensors and, as revealed by the results below, this structure was also not suitable for the sensing of gases selected for this research.

TiO_{2-x}/TiO_2 (400 °C) structure showed the most interesting and the highest quality photoluminescence signal. Therefore, during the next experiment, which was also based on photoluminescence spectrum registration, this structure was investigated under different constant voltages, which were applied by potentiostat on platinum-based electrodes deposited on the TiO_{2-x}/TiO_2 (400 °C)-based layer. The plots of photoluminescence spectra (Figure 6A) vs. applied voltage are shown in Figure 6B. The elevated voltage from 1 V to 5 V, results the decrease of intensity of the main photoluminescence maximum and a small shift of photoluminescence maximum position towards shorter wavelengths.

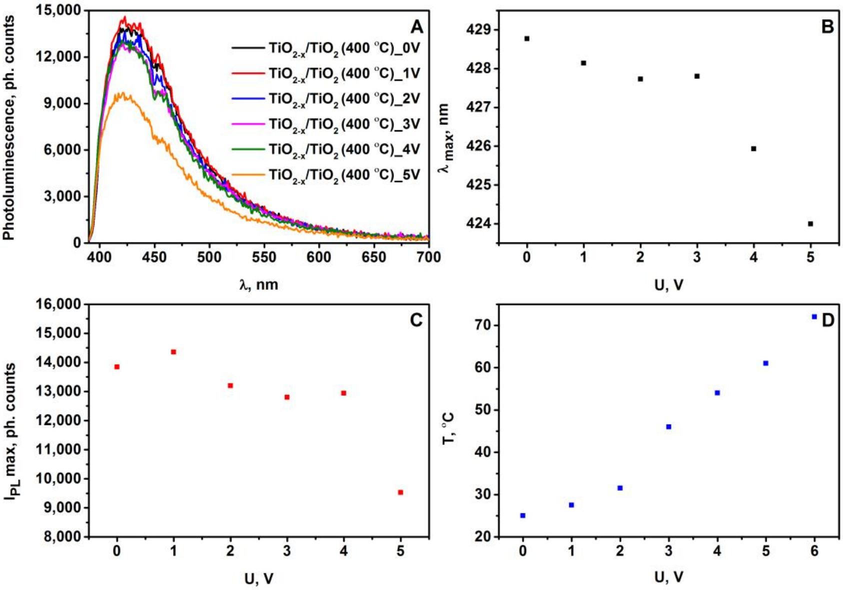

Figure 6. (**A**) Photoluminescence spectra of TiO_{2-x}/TiO_2 (400 °C)-based sample at different applied voltage; (**B**) The changes in spectral position of photoluminescence maximum vs. voltage of TiO_{2-x}/TiO_2 (400 °C)-based sample; (**C**) The changes in photoluminescence maximum intensity vs. voltage of TiO_{2-x}/TiO_2 (400 °C)-based sample; (**D**) The plot of temperature vs. voltage of TiO_{2-x}/TiO_2 (400 °C)-based sample.

Figure 6B,C show the position and the intensity of the photoluminescence maximum, which is changing depending on the voltage applied to TiO_{2-x}/TiO_2 (400 °C)-based sample. The position (Figure 6B) of the photoluminescence maximum was determined as a maximum of Gauss function, which represented the best fitting with registered photoluminescence spectra. At voltage values (from 1 V to 5 V) tested in this experiment the spectral position of the photoluminescence maximum (λ_{max}) gradually shifts towards the infrared (IR) region (Figure 6B). In general, the difference between the positions λ_{max} for TiO_{2-x}/TiO_2 (400 °C)-based sample at 0 V and 5 V is about 5 nm. A similar trend related to the decrease in photoluminescence intensity of the main maximum with increasing voltage was observed (Figure 6C). The decrease of photoluminescence intensity by the increase of applied voltage from 0 V to 5 V has been determined, and it shows that the concentration of photoluminescence emitting centers in TiO_{2-x}/TiO_2 (400 °C) hetero-structure is reducing by increasing voltage. The plot of temperature vs. voltage of TiO_{2-x}/TiO_2 (400 °C)-based sample (Figure 6D) illustrates dependence in tested potential interval, which can be predicted from Ohms law, followed by basic recalculations into the heat released by this system.

Such behavior of the photoluminescence spectra vs. applied voltage can be caused by an increased sample temperature, which is dependent on electrical current flowing through the TiO_{2-x}/TiO_2 (400 °C)-based hetero-structure. Thus, a rapid decrease in the photoluminescence intensity of TiO_2 with an increase in voltage at $U \geq 6$ V is related to the increase of the sample temperature, which leads to the temperature-based quenching of photoluminescence of $TiO_{2(anatase)}$ [43–45]. Photoluminescence studies of nanostructured TiO_2 at room-temperature were reported in some other research: (i) the photoluminescence of $TiO_{2(anatase)}$ colloidal particles of different sizes occurs from the shallow trap levels, which are located between 0.41 and 0.64 eV below the conduction band [46]; (ii) the narrow photoluminescence emission bands of $TiO_{2(anatase)}$ powder, which originated from the self-trapped exciton emission (STE) in crystalline $TiO_{2(anatase)}$ containing TiO_6 octahedral sheet-based structures, was reported [47,48]. In addition to registration of photoluminescence spectra, we have measured the photoluminescence decay kinetics for TiO_{2-x}/TiO_2 (400 °C)-based hetero-structure at different narrow photoluminescence emission bands (Figure 5D). The photoluminescence of $TiO_{2(anatase)}$ decay non-exponentially with dominating fast component, which is characterized by a decay of about 0.6 ns. The photoluminescence decay kinetics presented here clearly verify the self-trapped exciton emission origin of photoluminescence, which from the broad range of non-stoichiometric titanium oxides (TiO_{2-x}) and stoichiometric titanium oxides (TiO_2) is the most characteristic for crystalline $TiO_{2(anatase)}$ [49].

2.4. Electrical Resistance Variation with Temperature

Electrical resistance measurements of TiO_{2-x}/TiO_2-based structure revealed the oxidation of metallic titanium-based layer, because by thermal oxidation the resistance of the sample has increased from 0 Ω (for bare Ti-based layer) up to 72 Ω (for formed TiO_{2-x}/TiO_2-based structure). The increase of resistance together with the shift of photoluminescence signals clearly shows the formation of TiO_2 in the phase of anatase and rutile. However, stoichiometric TiO_2-based layers have relatively low electrical conductivity, which is typically of 10^{-10} S/m, but it was demonstrated that the conductivity of TiO_2-based layers can be significantly increased by heat-based treatment at a high temperature in a reducing gas-based environment [50]. Further investigations revealed the formation of TiO_{2-x}/TiO_2-based hetero-structures, because only TiO_2 based structures have relatively high band-gap and, therefore, they do not conduct well while the presence of TiO_{2-x} in forms of Ti_2O_3, Ti_3O_5 and/or Ti_4O_7 significantly increases the conductivity of such hetero-structures. It should be noted, that an important issue related to TiO_{2-x} conductivity is that these oxides at the stoichiometry of Ti_nO_{2n-1} (with $3 < n < 10$) are forming so called Magnéli phases [51], which possess some properties of metallic conductor [52,53]. As seen from resistance vs. temperature dependence (Figure 7, area 1), in the TiO_{2-x}/TiO_2-based hetero-structures at temperatures below 150–180 K reported here, we have also determined some signs of such transition into metallic conductivity, which is characteristic of presence of Magnéli phases.

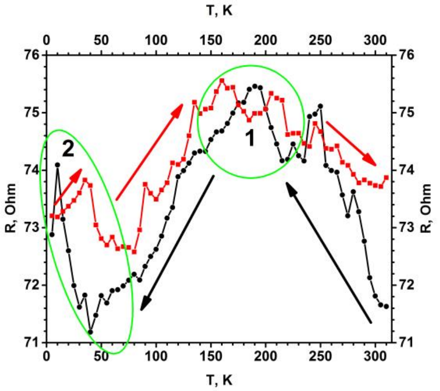

Figure 7. Temperature dependence of electrical resistance (R(T)) for the TiO_{2-x}/TiO_2 (400 °C)-based hetero-structure. Temperature was changed in two ways (indicated by black and red arrows): (i) black cycles shows points measured by cooling down, (ii) red squares shows points by increasing temperature. Measured was performed in vacuum using helium cryostat.

The R(T) dependence (temperature dependence of electrical resistance, Figure 7) is roughly temperature independent from 310 K down to relatively low temperatures 180–150. Such an R(T) dependence (almost constant R(T) with respect to T with some increase of conductivity when temperature is decreasing) is expected for a heterogeneous mixture of strongly disordered metal/(metal oxide)-based layer, and proves that the TiO_{2-x}/TiO_2 (400 °C)-based hetero-structure is strongly disordered and composed of many randomly oriented nanocrystals and of many different TiO_{2-x} phases and probably even some metal clusters randomly distributed in the volume of TiO_{2-x}/TiO_2-based hetero-structures. It is also remarkable that the roughly constant R(T) dependence also exhibits a series of small resistance jumps in the range of a few percent. These resistance jumps might be induced by the metal-semiconductor transitions within the involved Magneli phases, which is actually a combination of a variety of different Ti_nO_{2n-1} phases rather than a single phase. Interestingly at 40 K the increase of electrical resistance is observed (Figure 7, area 2), similar increase, which was followed by the drop of conductivity below 4 K, observed by some other authors [33], which have reported superconductivity in Ti_4O_7 and γ-Ti_3O_5 films. Some earlier research illustrated that so called Magnéli phases can be observed in TiO_{2-x}-based layers [54] as planes based on Ti_nO_{2n-1} that are penetrating through a matrix of TiO_2, and therefore, this shear plane based on Ti_nO_{2n-1} structure can conduct relatively well [52,53]. There are some indications that the conductivity of properly doped or reduced TiO_2, which partly turns into Ti_nO_{2n-1}, at low temperatures is based on n-type conductivity along the aforementioned shear planes. Similar conductivity features are exploited in memristor-type devices based on TiO_2, in which electrical resistance is changed by the oxidation/reduction of the TiO_2-based layer by applied corresponding potentials [55]. In other research, it has been reported that the Ti^{3+}-containing TiO_{2-x}/TiO_2, has localized oxygen vacancies, which are beneficial for the electron mobility in n-type semiconducting TiO_{2-x}/TiO_2 structure [56]. We predict that the aforementioned oxygen vacancies are offering advanced gas-sensing ability for TiO_{2-x}/TiO_2 hetero-structure evaluated in our research. The reduction of TiO_2-based layers leads to the formation of non-stoichiometric titanium oxides, which are represented by the general formula Ti_nO_{2n-1} (where n is in the range between 3 and 10 ($3 < n < 10$) and are known as Magneli phases [51]. In non-stoichiometric titanium dioxide (TiO_{2-x}) with a low x ($0 < x < 0.10$), the dominating point defects in the structure are based mainly on Ti^{3+} and Ti^{4+} interstitials and on oxygen vacancies [57]. However, the Magneli phases in which x is in the range between 0.10 and 0.34 ($0.10 < x < 0.34$) extended planar defects and crystallographic shear planes, which are varying according to the oxygen deficiency are observed [52,58]. TiO_{2-x}/TiO_2-based hetero-structure, which due to the formation of Ti^{3+} has Ti_nO_{2n-1} doped TiO_{2-x} clusters (Figure 1B, 3rd layer) with significantly advanced electrical conductivity, can be synthesized by several different methods: plasma treatment [59], metallic zinc-based reduction [60], high-energy particle bombardment [61], laser irradiation [62] and some reactions at higher temperatures [63]. In addition to these methods, in recent research we have demonstrated that the hydro-thermal approach applied here is also suitable for the formation of TiO_{2-x}/TiO_2-based hetero-structures from initially deposited titanium-based layer. Due to good electrical conductivity and chemical stability, the aforementioned Magneli phases are applied in variety of applications, e.g., cathodic protection, batteries, catalyst support for fuel cells, waste and contaminated water treatment [50,64,65]. However, the majority of Magneli phases based research has been related to the fabrication of powders [19,20], only few attempts to form Magneli phase based fibers of ~250 µm with tenable conductivity have been reported [54]. By contrast with those research projects, we have produced thin layer of TiO_{2-x}-based Magneli phases by oxidation of metallic titanium-based layer, which was deposited by magnetron sputtering. However, due to polymorphism of Ti_3O_5 based difficulties the growth of a single Ti_3O_5 crystal is still very challenging, therefore physical properties of Ti_3O_5 are still under debate [33]. Only several studies have dealt with the structural phase transitions accompanying metal–insulator transition of Ti_3O_5, which were induced: (i) by irradiation with visible-light pulses for $\beta \leftrightarrow \lambda$ transition [37], (ii) at 450 K temperatures for $\alpha \leftrightarrow \beta$ transition [34] and at 240 K temperatures for $\delta \leftrightarrow \gamma$ transition [35–38]. In addition, metal–insulator transition around 350 K was reported by Yoshimatsu et al. [33]. Such a temperature region (240–350–450 K), where the most significant variation of Ti_3O_5 conductivity was observed, is in good agreement with our recent research, because we clearly observed the variation of conductivity based on the presence/absence of gaseous compounds in temperature region between room temperature (298 K) and 180 °C (453 K).

2.5. Gas Sensing by TiO_{2-x}/TiO_2 (400 °C) Hetero-Structure-Based Sensor

Changes of electrical current passing through TiO_{2-x}/TiO_2-based hetero-structure at fixed potential were evaluated and recalculated into changes of resistance (ΔR %) using Equations (1) and (2). ΔR was evaluated as analytical signal of this sensor. Results presented in Figure 8 illustrate that already at room temperature (25 °C) the sensor shows some sensitivity towards humidity and to all four gaseous materials (methanol, ethanol, n-propanol, acetone) evaluated here. But the signals determined amperometrically at constant 0.5 V potential, which was required for the achievement of 25 °C, temperature towards humidity and towards all the aforementioned gases were very different. In the presence of water, the resistance decreased, while in the presence of methanol, ethanol, n-propanol and acetone the resistance of the sensor increased. It is observed due to different nature of these compounds. On the surface of TiO_{2-x}/TiO_2-based structure adsorbed water tends to fill the boundaries between TiO_{2-x} and TiO_2 grains and therefore it enhances the conductivity of TiO_{2-x}/TiO_2-based hetero-structure, while all other materials have much lower conductivity in comparison to species, which they are replacing during physical- and/or chemical-sorption of methanol, ethanol, n-propanol, acetone. Therefore, the conductivity of the TiO_{2-x}/TiO_2-based structure at some extent decreases (in the range of 1% in comparison to initial conductivity of TiO_{2-x}/TiO_2-based structure). There are clear indications that sensitivity towards humidity tends to decrease by elevation of temperature from 72 °C to 180 °C, because at higher temperatures H_2O evaporates from the surface of TiO_{2-x}/TiO_2-based hetero-structure. A similar tendency at 180 °C was observed for methanol and ethanol, but for n-propanol and acetone the highest sensitivity was observed at the highest evaluated temperature of 180 °C, while the best sensitivity towards methanol and ethanol was determined at 150 °C and the best selectivity towards methanol was achieved at 72 °C.

Different sensitivities towards various gaseous materials at different temperatures opens the avenue to apply the array based on similar TiO_{2-x}/TiO_2-based hetero-structures, where between Pt electrodes different constant potential will be applied and this will heat these structures up to different temperatures, where TiO_{2-x}/TiO_2-based structures will have different sensitivities. Therefore, the read-out signals from such arrays can be evaluated by analysis of variance (ANOVA)-based approaches and interpreted as analytical signals. With applied ‘self-heating’ of the sensor, the best selectivity towards methanol was achieved at 72 °C, and for ethanol the temperature was 150–180 °C. For n-propanol and acetone signals increase with heating and reaches its maximum at 180 °C. Thus TiO_2 thin films are the best for methanol detection at 72 °C, for ethanol at 150 °C and for acetone at 180 °C as the response to other gases are significantly lower. There are some indications that to all other gaseous materials investigated here, TiO_{2-x}/TiO_2-based hetero-structures were the most sensitive at even higher temperatures, but these temperatures were not available due to limitations of our experimental set up.

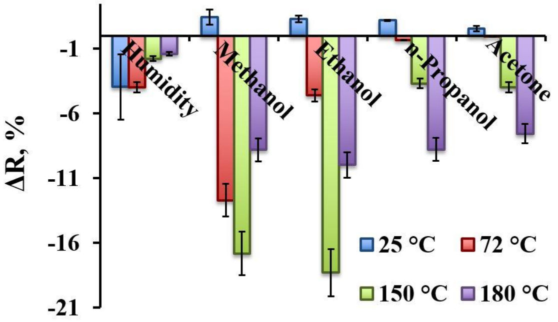

Figure 8. The response of TiO_{2-x}/TiO_2 (400 °C)-based hetero-structure towards humidity (H_2O), methanol, ethanol, n-propanol, and acetone at different temperatures (25–180 °C).

Figure 9 represents normalized response (Δ*R*, %) of TiO_{2-x}/TiO_2(400 °C) hetero-structure towards ethanol at four temperatures evaluated here: 25 °C, 72 °C, 150 °C and 180 °C. At 150 °C and 180 °C temperatures the limit of detection (LOD) was 2.6 ppm (Figure 9, lines 3 and 4), while at 72 °C it was 5.3 ppm and at room temperature (25 °C) it was 10.6 ppm, due to relatively low response in comparison to background noise. The coefficient of variation calculated from 12 measurements at 150 °C towards 53 ppm of ethanol, was 8.8%. During the measurements of different ethanol vapour concentrations, steady-state current was achieved within 4–20 s, dependently on ethanol concentration (4 s for the lowest measured ethanol concentration and 20 s for the highest measured ethanol concertation). It should be noted that for some volatile organic compounds evaluated here the response of sensing layer was even slower (e.g., towards the highest n-propanol concentration it exceeded 35 s). This fact can be related to: (i) some inertia of gas supply system and (ii) the dimensions of analyte-molecule larger molecules needs some more time to access deeper layers of TiO_{2-x}/TiO_2 (400 °C)-based hetero-structure.

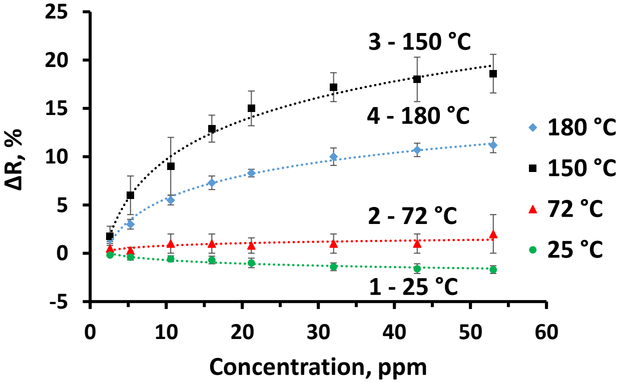

Figure 9. The response of TiO_{2-x}/TiO_2 (400 °C) hetero-structure towards ethanol, at different temperatures: 25 °C, 72 °C, 150 °C and 180 °C.

3. Conclusions and Future Developments

In this research we have succeeded in forming TiO_{2-x}/TiO_2-based hetero-structure from a thin metallic titanium-based layer. This structure as a sensing layer was integrated into a gas sensor suitable for the determination of some reducing gases. Relatively high conductivity of the TiO_{2-x}/TiO_2-based hetero-structure was exploited for 'self-heating' of this sensor. Such 'self-heating' is very beneficial for the development of TiO_{2-x}/TiO_2-based sensors, because only at higher temperatures (from 72 °C to 180 °C) was advanced sensitivity of TiO_{2-x}/TiO_2-based sensor towards methanol, ethanol, n-propanol and acetone achieved. Analytical performance of the sensor proposed here can be adjusted by the optimization of TiO_{2-x}/TiO_2-based sensing structure and analytical signal registration approach, e.g., different methods of analytical signal registration (e.g., various potentiostatic, potentiodynamic and galvanostatic methods), which at the same time will serve as heating protocols, can be also applied in order to change the sensitivity/selectivity of here proposed TiO_{2-x}/TiO_2-based hetero-structure. Therefore, after some further investigations it can be applied to the design of sensors with different selectivity and sensitivity.

Despite some progress in the preparation of TiO_2-based materials, practical exploitation of TiO_2-based structures self-doped by Ti_nO_{2n-1}-based structures is still very limited, because according to the best of our knowledge such hetero-structures have still been used for a limited number of practical applications. We expect that the aforementioned titanium oxide TiO_{2-x}/TiO_2-based hetero-structures can find more advanced applications in sensing devices, catalysts, electrode materials, energy storage devices, etc. However, better understanding of the structures formed by the procedure proposed here and their sensing ability, which will meet the requirements of other specific applications, is still required. In addition, more comprehensive understanding of the transition from the conducting metallic titanium-based layer towards the semiconducting TiO_{2-x}/TiO_2-based structure is still crucial in order to achieve desirable semiconducting properties, which are optimal for the applications mentioned above. Therefore, these challenges will be on the agenda of our further studies related to the development of TiO_{2-x}/TiO_2-structure-based materials and the application of these structures for practical purposes.

Author Contributions: Conceptualization: S.R., A.J. and A.R.; Methodology: R.K., A.T., V.R., S.R., A.M. and A.R.; Software: A.T. and R.K., formal analysis: A.T., R.K., V.R. and U.B., Writing:—original draft preparation: S.R. and A.R., Writing—review and editing: A.T., R.K. and A.R., Visualization: S.R., Supervision A.R. and U.B.; Project administration: A.T. and A.R.; Funding acquisition: A.T. and A.R. All authors have read and agreed to the published version of the manuscript.

Funding: This research was partially supported by Ukrainian-Lithuanian Research project "Application of hybrid nanostructures which are based on TiO_2 or ZnO and modified by biomolecules, in optoelectronic sensors" Lithuanian Research Council project No P-LU-18-53.

Acknowledgments: This research was partially supported by Ukrainian-Lithuanian Research project "Application of hybrid nanostructures which are based on TiO_2 or ZnO and modified by biomolecules, in optoelectronic sensors" Lithuanian Research Council project No P-LU-18-53. Authors are thankful to Valentina Plausinatiene for possibility to use XRD equipment, Skirmantas Keršulis for support during experiments of the closed-cycle helium cryostat equipment and their valuable consultations.

Conflicts of Interest: The authors declare no conflicts of interest.

References

1. Wang, Y.; Wu, T.; Zhou, Y.; Meng, C.; Zhu, W.; Liu, L. TiO_2-based nanoheterostructures for promoting gas sensitivity performance: Designs, developments, and prospects. *Sensors* **2017**, *17*, 1971. [CrossRef]
2. Wunderlich, W.; Oekermann, T.; Miao, L.; Hue, N.T.; Tanemura, S.; Tanemura, M. Electronic properties of nano-porous TiO_2-and ZnO-thin films-comparison of simulations and experiments. *J. Ceram. Proc. Res.* **2004**, *5*, 343–354.
3. Lin, J.; Heo, Y.U.; Nattestad, A.; Sun, Z.; Wang, L.; Kim, J.H.; Dou, S.X. 3D hierarchical rutile TiO_2 and metal-free organic sensitizer producing dye-sensitized solar cells 8.6% conversion efficiency. *Sci. Rep.* **2014**, *4*, 5769. [CrossRef] [PubMed]

4. Tereshchenko, A.; Smyntyna, V.; Ramanavicius, A. Interaction Mechanism between TiO_2 Nanostructures and Bovine Leukemia Virus Proteins in Photoluminescence-based Immunosensors. *RSC Adv.* **2018**, *8*, 37740–37748. [CrossRef]
5. Tereshchenko, A.; Viter, R.; Konup, I.; Ivanitsa, V.; Geveliuk, S.; Ishkov, Y.; Smyntyna, V. TiO_2 optical sensor for amino acid detection. In Proceedings of the SPIE 1st International Conference, Riga, Latvia, 26–31 august 2013; Volume 9032, p. 90320.
6. Wang, G.; Wang, J.; An, Y.; Wang, C. Anodization fabrication of 3D TiO_2 photonic crystals and their application for chemical sensors. *Superlattices Microstruct.* **2016**, *100*, 290–295. [CrossRef]
7. Si, H.; Pan, N.; Zhang, X.; Liao, J.; Rumyantseva, M.N.; Gaskov, A.M.; Lin, S. Areal-time online photoelectrochemical sensor toward chemical oxygen demand determination based on field-effect transistor using an extended gate with 3D-TiO_2 nanotube array. *Sens. Actuators B Chem.* **2019**, *289*, 106–113. [CrossRef]
8. Qiu, J.; Zhang, S.; Zhao, H. Recent applications of TiO_2 nanomaterials inchemical sensing in aqueous media. *Sens. Actuators B Chem.* **2011**, *160*, 875–890. [CrossRef]
9. Maziarz, W.; Kusior, A.; Trenczek-Zajac, A. Nanostructured TiO_2-based gas sensors with enhanced sensitivity to reducing gases. *Beilstein J. Nanotechnol.* **2016**, *7*, 1718–1726. [CrossRef]
10. Bai, J.; Zhou, B. Titanium dioxide nanomaterials for sensor applications. *Chem. Rev.* **2014**, *114*, 10131–10176. [CrossRef]
11. Kimura, M.; Sakai, R.; Sato, S.; Fukawa, T.; Ikehara, T.; Maeda, R.; Mihara, T. Sensing of vaporous organic compounds by TiO_2 porous films covered with polythiophene layers. *Adv. Funct. Mater.* **2012**, *22*, 469–476. [CrossRef]
12. Wang, Y.; Du, G.; Liu, H.; Liu, D.; Qin, S.; Wang, N.; Hu, C.; Tao, X.; Jiao, J.; Wang, J.; et al. Nanostructured sheets of Ti-O nanobelts for gas sensing and antibacterial applications. *Adv. Funct. Mater.* **2008**, *18*, 1131–1137. [CrossRef]
13. Linsebigler, A.L.; Lu, G.; Yates, J.T., Jr. Photocatalysis on TiO_2 surfaces: Principles, mechanisms, and selected results. *Chem. Rev.* **1995**, *95*, 735–758. [CrossRef]
14. Viter, R.; Tereshchenko, A.; Smyntyna, V.; Ogorodniichuk, J.; Starodub, N.; Yakimova, R.; Khranovskyy, V.; Ramanavicius, A. Toward development of optical biosensors based on photoluminescence of TiO_2 nanoparticles for the detection of Salmonella. *Sens. Actuators B Chem.* **2017**, *252*, 95–102. [CrossRef]
15. Ramanavicius, A.; Genys, P.; Ramanaviciene, A. Electrochemical impedance spectroscopy based evaluation of 1,10-phenanthroline-5,6-dione and glucose oxidase modified graphite electrode. *Electrochim. Acta* **2014**, *146*, 659–665. [CrossRef]
16. Wang, C.; Yin, L.; Zhang, L.; Qi, Y.; Lun, N.; Liu, N. Large scale synthesis and gas-sensing properties of anatase TiO_2 three-dimensional hierarchical nanostructures. *Langmuir* **2010**, *26*, 12841–12848. [CrossRef]
17. Barreca, D.; Comini, E.; Ferrucci, A.P.; Gasparotto, A.; Maccato, C.; Maragno, C.; Sberveglieri, G.; Tondello, E. First example of ZnO-TiO_2 nanocomposites by chemical vapor deposition: Structure, morphology, composition, and gas sensing performances. *Chem. Mater.* **2007**, *19*, 5642–5649. [CrossRef]
18. Lü, R.; Zhou, W.; Shi, K.; Yang, Y.; Wang, L.; Pan, K.; Tian, C.; Ren, Z.; Fu, H. Alumina decorated TiO_2 nanotubes with ordered mesoporous walls as high sensitivity NOx gas sensors at room temperature. *Nanoscale* **2013**, *5*, 8569–8576. [CrossRef]
19. Li, Z.; Ding, D.; Liu, Q.; Ning, C.; Wang, X. Ni-doped TiO_2 nanotubes for wide-range hydrogen sensing. *Nanoscale Res. Lett.* **2014**, *9*, 118–126. [CrossRef]
20. Galstyan, V.; Comini, E.; Faglia, G.; Sberveglieri, G. TiO_2 nanotubes: Recent advances in synthesis and gas sensing properties. *Sensors* **2013**, *13*, 14813–14838. [CrossRef]
21. Zakrzewska, K. Gas sensing mechanism of TiO_2-based thin films. *Vacuum* **2004**, *74*, 335–338. [CrossRef]
22. Du, P.; Song, L.; Xiong, J.; Li, N.; Xi, Z.; Wang, L.; Jin, D.; Guo, S.; Yuan, Y. Coaxial electrospun TiO_2/ZnO core–sheath nanofibers film: Novel structure for photoanode of dye-sensitized solar cells. *Electrochim. Acta* **2012**, *78*, 392–397. [CrossRef]
23. Ding, Y.; Wang, Y.; Zhang, L.; Zhang, H.; Li, C.M.; Lei, Y. Preparation of TiO_2-Pt hybrid nanofibers and their application for sensitive hydrazine detection. *Nanoscale* **2011**, *3*, 1149–1157. [CrossRef] [PubMed]
24. Li, Z.; Zhang, H.; Zheng, W.; Wang, W.; Huang, H.; Wang, C.; MacDiarmid, A.G.; Wei, Y. Highly sensitive and stable humidity nanosensors based on LiCl doped TiO_2 electrospun nanofibers. *J. Am. Chem. Soc.* **2008**, *130*, 5036–5037. [CrossRef] [PubMed]

25. Zeng, W.; Liu, T.; Wang, Z. Enhanced gas sensing properties by SnO2 nanosphere functionalized TiO_2 nanobelts. *J. Mater. Chem.* **2012**, *22*, 3544–3548. [CrossRef]
26. Bulakhe, R.N.; Patil, S.V.; Deshmukh, P.R.; Shinde, N.M.; Lokhande, C.D. Fabrication and performance of polypyrrole (Ppy)/TiO_2 heterojunction for room temperature operated LPG sensor. *Sens. Actuators B Chem.* **2013**, *181*, 417–423. [CrossRef]
27. Tai, H.; Jiang, Y.; Xie, G.; Yu, J.; Zhao, M. Self-assembly of TiO_2/polypyrrole nanocomposite ultrathin films and application for an NH3 gas sensor. *Int. J. Environ. Anal. Chem.* **2007**, *87*, 539–551. [CrossRef]
28. Wu, Y.; Xing, S.; Fu, J. Examining the use of TiO_2 to enhance the NH3 sensitivity of polypyrrole films. *Appl. Polym. Sci.* **2010**, *118*, 3351–3356. [CrossRef]
29. Wang, Q.; Dong, X.; Pang, Z.; Du, Y.; Xia, X.; Wei, Q.; Huang, F. Ammonia sensing behaviors of TiO_2-PANI/PA6 composite nanofibers. *Sensors* **2012**, *12*, 17046–17057. [CrossRef]
30. Gong, J.; Li, Y.; Hu, Z.; Zhou, Z.; Deng, Y. Ultrasensitive NH3 gas sensor from polyaniline nanograin enchased TiO_2 fibers. *J. Phys. Chem. C* **2010**, *114*, 9970–9974. [CrossRef]
31. Pawar, S.G.; Chougule, M.A.; Sen, S.; Patil, V.B. Development of nanostructured polyaniline-titanium dioxide gas sensors for ammonia recognition. *J. Appl. Polym. Sci.* **2012**, *125*, 1418–1424. [CrossRef]
32. Fukushima, J.; Takizawa. H. Size control of Ti_4O_7 nanoparticles by carbothermal reduction using a multimode Microwave furnace. *Crystals* **2018**, *8*, 444. [CrossRef]
33. Yoshimatsu, K.; Sakata, O.; Ohtomo, A. Superconductivity in Ti_4O_7 and γ-Ti_3O_5 films. *Sci. Rep.* **2017**, *7*, 12544. [CrossRef] [PubMed]
34. Åsbrink, S.; Magnéli, A. Crystal structure studies on Trititanium Pentoxide, Ti_3O_5. *Acta Cryst.* **1959**, *12*, 575. [CrossRef]
35. Hong, S.-H.; Åsbrink, S. The structure of γ-Ti_3O_5 at 297 K. *Acta Cryst.* **1982**, *B38*, 2570. [CrossRef]
36. Onoda, M. Phase transitions of Ti_3O_5. *J. Sol. State Chem.* **1998**, *136*, 67. [CrossRef]
37. Ohkoshi, S.; Tsunobuchi, Y.; Matsuda, T.; Hashimoto, K.; Namai, A.; Hakoe, F.; Tokoro, H. Synthesis of a metal oxide with a room-temperature photoreversible phase transition. *Nat. Chem.* **2010**, *2*, 539. [CrossRef] [PubMed]
38. Tanaka, K.; Nasu, T.; Miyamoto, Y.; Ozaki, N.; Tanaka, S.; Nagata, T.; Hakoe, F.; Yoshikiyo, M.; Nakagawa, K.; Umeta, Y.; et al. Structural phase transition between γ-Ti_3O_5 and δ-Ti_3O_5 by breaking of one-dimensionally conducting pathway. *Cryst. Growth Des.* **2015**, *15*, 653. [CrossRef]
39. Marezio, M.; Mcwhan, D.B.; Dernier, P.D.; Remeika, J.P. Structural aspects of the metal-insulator transitions in Ti_4O_7. *J. Sol. State Chem.* **1973**, *6*, 213. [CrossRef]
40. Lakkis, S.; Schlenker, C.; Chakraverty, B.K.; Buder, R.; Marezio, M. Metal-insulator transition in Ti_4O_7 single crystals: Crystal characterization, specific heat, and electron paramagnetic resonance. *Phys. Rev. B* **1976**, *14*, 1429. [CrossRef]
41. Grey, I.E.; Cranswick, L.M.D.; Li, C.; White, T.J.; Bursill, L.A. New M_3O_5-anatase intergrowth structures formed during low-temperature oxidation of anosovite. *J. Solid State Chem.* **2000**, *150*, 128–138. [CrossRef]
42. D'Angelo, A.M.; Webster, N.A.S. Evidence of anatase intergrowths formed during slow cooling of reduced ilmenite. *J. Appl. Cryst.* **2018**, *51*, 185–192. [CrossRef]
43. Kernazhitsky, L.; Shymanovska, V.; Gavrilko, T.; Naumov, V.; Fedorenko, L.; Kshnyakin, V.; Baran, J. Room temperature photoluminescence of anatase and rutile TiO_2 powders. *J. Lumin.* **2014**, *146*, 199–204. [CrossRef]
44. Glinka, Y.D.; Lin, S.-H.; Hwang, L.-P.; Chen, Y.-T.; Tolk, N.H. Size effect in self-trapped exciton photoluminescence from SiO_2-based nanoscale material. *Phys. Rev. B* **2001**, *64*, 085421–085432. [CrossRef]
45. Gallart, M.; Cottineau, T.; Hönerlage, B.; Keller, V.; Keller, N.; Gilliot, P. Temperature dependent photoluminescence of anatase and rutile TiO_2 single crystals: Polaron and self-trapped exciton formation. *J. Appl. Phys.* **2018**, *124*, 133104. [CrossRef]
46. Serpone, N.; Lawless, D.; Khairutdinov, R. Size effects on the photophysical properties of colloidal anatase TiO_2 particles: Size quantization versus direct transitions in this indirect semiconductor? *J. Phys. Chem.* **1995**, *99*, 16646. [CrossRef]
47. Saraf, L.V.; Patil, S.I.; Ogale, S.B.; Sainkar, S.R.; Kshirsager, S.T. Synthesis of nanophase TiO_2 by ion beam sputtering and cold condensation technique. *Int. J. Mod. Phys. B* **1998**, *12*, 2635. [CrossRef]
48. Zhang, Y.; Jiang, Z.; Huang, J.; Lim, L.Y.; Li, W.; Deng, J.; Gong, D.; Tang, Y.; Lai, Y.; Chen, Z. Nanosized titanate and titania nanostructured materials for environmental and energy applications. *RSC Adv.* **2015**, *5*, 79479–79510. [CrossRef]

49. Fujihara, K.; Izumi, S.; Ohno, T.; Matsumura, M. Time-resolved photoluminescence of particulate TiO_2 photocatalysts suspended in aqueous solutions. *J. Photochem. Photobiol. A* **2000**, *132*, 99. [CrossRef]
50. Hayfield, P.C.S. (Ed.) *Development of a New Material—Monolithic Ti4O7 Ebonex Ceramic*; Royal Society of Chemistry, Thomas Graham House: Cambridge, UK, 2002.
51. Andersson, S.; Magneli, A. Diskrete titanoxydphasen im zusammensetzungsbereich $TiO_{1,75}$-$TiO_{1,90}$. *Naturwissenschaften* **1956**, *43*, 495–496. [CrossRef]
52. Liborio, L.; Harrison, N. Thermodynamics of oxygen defective Magnéli phases in rutile: A first-principles study. *Phys. Rev. B* **2008**, *77*, 104104. [CrossRef]
53. Liborio, L.; Mallia, G.; Harrison, N. Electronic structure of the Ti4O7 Magnéli phase. *Phys. Rev. B* **2009**, *79*, 245133. [CrossRef]
54. Adamaki, V.; Clemens, F.; Ragulis, P.; Pennock, S.R.; Taylor, J.; Bowen, C.R. Manufacturing and characterization of magnéli phase conductive fibres. *J. Mater. Chem. A* **2014**, *2*, 8328–8333. [CrossRef]
55. Song, S.J.; Seok, J.Y.; Yoon, J.H.; Kim, K.M.; Kim, G.H.; Lee, M.H.; Hwang, C.S. Real-time identification of the evolution of conducting nano-filaments in TiO_2 thin film ReRAM. *Sci. Rep.* **2013**, *3*, 3443. [CrossRef] [PubMed]
56. Zhu, Q.; Peng, Y.; Lin, L.; Fan, C.M.; Gao, G.Q.; Wang, R.X.; Xu, A.W. Stable blue TiO_2-x nanoparticles for efficient visible light photocatalysts. *J. Mater. Chem.* **2014**, *A2*, 4429–4437. [CrossRef]
57. Seebauer, E.G.; Kratzer, M.C. Charged point defects in semiconductors. *Mater. Sci. Eng. R Rep.* **2006**, *55*, 57. [CrossRef]
58. Harada, S.; Tanaka, K.; Inui, H. Thermoelectric properties and crystallographic shear structures in titanium oxides of the Magnèli phases. *J. Appl. Phys.* **2010**, *108*, 083703. [CrossRef]
59. Nakamura, I.; Negishi, N.; Kutsuna, S.; Ihara, T.; Sugihara, S.; Takeuchi, K. Role ofoxygen vacancy in the plasma-treated TiO_2 photocatalyst with visible lightactivity for NO removal. *J. Mol. Catal. A Chem.* **2000**, *161*, 205–212. [CrossRef]
60. Zheng, Z.; Huang, B.; Meng, X.; Wang, J.; Wang, S.; Lou, Z.; Wang, Z.; Qin, X.; Zhang, X.; Dai, Y. Metallic zinc-assisted synthesis of Ti^{3+} self-doped TiO_2 with tunable phase composition and visible-light photocatalytic activity. *Chem. Commun.* **2013**, *49*, 868–870. [CrossRef]
61. Hashimoto, S.; Tanaka, A. Alteration of Ti 2p XPS spectrum for titanium oxideby low-energy Ar ion bombardment. *Surf. Interface Anal.* **2002**, *34*, 262–265. [CrossRef]
62. Lemercier, T.; Mariot, J.M.; Parent, P.; Fontaine, M.F.; Hague, C.F.; Quarton, M. Formation of Ti^{3+} ions at the surface of laser-irradiated rutile. *Appl. Surf. Sci.* **1995**, *86*, 382–386. [CrossRef]
63. Wang, W.K.; Gao, M.; Zhang, X.; Fujitsuka, M.; Majima, T.; Yu, H.Q. One-step synthesis of nonstoichiometric TiO_2 with designed (101) facets for enhanced photocatalytic H_2 evolution. *Appl. Catal. B Environ.* **2017**, *205*, 165–172. [CrossRef]
64. Smith, J.R.; Walsh, F.C.; Clarke, R.L. Electrodes based on Magnéli phase titanium oxides: The properties and applications of Ebonex® materials. *J. Appl. Electrochem.* **1998**, *28*, 1021. [CrossRef]
65. Walsh, F.C.; Wills, R.G.A. The continuing development of Magnéli phase titanium sub-oxides and Ebonex®electrodes. *Electrochim. Acta* **2010**, *55*, 6342. [CrossRef]

4th publication / 4 publikacija

Insights in the Application of Stoichiometric and Non-Stoichiometric Titanium Oxides for the Design of Sensors for the determination of Gases and VOCs (TiO_{2-x} and Ti_nO_{2-n} vs. TiO_2)

Simonas Ramanavičius, Arūnas Ramanavičius

Sensors 2020, 20(23), 6833

Reprinted by permission

The article could be find online at https://doi.org/10.3390/s20236833

sensors

Review

Insights in the Application of Stoichiometric and Non-Stoichiometric Titanium Oxides for the Design of Sensors for the Determination of Gases and VOCs (TiO_{2-x} and Ti_nO_{2n-1} vs. TiO_2)

Simonas Ramanavicius [1,2] and Arunas Ramanavicius [2,*]

[1] Department of Electrochemical Material Science, State Research Institute Center for Physical Sciences and Technology (FTMC), Sauletekio av. 3, LT-10257 Vilnius, Lithuania; simonas.ramanavicius@ftmc.lt
[2] Department of Physical Chemistry, Faculty of Chemistry and Geosciences, Institute of Chemistry, Vilnius University, Naugarduko 24, LT-03225 Vilnius, Lithuania
[*] Correspondence: Arunas.Ramanavicius@chf.vu.lt; Tel.: +37-060-032-332

Received: 3 November 2020; Accepted: 24 November 2020; Published: 29 November 2020

Abstract: In this review article, attention is paid towards the formation of various nanostructured stoichiometric titanium dioxide (TiO_2), non-stoichiometric titanium oxide (TiO_{2-x}) and Magnéli phase (Ti_nO_{2n-1})-based layers, which are suitable for the application in gas and volatile organic compound (VOC) sensors. Some aspects related to variation of sensitivity and selectivity of titanium oxide-based sensors are critically overviewed and discussed. The most promising titanium oxide-based hetero- and nano-structures are outlined. Recent research and many recently available reviews on TiO_2-based sensors and some TiO_2 synthesis methods are discussed. Some promising directions for the development of TiO_2-based sensors, especially those that are capable to operate at relatively low temperatures, are outlined. The applicability of non-stoichiometric titanium oxides in the development of gas and VOC sensors is foreseen and transitions between various titanium oxide states are discussed. The presence of non-stoichiometric titanium oxide and Magnéli phase (Ti_nO_{2n-1})-based layers in 'self-heating' sensors is predicted, and the advantages and limitations of 'self-heating' gas and VOC sensors, based on TiO_2 and TiO_{2-x}/TiO_2 heterostructures, are discussed.

Keywords: titanium dioxide (TiO_2); non-stoichiometric titanium oxide (TiO_n or TiO_{2-x}); Magnéli phases (Ti_nO_{2n-1}); gas and volatile organic compound (VOC) sensors; nanomaterials

1. Introduction

Gas and volatile organic compound (VOC) sensors are important for various safety and environmental control issues. Recently, rather simple gas and VOC sensors based on the measurement of the electrical resistance of the semiconducting layer are developed [1–6]. Mostly, semiconducting materials are applied in the design of sensing layer, which is responsible for the formation of analytical signal towards target gases and/or VOCs. Many semiconducting materials, including metal oxides (WO_3, SnO_2, Al_2O_3, ZnO, TiO_2, TiO_{2-x} and Ti_nO_{2n-1}) are used as a sensing materials for gas and VOC sensor design. Among many others, metal oxide-based semiconductors [7], many different forms of stoichiometric TiO_2 and various nonstoichiometric titanium oxides ($TiO_{n)}$ are applied in the design of gas and VOC sensors [8,9], because these titanium-based compounds are rather cheap, nontoxic, biocompatible, chemically stable and insoluble at neutral pHs. Stoichiometric TiO_2 is n-type semiconducting materials and exist in three main solid phases (anatase, rutile and brookite); therefore, during the formation of sensing layer phase transformations are very often exploited to modify sensitivity and selectivity of formed TiO_2 layers. [9]. In addition to stoichiometric TiO_2, recently,

Sensors **2020**, *20*, 6833; doi:10.3390/s20236833

various nanostructured non-stoichiometric titanium oxide, which by different authors is abbreviated as $TiO_{n,}$ or TiO_{2-x} and Magnéli phase (Ti_nO_{2n-1})-based layers, has received significant attention in the development of various sensors for the determination of gaseous materials [8]. These sensors are very sensitive; however, the selectivity of these sensors is still not sufficient, and in addition to that, some of them still have rather high demand of electrical power due to the necessity to power heating element, which almost always is required for the achievement of high temperatures required for the efficient operation of gas and VOC sensitive semiconducting layer. Therefore, some strategies were developed to overcome here mentioned drawbacks: (i) the possibility to apply the 'self-heating' mode in some gas and VOC sensors [1,10]; (ii) the engineering of advanced morphology, which offers better selectivity [11,12]; (iii) the formation of core-shell structures [13,14], e.g., quantum dots [15,16], where a core-forming material is covered by shell of particular material, which elicits advanced properties of the resulting hybrid sensing structure [17].

To date, number of reviews on various aspects of TiO_2 application has been published: (i) comprehensive review on synthesis, properties, modifications, and some applications of TiO_2-based nanomaterials were provided by Chen and Mao [18]; (ii) Zhang et al. have overviewed environmental and energy applications of titanate- and titania-based nanostructured materials [19]; (iii) principles, mechanisms, and some selected results of photocatalysis on TiO_2 surfaces were discussed by Linsebigler [20]; (iv) some authors addressed TiO_2-based nanomaterials [9] and nanoheterostructures [8], which are promoting advanced sensitivity of sensors towards some particular gaseous materials.

The aim of this review is to present insights for the applicability TiO_{2-}, TiO_{2-x}, Ti_nO_{2n-1} and TiO_{2-x}/TiO_2-based heterostructures in the design of gas and volatile organic compound (VOC) sensors. We are attracting attention that some of these sensors are able to operate at rather low temperatures and/or are capable of 'self-heating', both of which can significantly reduce the consumption of energy required for sensing device.

2. Main Structures of Stoichiometric and Non-Stoichiometric Titanium Oxides

The discovery of the semiconducting properties of TiO_2 facilitated the application of TiO_2 in the sensor design. Therefore, various TiO_2-based structures have been applied in chemical sensors [9,21–24] and even in biosensors [25,26]. TiO_2 is a semiconductor of n-type [27] characterized by the charge mobility of 0.4 cm^2/V s [28]. Three main phases of TiO_2 have different bandgaps: (i) 3.02 eV for anatase, (ii) 3.23 eV for rutile and (iii) 2.96 eV for brookite [29]. TiO_2 of all here mentioned phases can be simply formed and easily converted into any here mentioned form by annealing procedure. In addition to those three main phases, titanium oxide is forming various 'non-stoichiometric' structures depicted in Table 1. e.g., $TiO_{n\text{-}2}$ and/or TiO_n and so called Magnéli phases, which have the formula Ti_nO_{2n-1}, where n = 4, . . . , 10. The most nonstoichiometric structures of titanium oxide (see Figure 1) are exhibiting rather good electrical conductivity and possess sensing properties suitable for the development of gas VOC sensors [1]. Magnéli phases are very often advanced by a 'close neighbour' of the Magnéli phase titanium pentoxide (Ti_3O_5) with n = 3 for the formula of Ti_nO_{2n-1}. Titanium pentoxide is found in different polymorphic ($\alpha-$, $\beta-$, $\gamma-$, $\delta-$, and λ-forms) [30–34] and it is sometimes mentioned as very first Magnéli phase member, because it has stoichiometric chemical formula, which is consistent with Magnéli phase formula—Ti_nO_{2n-1} (where n = 3). Ti_3O_5 has a monoclinic crystal cell structure (with lattice constants of a = 9.9701 Å, b = 5.0747 Å, c = 7.1810 Å, β = 109.865°). Ti_3O_5 is exhibiting superconductivity at temperatures below 3 K, like some other Magnéli phases, e.g., Magnéli phase with n = 4 (Ti_4O_7) which is the 'most respectful' member of Magnéli phases [35]. Ti_4O_7 and other 'respectful' members of Magnéli phases in crystal structure are having $TiO_{2(rutile)}$-based shear planes [36,37], which is not the case for Ti_3O_5 [35]. Therefore, in our research of XRD-diffractograms, we observed clear signs of Ti_3O_5 and $TiO_{2(anatase)}$ without any signs of $TiO_{2(rutile)}$ [1]. It was reported that such Ti_3O_5 form of TiO_{2-x}/TiO_2-based heterostructures can be formed at a temperature of 400 °C, which is suitable for the formation of Ti_3O_5 with $TiO_{2(anatase)}$-intergrowths [38,39] at very different experimental conditions. The formation of the above-mentioned $TiO_{2(anatase)}$-intergrowths within Ti_3O_5 is valuable for the improvement of both electrical and optical sensing properties by the advancement of electrical conductivity and photoluminescence, which are enhanced by formed $TiO_{2(anatase)}$ [1]. However, despite clear advantages, the formation protocols of TiO_{2-x}/TiO_2- and Ti_nO_{2n-1}-based heterostructures are still not well elaborated and most of these structures tend to be oxidized in air atmosphere at higher temperatures. Therefore, such challenges are important to be solved during further research on the development of TiO_{2-x}/TiO_2- and Ti_nO_{2n-1}-based heterostructures and some other materials suitable for the application in gas and VOC sensor design.

Table 1. Variation of the crystal structure of titanium oxides with O/Ti stoichiometry. Adapted from [40].

Compound	**X in TiO_x**	**Structure**
TiO_2	2	Rutile
$Ti_{10}O_{19}$	1.9	Anatase
Ti_9O_{17}	1.89	Triclinic
Ti_8O_{15}	1.875	Triclinic
Ti_7O_{13}	1.857	Triclinic
Ti_6O_{11}	1.833	Triclinic
Ti_5O_9	1.8	Triclinic
Ti_4O_7	1.75	Triclinic
γTi_3O_5	1.67	Monoclinic
Ti_2O_3	1.5	Tetragonal
TiO	1	Hexagonal Cubic Monoclinic
Ti_2O	0.5	Hexagonal
Ti	0	Hexagonal

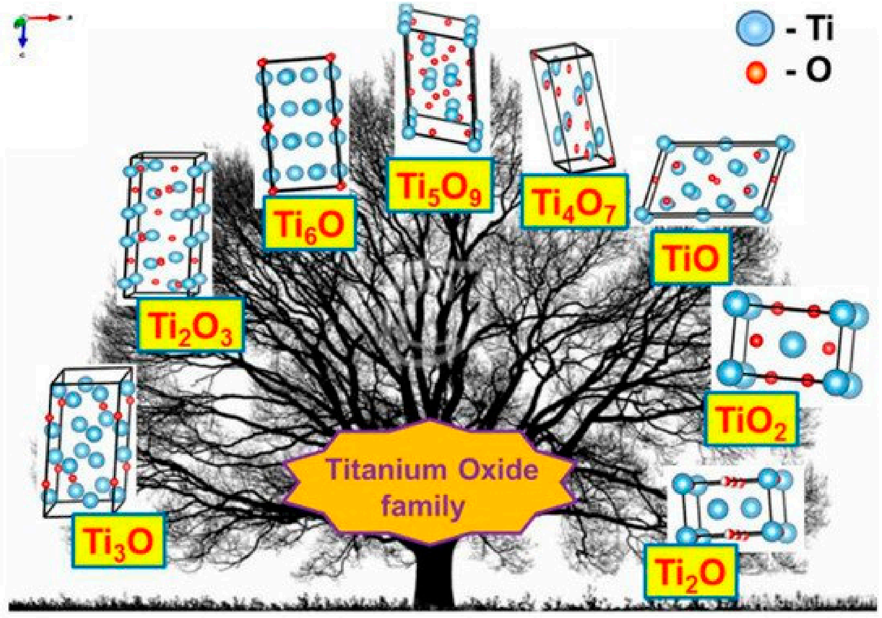

Figure 1. Crystal structures of various titanium oxides. Adapted from [40].

3. Application of Stoichiometric TiO_2 in the Design of Gas and VOC Sensors

Gas and VOC sensors based on TiO_2 are cheap, easily developed. In these sensors rather basic analytical signal registration and assessment methods have been applied for the gas- and VOC-detection procedures. Some TiO_2-based sensors have rather good sensitivity towards various gaseous materials, which due to their different sensing mechanisms are divided into two major types: (i) reductive gaseous materials—H_2S, H_2, CO, NH_3, CH_3OH, C_2H_5OH, some other gasses and VOCs, (ii) oxidative gases—O_2, NO_2 and CO_2 [20,41,42]. It should be noted that resistivity- or current-based responses of TiO_2-sensors towards reductive or oxidative gaseous materials are opposite and, due to rather low selectivity of sensing layers' analysis of gas and VOC mixtures, is still very complicated. Among many different options to measure analytical signal by semiconductor-based gas and VOC sensors, one of the simplest methods is to measure electrical resistivity of the layer. Here, it should be noted that in order to increase reliability of gas and VOC sensors in the analysis of gaseous compounds mixtures, in addition to basic resistivity measurements, it is reasonable to add some additional physicochemical methods, such as an evaluation of photoluminescence signals [1,2,7], which can be applied due to remarkable optical properties of a TiO_2 semiconductor [43]. It is worth noting that various TiO_2–based structures can be designed and enhanced by laser pulses, which improve the photocatalytic and photovoltaic performance of designed nano-structures [44].

4. Development of Heterostructures Based on TiO_2 'Hybridized' with Other Semiconductors and Application of Such Structures for the Design of Gas and VOC Sensors

Heterostructures based on TiO_2 are rather often applied in the design of gas and VOC sensors. Among them, many different TiO_2-based heterostructures were investigated: (i) V_2O_5/TiO_2 for chemi-resistive ozone sensors [45], TiO_2/perovskite heterojunctions for CO gas [46], (ii) TiO_2/(graphene-carbon)-based toluene VOC sensor operating at room temperature [47], (iii) TiO_2/SnO_2 for CO and NO_2 [48,49], (iv) TiO_{2-x}/TiO_2-structure-based 'self-heated' sensor for various reducing gases and VOCs [1]. Improved gas-sensing performance of TiO_2 by graphene oxide (GO) was demonstrated by Lee et al. [50] (Figure 2a,b), this effect was achieved by UV radiation. The authors claimed that n-n junction had been formed and proposed the band diagram of the GO/TiO_2, which represent an energetic levels at the hetero-junction. The authors also stated that in such a hetero-junction, the work function of GO was around 4.7 eV [51], which is higher than 4.4 eV that is more usual for GO [52]. An accumulation and depletion layers were formed in this heterostructure [53] (Figure 2b), where, due to the establishment of the Schottky barrier, the depletion layer of TiO_2 became thicker, and for this reason, the electron number in GO interface increased. The main influence to the change of electrical resistance of this TiO_2/GO structure was induced by the interaction of adsorbed VOC-molecules on oxygen-based GO functional groups. Moreover, negatively charged adsorbed oxygen supports the catalytic activity of TiO_2 by lowering the activation energy [54]. TiO_2 contributed to this heterostructure by its increased gas-adsorption sites and prevention of GO from agglomeration [55,56]. Due to above-mentioned properties, such a structure is sensitive to many reducing gasses, including ammonia gas. However, the active sites of GO were extremely sensitive to moisture, which increased resistance by the interaction of oxygen-based functional groups, such as hydroxyl, carboxylic and carboxyl [57]. This problem was solved by applying UV irradiation, which enabled the increase of both (i) the depletion layer of TiO_2 and (ii) the accumulation layer of GO (Figure 2c). Therefore, electrons were attracted to GO, where there are reduced oxygen-based groups, and in this way, moisture was removed [58]. The reduced GO was formed, with TiO_2, a p-n junction, which had a decreased junction width at the interface (Figure 2d). Moreover, photolysis of TiO_2 led to the injection of electrons into GO, which prevented the recombination of electron-hole pairs [59]. Moreover, the amount of adsorbed oxygen decreased, which also reduced adsorption of water [60]. In one reference [51] it is reported that the number of oxygen-based GO groups was partly restored by photocatalytic action of TiO_2, and these groups were suitable for the adsorption of reducing VOCs and remained sensitive for over the month.

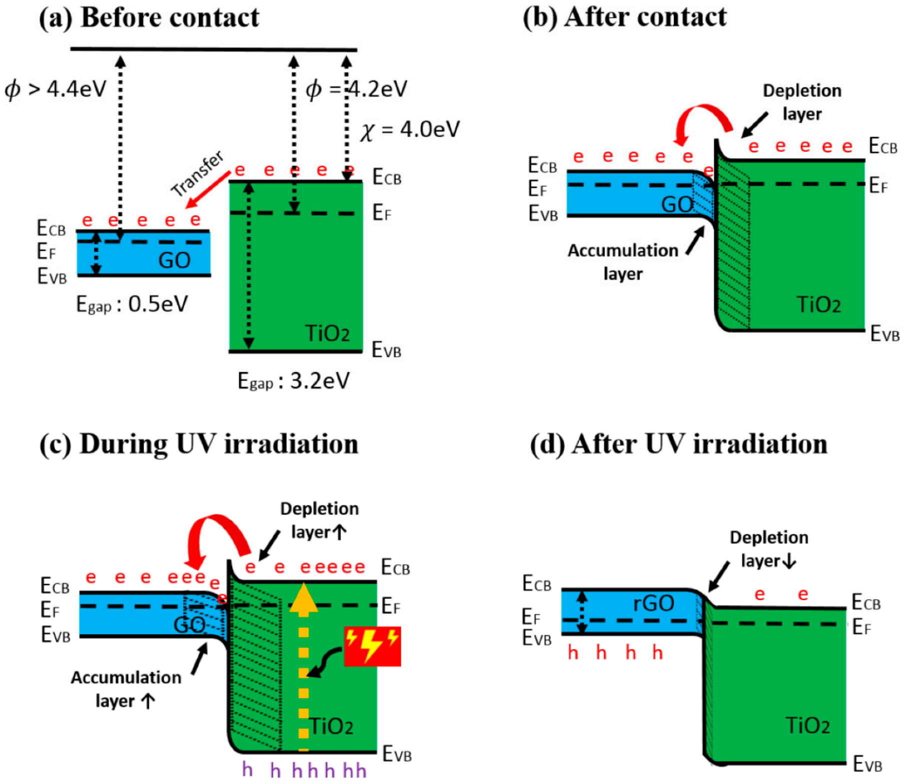

Figure 2. Band diagram of GO/TiO_2 composite (**a**) before contact, (**b**) after contact, (**c**) during UV irradiation, and (**d**) after UV irradiation. (e: electron, h: hole), adapted from [51].

TiO_2/SnO_2-based heterostructures also seem very attractive, due to the peculiarities of the energetic layers of molecular orbitals in TiO_2, the depletion of electrons is observed when it makes contact with SnO_2 [49]. Grains of some semiconductors and the most commonly used quantum dots, which are applied in forming the gas- and/or VOC-sensitive layer, are in the range of the Exciton Bohr radius; therefore, they have suitable physicochemical characteristics for the development of various gas and VOC sensors [16]. Therefore, advanced sensing properties can be established by small-grain-based structures [17]. SnO_2 is characterized by high charge-carrier mobility, which is critically important for the resistivity measurement-based gas and VOC sensors [50,61]. In addition, SnO_2 is chemically stabile, cheap and forms gas- and VOC-sensing layers, therefore, even in pristine form it is used in various gas and VOC sensors [62]. However, gas- and VOC-sensing temperatures of pristine forms of TiO_2 and SnO_2 are rather high, e.g., for pristine SnO_2 QDs, it is 225 °C [16], but for some SnO_2-based core-shell structures (e.g., Au/SnO_2 [63]), these temperatures can be decreased down to 25–80 °C, which makes such structures attractive for real applications because enables to save considerable amount of energy. Therefore, there are some expectations that the formation of SnO_2 and TiO_2-based heterostructures will reduce the working temperature of gas and VOC sensors. In the formation of TiO_2/SnO_2 heterostructures dedicated for gas and VOC sensors, a variety of different nano-structures were developed: SnO_2-coated TiO_2 nanobelts [64], core-shell TiO_2/SnO_2 nanofibers [65], TiO_2-doped SnO_2 thick films [66], thin films based on layered SnO_2/TiO_2 structures [67] and SnO_2 nanoparticles covered by TiO_2 nanofibers [49]; SnO_2 QDs deposited a thin layer of TiO_2 [68]. In the previously mentioned research, both pristine and modified SnO_2 QDs were tested in gas and VOC sensors operating in two different modes: (i) at external heating (ii) and at ‘self-heating’ mode, while applying voltages in the range of 1–20 V. Optimal voltage was 20 V and these sensors were sensitive towards NO_2 and CO. The atomic layer deposition (ALD) method was applied to form TiO_2-based layers of precise thickness and the authors showed that the selectivity towards both gases and VOCs can tuned by the variation of TiO_2 layer thickness, the best performance towards CO was yielded when the thickness of TiO_2 layer was of 30 nm. Moreover, anodic one-dimensional TiO_2 nanotube provided a large surface area and unidirectional electron transport pathway as a platform for accommodation of thin SnO_2 coating, which was sensitive towards NO_2 [69].

Such a finding opens an avenue to tuning the selectivity of sensors based on TiO_2 layer-modified QDs by rather simple ‘morphology engineering’ procedures.

5. Strategies to Reduce Energy Consumption in Gas and VOC Sensors

One strategy to overcome high energy consumption is based on the reduction of the sensing element dimension, another one is based on the application of ‘low temperature’ sensors, which are operating at the temperature of environment where target gases and VOCs are determined, while one additional recently emerging strategy relies on the possibility to apply so called ‘self-heating’ mode in some gas and VOC sensors [1,10]. When the sensing layer has relatively low resistance, if sufficient voltage is applied to the sensing layer and the continuous transfer of charges along this layer is induced by this voltage, then some kinetic energy of these moving charges is converted into the heat due to interaction with various structural elements of the layer. Therefore, during this process, generated heat can be exploited for the increase of sensing layer temperature. ‘Self-heating’ is beneficial in the application of TiO_{2-x}/TiO_2-based structures, because only at a temperature range of 72–180 °C sufficient sensitivity of TiO_{2-x}/TiO_2-based heterostructure towards reducing gases and VOCs has been observed. Such a ‘self-heating’ strategy reduces power consumption, increases the sensitivity of sensor and minimizes the adsorption of water vapour, which is mostly present as a moisture in the environment of interest, and at low temperatures may significantly decrease the sensitivity and selectivity of sensors towards gases and VOCs. Despite of this fact, some researchers are searching for gas- and VOC-sensing materials, which are sensitive towards gases and VOCs at low temperatures [70].

Stoichiometric TiO_2-based structures have rather high band-gap and, for this reason, they are not well conducting; therefore, it is not always easy to measure the electrical resistance of such layers and even elevation of temperature also does not always sufficiently increase the conductivity up to the suitable conductivity region. ‘Self-heating’ is also not possible if conductivity is low, because in order to get sufficient power, which will heat up the sensor until it reaches a suitable temperature, very high voltages should be applied to the TiO_2-based structures.

Due to the suitable combination of chemical and semiconducting properties, TiO_2 has catalytic activity and even photocatalytic activity, both of which can be expressed by the ‘water splitting ability’ or ‘oxidational activity’; these phenomena significantly strengthen when the sensing TiO_2 structure is irradiated by UV light [44,71]. It was demonstrated that the pulsed laser modification can be successfully employed as a large-scale method to enhance the electronic properties of TiO_2 nanotubes and such a structure can contribute to the improved photocatalytic or photovoltaic performance of these TiO_2 nanotubes [72]. Therefore, the additional application of catalytic activity in TiO_2-based gas and VOC sensors is foreseen; however, it is still rarely exploited, due to significant complexity in operation of such structures. TiO_2 has been used as a sensing material in room-temperature sensors for formaldehyde [72,73], ozone [45], O_2 [68], CO [46], C_7H_8 [47], ethanol [65,67,74], H_2 [75,76], and some other gases and VOCs [77].

However, at room temperature (25 °C), the operating sensors are sensitive towards humidity, which is present in the atmosphere. It should be noted that the analytical signals towards humidity and target-gases or VOCs can be very different, e.g., in the presence of humidity (water), conductivity of sensing layer increases, while the presence of the VOC conductivity of the sensing layer has decreased. Such a difference is observed due to different conductance mechanisms realized in the presence of water and the VOCs evaluated here. Water and VOCs adsorbed on the surface of the heterostructure tends to fill the 'gaps' between the TiO_{2-x} and/or TiO_2 grains and in such a way that it increases the conductivity of heterostructures, while the VOCs mostly have significantly lower conductivity compared with gas molecules that are replaced. In order to decrease sensitivity towards humidity, in most cases, the temperature of the sensing layer should be elevated over a room temperature, because the humidity at higher temperatures does not condense well on the sensing structure. A very interesting UV irradiation-based approach to reduce the influence of humidity was demonstrated by Lee et al. [51] and it is discussed in previous chapter. The differing sensitivity towards various gases and VOCs at different temperatures enables the design of sensor-arrays, consisting of similar TiO_{2-x}/TiO_2-based heterostructures, where the individual sensor will operate at the most reliable temperatures, and hence will provide individual signals towards the same mixture of gasses and VOCs [1]. The 'finger print' of analytical signals generated by the array can be assessed by ANOVA-based approaches and concentrations of individual gases can be decoded.

6. Sensing Mechanism of Some TiO_2-Based Heterostructures

The sensing mechanism of TiO_2-sensors is rather complex and it is based on superposition of several processes, such as: (i) target-gas or -VOC adsorption to TiO_2-surface and (ii) desorption of pre-adsorbed gas or VOC from TiO_2-surface. These adsorption/desorption processes depend on the nature of gases and lead to the formation of chemical bounds between adsorbed gas, and then the enrichment/depletion of TiO_2 upper layer by electrons, which are capable of being involved in the charge transfer process and, in such a way, are changing electrical conductivity of TiO_2-based layer. The conductivity of TiO_2-layer is based on two main variations: intrinsic conductivity of TiO_2-grains and the transfer of charge through the boundaries between separated grains. Therefore, both the (i) ratio of grain surface/volume and (ii) the number of such boundaries are very important for the development of the resistivity measurement-based analytical signal. The mechanism of conductance variation in the presence and absence of target gases (e.g., CO) has been discussed in detail by several research groups [78,79] (Figure 3.). The electrostatic interaction between the particular parts of the target analyte and TiO_2 surface, as well as with the surface of other similarly behaving semiconductors (e.g., WO_3 [2,7]), also play a significant role in the development of both (i) changes of resistivity [1,2] and (ii) variations of photoluminescence spectra [7,25], which can both be applied for the assessment of the analytical signal [1]. The 'Debay radius/length' and the size of grains and are the factors that are significantly affecting charge-transfer efficiency in TiO_2- and TiO_{2-x}-based layers. The TiO_{2-x}/TiO_2-based heterostructure was a highly porous and contained embedded 'nano-plates' and 'nano-sponges', which enhanced significantly ratio between surface area and volume. Such advanced surface-formations are very useful, because a significantly larger area is available for the target gas or VOC absorption and, in this way, the sensitivity of the sensing layer is enhanced. The above-mentioned factors should be controlled during the development of gas and/or VOC sensors based on TiO_2 nanostructured layers [42,80–84].

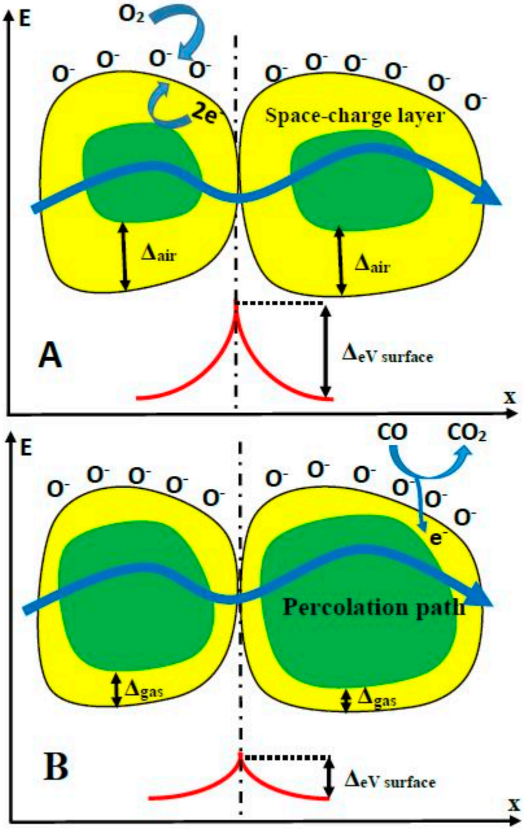

Figure 3. Structural and band models of conductive mechanism upon exposure to CO gas. (**A)** in the absence of CO, (**B)** in the presence of CO.

Sorption/desorption of gaseous materials on/from TiO_2-surface is also a rather complex process and is mainly based on electrostatic and Van der Waals interactions (sometimes called 'physical-adsorption/desorption'), without the formation/braking of chemical bounds and 'chemisorption', which is based on stronger chemical bound formation [85]. The physical sorption is mainly based on electrostatic and Van der Waals interactions between the adsorbed gas or VOC molecules and the TiO_2 surface. Gases (e.g.,: oxygen), which are present in the environment before the appearance of target gasses, play a critical role in the sensing mechanism, because even before the measurement, they are pre-adsorbed on the surface of the semiconducting layer and, therefore, they affect the initial conductivity of the semiconducting layer. Later, during the course of measurement, these gas molecules are replaced by target (analyte) gas molecules and/or by some interfering gas molecules, when these are present in environment, which is under investigation. In both cases, the adsorbed/desorbed molecules are increasing/decreasing the electrical conductivity and photoluminescence efficiency and some other spectral properties of the TiO_2-based layer, dependently on their abilities to donate/accept electrons to TiO_2-based structures and/or electrostatically interact with defect sites, which in the TiO_2 structure, are responsible for the charge transfer and emission of photoluminescence photons [25]. Both these changes can be interpreted as analytical signals. However, bare TiO_2-based gas and VOC sensors have rather high electrical resistance and low dynamic range, which determine rather low sensitivity and selectivity. Therefore, heterostructures based on TiO_2 and other metal oxides, carbides and other materials have been designed [82,83,86–89]. Conducting polymers (such as polypyrrole (Ppy) and polyaniline (PANI)) can be applied in the formation and modification of TiO_2-based heterostructures sensitive to gasses. The TiO_2/Ppy-based sensing heterostructures are able to operate at rather low temperatures. The TiO_2/Ppy-based sensor is suitable for the detection of gaseous NH_3 [90,91] and the main LPG components (propane and butane) [92]. The TiO_2/PANI-based sensors for the determination of NH_3 has been reported [92–95]. The advanced sensitivity of TiO_2/Ppy and TiO_2/PANI-based sensors is based on the establishment of n/p-junction at TiO_2/Ppy interphase.

7. Recent Achievements and Perspectives in the Application of Non-Stoichiometric Titanium Oxides for Gas and VOC Sensor Design

The conductivity of TiO_{2-x} is considerably higher than that of stoichiometric TiO_2. Especially well this effect is observed for Ti_nO_{2n-1} when ‘n’ is between 4 and 10, because at this stoichiometry, Magnéli phases can be formed rather easily [96]. These phases possess metallic conductivity, super-conductivity and some other valuable properties [97,98], which can be applied in the design of gas and VOC sensor. It was determined that Magnéli phases are forming in TiO_{2-x}-based layers [99] planes based on Ti_nO_{2n-1} moieties, which penetrate through a matrix of TiO_2, and along this shear-plane, rather good conducting zones with electron-transfer-based conductivity are observed [98]. Even the presence of not-real members of Magnéli phases (Ti_2O_3 and/or Ti_3O_5) significantly increases the conductivity of titanium oxide-based heterostructures [1,35]. Such conductivity variations are well exploited in the memristor-type logical elements, where the electrical resistivity of TiO_2 is increased and/or decreased by the reduction and/or oxidation of TiO_2-based structure when the corresponding potentials are applied [100].

The Ti^{3+}-containing TiO_{2-x}/TiO_2-based heterostructure possess some ‘oxygen vacancies’ that are responsible for the electron mobility in this n-type semiconducting structure [101]. In our earlier research, we predicted that such ‘oxygen vacancies’ provide increased sensitivity towards some reducing and oxidizing gases and VOCs [1]. TiO_2-based structures can be reduced and form non-stoichiometric titanium oxides (TiO_{2-x}) and even Ti_nO_{2n-1}-based Magnéli phases [97]. In the TiO_{2-x} structure characterized by low ‘x’ value, which varies in the range of $0 < x < 0.10$, ‘point defects’ dominate in the crystal structure, which possess great number of ‘oxygen vacancies’ and interstitials based on Ti^{3+} and Ti^{4+} [102]. The number of defects increases together with the increased ‘oxygen deficiency’ rate. In some research, it is reported that, in Magnéli phases with an ‘x’ value of $0.10 < x < 0.34$, crystallographic shear planes and planar defects are extended [99,103]. Magnéli phase-based titanium oxide structures conduct well and are chemically stabile; therefore, they have found many application areas in the development of fuel cells, batteries and waste water decontamination [104–106]. The same advantageous properties are suitable for the development of gas and VOC sensors. Hence, the presence of TiO_{2-x}/TiO_2-based heterostructures in TiO_2-based sensors can improve the sensitivity of semiconducting layer, due to the advanced conductivity.

The design and technical procedures applied during the creation of TiO_2-based sensors at high extent determines sensitivity and selectivity of developed gas and VOC sensors. Non-conducting substrates with formed interdigitated electrodes are mostly used for the deposition of TiO_2- and TiO_n- and TiO_{2-x}-based sensing structures. TiO_2/TiO_{2-x} TiO_{2-x}/TiO_2 heterostructure can be formed by hydrothermal oxidation (in aqueous alkaline solution) of metallic titanium layer, which should be pre-deposited by magnetron sputtering. Therefore, additional strategies for the increase of conductivity should be elaborated, and one of such strategies is the modification of stoichiometric TiO_2-based structures by some non-stoichiometric TiO_2 [1]. TiO_{2-x}/TiO_2-based structures, which, due to the formation of Ti^{3+}, has some Ti_nO_{2n-1} clusters characterized by significantly advanced electrical conductivity, can be formed using many different approaches, e.g., metallic zinc-based reduction [107], plasma treatment [108], laser irradiation [109], high-energy particle bombardment [110] and thermo-chemical treatment [111]. The growing of large Ti_3O_5 crystals is still very challenging due to polymorphism of titanium oxides [35]. XRD diffractograms (Figure 4) of designed TiO_{2-x}/TiO_2-based heterostructures, represents well some dispersion of Ti-based oxides [1], which form the TiO_{2-x}/TiO_2-structure, but the other research [112] confirms the broad 'XRD peak-reach area' between 27° and 37° in the XRD-diffractogram [1] is assigned to Ti_3O_5, Ti_4O_7 and/or Ti_8O_{15}, which reveals the formation of the Magnéli phases within the TiO_{2-x}/TiO_2-based heterostructure. Meanwhile, the XRD peak between 34° and 37° reveals the presence of γ-Ti_3O_5, similar peaks were present in XRD-PDF file '00-040-0806 for γ-Ti_3O_5' and by some other researchers [35], where the γ-Ti_3O_5 was formed by pulsed laser deposition. Low-temperature superconductivity was reported for both Ti_4O_7 and γ-Ti_3O_5 layers [35]; moreover, this research reports rather broad peaks in XRD-difractograms of γ-Ti_3O_5 and of Ti_4O_7 at 36–38° and at 42–43°, respectively. XRD peaks and some other shape-like-features in the same area of XRD-difractograms at very similar signal to noise ratio were also registered in the research, which is dedicated for sensing application of TiO_{2-x}/TiO_2-based heterostructures [1]. It should be noted that here commented XRD-diffractograms of TiO_{2-x}-based layers [1,35,113] despite of the here-mentioned very distinct similarities in all XR-difractograms have also some peculiarities, which appeared due to the different preparation procedures of TiO_{2-x}-based layers during each of the here-mentioned research. This fact reveals that there is a lot of space to change/vary the intrinsic morphology and composition of TiO_{2-x}/TiO_2-based heterostructures and to tune selectivity a sensitivity of such heterostructures by the establishment of different TiO_{2-x}/TiO_2-stoichiometry that is achieved by different annealing temperatures and/or durations [1].

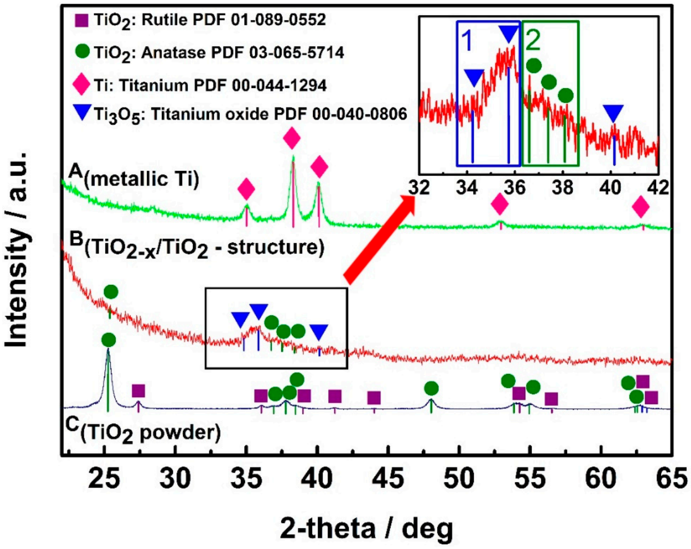

Figure 4. XRD patterns of: $\mathbf{A}_{\mathbf{(metallic\ Ti)}}$—metallic Ti layer of 100 nm thickness, which was formed by magnetron sputtering; $\mathbf{B}_{\mathbf{(TiO2-x/TiO2\text{-}structure)}}$—$TiO_{2-x}$/$TiO_2$(400 °C)-based heterostructure, which was formed from above mentioned metallic 100 nm thick Ti layer; $\mathbf{C}_{\mathbf{(TiO2\ powder)}}$—$TiO_2$-powder, which was used as 'control sample' and by supplier (Sigma-Aldrich) was declared as 99.3% TiO_2 in anatase phase. Figure adapted from [1].

It should be noted that a significant part of the here-covered research on Magnéli phases has been based on the evaluation of powders and little research was performed on other structures, such as fibres [101] or planar structures [1]. In our research, we formed TiO_n-based 'Magnéli phase like structures' using the hydrothermal oxidation of thin metallic layer of titanium sputtered by magnetron deposited [1]. Differently from above-mentioned research, in some particular cases, the ratio of non-stoichiometric titanium oxides vs. stoichiometric titanium oxides in TiO_{2-x}/TiO_2-based heterostructures and/or in TiO_2-based layers can be increased by the treatment based on heating at a high temperature in the presence of reducing gasses and VOCs [113]. Some studies were dedicated for the investigations of transition between metal and insulator states of Ti_3O_5 that were performed: (i) applying visible-light pulses that have induced transition between β and λ forms of Ti_3O_5 [33], (ii) thermal treatment induces transition between α and β forms at 450 K [30] and between δ and γ at 240 K [31–34]. The transition between metal and insulator states at 350 K was observed [35]. Various research illustrates that temperature range between 240 and 450 K is important for the phase changes of Ti_3O_5 and is important for the tuning of titanium oxide layer conductivity and the adaptation of this layer for the determination of gaseous compounds. Hence, TiO_2 can be turned into Ti_nO_{2n-1} by proper doping, reduction and/or partial oxidation of metallic titanium [1] and later particular temperature-based treatment enables the establishment of the optimal TiO_{2-x}/TiO_2-based heterostructures. Therefore, such structures after some further adjustments can be applied in the design of sensors, which will have different levels of sensitivity and selectivity. Therefore, such sensors with different levels of selectivity will be suitable for the establishment of sensor arrays. However, despite their advantageous conductivity, catalytic activity and sensing performance, which are all very suitable for the development of gas and VOC sensors, non-stoichiometric titanium oxides have a significant disadvantage in comparison to stoichiometric ones, which is based on lower stability at the atmospheric condition, due to the continuous oxidation into stoichiometric TiO_2. Moreover, the selectivity of all the above-mentioned sensors is still rather low. Therefore, significantly better understanding of the formed structures and the correlation of the here-mentioned procedures with the sensing properties of the formed semiconducting TiO_{2-x}/TiO_2-based heterostructures, which will meet all the specific requirements of the particular applications, is still required.

8. Analytical Signal Registration Protocols

The selection of a suitable method for the registration of the analytical signal is an important issue in the design of gas and VOC sensors; therefore, for this purpose, various methods can be applied: most of them are based on galvanostatic, potentiostatic and variety of potentiodynamic measurements. Some of these electrical signal registration methods can, at the same time, be useful for the 'self-heating' of sensing structure and/or, if well-adjusted, are suitable for the increase of sensitivity and selectivity of sensors. Electrical conductivity measurements are the most frequently applied for the determination of the analytical signal by sensors based on all types of stoichiometric and non-stoichiometric titanium oxides [1,3,4,6,9,12,14–16,23,24,41,67,74,77,81,86,90,91,94]. The conductivity of TiO_{2-x}/TiO_2-based gas- and/or VOC-sensitive structure is rather high in comparison to that of stoichiometric TiO_2, therefore, current passing through TiO_{2-x}/TiO_2-based structure heats-up sensing layer, which is very useful for the achievement of different selectivity at different temperatures, while the analytical signal can be based on changes of current registered at the same constant potential, which is applied for the heating of system and/or the evaluation of photoluminescence spectra [1]. However, it should be noted that stoichiometric titanium oxide-based sensors are characterized by rather low electrical conductivity (~10^{-10} S/m); therefore, the significant elevation of temperature up to 200–400 °C is required to increase the conductivity, in order to reach optimal sensing conditions. This requirement is typical for most of the sensors based on stoichiometric TiO_2-based semiconducting materials; therefore, in most of the stoichiometric TiO_2-based sensors, significantly higher temperatures should be applied in comparison to optimal temperatures for nonstoichiometric TiO_2-based sensors [1]. Operation at higher temperatures increases the energy consumption of sensor, which becomes very actual if the sensors are operating at autonomous powering.

Despite of its very good sensitivity, the selectivity of all types of titanium oxide based sensors is still rather poor. Therefore, additional signal registration methods are very beneficial, especially if they are applied simultaneously with electrical resistance measurements. The application of photoluminescence detection-based analytical methods in the development of TiO_2- and TiO_{2-x}/TiO_2-based gas and VOC sensors can significantly advance analytical information, which can be gathered by electrochemical methods. Most of the stoichiometric and nonstoichiometric titanium oxide structures are characterized by photoluminescence spectra with a maximum in the range between λ = 415–500 nm. Differences of photoluminescence spectra of titanium oxide structures depends on annealing conditions (manly on the duration of heating and temperature changing protocol), both of which are very important during the formation of the structures. Dependently of these conditions, different phases of stoichiometric and/or nonstoichiometric titanium oxide are formed, e.g., when TiO_{2-x}/TiO_2-based structure is formed using annealing at 400 °C, then significantly more intense photoluminescence signal (higher about 10 times) has been created in comparison to that determined for the TiO_{2-x}/TiO_2-based heterostructure formed using annealing at 600 °C, and if TiO_{2-x}/TiO_2-based structure is formed by annealing at 800 °C the photoluminescence of such a structure is very weak—over hundred times lower than that of TiO_{2-x}/TiO_2 -based heterostructure prepared at 400 °C [1]. Therefore, during the design of stoichiometric and nonstoichiometric titanium oxide-based structures for optoelectronics-based sensors preparation conditions should be followed and photoluminescence and sensing properties of these structures can be rather easily tuned by the adapting proper annealing conditions.

The increase of heating voltage, which is simultaneously used for the measurement of conductivity of the TiO_{2-x}/TiO_2-based heterostructure, gradually decreases photoluminescence peak intensity [1], due to the temperature dependent reduction of number of photoluminescence emitting centers at higher temperatures and temperature-based photoluminescence quenching [106,114,115]. In addition, the shift of peak maximum (λ_{max}), which is usually determined as a maximum of Gauss function, towards shorter wavelengths was observed [1]; this fact reveals that photoluminescence emitting centers, which are located close to the surface of TiO_{2-x}/TiO_2-based heterostructure are electrostatically affected by adsorbed gaseous material [25]. The evaluation of $TiO_{2(anatase)}$ photoluminescence was evaluated in some research and it was determined that photoluminescence is excited at shallow trap levels that have energy levels in the range of 0.41–0.64 eV, which is below the conduction band of this oxide [116]. Narrow photoluminescence emission bands were determined for $TiO_{2(anatase)}$ powder; they were emitted by self-trapped excitons that are appearing in crystal structure of $TiO_{2(anatase)}$, which is based on octahedral sheets of 'TiO_6' structural elements [19,117]. Therefore, electrical resistivity measurements can be extended by the determination of photoluminescence signal, which can also be applied for target gas and VOC determination by titanium oxide-based sensors. The evaluation of photoluminescence-decay kinetics can be applied for the determination of self-trapped exciton-based origin of photoluminescence, which, among titanium oxides, is the most characteristic for crystalline $TiO_{2(anatase)}$ [118], and during the formation of sensing layer, it can be exploited as a confirmation of $TiO_{2(anatase)}$ presence in the composition of sensing layer [1] and for the determination of analytical signal. In addition to registration of conventional photoluminescence signal, the evaluation of photoluminescence-decay kinetics can provide new options for the evaluation of quality of sensing layer [1,7] and the determination of analytical signal by sensors based on stoichiometric and non-stoichiometric titanium oxides.

It should be noted that the selectivity of gas and VOC sensors still remains not very high, even if very good sensitivity has been achieved in a lot of research [1,3,4,6,9,12,14–16,23,24,41,67,74,77,81,86,90,91,94]. Therefore, approaches suitable for the evaluation of gas and/or VOC mixtures should be elaborated. In this context, it is very promising that the variation of sensing layer temperature significantly changes both the selectivity and sensitivity of gas and/or VOC sensors, which was well demonstrated by the gas- and VOC sensor based on TiO_{2-x}/TiO_2-layer [1], and this effect can be applied in the design of sensor arrays, where sensors with different selectivity and sensitivity can provide very different responses in the same gas and VOC mixture and these 'finger prints' registered by such a sensor array can be assessed and decoded by applying the corresponding methods of the multi-variation mathematical analysis.

9. Conclusions and Future Developments

Despite the significant progress in the development of stoichiometric TiO_2-based heterostructures, practical application in real sensing devices is still limited. However, recently, some research has demonstrated that hydro-thermal oxidation of metallic titanium or reduction of TiO_2 layers leads to the formation of heterostructures based on TiO_{2-x}/TiO_2 and/or Ti_nO_{2n-1} heterostructures. Recent developments turn to the prediction that analytical characteristics of these sensing layers can be tuned by the adjustment of $TiO_{2-x}/TiO_2/Ti_nO_{2n-1}$ ratio in formed heterostructures. Formed structures can be integrated into gas and VOC sensors as the 'self-heated' sensing layer. In the sensor based on this heterostructures, the variation of electrical current, which is flowing through TiO_{2-x}/TiO2-based heterostructure, at fixed potential, is registered. 'Self-heating' is beneficial for the application of TiO_{2-x}/TiO_2-based structures, because only in the temperature range of 72–180 °C sufficient sensitivity of TiO_{2-x}/TiO_2-based heterostructure towards reducing gases and VOCs has been observed. We expect that titanium oxide-based heterostructures, in the future, will find more advanced applications in gas and VOC sensors. However, a more advanced and comprehensive understanding of how to control the transition between the differently conducting titanium oxide-based layers is still required, in order to achieve desirable semiconducting properties, which are the most optimal for applications in sensors for the determination of gases and VOCs. Therefore, by the elaboration of the successful sensing layer formation and signal registration protocols, the advantageous properties of nonstoichiometric titanium oxide (TiO_{2-x} and/or Ti_nO_{2n-1})-based structures can be well applied in the design of gas and VOCs sensors.

Author Contributions: S.R. performed literature research, analysis, and drafted the paper. A.R. initiated and supervised the work and provided insights. All authors have read and agreed to the published version of the manuscript.

Funding: This research was partially supported by Lithuanian Research Council Project No.: 09.3.3-ESFA V-711-01-00.

Acknowledgments: This research was supported by Lithuanian Research Council project No P-LU-18-53.

Conflicts of Interest: The authors declare no conflict of interest.

References

1. Ramanavicius, S.; Tereshchenko, A.; Karpicz, R.; Ratautaite, V.; Bubniene, U.; Maneikis, A.; Jagminas, A.; Ramanavicius, A. TiO_{2-x}/TiO_2-structure based 'self-heated' sensor for the determination of some reducing gases. *Sensors* **2020**, *20*, 74. [CrossRef] [PubMed]
2. Ramanavičius, S.; Petrulevičienė, M.; Juodkazytė, J.; Grigucevičienė, A.; Ramanavičius, A. Selectivity of tungsten oxide synthesized by sol-gel method towards some volatile organic compounds and gaseous materials in a broad range of temperatures. *Materials* **2020**, *13*, 523. [CrossRef] [PubMed]
3. Mirzaei, A.; Kim, S.S.; Kim, H.W. Resistance-based H_2S gas sensors using metal oxide nanostructures: A review of recent advances. *J. Hazard. Mater.* **2018**, *357*, 314–331. [CrossRef] [PubMed]
4. Mirzaei, A.; Leonardi, S.G.; Neri, G. Detection of hazardous volatile organic compounds (VOCs) by metal oxide nanostructures-based gas sensors: A review. *Ceram. Int.* **2016**, *42*, 15119–15141. [CrossRef]
5. Mirzaei, A.; Kim, J.-H.; Kim, H.W.; Kim, S.S. How shell thickness can affect the gas sensing properties of nanostructure materials: Survey of literature. *Sens. Actuators B Chem.* **2018**, *258*, 270–294. [CrossRef]
6. Mirzaei, A.; Kim, J.-H.; Kim, H.W.; Kim, S.S. Resistive-based gas sensors for detection of benzene, toluene and xylene (BTX) gases: A review. *J. Mater. Chem. C* **2018**, *6*, 4342–4370. [CrossRef]
7. Petruleviciene, M.; Juodkazyte, J.; Parvin, M.; Tereshchenko, A.; Ramanavicius, S.; Karpicz, R.; Samukaite-Bubniene, U.; Ramanavicius, A. Tuning of photo-luminescence properties of WO_3-based layers by the adjustment of layer formation conditions. *Materials* **2020**, *13*, 2814. [CrossRef]
8. Wang, Y.; Wu, T.; Zhou, Y.; Meng, C.; Zhu, W.; Liu, L. TiO_2-Based Nanoheterostructures for Promoting Gas Sensitivity Performance: Designs, Developments, and Prospects. *Sensors* **2017**, *17*, 1971. [CrossRef]
9. Bai, J.; Zhou, B. Titanium dioxide nanomaterials for sensor applications. *Chem. Rev.* **2014**, *114*, 10131–10176. [CrossRef]
10. Prades, J.D.; Jimenez-Diaz, R.; Hernandez-Ramirez, F.; Barth, S.; Cirera, A.; Romano-Rodriguez, A.; Mathur, S.; Morante, J.R. Ultralow power consumption gas sensors based on self-heated individual nanowires. *Appl. Phys. Lett.* **2008**, *93*, 123110. [CrossRef]

11. Smulko, J.M.; Trawka, M.; Granqvist, C.G.; Ionescu, R.; Annanouch, F.; Llobet, E.; Kish, L.B. New approaches for improving selectivity and sensitivity of resistive gas sensors: A review. *Sens. Rev.* **2015**, *35*, 340–347. [CrossRef]
12. Simon, I.; Bârsan, N.; Bauer, M.; Weimar, U. Micromachined metal oxide gas sensors: Opportunities to improve sensor performance. *Sens. Actuators B Chem.* **2001**, *73*, 1–26. [CrossRef]
13. Karnati, P.; Akbar, S.; Morris, P.A. Conduction mechanisms in one dimensional coreshell nanostructures for gas sensing: A review. *Sens. Actuators B Chem.* **2019**, *295*, 127–143. [CrossRef]
14. Kim, J.-H.; Mirzaei, A.; Kim, H.W.; Kim, S.S. Low power-consumption CO gas sensors based on Au-functionalized SnO_2-ZnO core-shell nanowires. *Sens. Actuators B Chem.* **2018**, *267*, 597–607. [CrossRef]
15. Deng, J.; Fu, Q.; Luo, W.; Tong, X.; Xiong, J.; Hu, Y.; Zheng, Z. Enhanced H_2S gas sensing properties of undoped ZnO nanocrystalline films from QDs by low-temperature processing. *Sens. Actuators B Chem.* **2016**, *224*, 153–158. [CrossRef]
16. Sedghi, S.M.; Mortazavi, Y.; Khodadadi, A. Low temperature CO and CH4 dual selective gas sensor using SnO_2 quantum dots prepared by sonochemical method. *Sens. Actuators B Chem.* **2010**, *145*, 7–12. [CrossRef]
17. Mirzaei, A.; Janghorban, K.; Hashemi, B.; Bonavita, A.; Bonyani, M.; Leonardi, S.; Neri, G. Synthesis, characterization and gas sensing properties of Ag@ α-Fe_2O_3 core–shell nanocomposites. *Nanomaterials* **2015**, *5*, 737. [CrossRef]
18. Chen, X.; Mao, S.S. Titanium dioxide nanomaterials: Synthesis, properties, modifications, and applications. *Chem. Rev.* **2007**, *107*, 2891–2959. [CrossRef]
19. Zhang, Y.; Jiang, Z.; Huang, J.; Lim, L.Y.; Li, W.; Deng, J.; Gong, D.; Tang, Y.; Lai, Y.; Chen, Z. Titanate and titania nanostructured materials for environmental and energy applications: A review. *RSC Adv.* **2015**, *5*, 79479–79510. [CrossRef]
20. Linsebigler, A.L.; Lu, G.; Yates, J.T. Photocatalysis on TiO_2 surfaces: Principles, mechanisms, and selected results. *Chem. Rev.* **1995**, *95*, 735–758. [CrossRef]
21. Wang, G.; Wang, J.; An, Y.; Wang, C. Anodization fabrication of 3D TiO2 photonic crystals and their application for chemical sensors. *Superlattices Microstruct.* **2016**, *100*, 290–295. [CrossRef]
22. Si, H.; Pan, N.; Zhang, X.; Liao, J.; Rumyantseva, M.N.; Gaskov, A.M.; Lin, S. A real-time online photoelectrochemical sensor toward chemical oxygen demand determination based on field-effect transistor using an extended gate with 3D-TiO_2 nanotube array. *Sens. Actuators B Chem.* **2019**, *289*, 106–113. [CrossRef]
23. Qiu, J.; Zhang, S.; Zhao, H. Recent applications of TiO_2 nanomaterials in chemical sensing in aqueous media. *Sens. Actuators B Chem.* **2011**, *160*, 875–890. [CrossRef]
24. Maziarz, W.; Kusior, A.; Trenczek-Zajac, A. Nanostructured TiO_2-based gas sensors with enhanced sensitivity to reducing gases. *Beilstein J. Nanotechnol.* **2016**, *7*, 1718–1726. [CrossRef]
25. Tereshchenko, A.; Smyntyna, V.; Ramanavicius, A. Interaction Mechanism between TiO_2 Nanostructures and Bovine Leukemia Virus Proteins in Photoluminescence-based Immunosensors. *RSC Adv.* **2018**, *8*, 37740–37748. [CrossRef]
26. Tereshchenko, A.; Viter, R.; Konup, I.; Ivanitsa, V.; Geveliuk, S.; Ishkov, Y. TiO_2 Optical Sensor for Amino Acid Detection. *Proc. SPIE* **2013**, *9032*, 90320T.
27. Soni, P.; Murty, V.V.S.; Kushwaha, K.K. The effect of Ni^{2+} ions on energy band gap of TiO_2 nanoparticles for solar cell applications. *J. Nanosci. Nanoeng. Appl.* **2018**, *8*, 69–74.
28. Yamazoe, N.; Sakai, G.; Shimanoe, K. Oxide semiconductor gas sensors. *Catal. Surv. Asia* **2003**, *7*, 63–75. [CrossRef]
29. Wunderlich, W.; Oekermann, T.; Miao, L.; Hue, N.T.; Tanemura, S.; Tanemura, M. Electronic properties of Nano-porous TiO_2- and ZnO-thin films- comparison of simulations and experiments. *J. Ceram. Proc. Res.* **2004**, *5*, 343–354.
30. Åsbrink, S.; Magnéli, A. Crystal structure studies on Trititanium Pentoxide, Ti_3O_5. *Acta Cryst.* **1959**, *12*, 575. [CrossRef]
31. Hong, S.-H.; Åsbrink, S. The structure of γ-Ti_3O_5 at 297 K. *Acta. Cryst.* **1982**, *B38*, 2570. [CrossRef]
32. Onoda, M. Phase transitions of Ti_3O_5. *J. Solid State Chem.* **1998**, *136*, 67. [CrossRef]
33. Ohkoshi, S.; Tsunobuchi, Y.; Matsuda, T.; Hashimoto, K.; Namai, A.; Hakoe, F.; Tokoro, H. Synthesis of a metal oxide with a room-temperature photoreversible phase transition. *Nat. Chem.* **2010**, *2*, 539. [CrossRef] [PubMed]

34. Tanaka, K.; Nasu, T.; Miyamoto, Y.; Ozaki, N.; Tanaka, S.; Nagata, T.; Hakoe, F.; Yoshikiyo, M.; Nakagawa, K.; Umeta, Y.; et al. Structural phase transition between γ-Ti_3O_5 and δ-Ti_3O_5 by breaking of one-dimensionally conducting pathway. *Cryst. Growth Des.* **2015**, *15*, 653. [CrossRef]
35. Yoshimatsu, K.; Sakata, O.; Ohtomo, A. Superconductivity in Ti_4O_7 and γ-Ti_3O_5 films. *Sci. Rep.* **2017**, *7*, 12544. [CrossRef]
36. Marezio, M.; Mcwhan, D.B.; Dernier, P.D.; Remeika, J.P. Structural aspects of the metal-insulator transitions in Ti_4O_7. *J. Solid State Chem.* **1973**, *6*, 213. [CrossRef]
37. Lakkis, S.; Schlenker, C.; Chakraverty, B.K.; Buder, R.; Marezio, M. Metal-insulator transition in Ti_4O_7 single crystals: Crystal characterization, specific heat, and electron paramagnetic resonance. *Phys. Rev. B* **1976**, *14*, 1429. [CrossRef]
38. D'Angelo, A.M.; Webster, N.A.S. Evidence of anatase intergrowths formed during slow cooling of reduced ilmenite. *J. Appl. Cryst.* **2018**, *51*, 185–192. [CrossRef]
39. Grey, I.E.; Cranswick, L.M.D.; Li, C.; White, T.J.; Bursill, L.A. New M_3O_5-Anatase Intergrowth Structures Formed during Low-Temperature Oxidation of Anosovite. *J. Solid State Chem.* **2000**, *150*, 128–138. [CrossRef]
40. Jayashree, S.; Ashokkumar, M. Switchable Intrinsic Defect Chemistry of Titania for Catalytic Applications (Review). *Catalysts* **2018**, *8*, 601. [CrossRef]
41. Kimura, M.; Sakai, R.; Sato, S.; Fukawa, T.; Ikehara, T.; Maeda, R.; Mihara, T. Sensing of vaporous organic compounds by TiO_2 porous films covered with polythiophene layers. *Adv. Funct. Mater.* **2012**, *22*, 469–476. [CrossRef]
42. Wang, Y.; Du, G.; Liu, H.; Liu, D.; Qin, S.; Wang, N.; Hu, C.; Tao, X.; Jiao, J.; Wang, J.; et al. Nanostructured sheets of Ti-O nanobelts for gas sensing and antibacterial applications. *Adv. Funct. Mater.* **2008**, *18*, 1131–1137. [CrossRef]
43. Viter, R.; Tereshchenko, A.; Smyntyna, V.; Ogorodniichuk, J.; Starodub, N.; Yakimova, R.; Khranovskyy, V.; Ramanavicius, A. Toward development of optical biosensors based on photoluminescence of TiO_2 nanoparticles for the detection of Salmonella. *Sens. Actuators B Chem.* **2017**, *252*, 95–102. [CrossRef]
44. Haryński, Ł.; Grochowska, K.; Karczewski, J.; Ryl, J.; Siuzdak, K. Scalable Route toward Superior Photoresponse of UV-Laser-Treated TiO2 Nanotubes. *ACS Appl. Mater. Interfaces* **2020**, *12*, 3225–3235. [CrossRef]
45. Avansi Jr, W.; Catto, A.C.; da Silva, L.F.; Fiorido, T.; Bernardini, S.; Mastelaro, V.R.; Aguir, K.; Arenal, R. One-dimensional V_2O_5/TiO_2 heterostructures for chemiresistive ozone sensors. *ACS Appl. Nano Mater.* **2019**, *2*, 4756–4764. [CrossRef]
46. Hsu, K.C.; Fang, T.H.; Hsiao, Y.J.; Wu, P.C. Response and characteristics of TiO_2/perovskite heterojunctions for CO gas sensors. *J. Alloys Compd.* **2019**, *794*, 576–584. [CrossRef]
47. Seekaew, Y.; Wisitsoraat, A.; Phokharatkul, D.; Wongchoosuk, C. Room temperature toluene gas sensor based on TiO_2 nanoparticles decorated 3D graphene-carbon nanotube nanostructures. *Sens. Actuators B Chem.* **2019**, *279*, 69–78. [CrossRef]
48. Chen, K.; Chen, S.; Pi, M.; Zhang, D. SnO_2 nanopaticles/TiO_2 nanofibers heterostructures: In situ fabrication and enhanced gas sensing performance. *Solid State Electron* **2019**, *157*, 42–47. [CrossRef]
49. Yu, Q.; Zhu, J.; Xu, Z.; Huang, X. Facile synthesis of α-Fe_2O_3@ SnO_2 core–shell heterostructure nanotubes for high performance gas sensors. *Sens. Actuators B Chem.* **2015**, *213*, 27–34. [CrossRef]
50. Lee, E.; Lee, D.; Yoon, J.; Yin, Y.; Lee, Y.N.; Uprety, S.; Yoon, Y.S.; Kim, D.-J. Enhanced Gas-Sensing Performance of GO/TiO2 Composite by Photocatalysis. *Sensors* **2018**, *18*, 3334. [CrossRef]
51. Stratakis, E.; Savva, K.; Konios, D.; Petridis, C.; Kymakis, E. Improving the efficiency of organic photovoltaics by tuning the work function of graphene oxide hole transporting layers. *Nanoscale* **2014**, *6*, 6925–6931. [CrossRef] [PubMed]
52. Chen, C.; Cai, W.; Long, M.; Zhou, B.; Wu, Y.; Wu, D.; Feng, Y. Synthesis of visible-light responsive grapheneoxide/TiO2 composites with p/n heterojunction. *ACS Nano* **2010**, *4*, 6425–6432. [CrossRef] [PubMed]
53. Lightcap, I.V.; Kosel, T.H.; Kamat, P.V. Anchoring semiconductor and metal nanoparticles on a two-dimensional catalyst mat. Storing and shuttling electrons with reduced graphene oxide. *Nano Lett.* **2010**, *10*, 577–583. [CrossRef] [PubMed]
54. Ye, Z.; Tai, H.; Xie, T.; Yuan, Z.; Liu, C.; Jiang, Y. Room temperature formaldehyde sensor with enhanced performance based on reduced graphene oxide/titanium dioxide. *Sens. Actuators B Chem.* **2016**, *223*, 149–156. [CrossRef]

55. Ammu, S.; Dua, V.; Agnihotra, S.R.; Surwade, S.P.; Phulgirkar, A.; Patel, S.; Manohar, S.K. Flexible, all-organic chemiresistor for detecting chemically aggressive vapors. *J. Am. Chem. Soc.* **2012**, *134*, 4553–4556. [CrossRef]
56. Lam, K.C.; Huang, B.; Shi, S.-Q. Room-temperature methane gas sensing properties based on in situ reduced graphene oxide incorporated with tin dioxide. *J. Mater. Chem. A* **2017**, *5*, 11131–11142. [CrossRef]
57. Buchsteiner, A.; Lerf, A.; Pieper, J. Water dynamics in graphite oxide investigated with neutron scattering. *J. Phys. Chem. B* **2006**, *110*, 22328–22338. [CrossRef]
58. Phan, D.-T.; Chung, G.-S. Effects of rapid thermal annealing on humidity sensor based on graphene oxide thin films. *Sens. Actuators B Chem.* **2015**, *220*, 1050–1055. [CrossRef]
59. Wang, P.; Zhai, Y.; Wang, D.; Dong, S. Synthesis of reduced graphene oxide-anatase TiO_2 nanocomposite and its improved photo-induced charge transfer properties. *Nanoscale* **2011**, *3*, 1640–1645. [CrossRef]
60. Cui, S.; Wen, Z.; Huang, X.; Chang, J.; Chen, J. Stabilizing MoS2 Nanosheets through SnO_2 Nanocrystal Decoration for High-Performance Gas Sensing in Air. *Small* **2015**, *11*, 2305–2313. [CrossRef]
61. Mirzaei, A.; Janghorban, K.; Hashemi, B.; Neri, G. Metal-core@metal oxide-shell nanomaterials for gas-sensing applications: A review. *J. Nanopart. Res.* **2015**, *17*, 371. [CrossRef]
62. Rieu, M.; Camara, M.; Tournier, G.; Viricelle, J.-P.; Pijolat, C.; De Rooij, N.F.; Briand, D. Fully inkjet printed SnO_2 gas sensor on plastic substrate. *Sens. Actuators B Chem.* **2016**, *236*, 1091–1097. [CrossRef]
63. Chung, F.-C.; Wu, R.-J.; Cheng, F.-C. Fabrication of a Au@ SnO_2 core–shell structure for gaseous formaldehyde sensing at room temperature. *Sens. Actuators B Chem.* **2014**, *90*, 1–7. [CrossRef]
64. Chen, G.; Ji, S.; Li, H.; Kang, X.; Chang, S.; Wang, Y.; Yu, G.; Lu, J.; Claverie, J.; Sang, Y.; et al. High-energy faceted SnO_2-coated TiO_2 nanobelt heterostructure for nearambient temperature-responsive ethanol sensor. *ACS Appl. Mater. Inter.* **2015**, *7*, 24950–24956. [CrossRef] [PubMed]
65. Li, F.; Gao, X.; Wang, R.; Zhang, T.; Lu, G. Study on TiO_2-SnO_2 core-shell heterostructure nanofibers with different work function and its application in gas sensor. *Sens. Actuators B Chem.* **2017**, *248*, 812–819. [CrossRef]
66. Zeng, W.; Liu, T.; Wang, Z. UV light activation of TiO_2-doped SnO_2 thick film for sensing ethanol at room temperature. *Mater. Trans.* **2010**, *51*, 0912140962. [CrossRef]
67. Lee, H.C.; Hwang, W.S. Substrate effects on the oxygen gas sensing properties of SnO_2/TiO_2 thin films. *Appl. Surf. Sci.* **2006**, *253*, 1889–1897. [CrossRef]
68. Leea, J.H.; Mirzaei, A.; Kim, J.H.; Kim, J.Y.; Nasriddinov, A.F.; Rumyantseva, M.N.; Kim, H.W.; Kim, S.S. Gas-sensing behaviors of TiO_2-layer-modified SnO_2 quantum dots in self-heating mode and effects of the TiO_2 layer. *Sens. Actuators B Chem.* **2020**, *310*, 127870. [CrossRef]
69. Ng, S.; Prášek, J.; Zazpe, R.; Pytlíček, Z.; Spotz, Z.; Pereira, J.R.; Michalička, J.; Přikryl, J.; Krbal, M.; Sopha, H.; et al. Atomic Layer Deposition of SnO2-Coated Anodic One-Dimensional TiO_2 Nanotube Layers for Low Concentration NO_2 Sensing. *ACS Appl. Mater. Interfaces* **2020**, *12*, 33386–33396. [CrossRef]
70. Song, Z.; Wei, Z.; Wang, B.; Luo, Z.; Xu, S.; Zhang, W.; Yu, H.; Li, M.; Huang, Z.; Zang, J.; et al. Sensitive room-temperature H_2S gas sensors employing SnO_2 quantum wire/reduced graphene oxide nanocomposites. *Chem. Mater.* **2016**, *28*, 1205–1212. [CrossRef]
71. Lin, J.; Heo, Y.U.; Nattestad, A.; Sun, Z.; Wang, L.; Kim, J.H.; Dou, S.X. 3D hierarchical rutile TiO_2 and metal-free organic sensitizer producing dye-sensitized solar cells 8.6% conversion efficiency. *Sci. Rep.* **2014**, *4*, 5769. [CrossRef] [PubMed]
72. Nasriddinov, A.; Rumyantseva, M.; Marikutsa, A.; Gaskov, A.; Lee, J.-H.; Kim, J.-H.; Kim, S.S.; Kim, H.W. Sub-ppm formaldehyde detection by n-n TiO_2@SnO_2 nanocomposites. *Sensors* **2019**, *19*, 3182. [CrossRef] [PubMed]
73. Li, X.; Li, X.; Wang, J.; Lin, S. Highly sensitive and selective room-temperature formaldehyde sensors using hollow TiO_2 microspheres. *Sens. Actuators B Chem.* **2015**, *219*, 158–163. [CrossRef]
74. Tricoli, A.; Righettoni, M.; Pratsinis, S.E. Minimal cross-sensitivity to humidity during ethanol detection by SnO_2–TiO_2 solid solutions. *Nanotechnology* **2009**, *20*, 315502. [CrossRef]
75. Li, Z.; Yao, Z.; Haidry, A.A.; Plecenik, T.; Xie, L.; Sun, L.; Fatima, Q. Resistive-type hydrogen gas sensor based on TiO_2: A review. *Int. J. Hydrogen Energy* **2018**, *43*, 21114–21132. [CrossRef]
76. Shaposhnik, D.; Pavelko, R.; Llobet, E.; Gispert-Guirado, F.; Vilanova, X. Hydrogen sensors on the basis of SnO_2-TiO_2 systems. *Procedia Eng.* **2011**, *25*, 1133–1136. [CrossRef]

77. Plecenik, T.; Moško, M.; Haidry, A.A.; Ďurina, P.; Truchlý, M.; Grančič, B.; Gregor, M.; Roch, T.; Satrapinskyy, L.; Mošková, A. Fast highly-sensitive room-temperature semiconductor gas sensor based on the nanoscale Pt–TiO_2–Pt sandwich. *Sens. Actuators B Chem.* **2005**, *207*, 351–361. [CrossRef]
78. Wang, C.; Yin, L.; Zhang, L.; Xiang, D.; Gao, R. Metal Oxide Gas Sensors: Sensitivity and Influencing Factors. *Sensors* **2010**, *10*, 2088–2106. [CrossRef]
79. Franke, M.E.; Koplin, T.J.; Simon, U. Metal and Metal Oxide Nanoparticles in Chemiresistors: Does the Nanoscale Matter? *Small* **2006**, *2*, 36–50. [CrossRef]
80. Wang, C.; Yin, L.; Zhang, L.; Qi, Y.; Lun, N.; Liu, N. Large scale synthesis and gas-sensing properties of anatase TiO_2 three-dimensional hierarchical nanostructures. *Langmuir* **2010**, *26*, 12841–12848. [CrossRef]
81. Barreca, D.; Comini, E.; Ferrucci, A.P.; Gasparotto, A.; Maccato, C.; Maragno, C.; Sberveglieri, G.; Tondello, E. First example of ZnO-TiO_2 nanocomposites by chemical vapor deposition: Structure, morphology, composition, and gas sensing performances. *Chem. Mater.* **2007**, *19*, 5642–5649. [CrossRef]
82. Lü, R.; Zhou, W.; Shi, K.; Yang, Y.; Wang, L.; Pan, K.; Tian, C.; Ren, Z.; Fu, H. Alumina decorated TiO_2 nanotubes with ordered mesoporous walls as high sensitivity NOx gas sensors at room temperature. *Nanoscale* **2013**, *5*, 8569–8576. [CrossRef] [PubMed]
83. Li, Z.; Ding, D.; Liu, Q.; Ning, C.; Wang, X. Ni-doped TiO_2 nanotubes for wide-range hydrogen sensing. *Nanoscal. Res. Lett.* **2014**, *9*, 118–126. [CrossRef] [PubMed]
84. Galstyan, V.; Comini, E.; Faglia, G.; Sberveglieri, G. TiO_2 nanotubes: Recent advances in synthesis and gas sensing properties. *Sensors* **2013**, *13*, 14813–14838. [CrossRef]
85. Zakrzewska, K. Gas sensing mechanism of TiO_2-based thin films. *Vacuum* **2004**, *74*, 335–338. [CrossRef]
86. Du, P.; Song, L.; Xiong, J.; Li, N.; Xi, Z.; Wang, L.; Jin, D.; Guo, S.; Yuan, Y. Coaxial electrospun TiO_2/ZnO core–sheath nanofibers film: Novel structure for photoanode of dye-sensitized solar cells. *Electrochim. Acta* **2012**, *78*, 392–397. [CrossRef]
87. Ding, Y.; Wang, Y.; Zhang, L.; Zhang, H.; Li, C.M.; Lei, Y. Preparation of TiO_2-Pt hybrid nanofibers and their application for sensitive hydrazine detection. *Nanoscale* **2011**, *3*, 1149–1157. [CrossRef]
88. Li, Z.; Zhang, H.; Zheng, W.; Wang, W.; Huang, H.; Wang, C.; MacDiarmid, A.G.; Wei, Y. Highly sensitive and stable humidity nanosensors based on LiCl doped TiO_2 electrospun nanofibers. *J. Am. Chem. Soc.* **2008**, *130*, 5036–5037. [CrossRef]
89. Zeng, W.; Liu, T.; Wang, Z. Enhanced gas sensing properties by SnO_2 nanosphere functionalized TiO_2 nanobelts. *J. Mater. Chem.* **2012**, *22*, 3544–3548. [CrossRef]
90. Wu, Y.; Xing, S.; Fu, J. Examining the use of TiO_2 to enhance the NH_3 sensitivity of polypyrrole films. *Appl. Polym. Sci.* **2010**, *118*, 3351–3356. [CrossRef]
91. Tai, H.; Jiang, Y.; Xie, G.; Yu, J.; Zhao, M. Self-assembly of TiO_2/polypyrrole nanocomposite ultrathin films and application for an NH_3 gas sensor. *Int. J. Environ. Anal. Chem.* **2007**, *87*, 539–551. [CrossRef]
92. Bulakhe, R.N.; Patil, S.V.; Deshmukh, P.R.; Shinde, N.M.; Lokhande, C.D. Fabrication and performance of polypyrrole (Ppy)/TiO_2 heterojunction for room temperature operated LPG sensor. *Sens. Actuators B Chem.* **2013**, *181*, 417–423. [CrossRef]
93. Gong, J.; Li, Y.; Hu, Z.; Zhou, Z.; Deng, Y. Ultrasensitive NH_3 gas sensor from polyaniline nanograin enchased TiO_2 fibers. *J. Phys. Chem. C* **2010**, *114*, 9970–9974. [CrossRef]
94. Pawar, S.G.; Chougule, M.A.; Sen, S.; Patil, V.B. Development of nanostructured polyaniline-titanium dioxide gas sensors for ammonia recognition. *J. Appl. Polym. Sci.* **2012**, *125*, 1418–1424. [CrossRef]
95. Wang, Q.; Dong, X.; Pang, Z.; Du, Y.; Xia, X.; Wei, Q.; Huang, F. Ammonia sensing behaviors of TiO_2-PANI/PA6 composite nanofibers. *Sensors* **2012**, *12*, 17046–17057. [CrossRef]
96. Andersson, S.; Magneli, A. Diskrete Titanoxydphasen im Zusammensetzungsbereich $TiO_{1,75}$-$TiO_{1,90}$. *Naturwissenschaften* **1956**, *43*, 495–496. [CrossRef]
97. Liborio, L.; Mallia, G.; Harrison, N. Electronic structure of the Ti_4O_7 Magnéli phase. *Phys. Rev. B* **2009**, *79*, 245133. [CrossRef]
98. Liborio, L.; Harrison, N. Thermodynamics of oxygen defective Magnéli phases in rutile: Afirst-principles study. *Phys. Rev. B* **2008**, *77*, 104104. [CrossRef]
99. Adamaki, V.; Clemens, F.; Ragulis, P.; Pennock, S.R.; Taylor, J.; Bowen, C.R. Manufacturing and Characterization of Magnéli Phase Conductive Fibres. *J. Mater. Chem. A* **2014**, *2*, 8328–8333. [CrossRef]
100. Song, S.J.; Seok, J.Y.; Yoon, J.H.; Kim, K.M.; Kim, G.H.; Lee, M.H.; Hwang, C.S. Real-time identification of the evolution of conducting nano-filaments in TiO_2 thin film ReRAM. *Sci. Rep.* **2013**, *3*, 3443. [CrossRef]

101. Zhu, Q.; Peng, Y.; Lin, L.; Fan, C.M.; Gao, G.Q.; Wang, R.X.; Xu, A.W. Stable blue $TiO_{2\text{-x}}$ nanoparticles for efficient visible light photocatalysts. *J. Mater. Chem.* **2014**, *A2*, 4429–4437. [CrossRef]
102. Seebauer, E.G.; Kratzer, M.C. Charged point defects in semiconductors. *Mater. Sci. Eng. R Rep.* **2006**, *55*, 57. [CrossRef]
103. Harada, S.; Tanaka, K.; Inui, H. Thermoelectric properties and crystallographic shear structures in titanium oxides of the Magnéli phases. *J. Appl. Phys.* **2010**, *108*, 083703. [CrossRef]
104. Smith, J.R.; Walsh, F.C.; Clarke, R.L. Electrodes based on Magnéli phase titanium oxides: The properties and applications of Ebonex® materials. *J. Appl. Electrochem.* **1998**, *28*, 1021. [CrossRef]
105. Walsh, F.C.; Wills, R.G.A. The continuing development of Magnéli phase titanium sub-oxides and Ebonex® electrodes. *Electrochim. Acta* **2010**, *55*, 6342. [CrossRef]
106. Kernazhitsky, L.; Shymanovska, V.; Gavrilko, T.; Naumov, V.; Fedorenko, L.; Kshnyakin, V.; Baran, J. Room temperature photoluminescence of anatase and rutile TiO_2 powders. *J. Lumin.* **2014**, *146*, 199–204. [CrossRef]
107. Zheng, Z.; Huang, B.; Meng, X.; Wang, J.; Wang, S.; Lou, Z.; Wang, Z.; Qin, X.; Zhang, X.; Dai, Y. Metallic zinc-assisted synthesis of Ti^{3+} self-doped TiO_2 with tunable phase composition and visible-light photocatalytic activity. *Chem. Commun.* **2013**, *49*, 868–870. [CrossRef]
108. Nakamura, I.; Negishi, N.; Kutsuna, S.; Ihara, T.; Sugihara, S.; Takeuchi, K. Role ofoxygen vacancy in the plasma-treated TiO_2 photocatalyst with visible lightactivity for NO removal. *J. Mol. Catal. A Chem.* **2000**, *161*, 205–212. [CrossRef]
109. Lemercier, T.; Mariot, J.M.; Parent, P.; Fontaine, M.F.; Hague, C.F.; Quarton, M. Formation of Ti^{3+} ions at the surface of laser-irradiated rutile. *Appl. Surf. Sci.* **1995**, *86*, 382–386. [CrossRef]
110. Hashimoto, S.; Tanaka, A. Alteration of Ti 2p XPS spectrum for titanium oxide by low-energy Ar ion bombardment. *Surf. Interface Anal.* **2002**, *34*, 262–265. [CrossRef]
111. Wang, W.K.; Gao, M.; Zhang, X.; Fujitsuka, M.; Majima, T.; Yu, H.Q. One-step synthesis of nonstoichiometric TiO_2 with designed (101) facets for enhanced photocatalytic H_2 evolution. *Appl. Catal. B Environ.* **2017**, *205*, 165–172. [CrossRef]
112. Fukushima, J.; Takizawa, H. Size Control of Ti_4O_7 Nanoparticles by Carbothermal Reduction Using a Multimode Microwave Furnace. *Crystals* **2018**, *8*, 444. [CrossRef]
113. Hayfield, P.C.S. *Development of a New Material—Monolithic Ti_4O_7 Ebonex Ceramic*; Royal Society of Chemistry, Thomas Graham House: Cambridge, UK, 2002.
114. Glinka, Y.D.; Lin, S.-H.; Hwang, L.-P.; Chen, Y.-T.; Tolk, N.H. Size effect in self-trapped exciton photoluminescence from SiO_2-based nanoscale material. *Phys. Rev. B* **2001**, *64*, 085421–085432. [CrossRef]
115. Gallart, M.; Cottineau, T.; Hönerlage, B.; Keller, V.; Keller, N.; Gilliot, P. Temperature dependent photoluminescence of anatase and rutile TiO_2 single crystals: Polaron and self-trapped exciton formation. *J. Appl. Phys.* **2018**, *124*, 133104. [CrossRef]
116. Serpone, N.; Lawless, D.; Khairutdinov, R. Size Effects on the Photophysical Properties of Colloidal Anatase TiO_2 Particles: Size Quantization versus Direct Transitions in This Indirect Semiconductor? *J. Phys. Chem.* **1995**, *99*, 16646. [CrossRef]
117. Saraf, L.V.; Patil, S.I.; Ogale, S.B.; Sainkar, S.R.; Kshirsager, S.T. Synthesis of Nanophase TiO_2 by Ion Beam Sputtering and Cold Condensation Technique. *Int. J. Mod. Phys. B* **1998**, *12*, 2635. [CrossRef]
118. Fujihara, K.; Izumi, S.; Ohno, T.; Matsumura, M. Time-resolved photoluminescence of particulate TiO_2 photocatalysts suspended in aqueous solutions. *J. Photochem. Photobiol. A* **2000**, *132*, 99. [CrossRef]

5th publication / 5 publikacija

Selective Enhancement of SERS Spectral Bands of Salicylic Acid Adsorbate on 2D $Ti_3C_2T_x$-Based MXene Film

Sonata Adomavičiūtė-Grabusovė, **Simonas Ramanavičius**, Anton Popov,
Valdas Šablinskas, Oleksiy Gogotsi, Arūnas Ramanavičius
Chemosensors 2021, 9(8), 223
Reprinted by permission
The article could be find online at
https://doi.org/10.3390/chemosensors9080223

chemosensors

MDPI

Article

Selective Enhancement of SERS Spectral Bands of Salicylic Acid Adsorbate on 2D $Ti_3C_2T_x$-Based MXene Film

Sonata Adomavičiūtė-Grabusovė [1,*], Simonas Ramanavičius [2,3], Anton Popov [4], Valdas Šablinskas [1], Oleksiy Gogotsi [5] and Arūnas Ramanavičius [2,*]

[1] Institute of Chemical Physics, Vilnius University, Sauletekio Av. 3, LT-10257 Vilnius, Lithuania; valdas.sablinskas@ff.vu.lt
[2] Department of Physical Chemistry, Faculty of Chemistry and Geosciences, Institute of Chemistry, Vilnius University, Naugarduko 24, LT-03225 Vilnius, Lithuania; simonas.ramanavicius@ftmc.lt
[3] Center for Physical Sciences and Technology, Sauletekio Av. 3, LT-10257 Vilnius, Lithuania
[4] NanoTechnas—Center of Nanotechnology and Materials Science, Faculty of Chemistry and Geosciences, Institute of Chemistry, Vilnius University, Naugarduko St. 24, LT-03225 Vilnius, Lithuania; anton.popov@chgf.vu.lt
[5] Materials Research Center Ltd., Krzhyzhanovskogo Str. 3, 01001 Kiev, Ukraine; agogotsi@mrc.org.ua
* Correspondence: sonata.adomaviciute@ff.vu.lt (S.A.-G.); Arunas.Ramanavicius@chf.vu.lt (A.R.)

Abstract: In this research, we have demonstrated that 2D $Ti_3C_2X_n$-based MXene (MXene) films are suitable for the design of surface-enhanced Raman spectroscopy (SERS)-based sensors. The enhanced SERS signal was observed for a salicylic acid molecule on $Ti_3C_2T_x$-based MXene film. Confirmation of the adsorption of the salicylic acid molecule and the formation of a salicylic acid–MXene complex were determined by experimental SERS-based spectral observations such as greatly enhanced out-of-plane bending modes of salicylic acid at 896 cm^{-1} and a band doublet at 681 cm^{-1} and 654 cm^{-1}. Additionally, some other spectral features indicate the adsorption of salicylic acid on the MXene surface, namely, a redshift of vibrational modes and the disappearance of the carboxyl deformation spectral band at 771 cm^{-1}. The determined enhancement factor indicates the value that can be expected for the chemical enhancement mechanism in SERS of 220 for out-of-plane vibrational modes. Theoretical modeling based on density functional theory (DFT) calculations using B3LYP/6311G++ functional were performed to assess the formation of the salicylic acid/MXene complex. Based on the calculations, salicylic acid displays affinity of forming a chemical bond with titanium atom of $Ti_3C_2(OH)_2$ crystal via oxygen atom in hydroxyl group of salicylic acid. The electron density redistribution of the salicylic acid–MXene complex leads to a charge transfer effect with 2.2 eV (428 nm) and 2.9 eV (564 nm) excitations. The experimentally evaluated enhancement factor can vary from 220 to 60 when different excitation wavelengths are applied.

Keywords: MXenes; SERS sensor; 2D materials; Ti_2C_3; salicylic acid; density functional theory (DFT)

check for updates

Citation: Adomavičiūtė-Grabusovė, S.; Ramanavičius, S.; Popov, A.; Šablinskas, V.; Gogotsi, O.; Ramanavičius, A. Selective Enhancement of SERS Spectral Bands of Salicylic Acid Adsorbate on 2D $Ti_3C_2T_x$-Based MXene Film. *Chemosensors* **2021**, *9*, 223. https://doi.org/10.3390/chemosensors9080223

Academic Editor: Santiago Sanchez-Cortés

Received: 7 July 2021
Accepted: 9 August 2021
Published: 13 August 2021

1. Introduction

A recently discovered class of specific two-dimensional (2D) materials—MXenes—promises a variety of applications with encouraging improvement in plasmonics, conductivity and catalysis compared to these properties of conventional non-metallic substances such as graphene. Due to the high concentration of free charges, the conductivity of these substances is metallic-like and higher than that of graphene [1,2]. Nevertheless, these materials are quite new, and the most relevant publications considering the optical and electric properties of MXenes have appeared just in the last decade.

MXenes were synthesized from MAX ($M_{n+1}AX_n$, where n = 1, 2 or 3) phase for the first time in 2011 [3]. Here, M represents a III–VI group transition metal, A is typically an element from IIIA or IVA group (e.g., Al, Si, Cd, Ga, etc.) and X usually depicts carbides, nitrides or carbonitrides, though over 30 different types of MXenes have been reported so far and even more are predicted to exist [4]. Henceforth, MXenes are generally produced by selectively etching the middle element of the MAX three-dimensional lattice A, thus obtaining layers of MAX phase that ought to be further separated by various intercalant agents or sonication yielding 2D MXenes. Recently, research of this material class expanded rapidly. This is especially obvious for the $Ti_3C_2T_x$ MXene compounds (T_x here denotes the terminal functional group, usually -O, -OH or -F) formed from Ti_3AlC_2 (MAX phase). These MXenes are studied most extensively since their synthesis is widely established, and they exhibit higher metallic conductivity in comparison to that of molybdenum and nitride-based MXenes [5–8]. Nevertheless, further investigations are directed towards the efficient synthesis of other MXene types that can yield more defect-less 2D MXene layers [4,6].

Due to unique morphology and composition, these materials have the potential to be used in sensor design [9,10] as catalysts [11–13]. High conductivity, transparency and tunable work function enable the application of these materials in the design of optoelectronic devices, including solar cells. $Ti_3C_2T_x$ MXene has the potential to be used as an additive in a charge transport layer or as an electrode in perovskite and organic solar cells [14]. In addition, intriguing metal-like properties (e.g., the decrease of conductivity by the increase of temperature) and high conductivity determined by a high density of charge carriers were observed for MXenes [15–17]. The reported concentration of free charge carriers for $Ti_3C_2T_x$ MXene is 2×10^{21} cm^{-3} [18], while in noble metal nanoparticles, it is approximately 6×10^{22} cm^{-3} [19] and for graphene, 3×10^{13} cm^{-2} [1,2]. The conductivity of MXenes can be altered by their surface termination groups [20], leading to a possible application as supercapacitors [21,22], resistive sensors [23–25] and other applications in electrochemistry [26], electronics [27]. As a result of the relatively high concentration of free electrons, the plasmonic effect of MXenes reclassifies these materials into a class of metals because the plasmon frequency depends on the density of free electrons [19]. For this reason, MXenes might be used as a substitute for metallic nanostructures with the ability to enhance internal vibrations of molecules at near proximity as is in surface-enhanced Raman spectroscopy (SERS) [28–30].

It is widely accepted that two mechanisms can cause the SERS effect: (i) electromagnetic mechanism occurring due to localized plasmon resonance of noble metal nanostructures (such as silver, gold, platinum), which enhances the intensity of Raman spectral bands up to six orders of magnitude and (ii) chemical mechanism, which occurs because of interacting electronic energy levels between the substrate and the adsorbed molecule that causes a shift in electronic energy levels of the molecule. The enhancement due to chemical mechanism is lower and usually does not exceed two orders of magnitude [31]. However, until now, only enhanced resonance Raman spectra of dye molecules (such as rhodamine 6G, crystal violet, methylene blue, malachite green) adsorbed on the MXene surface were observed, and the enhancement was explained by the chemical mechanism [28–30]. The chemical enhancement between the MXene materials and the adsorbed dye molecules occurs because of the coupling between the dye and MXene energy levels. This coupling can be considered as a chemical mechanism of SERS [30,32,33]. Nevertheless, the electromagnetic mechanism of enhancing the SERS signal due to the free electron oscillations in MXene layers cannot be neglected as well [34,35].

The application of MXenes as SERS substrates is desirable in such cases when non-metal SERS substrates with a different chemical affinity towards molecules are needed. Moreover, the enhancement from 2D thin materials is beneficial in comparison to three-dimensional surfaces due to the larger specific surface area of 2D materials. Additionally, the localized plasmon resonance frequency in the metal nanoparticles depends on the shape and size of these nanoparticles which are determined during the synthesis of the nanoparticles, whereas for 2D materials such as graphene and MXenes, the surface plasmon resonance frequency can be influenced by different functional groups and/or controlled by an external electric field [20,36]. The possibility to use MXenes as a SERS substrate not only for sensing molecules with electron-level energy similar to that of MXenes would provide a wider field of application and, therefore, is highly desirable. SERS-based sensing is used for the detection of various molecules (or ions), usually at much lower limits of detection than by conventional spectroscopic methods. The high sensitivity of the method is directly related to the adsorption of the analyte molecules on the nanoparticles. Thus, the adsorption of the molecules leads to enhanced intensity of the Raman spectrum.

Salicylic acid can act as a model molecule for studies of SERS enhancement on MXene film. This molecule consists of a benzene ring and carboxyl group. The Carboxyl group is involved in the adsorption of salicylic acid on the customary SERS substrates—silver or gold nanoparticles. Salicylic acid is known to be SERS-active when silver and gold nanoparticles are used, but this molecule does not exhibit electronic absorption in the visible spectral range.

In this research, the adsorption of salicylic acid molecules and the formation of salicylic acid–MXene complex were confirmed by experimental SERS-based spectral observations. The enhanced SERS signal was observed for salicylic acid molecules on $Ti_3C_2T_x$-based MXene film. The goal of this work is to study the enhancement of Raman spectral bands of salicylic acid when it is adsorbed on MXene film and to elucidate the enhancement features of MXenes when they are used as SERS substrates.

2. Materials and Methods

2.1. Synthesis of $Ti_3C_2T_x$ MXene Substrates

In this study, MXenes were prepared by etching 0.1 g of Ti_2AlC_3 MAX phase in 10 mL of 5 wt.% hydrofluoric acid solution. Solution was stirred for 24 h at 25 °C temperature. After this step, the solution was centrifuged in order to remove residue of hydrofluoric acid. Centrifugation proceeded until the pH of solution became neutral. Finally, the MXene films on a microscope glass slide were prepared. For this purpose, the glass slides were covered with 0.5 mL of aqueous MXene solution (0.01 g/mL) and dried under nitrogen atmosphere.

2.2. Characterization of MXene Film and Its Interaction with Adsorbate

Sample images and elemental analysis were performed by scanning electron microscope *Helios Nanolab 650* (FEI, Eindhoven, Netherlands) equipped with an EDX spectrometer X-Max (Oxford Instruments, Abingdon, UK). X-ray diffraction (XRD) analysis was performed using Ni-filtered Cu Kα radiation on *MiniFlex II* diffractometer (Rigaku, Tokyo, Japan) working in Bragg–Brentano ($\theta/2\theta$) geometry. The diffractograms were recorded within 2θ angle range from 5° to 60° at a step width of 0.02° and speed of 2/min. Resistivity measurements were performed on a thin-film gold interdigitated electrode *ED-IDE3-Au* (Micrux Technologies, Oviedo, Spain).

Characteristic spectroscopic range of interband transition and plasmonic response of MXenes were determined by ultraviolet, visible and near-infrared range (UV-Vis-NIR) absorption spectroscopy. UV-Vis-NIR electronic absorption spectra were acquired with dual-channel *Lambda-1050* spectrometer (PerkinElmer, Boston, MA, USA). The spectra were obtained in the range 350–2300 nm with 5 nm resolution.

$Ti_3C_2T_x$-based MXene film and its interaction with salicylic acid (SA) were investigated by means of Raman spectroscopy. *MonoVista CRS+* Raman microscope system (S & I GmbH, Warstein, Germany) equipped with four excitation lasers (457 nm, 532 nm, 633 nm and 785 nm) and a liquid-nitrogen-cooled CCD detector were used for acquiring the spectra. Diameter of the focused laser beam on the sample was $\approx 1\ \mu m$, and its power density on the sample was $\approx 20\ kW/cm^2$ (for 633 nm excitation) and $\approx 45\ kW/cm^2$ (for 785 nm excitation). Before the measurements, the spectrometer was calibrated to a fundamental vibrational band at $520.7\ cm^{-1}$ of silicon wafer. Fourier transform *MultiRAM* spectrometer (Bruker, Mannheim, Germany) equipped with liquid-nitrogen-cooled Ge diode detector was used for the calculations of enhancement factor for salicylic acid–MXene complex with 1064 nm excitation wavelength.

Solution of salicylic acid in water with concentration equal to 2 mM was prepared. Two drops (5 μL each) of the solution were dried on the glass substrate covered by the MXene film. To ensure the most homogenous distribution of salicylic acid molecules, the drying was performed in a confined space when the saturated vapor diminishes the surface tension in air–water interface and more uniform distribution can be achieved. The same volume of salicylic acid solution was dried on the aluminum foil as a reference. Salicylic acid solution spread to form a 2 mm spot on the film. After drying out, no crystallization occurred on the MXene film, while on the reference glass substrate, crystals of salicylic acid were formed. Presented SERS spectra of salicylic acid were recorded on 20 randomly chosen positions on the MXene surface and averaged. The standard deviation for the spectral intensity of salicylic acid on MXene substrate was calculated while applying 3 s acquisition time.

2.3. Computational Methods

In order to make more detailed analysis of the interaction between salicylic acid and MXene, theoretical calculations of structure and vibrational spectra of monomeric salicylic acid and salicylic acid dimer were performed by means of quantum chemistry calculations implemented in Gaussian 09W software package [37]. The salicylic acid dimer was chosen to resemble the crystalline structure of solid-state salicylic acid. The density functional theory (DFT) calculations using B3LYP/6311G^{++} functional were performed. For the investigation of the salicylic acid–MXene complex, the 2 × 2 × 1 supercell expansion of $Ti_3C_2(OH)_2$ MXene crystal structure (of 20 atoms) was built and optimized. Initially, geometry optimization was performed separately for salicylic acid (B3LYP/6311G^{++}) and $Ti_3C_2(OH)_2$ cluster (B3LYP/LanL2DZ) and for their complex afterward (B3LYP/LanL2DZ). No virtual frequencies were present after the complex optimization. The excited-state calculations were performed to assess the redistribution of the electronic energy levels.

3. Results

3.1. Characterization of MXene Films

The structure and morphology of the MAX phase and synthesized MXene-based materials were evaluated using the scanning electron microscopy (SEM) imaging technique (Figure 1). The compact and layered morphology, which is typical for ternary carbide [38], was obtained in the case of the MAX phase. Etching with 5 wt.% HF solution allows preparing $Ti_3C_2T_x$, for which the structure is quite similar to that of the MAX phase. However, MXene layers were slightly opened. The 'accordion-like' structure was not observed. A possible explanation may be found in low hydrofluoric acid concentration, which is insufficient for the formation of a sufficient amount of H_2 evolving during the exothermic reaction of hydrofluoric acid with aluminum atoms. Successful etching of aluminum atoms was confirmed by energy-dispersive X-ray spectroscopy (EDX) analysis (Table 1). It was revealed that the number of aluminum atoms in MXenes decreased by five times in comparison with the initial amount of these atoms in the MAX phase.

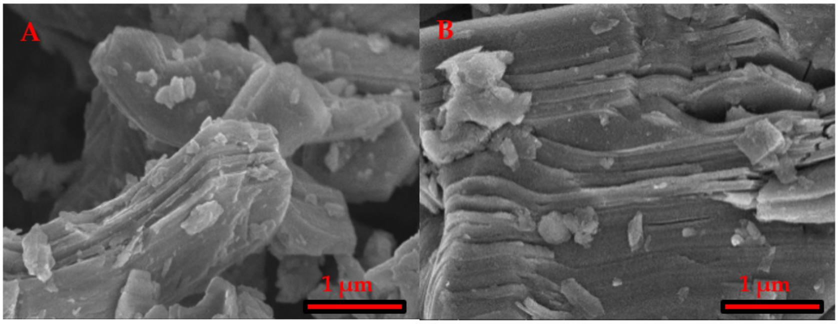

Figure 1. SEM images of (**A**) MAX phase (Ti_3AlC_2) and (**B**) MXenes ($Ti_3C_2T_x$).

Table 1. EDX analysis results for aluminum (Al) and titanium (Ti) atomic ratio in MAX phase and MXene samples.

Sample	Atomic Ratio, %	
	Aluminum (Al)	Titanium (Ti)
MAX phase (Ti_3AlC_2)	39.39 ± 0.96	60.61 ± 0.96
MXenes ($Ti_3C_2T_x$)	6.33 ± 1.97	93.67 ± 1.97

Comparing resistivity of MAX phase and MXenes etched in 5 wt.% HF, it was measured that the resistivity of samples at room temperature decreased from 36 Ω to 20.5 Ω. A decrease in sample resistivity might be explained by a reduced amount of aluminum by etching and the formation of semi-metallic Ti_3C_2 MXene structures.

The synthesis of MXenes was confirmed using XRD analysis (Figure 2). A shift of the (002) peak of Ti_3AlC_2 at 9.5° to 7.3° for the $Ti_3C_2T_x$ was observed. Such sufficiently large shift is typical for wet multilayered MXene samples [39], whereas an intense and sharp (002) peak is characteristic for MXenes etched by hydrofluoric acid [40]. Such results, together with the absence of other MAX phase characteristic peaks in MXene spectra, coincide with EDX analysis results and confirm successful etching of Al out of Ti_3AlC_2.

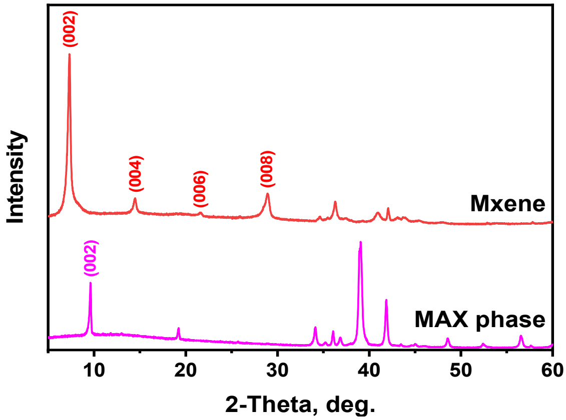

Figure 2. XRD patterns of MAX phase (Ti_3AlC_2) and MXene ($Ti_3C_2T_x$) powders.

Usually, MXene films are composed of various sizes of $Ti_3C_2T_x$ flakes (lateral sizes vary from 0.1 to ~5 µm). In contrast, the thickness of monolayered MXene is supposed to be about 0.95 nm [41]

Due to weak interaction between neighboring individual MXene flakes, the electric and plasmonic properties of the film do not significantly depend on the thickness of MXene structures, though the correlation between metallic behavior and the origin of the terminal chemical groups of MXenes is well expressed [17,21,34,42]. MXenes terminated with -F and -OH feature higher conductivity and plasmonic response to incident radiation in comparison to the oxidized MXenes.

The plasmonic response and other optical properties of the MXene substrate were assessed by the mean of UV-Vis-NIR absorption spectroscopy (Figure 3). Relying on the correlation between the optical density and the thickness of the film [17,21,43], we estimated the thickness to be approximately 70 nm.

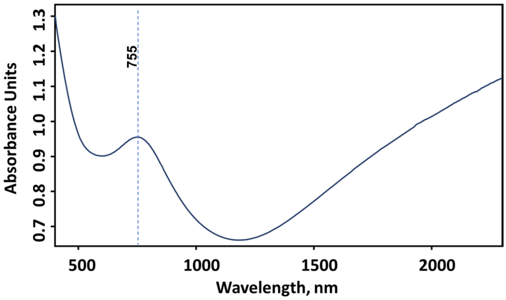

Figure 3. UV-Vis-NIR absorption spectrum of dried 70 nm thick $Ti_3C_2T_x$ MXene film on the glass slide.

The UV-Vis-NIR absorption spectrum of 70 nm thick $Ti_3C_2T_x$-based MXene film contains a broad spectral band (full width at half maximum—195 nm) characteristic for delaminated MXenes. The center of this band is located at 750 nm (1.65 eV). The origin of the spectral band is attributed to the interband transition. The plasmonic nature of this band is controversial. Some researchers assign bands in this spectral range to transversal plasmon resonance [42,44], while other studies suggest that the plasmonic activity of MXenes occurs as a consequence of the real part of the dielectric function, becoming negative only in the near-infrared spectral range, implying that the plasma frequency of MXenes is also in this range and excitation of surface plasmons can be expected at longer wavelengths. During this research, we adhere to the assignment of this absorption band to the interband transition because: (i) no plasmonic activities were observed in this spectral range and (ii) the characteristics of enhanced SERS spectra of salicylic acid indicate a chemical enhancement mechanism. It is important to note that the thickness of the MXene film or the size and shape of the individual $Ti_3C_2T_x$ flakes have no influence on the interband gap. The position of the spectral band can only be shifted by changing the concentration of free charge carriers that can be altered with different terminal groups of $Ti_3C_2T_x$ MXene lattice [17,21,34,42]. Therefore, we did not observe a shift in the interband transition energy when a thicker (120 nm thick) MXene film was deposited.

Considering the origin of the absorption band, transversal and longitudinal plasmon resonances are predicted to be closer to the middle infrared spectral range. It is notable that the maximum of the spectral band related to the plasmon resonance is located at $\lambda > 2200$ nm (see Figure 2). According to the calculations, the width of the plasmon band might be influenced by the high size dispersion of MXene flakes [45]. It should be noted that in order to increase the contribution of the electromagnetic enhancement mechanism into the amplification of the SERS spectrum together with the chemical enhancement mechanism, the plasmon resonance should be observed in the visible region of the spectrum. Fortunately, the plasmon resonance wavelength can be tailored by changing the flake dimensions [45,46].

3.2. Raman Spectra of MXene Films

Further assessment of MXene film composition can be performed using Raman spectroscopy data. The positions of Raman spectral bands of the MXene by itself are mostly caused by various vibrations of $Ti_3C_2T_x$ lattice and the terminal groups. Consequently, the presence of different terminal groups and even interactions with the target molecules can be distinguished by examining the spectral changes.

The Raman spectra of an MXene film on a glass plate obtained with 532 nm, 633 nm and 785 nm excitation are presented in Figure 4. The spectral bands of $Ti_3C_2T_x$ lattice vibrations that interest us occur in the range of 100–850 cm^{-1}. Excitation with a 532 nm laser yields a Raman spectrum with a relatively low signal-to-noise ratio ($S/N \approx 52$), whereas it is higher in the case of 633 nm and 785 nm excitations ($S/N > 100$).

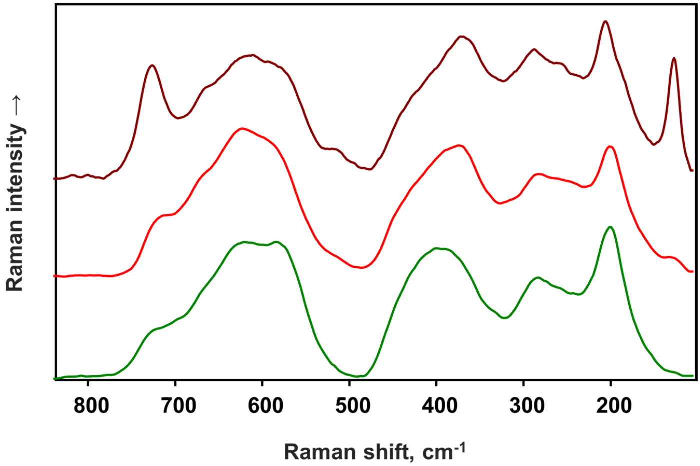

Figure 4. Raman spectra of MXene film with 532 nm (bottom), 633 nm (middle) and 785 nm (top) excitation.

It is worth mentioning that only a rather low power of 532 nm laser excitation could be used for acquiring the spectra. Structural and chemical changes of MXene film have been observed due to rapid oxidation when laser power exceeded 5 mW. In this case, the power density on the sample exceeded 1.5 MW/cm^2. Some degradation of the film was noticeable starting from 17 kW/cm^2 excitation beam power density. In the case of rapid oxidation, the intense G and D spectral bands arising from allotropic forms of carbon (formed from $Ti_3C_2T_x$ lattice) emerge along with the Raman spectrum of TiO_2 in anatase form, exhibiting the most intense spectral band at 143 cm^{-1}. Rapid oxidation is known to disrupt the structure of the MXene film [47]. Due to the disruption, Ti is oxidized into TiO_2 by the formation of anatase nanoparticles and graphitic or amorphous carbon [48]. Raman spectra acquired with 532 nm and 633 nm excitation fit very well with the literature data [22,48]. The lattice phonon modes of $Ti_3C_2T_x$ MXene terminated with different chemical groups are observed as a combination of the broader spectral bands at 129 cm^{-1} (ω_1), 198 cm^{-1} (ω_2), 709 cm^{-1} (ω_3), 667 cm^{-1} (ω_4), 281 cm^{-1} (ω_5) and 371 cm^{-1} (ω_7) [49]. Higher energy vibrational spectral bands presumably occur from non-uniform, defected MXene films and the presence of free carbon materials [24,48,50]. G and D spectral bands distinctive for the carbon materials are also present in the MXene spectra. The G band in MXene samples was observed at 1581 cm^{-1}, and the D band was almost imperceptible. Generally, the G band in carbon materials occurs because of sp^2 hybridization caused by C-C stretching being observed in both chain and ring structures, whereas the D band is observable only in the defected ring structures [51]. In our observations, the appearance of graphene bands indicates the disruption in MXene lattice structure and oxidation of MXenes. We will further address this issue in our forthcoming research.

The spectrum obtained with 785 nm excitation is somewhat different from other spectra. As can be seen in the UV-Vis-NIR absorption spectrum (Figure 3). MXenes in this spectral region have a spectral band arising due to IBT (the corresponding absorption band center, in our case, is at 750 nm). Thus, resonance effects are expected in the Raman spectrum with a 785 nm excitation laser. As a consequence of resonant lattice vibrations, the new spectral bands become observable. The new band at 120 cm^{-1} arises from the in-plane vibration mode of Ti and C atoms of the MXene lattice. In addition, the new out-of-plane breathing mode (ω_6) band at 513 cm^{-1} becomes discernible. During this vibration, terminal atoms are mainly moving in a transversal direction to the lattice plane. The intensity increase for the band at 722 cm^{-1} is observed as well. The spectral band at 722 cm^{-1} represents out-of-plane vibrations of C atoms perpendicular to the 2D plane of MXene film. The gradual increase in the intensity of these bands is observed when excitation wavelength changes from 532 nm, 633 nm to 785 nm.

The appearance of new spectral bands can be explained by the resonant condition of excitation [44,45,49]. The enhancement of certain vibrational modes occurs when the exciting frequency comes into resonance with the lowest excited state. Usually, total symmetric modes experience the greatest enhancement (through A term). In this case, the symmetric normal modes, in which vibrations involve bonds that are affected by the change in the electronic state of excited molecules, are enhanced. Nevertheless, the enhancement of non-symmetric normal modes is possible when two excited states are coupled by the normal mode vibration (B term). Hence, in both cases, the enhanced modes correspond to the interaction between the molecule ground and excited states [52,53].

Furthermore, the lower energy vibrational spectral bands of $Ti_3C_2T_x$ MXenes can be used for the determination of the changes in surface terminal groups (=O, –OH or –F) [49,54,55]. The most stable MXene film is the one with carbonyl (=O) terminal group, e.g., $Ti_3C_2O_2$ [56] whilst, during the first step of synthesis of MXene—etching of Al—they are terminated with the -F group. Usually, it is considered that MXenes are terminated with all these functional groups to some degree [57]. Very promising spectral bands for the determination of terminal groups are the out-of-plane mode of C vibrations (ω_3), which is calculated to be located at 694 cm^{-1} in $Ti_3C_2(OH)_2$ MXene and at 730 cm^{-1} in $Ti_3C_2O_2$ and the out-of-plane mode of mainly Ti and terminal atoms vibrations (ω_2). It was experimentally proved that ω_3 mode becomes red-shifted when the =O terminal group is reduced into the –OH group [30], while ω_2 redshifts from 218 cm^{-1} to 208 cm^{-1} [49]. Other distinct Raman spectral bands of $Ti_3C_2O_2$ are the out-of-plane mode of =O at 371 cm^{-1} and Ti and the =O in-plane vibrational mode at 589 cm^{-1}. The bands at 281 cm^{-1} –OH in-plane and 667 cm^{-1}—C atom out-of-plane vibrational modes arise from $Ti_3C_2(OH)_2$. Raman vibrational frequencies observed for MXene films and assignments of the spectral bands are presented in Table 2.

Table 2. Vibrational frequencies of $Ti_3C_2T_x$-based MXene films.

Vibrational Freq., cm^{-1}			**Calculated Freq., cm^{-1} [49]**	**Assignments [49]**
532 nm	**633 nm**	**785 nm**		
[W]	129	120	128	$(Ti,C)^{ip}$, $Ti_3C_2F_2$; ω_1
198	198	199	190	$(Ti,F)^{oop}$, $Ti_3C_2F_2$; ω_2
257	W	258	231	$(F)^{ip}$, $Ti_3C_2F_2$; ω_5
287	281	280	278	$(OH)^{ip}$, $Ti_3C_2(OH)_2$; ω_5
390	371	366	347	$(O)^{ip}$, $Ti_3C_2O_2$; ω_5
[W]	511 [a]	513 [b]	514	$(OH)^{oop}$, $Ti_3C_2(OH)_2$; ω_6
590 [a]	589 [a]	584 [a]	586	$(O)^{oop}$, $Ti_3C_2O_2$; ω_6
621	620	615	622	$(C)^{ip}$, $Ti_3C_2(OH)_2$; ω_4
673 [a]	667 [a]	655	684	$(C)_{oop}$, $Ti_3C_2(OH)_2$; ω_3
715	709 [a]	722 [b]	730	$(C)^{oop}$, $Ti_3C_2O_2$; ω_3
[W]	[W]	[W]		D band
1550	1581	1520 [a]		G band

[a] Decreased intensity in spectral band compared to 785 nm excitation. [b] Increased intensity in spectral band compared to 785 nm excitation. [W] Not prominent or weak band. [ip] In-plane phonon mode. [oop] Out-of-plane phonon mode.

3.3. Interaction between Salicylic Acid and MXenes

An interesting effect was observed when salicylic acid (SA) solution was dried on the MXene film. The measured Raman spectrum of salicylic acid on MXene film clearly differs from that of crystalline salicylic acid (Figure 5). The redshifts of the vibrational bands are evident and indicate an interaction between salicylic acid molecules and the $Ti_3C_2T_x$-based MXene film. The appearance of prominent Raman spectral bands at 896 cm^{-1} and a band doublet at 681 cm^{-1} and 654 cm^{-1} confirms the interaction between salicylic acid and the MXene. Based on our DFT calculations performed for monomeric salicylic acid molecule and salicylic acid dimer (as in crystalline salicylic acid form), these newly emerged bands can be assigned to out-of-plane vibrations of CH groups and out-of-plane ring deformation, respectively. The latter usually displays a low Raman signal intensity of the crystalline form of SA. The increased intensity of out-of-plane vibrational bands was evaluated by calculating enhancement factor for intensified bands as:

$$Enhancement\ factor = (I_{SERS} \times N_{Raman})/(I_{Raman} \times N_{SERS}) \quad (1)$$

where I_{SERS} and I_{Raman} are SERS and Raman spectral band intensities, N_{Raman} and N_{SERS}—number of excited molecules for Raman and SERS experiments.

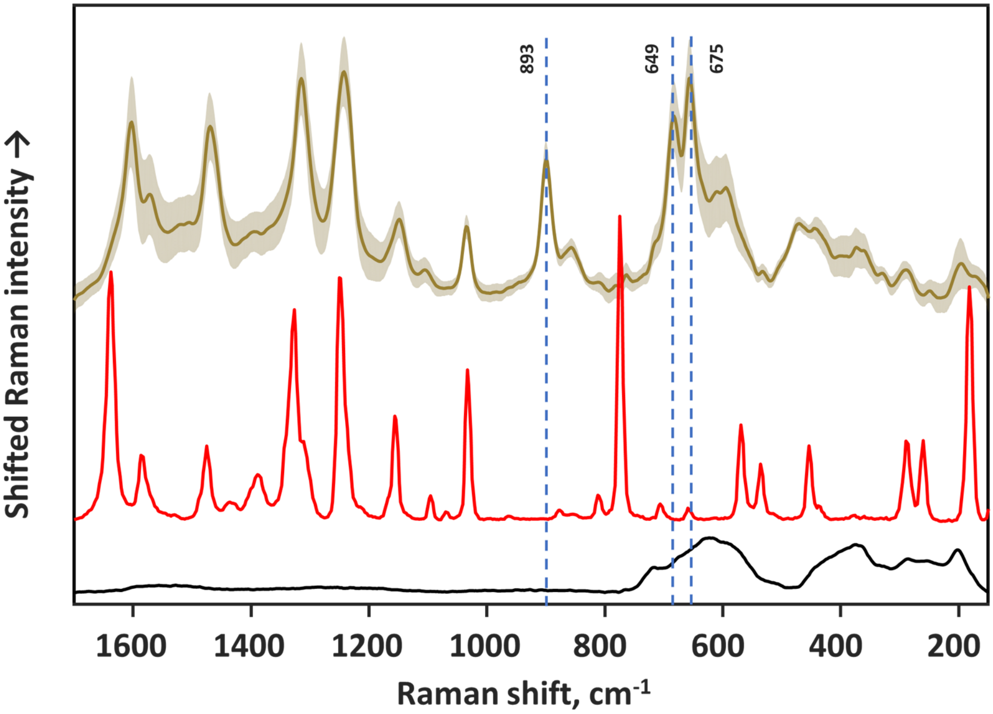

Figure 5. Raman spectra of MXene film (bottom) and salicylic acid: dried on MXene surface (middle) and on aluminum foil (top). Excitation wavelength—633 nm.

Comparing salicylic acid deposited directly on aluminum surface and on the MXene film, enhancement factor reached 125, 110 and 220 for the band at 896 cm^{-1} and band doublet at 681 cm^{-1} and 654 cm^{-1}, respectively (532 nm excitation).

Additionally, an increase in intensities and redshifts were observed for the other salicylic acid spectral bands. The largest shift occurred for the C=O stretching vibrational band of the carboxylic group at 1636 cm^{-1} which shifted by 39 cm^{-1} to 1597 cm^{-1}; the other bands experienced smaller redshifts—from 12 to 15 cm^{-1}. For example, the vibrational modes of the benzene ring observed at 1583 cm^{-1} and 1473 cm^{-1} were shifted to 1567 cm^{-1} and 1467 cm^{-1}, respectively. The C–O stretching band at 1325 cm^{-1} is shifted down to 1311 cm^{-1}; the spectral band of the C–O deformation of the hydroxyl group at 1244 cm^{-1} is shifted to 1232 cm^{-1}. Indeed, the only spectral band that did not experience observable shift is the benzene ring mode at 1031 cm^{-1}. The assignments of the experimental spectral bands for (i) salicylic acid crystals formed on the pure aluminum surface and (ii) vibrational shifts for salicylic acid on MXene film are provided in Table 3.

Table 3. Vibrational frequencies of crystalline salicylic acid and SA–MXene complex.

Crystalline Salicylic Acid, Freq. cm^{-1}	Salicylic Acid on MXenes, Freq. cm^{-1}	Assignments
180	-	δ_{oop}(C-COOH)
258	-	δ_{ip}(C-COOH)
286	-	δ_{ip}(C-OH)
452	-	δ_{ip}(C-COOH)
-	473	δ_{oop}(ring) + δ_{oop} (OH)
534	-	δ_{oop}(ring)
568	-	δ_{oop}(O-H) [a] + δ_{oop}(ring)
-	595	δ_{ip}(C-C, ring)+ δ_{oop}(OH)
657	654 $^{\uparrow}$	δ_{ip}(-COOH) + δ_{oop}(ring)
705	681 $^{\uparrow}$	δ_{oop}(ring) + δ_{oop}(O-H) [a]
773	-	δ_{ip}(C-H) [a] + 6 [c]
850	861	ν(C-OH) [b]+ δ_{ip}(ring)
876	896 $^{\uparrow}$	δ_{oop}(C-H); 17 [c]
1031	1031	18 [c]?
1093		δ(O-H) [b]
1154	1145	δ(O-H) [a]
1164	-	15 [c]
1244	1232	δ(O-H) [a] + ν(C-COOH)
1307	-	δ(O-H) [a]
1325	1311	δ(C-O) [b]
1386	1397	14 [c] + δ(C-O) [b]
1473	1467	19 [c]
1583	1567	8 [c]
1636	1597 $^{\downarrow}$	ν(C=O) [a]

[a] Vibration of atoms in –COOH functional group. [b] Vibration of atoms in –OH functional group. $^{\uparrow}$ Increased intensity. $^{\downarrow}$ Decreased intensity. Stretching vibration. δ Deformation vibration. $_{oop}$ Out-of-plane. $_{ip}$ In-plane. [c] Modes derived from benzene [58].

Partly due to the porous MXene surface and high surface area, salicylic acid molecules can spread easily and interact with the MXenes. Indication of such interaction is the change in color from purple to yellowish when salicylic acid is dried on the MXene film (Figure 6 inset). Salicylic acid molecules are prone to form crystals when drying, though: after drying on the MXene film, no crystals are visible.

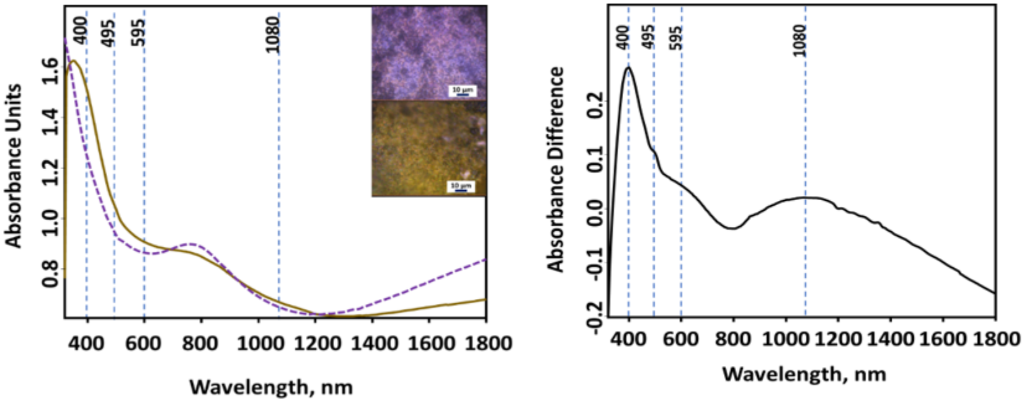

(**a**) (**b**)

Figure 6. UV-Vis-NIR absorption spectra of the $Ti_3C_2T_x$-based MXene film (dotted line) and salicylic acid (straight line) dried on the MXene (**a**); differential spectrum (**b**). Inset—optical microscope images of MXene film (left) and salicylic acid dried on the MXene film (right).

Detailed investigation of the interaction between salicylic acid molecules and $Ti_3C_2T_x$ MXene can be completed by analyzing UV-Vis-NIR spectra. The change in UV-Vis-NIR absorption spectrum of salicylic acid–MXene film is clearly seen in the differential spectrum where the MXene spectrum is subtracted from salicylic acid on the MXene spectrum (Figure 6b). Salicylic acid water solution features absorption bands from π to π^* and n to π^* transitions at $\approx$ 230 nm and $\approx$ 300 nm, whereas salicylic acid–MXene film possesses the highest intensity band at 400 nm. Other, less distinct bands are at 495 nm, 595 nm and 1080 nm. The decrease in near-infrared absorption range from MXene film is probably caused by redistribution of conduction band electrons—free charge carriers. These changes in the absorption spectrum confirm that salicylic acid and MXene are forming complex structures.

These spectral changes can be explained by the formation of the salicylic acid–MXene complex and the charge-transfer effect. It is already known that certain molecules form complexes with $Ti_3C_2T_x$ MXenes and, therefore, can undergo charge transfer [30,32,33]. For that matter, the SERS enhancement derived from the MXene films is explained using this charge transfer mechanism and, naturally, by the chemical enhancement mechanism. Briefly, the chemical enhancement is thought to be active because of one of these factors: (i) the charge transfer mechanism between the adsorbed molecule and the substrate and (ii) the influence of the substrate on the molecular polarizability tensor elements that changes the efficiency of Raman scattering. In the case of charge transfer, the Raman signal is enhanced because of the pre-resonance or resonance condition of the excitation to the adsorbate–substrate complex. Thus, the charge transfer mechanism can be traced by: (i) the greater enhancement of the antisymmetric vibrations compared to symmetric ones (due to the B term excitation of resonance Raman); (ii) enhancement of the stretching vibrations (in the resonant condition of excitation, the totally symmetric vibrations in accordance with the excited state geometry of the molecule are enhanced (due to A term mechanism). The bond length between atoms usually increases in the excited molecule state); (iii) high dependence of the EF on the excitation wavelength.

The first indication of the charge transfer effect in the salicylic acid–MXene complex is the greater enhancement of asymmetric vibrational modes. Since the salicylic acid molecule is in the C_s point symmetry group, the vibrational modes of salicylic acid can only be classified as in-plane (A′) or out-of-plane (A″) vibrations. The latter is less symmetric and, as seen in Figure 5, was enhanced via salicylic acid–MXene interaction. The dependence of salicylic acid–MXene Raman spectra on the excitation wavelength is presented in Figure 7.

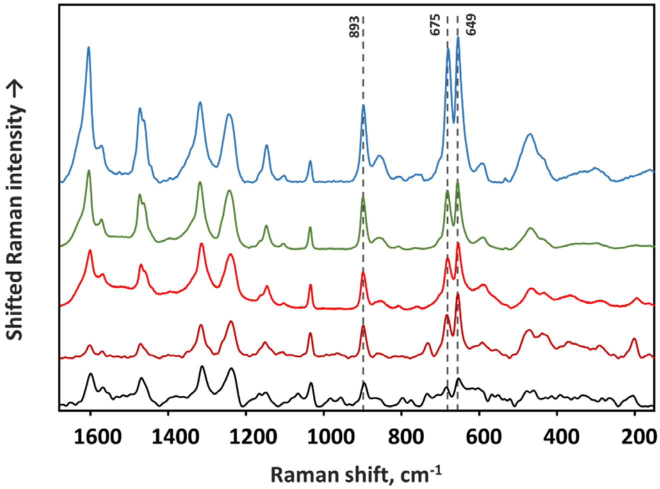

Figure 7. Raman spectra of salicylic acid–MXene complex with different excitations. Excitations from top to bottom: 457 nm; 532 nm; 633 nm; 785 nm; 1064 nm.

Based on the spectra acquired at different excitations, the enhancement factor dependence on the excitation can be evaluated (Figure 8). To minimize the influence of spectrometer response to different wavelength, the crystalline salicylic acid was acquired with each excitation, and the salicylic acid–MXene complex spectrum was compared to crystalline salicylic acid spectrum acquired at the same conditions.

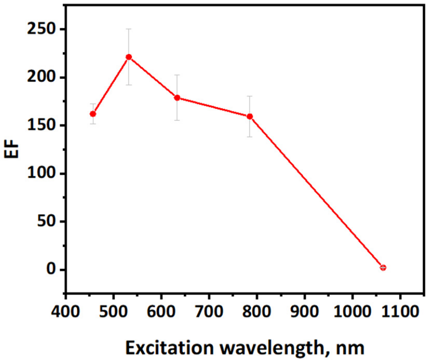

Figure 8. Calculated SERS enhancement factor (EF) for 2 mM salicylic acid dried on the MXene film with different excitation wavelengths.

Indeed, the SERS enhancement factor for out-of-plane vibrations is as expected for the chemical enhancement mechanism. The enhancement factor for the substrate covered by the salicylic acid–MXene complex was calculated for the most enhanced vibrational band at 654 cm^{-1} (carboxyl deformation + out-of-plane C-C bending). As the enhancement factor value dependency on the excitation wavelength indicates, the highest enhancement of 220 is achieved with a 532 nm laser (Figure 8). Nevertheless, 457 nm and 633 nm excitations also yield comparable enhancement of 165 and 178, respectively. The 785 nm excitation fell into the absorption of MXenes; for this reason, the Raman spectral bands of MXene phonon modes are still observable in the spectrum, and the enhancement factor reaches 150. For the excitation profile of 1064 nm, an entirely different Fourier Transform-Raman spectrometer was used. It was observed that MXene film without salicylic acid highly absorbs this wavelength, generates heat and makes the registration of spectrum with this excitation impossible. Nevertheless, when the salicylic acid–MXene complex is excited, the characteristic spectrum is observed, which is indicating changes in the electron distribution of the MXene layer.

It is worth mentioning that based on our results, the chemical mechanism of enhancement takes place between salicylic acid and MXenes. The observable hot spot effect of SERS substrates arises when the intensity crucially depends on the different spots of the sample, because of the electromagnetic mechanism of enhancement when the analyte molecule is trapped between two nanoparticles [31]. The random distribution of these hot spots varies the absolute intensity of SERS bands. In our case, the chemical enhancement mechanism makes the substrate more uniform in the sense of changes in the intensity of the Raman bands. For the calculations of the enhancement factor, the absolute intensity is important, but for further studies, the normalization to a specific spectral band can be considered (for salicylic acid, it was the only spectral band at 1031 cm^{-1} that did not shift, and for this reason, it is considered to be unaffected by chemical enhancement mechanism).

However, the comparison of the achieved enhancement factor for salicylic acid with that of conventional SERS materials such as silver and gold nanostructures is difficult. Limited literature is available concerning the SERS enhancement factor of salicylic acid. To the best of our knowledge, the evaluation of the analytical enhancement factor for salicylic acid adsorbed on silver and gold nanoparticles with 1064 nm excitation is presented only in one of our previous works [59]. The determined enhancement factors for gold and silver nanoparticles prepared with different synthesis methods and stabilizing agents are presented in Table 4.

Table 4. Comparison of enhancement factors for salicylic acid achieved with different materials.

Substrate Material	Excitation	Enhancement Factor
Citrate-stabilized AgNPs	1064 nm	2.5×10^4
Polymer-stabilized AgNPs	1064 nm	1.2×10^4
Citrate-stabilized AuNPs	1064 nm	2.5×10^3
Polymer-stabilized AuNPs	1064 nm	3.8×10^3
$Ti_3C_2T_x$ MXene	532 nm	2.2×10^2

AgNPs—silver nanoparticles. AuNPs—gold nanoparticles.

3.4. Computational Results of Salicylic Acid Interaction with MXene

In order to make a more detailed investigation of the salicylic acid and MXene interaction, the first-principle calculations based on DFT were performed. For salicylic acid–MXene complex investigation, the cluster of $Ti_3C_2(OH)_2$ supercell was built and optimized (B3LYP/LanL2DZ). According to the calculations, salicylic acid displays affinity of forming a chemical bond with titanium atom of $Ti_3C_2(OH)_2$ crystal via oxygen atom in carboxyl group of salicylic acid. The likeness of the complex formation is assured based on geometrical parameters of optimized geometry of the salicylic acid–MXene complex. The length of the O-H interatomic bond in the salicylic acid carboxyl group increased from 0.976 to 1.536 Å, whereas the distance between the $Ti_3C_2(OH)_2$ MXene OH-H group was 1.034 Å, indicating the possible proton transfer between SA and the MXene cluster. The C-O bond length in the carboxyl group also increased from 1.232 to 1.339 Å. The bond formation between salicylic acid and $Ti_3C_2(OH)_2$ MXene can explain the drastic experimental shift of 40 cm^{-1} for the C=O stretching vibrational band of the carboxylic group at 1636 cm^{-1} and the disappearance of the salicylic acid band at 771 cm^{-1} (benzene ring bending + carboxyl deformation modes). The formed bond between salicylic acid and the MXene cluster can become a channel for electron density redistribution around the salicylic acid and MXene cluster. Moreover, the charge distribution on the atoms from the performed Mulliken population analysis indicates a slight charge redistribution by −0.66 when from −0.32 (monomeric salicylic acid) to −0.98 (salicylic acid–MXene complex).

As can be expected, the electron density in the highest occupied molecular orbital minus 1 (HOMO-1) and lower molecular orbitals is focused on the donor $Ti_3C_2(OH)_2$ MXene. In the HOMO molecular orbital, the electron density redistribution is already observed, also indicating the formation of a complex bond between the carboxyl group of salicylic acid and MXene, whereas in the lowest unoccupied molecular orbital (LUMO), the high electron density shifts from MXene to salicylic acid (1.45 eV). Based on the electron density in molecular orbitals, other charge transfer excitations are observed at LUMO + 4 (2.2 eV) and LUMO + 10 (2.9 eV) (Figure 9). The calculated salicylic acid–MXene complex excitations are in accordance with the observed UV-Vis absorption spectrum (Figure 6), where the most intense absorption band is observed at 400 nm (calculated—428 nm) and lower bands—at 495 nm and 595 nm (calculated—564 nm) and 1080 nm. By comparing the HOMO-LUMO excitation of the monomeric salicylic acid molecule, the required salicylic acid molecule excitation energy decreased from 4.5 eV to 2.9 eV.

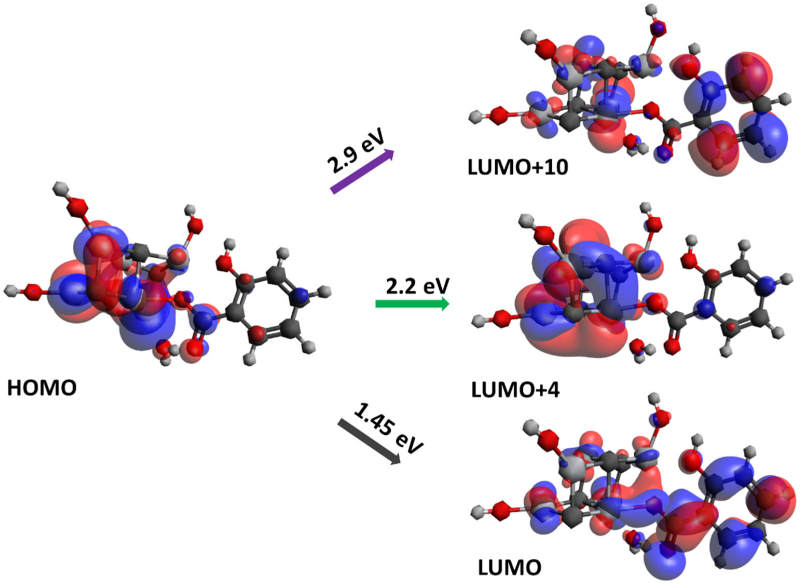

Figure 9. Calculated (B3LYP/LanL2DZ) molecular orbitals of salicylic acid–MXene complex and required transition energy.

4. Discussion

In the search for non-metallic SERS substrates, a very big role is placed on the very high enhancement of vibrations. Briefly, the chemical enhancement mechanism of SERS in widely used metal nanoparticles contributes to the total enhancement effect only on the order of 10–100, whereas the electromagnetic enhancement mechanism is thought to be responsible for spectral enhancement as high as 10^6 times [31]. Thus, the electromagnetic enhancement should enhance the molecular spectra by a huge amount. Nevertheless, the electromagnetic enhancement mechanism depends strongly on the charge carrier concentration in materials and thus their metallic properties.

During the last decade, the metallic properties of MXenes were investigated rather comprehensively. Similar to other 2D semimetals [16], MXenes show plasmonic behavior and the negative real part of the dielectric function in the near-infrared range [17,34,42,46]. Experimental findings for highly oriented MXene films reveal that at wavelengths longer than 1000 nm, the real part of the dielectric function becomes negative, indicating the onset of free-electron plasma oscillations [17,42,46]. The wavelength threshold at which MXene films become metallic depends on the film thickness [34,46], and thus can be slightly shifted. Furthermore, SEM [22] and atomic force microscopy [55] images clearly reveal the structure of MXenes as the flakes are packed in the form of multilayer sheets. After the delamination, these sheets part out. Extended studies of optical properties of the monolayer flake revealed that the free-electron plasma oscillations occur in two spectral regions: (I) at wavelengths longer than 885 nm and (II) in the narrow 615–740 nm region [42]. The surface plasmon in the latter region was assigned to transversal plasmon resonance (1.7 eV). The transversal plasmon resonance is insensitive to the size and shape of the flake, but it depends on the concentration of free charge carriers that can be altered with the different terminal groups [17,34,42,46].

In performed studies, it was reported that some molecules could interact with multilayered MXenes. Intercalated molecules increase the distance between individual $Ti_3C_2T_x$ mono-sheets and, due to mechanical agitation, cause the delamination of multilayered MXene flakes. Usually, such intercalants are dimethyl sulfoxide DMSO, tetraalkylammonium hydroxide, isopropylamine, hydrazine, urea, Li^+ ions [60,61] or even water molecules [62].

As a result of this process, a large surface area of MXene layers becomes available for interaction, which is desirable for the SERS enhancement. In this work, SERS spectra of the salicylic acid–MXene complex was observed for both the multilayered and delaminated MXenes (it should be noted that for the latter, SERS intensity and reproducibility were higher). This supports our prediction that salicylic acid was also responsible for partial delamination of MXene layers.

MXenes have a mixture of oxygen, hydroxyl and fluoride terminal groups that can be protonated/deprotonated at different pHs [23]. At higher hydrogen ion concentration (lower pH), the oxidation of MXenes is slowed down; therefore, a higher surface concentration of hydroxyl terminal groups is favored. Due to pronation at low pH, the hydroxyl terminal groups provide a slightly positive charge on the surface of the MXene layer. This fact should be considered while investigating the mechanism of interaction between MXene and salicylic acid. Moreover, salicylic acid is deprotonated in deionized water (loses hydrogen ions from the carboxylic group); thus, it has a negative charge localized at the carboxylic group that also favors the formation of hydrogen bonds with terminal hydroxyl groups. Therefore, salicylic acid adsorbs well to the hydroxyl-terminated MXene layer.

Out-of-plane vibrations of salicylic acid are enhanced when the molecule interacts with MXene. These spectral changes indicate the molecule of salicylic acid is lying flat on the MXene film. It is known that for dye molecules, charge transfer between the electronic dye level and MXene electronic level takes place, and as a consequence, the dye molecules experience enhancement. Nevertheless, the electromagnetic enhancement mechanism from MXenes, which is expected, was still not observed, neither in our study nor to the best of our knowledge in any other studies.

5. Conclusions

The surface-enhanced effect of spectral Raman bands of salicylic acid adsorbed on $Ti_3C_2T_x$-based MXene film was observed for the first time. The adsorption of the salicylic acid molecule and the formation of a salicylic acid–MXene complex was confirmed by experimental spectral observations such as substantial enhancement of out-of-plane bending modes of salicylic acid at 896 cm^{-1}, 681 cm^{-1} and 654 cm^{-1}. Additionally, other spectral features indicate the adsorption of salicylic acids, such as the redshift of some vibrational frequencies as well as the disappearance of the carboxyl deformation spectral band at 771 cm^{-1}. The values of calculated experimental enhancement factors indicate that chemical enhancement mechanisms are dominant in SERS spectra of salicylic acid adsorbed on the MXene surface. For the deformation out-of-plane vibrational modes, this factor varies from 220 (at λ = 532 nm) to 60 (at λ = 1064 nm).

Author Contributions: Conceptualization: S.A.-G. and A.R.; Methodology: S.A.-G., A.P., S.R. and O.G.; Software: S.A.-G. and V.Š., formal analysis: S.A.-G., A.P., S.R. and O.G.; Writing—original draft preparation: S.A.-G.; Writing—review and editing: V.Š. A.P., S.R. and A.R.; Supervision: V.Š. and A.R. All authors have read and agreed to the published version of the manuscript.

Funding: This project has received funding from H2020 Marie Skłodowska-Curie Actions (CanBioSe 778157, SALSETH 872370).

Institutional Review Board Statement: Not applicable.

Informed Consent Statement: Not applicable.

Data Availability Statement: Not applicable.

Acknowledgments: Computations were performed on resources at the High Performance Computing Center, 'HPC Sauletekis', at the Vilnius University Faculty of Physics.

Conflicts of Interest: The authors declare no conflict of interest.

References

1. Yan, Y.; Cheng, Z.; Li, W.; Jin, K.; Wang, W. Graphene, a material for high temperature devices—Intrinsic carrier density, carrier drift velocity and lattice energy. *Sci. Rep.* **2014**, *4*, 5758. [CrossRef]

2. Song, Q.; Ye, F.; Kong, L.; Shen, Q.; Han, L.; Feng, L.; Yu, G.; Pan, Y.; Li, H. Graphene and MXene Nanomaterials: Toward High-Performance Electromagnetic Wave Absorption in Gigahertz Band Range. *Adv. Funct. Mater.* **2020**, *30*, 2000475. [CrossRef]
3. Naguib, M.; Kurtoglu, M.; Presser, V.; Lu, J.; Niu, J.; Heon, M.; Hultman, L.; Gogotsi, Y.; Barsoum, M.W. Two-dimensional nanocrystals produced by exfoliation of Ti_3AlC_2. *Adv. Mater.* **2011**, *23*, 4248–4253. [CrossRef]
4. Gogotsi, Y.; Anasori, B. The rise of MXenes. *CS Nano* **2019**, *13*, 8491–8494. [CrossRef]
5. Bhat, A.; Anwer, S.; Bhat, K.S.; Mohideen, M.I.H.; Liao, K.; Qurashi, A. Prospects challenges and stability of 2D MXenes for clean energy conversion and storage applications. *NPJ 2D Mater. Appl.* **2021**, *5*, 61. [CrossRef]
6. Papadopoulou, K.A.; Chroneos, A.; Parfitt, D.; Christopoulos, S. A perspective on MXenes: Their synthesis, properties, and recent applications. *J. Appl. Phys.* **2020**, *128*, 17. [CrossRef]
7. Anasori, B.; Luhatskaya, M.R.; Gogotsi, Y. 2D metal carbides and nitrides (MXenes) for energy storage. *Nat. Rev. Mater.* **2017**, *2*, 16098. [CrossRef]
8. Shahzad, F.; Iqbal, A.; Kim, H.; Koo, C.M. 2D Transition Metal Carbides (MXenes): Applications as an Electrically Conducting Material. *Adv. Mater.* **2020**, *32*, 2002159. [CrossRef]
9. Sinha, A.; Zhao, H.; Huang, Y.; Lu, X.; Chen, J.; Jain, R. MXene: An emerging material for sensing and biosensing. *TrAC Trends Anal. Chem.* **2018**, *105*, 424–435. [CrossRef]
10. Ramanavicius, S.; Ramanavicius, A. Progress and Insights in the Application of MXenes as New 2D Nano-Materials Suitable for Biosensors and Biofuel Cell Design. *Int. J. Mol. Sci.* **2020**, *21*, 9224. [CrossRef]
11. Xie, X.; Chen, S.; Ding, W.; Nie, Y.; Wei, Z. An extraordinarily stable catalyst: Pt NPs supported on two-dimensional $Ti_3C_2X_2$ (X= OH, F) nanosheets for oxygen reduction reaction. *Chem. Commun.* **2013**, *49*, 10112–10114. [CrossRef] [PubMed]
12. Zhang, J.; Zhao, Y.; Guo, X.; Chen, C.; Dong, C.L.; Liu, R.S.; Han, C.P.; Li, Y.; Gogotsi, Y.; Wang, G. Single platinum atoms immobilized on an MXene as an efficient catalyst for the hydrogen evolution reaction. *Nat. Catal.* **2018**, *1*, 985–992. [CrossRef]
13. Ran, J.; Gao, G.; Li, F.T.; Ma, T.Y.; Du, A.; Qiao, S.Z. Ti_3C_2 MXene co-catalyst on metal sulfide photo-absorbers for enhanced visible-light photocatalytic hydrogen production. *Nat. Commun.* **2017**, *8*, 13907. [CrossRef]
14. Yin, L.; Li, Y.; Yao, X.; Wang, Y.; Jia, L.; Liu, Q.; Li, J.; Li, Y.; He, D. MXenes for Solar Cells. *Nano-Micro Lett.* **2021**, *13*, 78. [CrossRef]
15. Enyashin, A.N.; Ivanovskii, A.L. Two-dimensional titanium carbonitrides and their hydroxylated derivatives: Structural, electronic properties and stability of MXenes $Ti_3C_{2-x}N_x(OH)_2$ from DFTB calculations. *J. Solid State Chem.* **2013**, *207*, 42–48. [CrossRef]
16. Zhu, Z.; Zou, Y.; Hu, W.; Li, Y.; Gu, Y.; Cao, B.; Guo, N.; Wang, L.; Song, J.; Zhang, S.; et al. Near-Infrared Plasmonic 2D Semimetals for Applications in Communication and Biology. *Adv. Funct. Mater.* **2016**, *26*, 1793–1802. [CrossRef]
17. Dillon, A.D.; Ghidiu, M.J.; Krick, A.L.; Griggs, J.; May, S.J.; Gogotsi, Y.; Barsoum, M.W.; Fafarman, A.T. Highly conductive optical quality solution-processed films of 2D titanium carbide. *Adv. Funct. Mater.* **2016**, *26*, 4162–4168. [CrossRef]
18. Miranda, A.; Halim, J.; Barsoum, M.W.; Lorke, A. Electronic properties of freestanding $Ti_3C_2T_x$ MXene monolayers. *Appl. Phys. Lett.* **2016**, *108*, 033102. [CrossRef]
19. Lee, K.S.; El-Sayed, M.A. Gold and Silver Nanoparticles in Sensing and Imaging: Sensitivity of Plasmon Response to size, shape, and metal composition. *J. Phys. Chem. B* **2016**, *110*, 19220–19225. [CrossRef] [PubMed]
20. Hart, J.L.; Hantanasirisakul, K.; Lang, A.C.; Anasori, B.; Pinto, D.; Pivak, Y.; van Omme, J.T.; May, S.J.; Gogotsi, Y.; Taheri, M.L. Control of MXenes' electronic properties through termination and intercalation. *Nat. Commun.* **2019**, *10*, 522. [CrossRef]
21. Mariano, M.; Mashtalir, O.; Antonio, F.Q.; Ryu, W.H.; Deng, B.; Xia, F.; Gogotsi, Y.; Taylor, A.D. Solution-processed titanium carbide MXene films examined as highly transparent conductors. *Nanosale* **2016**, *8*, 16371–16378. [CrossRef] [PubMed]
22. Melchior, S.A.; Raju, K.; Ike, I.S.; Erasmus, R.M.; Kabongo, G.; Sigalas, I.; Iyuke, S.E.; Ozoemena, K.I. High-voltage symmetric supercapacitor based on 2d titanium carbide (mxene, Ti_2CT_x)/carbon nanosphere composites in a neutral aqueous electrolyte. *J. Electrochem. Soc.* **2018**, *165*, A501–A511. [CrossRef]
23. Echols, I.J.; An, H.; Zhao, X.; Prehn, E.M.; Tan, Z.; Radovic, M.; Green, M.J.; Lutkenhaus, J.L. pH-Response of polycation/$Ti_3C_2T_x$ MXene layer-by-layer assemblies for use as resistive sensors. *Mol. Syst. Des. Eng.* **2020**, *5*, 366–375. [CrossRef]
24. Lorencova, L.; Bertok, T.; Dosekova, E.; Holazova, A.; Paprckova, D.; Vikartovska, A.; Sasinkova, V.; Filip, J.; Kasak, P.; Jerigova, M.; et al. Electrochemical performance of $Ti_3C_2T_x$ MXene in aqueous media: Towards ultrasensitive H_2O_2 sensing. *Electrochim. Acta* **2017**, *235*, 471–479. [CrossRef]
25. An, H.; Habib, T.; Shah, S.; Gao, H.; Patel, A.; Echols, I.; Zhao, X.; Radovic, M.; Green, M.J.; Lutkenhaus, J.L. Water sorption in MXene/polyelectrolyte multilayers for ultrafast humidity sensing. *ACS Appl. Nano Mater.* **2019**, *2*, 948–955. [CrossRef]
26. Song, D.; Jiang, X.; Li, Y.; Lu, X.; Luan, S.; Wang, Y.; Li, Y.; Gao, F. Metal–organic frameworks-derived MnO_2/Mn_3O_4 microcuboids with hierarchically ordered nanosheets and Ti_3C_2 MXene/Au NPs composites for electrochemical pesticide detection. *J. Hazard. Mater.* **2019**, *373*, 367–376. [CrossRef]
27. Kim, H.; Wang, Z.; Alshareef, H.N. MXetronics: Electronic and photonic applications of MXenes. *Nano Energy* **2019**, *60*, 179–197. [CrossRef]
28. Velusamy, D.B.; El-Demellawi, J.K.; El-Zohry, A.M.; Giugni, A.; Lopatin, S.; Hedhili, M.N.; Mansour, A.E.; Fabrizio, E.D.; Mohammed, O.F.; Alshareef, H.N. MXenes for Plasmonic Photodetection. *Adv. Mater.* **2019**, *31*, 1807658. [CrossRef]
29. Zhu, X.; Liu, P.; Xue, T.; Ge, Y.; Ai, S.; Sheng, Y.; Wu, R.; Xu, L.; Tang, K.; Wen, Y. A novel graphene-like titanium carbide MXene/Au–Ag nanoshuttles bifunctional nanosensor for electrochemical and SERS intelligent analysis of ultra-trace carbendazim coupled with machine learning. *Ceram. Int.* **2021**, *47*, 173–184. [CrossRef]

30. Hu, M.; Li, Z.; Hu, T.; Zhu, S.; Zhang, C.; Wang, X. High-Capacitance Mechanism for $Ti_3C_2T_x$ MXene by in Situ Electrochemical Raman Spectroscopy Investigation. *ACS Nano* **2016**, *10*, 11344–11350. [CrossRef]
31. Le Ru, E.; Etchegoin, P. *Principles of Surface-Enhanced Raman Spectroscopy: And Related Plasmonic Effects*; Elsevier: Amsterdam, The Netherlands, 2008.
32. Liu, R.; Jiang, L.; Lu, C.; Yu, Z.; Li, F.; Jing, X.; Xu, R.; Zhou, W.; Jin, S. Large-scale two-dimensional titanium carbide MXene as SERS-active substrate for reliable and sensitive detection of organic pollutants. *Spectrochim. Acta Part A Mol. Biomol. Spectrosc.* **2020**, *236*, 118336. [CrossRef] [PubMed]
33. Elumalai, S.; Lombardi, J.R.; Yoshimura, M. The surface-enhanced resonance Raman scattering of dye molecules adsorbed on two-dimensional titanium carbide $Ti_3C_2T_x$ (MXene) film. *Mater. Adv.* **2020**, *1*, 146–152. [CrossRef]
34. Mauchamp, V.; Bugnet, M.; Bellido, E.P.; Botton, G.A.; Moreau, P.; Magne, D.; Naguib, M.; Cabioc'h, T.; Barsoum, M.W. Enhanced and tunable surface plasmons in two-dimensional Ti_3C_2 stacks:Electronic structure versus boundary effects. *Phys. Rev. B* **2014**, *89*, 235428. [CrossRef]
35. Lashgari, H.; Abolhassani, M.R.; Boochani, A.; Elahi, S.M.; Khodadadi, J. Electronic and optical properties of 2D graphene-like compounds titanium carbides and nitrides: DFT calculations. *Solid State Commun.* **2014**, *195*, 61–69. [CrossRef]
36. Kumada, N.; Tanabe, S.; Hibino, H.; Kamata, H.; Hashisaka, M.; Muraki, K.; Fujisawa, T. Plasmon transport in graphene investigated by time-resolved electrical measurements. *Nat. Commun.* **2013**, *4*, 1363. [CrossRef]
37. Frish, M.J.; Trucks, G.W.; Schlegel, H.B.; Scuseria, G.E.; Robb, M.A.; Cheeseman, J.R.; Scalmani, G.; Barone, V.; Mennucci, B.; Paterson, G.A. *Gaussian 09, Revision A.02*; Gaussian Inc.: Wallingford, CT, USA, 2009.
38. Alhabeb, M.; Maleski, K.; Anasori, B.; Lelyukh, P.; Clark, L.; Sin, S.; Gogotsi, Y. Guidelines for Synthesis and Processing of Two-Dimensional Titanium Carbide ($Ti_3C_2T_x$ MXene). *Chem. Mater.* **2017**, *29*, 7633–7644. [CrossRef]
39. Shekhirev, M.; Shuck, C.E.; Sarycheva, A.; Gogotsi, Y. Characterization of MXenes at every step, from their precursors to single flakes and assembled films. *Prog. Mater. Sci.* **2020**, *120*, 100757. [CrossRef]
40. Rasool, K.; Helal, M.; Ali, A.; Ren, C.; Gogotsi, Y.; Mahmoud, K. Antibacterial Activity of $Ti_3C_2T_x$ MXene. *ACS Nano* **2016**, *10*, 3674–3684. [CrossRef] [PubMed]
41. Xia, Y.; Mathis, T.S.; Zhao, M.Q.; Anasori, B.; Dang, A.; Zhou, Z.; Cho, H.; Gogotsi, Y.; Yang, S. Thickness-independent capacitance of vertically aligned liquid-crystalline MXenes. *Nature* **2018**, *557*, 409–412. [CrossRef]
42. El-Demellawi, J.K.; Lopatin, S.; Yin, J.; Mohammed, O.F.; Alshareef, H.N. Tunable Multipolar Surface Plasmons in 2D $Ti_3C_2T_x$ MXene Flakes. *ACS Nano* **2018**, *12*, 8485–8493. [CrossRef] [PubMed]
43. Halim, J.; Lukatskaya, M.R.; Cook, K.M.; Lu, J.; Smith, C.R.; Näslund, L.Å.; May, S.J.; Hultman, L.; Gogotsi, Y.; Eklund, P.; et al. Transparent Conductive Two-Dimensional Titanium Carbide Epitaxial Thin Films. *Chem. Mater.* **2014**, *26*, 2374–2381. [CrossRef]
44. Lioi, D.B.; Neher, G.; Heckler, J.E.; Back, T.; Mehmood, F.; Nepal, D.; Pachter, R.; Vaia, R.; Kennedy, W.J. Electron-Withdrawing Effect of Native Terminal Groups on the Lattice Structure of $Ti_3C_2T_x$ MXenes Studied by Resonance Raman Scattering: Implications for Embedding MXenes in Electronic Composites. *ACS Appl. Nano Mater.* **2019**, *2*, 6087–6091. [CrossRef]
45. Sarycheva, A.; Makaryan, T.; Maleski, K.; Satheeshkumar, E.; Melikyan, A.; Minassian, H.; Yoshimura, M.; Gogotsi, Y. Two-dimensional titanium carbide (MXene) as surface-enhanced Raman scattering substrate. *J. Phys. Chem. C* **2017**, *121*, 19983–19988. [CrossRef]
46. Chaudhuri, K.; Alhabeb, M.; Wang, Z.; Shalaev, V.M.; Gogotsi, Y.; Boltasseva, A. Highly Broadband Absorber Using Plasmonic Titanium Carbide. *ACS Photonics* **2018**, *5*, 1115–1122. [CrossRef]
47. Lotfi, R.; Naguib, M.; Yilmaz, D.E.; Nanda, J.; Van Duin, A.C. A comparative study on the oxidation of two-dimensional Ti 3 C 2 MXene structures in different environments. *J. Mater. Chem. A* **2018**, *6*, 12733–12743. [CrossRef]
48. Naguib, M.; Mashtalir, O.; Lukatskaya, M.R.; Dyatkin, B.; Zhang, C.; Presser, V.; Gogotsi, Y.; Barsoum, M.W. One-step synthesis of nanocrystalline transition metal oxides on thin sheets of disordered graphitic carbon by oxidation of MXenes. *Chem. Commun.* **2014**, *50*, 7420–7423. [CrossRef]
49. Hu, T.; Wang, J.; Zhang, H.; Li, Z.; Hu, M.; Wang, X. Vibrational properties of Ti_3C_2 and $Ti_3C_2T_2$ (T = O, F, OH) monosheets by first-principles calculations: A comparative study. *Phys. Chem. Chem. Phys.* **2015**, *17*, 9997–10003. [CrossRef]
50. Sang, X.; Xie, Y.; Lin, M.W.; Alhabeb, M.; Van Aken, K.L.; Gogotsi, Y.; Kent, P.R.; Xiao, K.; Unocic, R.R. Atomic Defects in Monolayer Titanium Carbide ($Ti_3C_2T_x$) MXene. *ACS Nano* **2016**, *10*, 9193–9200. [CrossRef] [PubMed]
51. Childres, I.; Jauregui, L.A.; Park, W.; Cao, H.; Chen, Y.P. Raman spectroscopy of graphene and related materials. *New Dev. Photon Mater. Res.* **2013**, *1*, 1–20.
52. Albrecht, A.C. On the theory of Raman intensities. *J. Chem. Phys.* **1961**, *34*, 1476–1484. [CrossRef]
53. Hirakawa, A.Y.; Tsuboi, M. Molecular geometry in an excited electronic state and a preresonance Raman effect. *Science* **1975**, *188*, 359–361. [CrossRef]
54. Hu, M.; Hu, T.; Li, Z.; Yang, Y.; Cheng, R.; Yang, J.; Cui, C.; Wang, X. Surface functional groups and interlayer water determine the electrochemical capacitance of $Ti_3C_2T_x$ MXene. *ACS Nano* **2018**, *12*, 3578–3586. [CrossRef] [PubMed]
55. Sarycheva, A.; Gogotsi, Y. Raman Spectroscopy Analysis of the Structure and Surface Chemistry of $Ti_3C_2T_x$ MXene. *Chem. Mater.* **2020**, *32*, 3480–3488. [CrossRef]
56. Wang, H.W.; Naguib, M.; Page, K.; Wesolowski, D.J.; Gogotsi, Y. Resolving the structure of $Ti_3C_2T_x$ mxenes through multilevel structural modeling of the atomic pair distribution function. *Chem. Mater.* **2016**, *28*, 349–359. [CrossRef]

57. Ibragimova, R.; Puska, M.J.; Komsa, H.P. pH-dependent distribution of functional groups on titanium-based MXenes. *ACS Nano* **2019**, *13*, 9171–9181. [CrossRef]
58. Wilson, E.B. The Normal Modes and Frequencies of Vibration of the Regular Plane Hexagon Model of the Benzene Molecule. *Phys. Rev.* **1934**, *45*, 706–714. [CrossRef]
59. Adomavičiūtė, S.; Velička, M.; Šablinskas, V. Detection of aspirin traces in blood by means of surface-enhanced Raman scattering spectroscopy. *J. Raman Spectrosc.* **2020**, *51*, 919–931. [CrossRef]
60. Mashtalir, O.; Naguib, M.; Mochalin, V.N.; Dall'Agnese, Y.; Heon, M.; Barsoum, M.W.; Gogotsi, Y. Intercalation and delamination of layered carbides and carbonitrides. *Nat. Commun.* **2013**, *4*, 1716. [CrossRef] [PubMed]
61. Naguib, M.; Come, J.; Dyatkin, B.; Presser, V.; Taberna, P.L.; Simon, P.; Barsoum, M.W.; Gogotsi, Y. MXene: A promising transition metal carbide anode for lithium-ion batteries. *Electrochem. Commun.* **2012**, *16*, 61–64. [CrossRef]
62. Ghidiu, M.; Lukatskaya, M.R.; Zhao, M.Q.; Gogotsi, Y.; Barsoum, M.W. Conductive two-dimensional titanium carbide 'clay'with high volumetric capacitance. *Nature* **2014**, *516*, 78–81. [CrossRef] [PubMed]

6th publication / 6 publikacija

Progress and Insights in the Application of MXenes as New 2D Nano-Materials Suitable for Biosensors and Biofuel Cell Design

Simonas Ramanavičius, Arūnas Ramanavičius
Int. J. Mol. Sci. 2020, 21(23), 9224
Reprinted by permission
The article could be find online at https://doi.org/10.3390/ijms21239224

International Journal of
Molecular Sciences

MDPI

Review

Progress and Insights in the Application of MXenes as New 2D Nano-Materials Suitable for Biosensors and Biofuel Cell Design

Simonas Ramanavicius [1,2] and Arunas Ramanavicius [2,*]

[1] Center for Physical Sciences and Technology (FTMC), Sauletekio av. 3, LT-10257 Vilnius, Lithuania; simonas.ramanavicius@ftmc.lt

[2] Institute of Chemistry, Department of Physical Chemistry, Faculty of Chemistry and Geosciences, Vilnius University, Naugarduko 24, LT-03225 Vilnius, Lithuania

[*] Correspondence: Arunas.Ramanavicius@chf.vu.lt; Tel.: +37-06-003-2332

Received: 11 November 2020; Accepted: 29 November 2020; Published: 3 December 2020

Abstract: Recent progress in the application of new 2D-materials—MXenes—in the design of biosensors, biofuel cells and bioelectronics is overviewed and some advances in this area are foreseen. Recent developments in the formation of a relatively new class of 2D metallically conducting MXenes opens a new avenue for the design of conducting composites with metallic conductivity and advanced sensing properties. Advantageous properties of MXenes suitable for biosensing applications are discussed. Frontiers and new insights in the area of application of MXenes in sensorics, biosensorics and in the design of some wearable electronic devices are outlined. Some disadvantages and challenges in the application of MXene based structures are critically discussed.

Keywords: MXenes; 2D-nanoparticles; 2D-nanomaterials; catalytic electrochemical biosensors; redox enzymes; nonstoichiometric titanium oxides TiO_{2-x}/TiO_2 and Ti_nO_{2n-1}; immunosensors; antibodies; enzymatic biofuel cells; microbial biofuel cells; bioelectrochemistry

---

1. Introduction

MXenes have appeared very recently (in 2011) as a new class of 2D materials with either metallic conductivity [1,2], or some attractive semiconducting properties, or both, which can be well exploited in the design of sensors, biosensors, biofuel cells and in the development of some wearable bioelectronic devices. MXenes have some structural relation and even similarity of some physical properties with other 2D materials such as graphene [3,4]. Most MXenes are based on 2D transition metal carbides [2]. The most of MXenes are based on 2D transition metal nitrides carbonitrides are appointed to this class of MXene materials [5]. MXenes are usually prepared by etching of initial materials, called “MAX phases”, which can be presented by generalized formula $M_{n+1}AX_n$ in which “M” representing the transition metals (that are Ti, Sc, Zr, Cr, V, Mn, Hf, Nb, Mo or Ta), “A” is an element from group 12, 13, 14, 15 or 16 (that are Al, Cd, Si, S, P, Ga, As, Ge, In, Tl, Sn or Pb) in the periodic table, “X” is either carbon (C), nitrogen (N) or a mixture of both of them [6–9], and “n” in this formula can be in the range of 1–3 [6,7,9–11] (Figure 1).

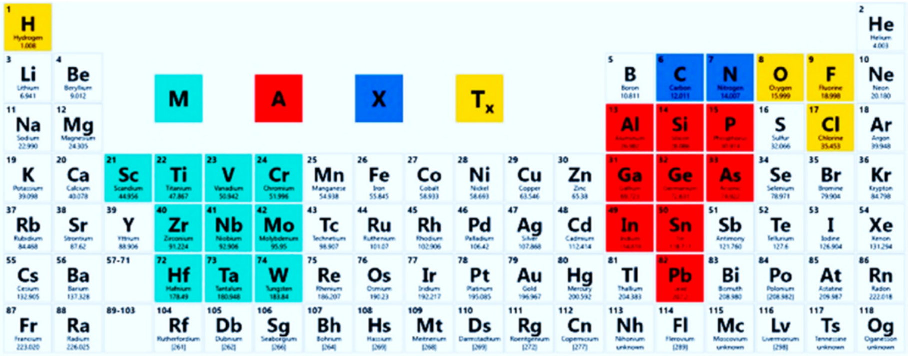

Figure 1. The composition of MXenes and MAX phases from the periodic table. Reprinted from [12].

It should be noted that MAX phases are characterized by metal-like electrical/thermal conductivity behavior and they are mostly chemically stable materials. MXenes possess great and rather unusual physical and chemical properties that can be well adapted for the design of electrochemical sensors and biosensors. The properties of MXenes can be well tailored through proper variation of M and X elements in MXene structure and by the introduction of various surface terminal groups [13–15]. Due to this option of applying very different surface “finishing”, recent advances in surface chemistry enables the introduction of particular surface “terminal functional groups” [13–15], which can be suitable for the immobilization of enzymes and some other proteins. Hence, MXenes can be efficiently modified by particular biomolecules and many other compounds that are required for the action of biosensors. In addition, the above mentioned “terminal functional groups” can provide tailored electronic, electrochemical and optical properties to MXene-based biosensing structures [13–15]. Optical properties of MXenes are highly applicable for biosensing purposes [16], especially those which are based on fluorescence resonance energy transfer and induce changes in photoluminescence signal [17]; however, the applicability of MXenes in optical biosensors is well reported in specialized review [18], therefore, in this paper we are not aiming to address many details of optical MXene-based biosensors. In some researches [19–27] and reviews [18,28] it is reported, that MXenes are compatible with enzymes and other protein molecules, which are used in the development of catalytic biosensors and affinity sensors. Biocompatibility of MXenes towards some microorganisms [29,30] and even towards mammalian neural cells [31], was also determined. Catalytic activity has been reported for some MXenes, but immobilized enzymes and microorganisms can significantly extend the ability to utilize significantly broader ranges of substrates, which can provide chemical energy for biofuel cells. Bioelectronics devices dependent on the type of applied bio-recognition elements can be divided into several classes, such as: (i) catalytic sensors and biofuel cells based on enzymes [32] and non-enzymatic structures [33], (ii) whole-cell-based biosensors and biofuel cells [34], (iii) affinity sensors based on immobilized antibodies or antigens (immunosensors) [35], (iv) immobilized single stranded DNA (ssDNA)-based sensors (DNA-sensors) [36], molecularly imprinted polymer-based sensors, [37] et cetera. Applicability of various nanomaterials in some of these classes of biosensors has been demonstrated [38]. Some researchers predicted that MXenes will form the basis for various MXene nanocomposites and development of commercially available MXene-based biosensors [39]. Therefore, in this review we are addressing recent advances in the applicability of MXenes in these areas and are predicting future developments in this expanding area.

The aim of this review is to present insights for the applicability of MXenes in the design of biosensors and biofuel cells. A very attractive property of biofuel cells is that they operate at room temperature and are capable of producing electricity from highly diluted solutions of chemical fuels.

2. Catalytic Sensors Based on Enzymes

Catalytic sensors based on enzymes and some other redox proteins have several advantages over other analytical systems because they can provide high selectivity. One of the mostly expanded areas of enzymatic sensors is related to the development of electrochemical sensors and advantages of such sensors are based on low costs, simple operation and ability to being applied for the evaluation of optically badly transparent and turbid samples, for example, blood. Moreover, recently implantable biosensors are appearing in the market and these require biocompatible materials for the design of electrodes and biofuel cells, which will supply power for these implantable devices. Therefore, efficient charge transfer between electrodes and immobilized enzymes is very important issues [40,41]. Moreover, sometimes it is possible to establish direct charge transfer (DCT), which is sometimes called direct electron transfer but this fact is not always correct, because our recent researches show that sometimes DCT is established between p-type semiconducting polymers and redox enzyme, glucose oxidase (GOx) [42,43]. The establishment of direct charge transfer (DCT) between redox enzymes enables exploiting of inherent thermodynamic potential of the enzyme-catalyzed reaction in the design of electrochemical-catalytic biosensors and all types of biofuel cells, which in the most optimal cases are free of soluble redox mediators [40,41,44–46]. Cytochromes can be applied in the design of enzymatic sensors and biofuel cells as catalysts and as redox mediators that are capable of establishing DCT between enzymes and electrodes [32]; and due to this charge-transfer based interaction they can change the optical properties of either Ti_3C_2 MXene based ultra-thin nanosheets, quantum dots, or both, which were applied in the design of biosensors dedicated to the determination of human papilloma virus [47] and trypsin [48]. Charge transfer property was also applied in the design of glucose sensors, where titanium carbide based MXenes were combined with red-emitting carbon dots [49]. Hence, the application of MXenes in DCT-based systems is rather promising; the Nafion stabilized $Ti_3C_2T_x$-based MXene (where T_x was some transition metal) was applied for sensing of dopamine [50], and electrochemical characterization of glassy carbon electrode (GCE) modified by Nafion (Nafion/$Ti_3C_2T_x$/GCE) revealed large surface area, large intrinsic conductivity and low charge transfer resistance. Therefore, it was predicted that MXenes can be well implemented into the construction of enzymatic sensors and biosensors and probably direct charge transfer between MXenes and some redox enzymes can be established. However, establishment of DCT between redox enzymes and solid electrodes is rarely possible, because redox-active sites of most enzymes are rather deeply encapsulated within "electrically insulating" protein structures, which have low electric permittivity (ε) [51,52]. Therefore, various soluble redox mediators are applied in the design of such biosensors [53] and biofuel cells [32]. However, soluble redox mediator based strategies are not very efficient, therefore, some conducting nanomaterials including carbon nanotubes [54], gold nanoparticles [44], conducting polymers [55] and very recently, MXenes, can be applied for the purpose of either establishing direct charge transfer between redox enzymes and electrode surfaces, facilitating charge transfer from products formed during enzymatic reaction [56–59], or both. An even more complicated situation is charge transfer from microorganisms because most of them are wrapped within an "electrically insulating" layer of polysaccharides [60,61], but recently we have found how conductivity of cell-walls can be improved by the formation of conducting polymer nanoparticles [60,62] and even some larger structures [61] within the cell wall of microorganisms, and in such a way the conductivity of this initially nonconducting structure can be remarkably improved [34,63]. This formation of conducting polymers can be induced by the metabolic cycle of these microorganisms [64] and conducting polymer-based structures are well distributed within either cell wall, in the periplasm of microorganism [62,65], or both.

Ti_3C_2-based MXene was used for the immobilization of tyrosinase within the pre-adsorbed chitosan (CS) layer and Tyr/MXene/CS/GCE was applied for the determination of phenol in water with sensitivity of 414.4 mA M, linear range between 0.05–15.5 mM and with LOD of 12 nM [21]. Drop-casting based dispersion was performed and electrostatic effects between MXene and tyrosinase enabled proper orientation of the enzyme during the immobilization and preserved catalytic activity of immobilized tyrosinase; therefore, very efficient direct charge transfer between tyrosinase and the electrode has been established [19,66].

It should be noted that not only electrons, but holes, can be involved in direct charge transfer within redox enzyme structure and at interphase between enzyme and electrode [42,43], therefore, MXenes in this charge-transfer related context are especially interesting, because they can act as metallic conductors with varied conductivity, which depends on applied "M" and "X" elements in the structure of MXenes ($M_{n+1}X_nT_x$) and covalent surface modifications in their structure [67]. It is remarkable that covalent surface modifications in the structure of MXenes enable achieving superconductivity [67]. The redox-ability, in addition to good conductivity, enables MXenes to facilitate electrochemical redox processes [68]. Hence, some attempts to demonstrate the applicability of MXenes in the design of redox mediator free sensors was demonstrated [19,31] and discussed [5,69], which promises great applicability for MXenes to be applied in various bioelectronics devices including biosensors and biofuel cells. It was demonstrated that if some redox enzymes are trapped within MXene sheets, then rather efficient charge transfer from the active site of enzyme towards electrode can be achieved due to the sufficient mobility of charge within MXene-based structure [70]. In this way β-hydroxybutyrate dehydrogenase decorated MXene nano-sheets were applied for the amperometric determination of β-hydroxybutyrate [71].

MXene and platinum nanoparticle (PtNPs) based nanocomposite was developed and deposited on GCE electrode (Ti_3C_2T/PtNPs/GCE) [27], PtNPs significantly enhanced electro-catalytic activity of this MXene-based electrode, and it was sensitive to various compounds that are important during the development of biosensors and biofuel cells, including dopamine, ascorbic acid, uric acid, acetaminophen and H_2O_2. Such advantageous sensitivity of Ti_3C_2T/PtNPs/GCE electrodes can be potentially adapted for the design of biofuel cell cathodes.

An electrochemical biosensor based on MXene/DNA/Pd/Pt/GCE electrode was developed and applied for amperometric determination of dopamine in the range between 0.2 and 1000 mM with LOD of 30 nM [72]. In this research DNA was important for the dispersion of Ti_3C_2-based nano-sheets and formation of Pd and Pd/Pt structures, while Ti_3C_2-based MXene acted as a conducting support. However, this MXene/DNA/Pd/Pt/GCE structure was highly sensitive to glucose, uric acid and ascorbic acid. Therefore, this structure is probably better suited for development of biofuel cells, which will be able to consume much broader ranges of biological fuels.

In many researches it was demonstrated that if electrochemically active surface areas of electrode are not sufficient, then a decoration by metal nanoparticles [52,56,58] or some other nanoparticles can be applied in order to increase catalytic activity and thus the currents registered by electrodes modified by enzymes. A similar strategy was applied during the development of some MXene-based catalytic sensors [31,73]. Ti_3C_2-based MXene modified by gold nanoparticles (AuNPs) was applied for the Nafion-based immobilization of glucose oxidase (GOx) in order to design a biosensor for the determination of glucose, which was based on Nafion/GOx/AuNPs/Ti_3C_2/GCE structure [31]. It was predicted that in this structure, AuNPs are involved in charge transfer between the catalytic site of the enzyme and electrode. In another research, GOx was entrapped within three-dimensional porous $Ti_3C_2T_x$ MXene, graphene hybrid films, and also applied for glucose determination [74].

Amperometric biosensor based on acetylcholinesterase (AChE) immobilized on $Ti_3C_2T_x$ and chitosan (CS) modified glassy carbon electrode (AChE/CS/$Ti_3C_2T_x$/GCE) has been developed and applied for the determination of organophosphorus pesticide—malathion [26]. CS/$Ti_3C_2T_x$-based heterostructures provided great environments for the immobilized AChE. A similar AChE/CS/$Ti_3C_2T_x$/GCE-heterostructure was applied for the determination of malathion in tap water [73], while acetylcholinesterase (AChE) immobilized on $Ti_3C_2T_x$ modified by silver nanoparticles (AgNPs) was developed and also applied for differential pulse voltammetry (DPV)-based determination of organophosphate pesticide – malathion [75]. In this sensor, negatively charged acetylcholinesterase was electrostatically attracted to the surface of positively charged Ag/$Ti_3C_2T_x$-composite, which improved charge transfer from acetylcholinesterase.

Electrochemical biosensors based on acetylcholinesterase, MnO_2/Mn_3O_4 micro-cuboids, AuNPs and MXenes (AChE/CS/Ti_3C_2/AuNPs/MnO_2/Mn_3O_4/GCE) were developed for the determination of some organophosphate—methamidophos, which has acted as inhibitor of immobilized enzyme—AchE [76]. Some researchers are reporting that anodic potentials, which are exceeding +200 mV, lead to the oxidation of its outer surface of Ti_3C_2T-based MXenes and can be applied for the oxidation of NADH [20]; this remarkable finding is eternally important for the development of enzyme- and microorganism-based biofuel cells because the NAD/NADH system can be served as redox mediator for many enzymes and redox-proteins, and in addition, NAD is a cofactor of NAD-dependent enzymes.

The application of MXenes for the design of catalytic sensors based on enzymes seems rather effective due to metallic conductivity of these compounds.

Ti_3C_2-based MXene, which was modified by Persian blue (PB), was applied in the design of "wearable" electrochemical biosensors [77] and showed good sensitivity to glucose and lactose applied MXene increased immobilization efficiency of immobilized enzyme, permeability of oxygen into biosensing structure, where it has taken part in the charge transfer from GOx. These sensors were integrated within flexible polymeric structures and used as wearable biosensing devices for the determination of lactose and glucose in actual concentration range of 1–20 mM with the sensitivity of 11.4 mA × mM^{-1} × $1cm^{-2}$ and 35.3 mA × $mM^{-1}cm^{-2}$, respectively.

Two types of screen-printed-electrodes: (i) urease, methylene blue (MB), and $Ti_3C_2T_x$ based screen-printed-electrode (urease/MB/MXene/SPE); and (ii) $Ti_3C_2T_x$ based screen-printed-electrode (MXene/SPE) were designed and applied in microfluidic electrochemical systems dedicated to continuous monitoring of urea and creatinine in whole blood were developed [78]. During the development of this biosensor enzyme, urease was immobilized using glutaraldehyde as a cross-linking agent, which binds enzymes well on electrode surfaces [58]. The first electrode based on urease/MB-MXene deposited on a screen printed electrode was used for the determination of urea in the range of 0.1–3 mM and the second one, MXene deposited on screen printed electrode, was used for the determination of creatinine in the range of 0.02–1.2 mM; in this electrode MXene was served as the electro-catalyst. These electrodes are incorporated within a microfluidic system and applied for the determination of urea and creatinine in whole blood. It is very remarkable that some MXenes involved in composite structures are exhibiting peroxidase-like activity and have been applied in the design of biosensors, for example, MXene-Ti_3C_2/CuS nanocomposite based sensor dedicated to colorimetric determination of cholesterol [79] and lactate dehydrogenase (LDH) based heterostructure of a MXene@NiFe-LDH for the detection of glutathione [80].

Nowadays some sensors are implantable; therefore, biocompatibility aspects of such sensors are very important. Here MXenes are especially welcome because some MXenes are biocompatible and almost non-toxic to some living cells such as mouse preosteoblast cell and mouse fibroblast cell lines [81] and mammalians such as mice [82]. However, despite some positive results, further investigations on biocompatibility of MXenes in both in vitro and in vivo toxicity assessment based on the determination of either reproductive toxicity, genotoxicity, or both, are needed before the design of implantable MXene-based biosensors and biofuel cells.

3. Direct Charge Transfer between Redox Proteins and MXenes

Direct charge transfer was observed in electrochemical biosensors based on Ti_3C_2 MXene deposited on glassy carbon electrode (GCE) and modified by immobilized hemoglobin (Hb) and Nafion in order to establish a Nafion/Hb/Ti_3C_2/MXene/GCE-based structure [22]. This sensor was suitable for the determination of nitrite in water samples. Catalytic activity of NO_2^- reduction in this sensor [19] was based on proton-coupled reaction [83]. The other research group designed a mediator-free enzymatic electrochemical biosensor based on Ti_3C_2 MXene and immobilized hemoglobin and reported the sensitivity of this sensor towards hydrogen peroxide (H_2O_2), with linear range between 0.1 and 260 mM [22]; the authors speculated that this structure exhibits some "organ-like" properties because it shows high efficiency towards reduction of hydrogen peroxide. This efficiency was achieved due to exfoliation of the MAX-phase, and it was determined that even layers that are thinner than 20 nm still show very high catalytic activity [22]. Exfoliation of separated sheets is observed each time when MXenes are formed [84,85], and there are some evidences that MXenes are providing both compatible environments for immobilized proteins where they retain catalytic activity, very large surface area (Figure 2a) and some functional groups, which can be used for the immobilization of enzymes (Figure 2b) [77].

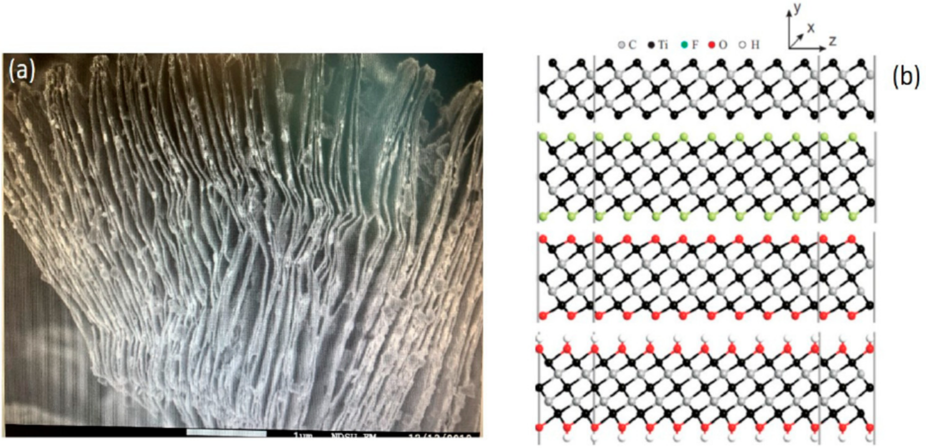

Figure 2. 2D multi-layered Ti_3C_2 MXene sheets (**a**) scanning electron microscopy image; (**b**) pristine and surface-terminated Ti_3C_2 MXene with different functional groups. Reprinted from [86].

It should be noted that hemoglobin (Hb) is a very suitable candidate for the development of cathodes for biofuel cells [32]; therefore, this MXene/Hb based electrode seems very pertinent for the design of biofuel cells. It was demonstrated that even better current density can be achieved if, instead of bare Ti_3C_2, a heterostructure based on TiO_2-Ti_3C_2 nanocomposite is deposited on the GCE electrode and later it is modified by hemoglobin [22]. In this research, a designed Nafion/Hb/TiO_2-Ti_3C_2-structure based biosensor was characterized by good sensitivity (of 447.3 mA × mM^{-1} × cm^{-2}) towards H_2O_2 with a linear range of 0.1–380 mM, and LOD of 14 nM [22]. The Nafion/Hb/TiO_2-Ti_3C_2/GCE biosensor [22] showed much better long-term stability in comparison with previously described Nafion/Hb/Ti_3C_2/GCE biosensors [22]. It seems that TiO_2 significantly improves the biocompatibility and can advance the conductivity of the formed structure, especially if the nonstoichiometric form of titanium oxide TiO_{2-x}/TiO_2 is formed, which increases both conductivity and catalytic activity of formed heterostructures [87]. This effect is based on the fact that the TiO_{2-x}/TiO_2^- based structure has rather high concentrations of "oxygen vacancies", which are responsible for n-type charge mobility in this semiconducting heterostructure [88]. Very recently, in one research conducted by our group, we predicted that such oxygen vacancies are providing increased sensitivity towards some reducing and oxidizing gases and VOCs [87]. These TiO_2-based structures can be reduced and can form nonstoichiometric titanium oxides (TiO_{2-x}), which can be partly based on Magnéli phases with stoichiometry of Ti_nO_{2n-1} [89,90]. It was determined that in the TiO_{2-x} structure, which has a rather low "x" value varying between 0 and 0.10, therefore, so called "point defects" dominate in TiO_{2-x} crystal structure [91], and such structures possess high numbers of interstitials based on either Ti^{3+} and Ti^{4+}, great ability of oxygen vacancies, or both. The concentration of above mentioned defects in the crystal structure of TiO_{2-x} is increased by increased "oxygen deficiency" rate. Some researches revealed that in Magnéli phases having rather high "x" values between 0.10 and 0.34 crystallographic shear planes are significantly extended [92]. These TiO_{2-x} heterostructures are stable, therefore, they are finding many applications in catalytic decontamination of waste-water and in the development of batteries and fuel cells [93,94]. Hence, there are some expectations that these physical properties of TiO_{2-x}/TiO_2-based heterostructures will improve performance of some MXene-based sensors and biosensors based on enzymes that are exhibiting direct charge transfer [40,41]. There are some indications that tungsten-based MXenes [95] can be advanced by the incorporation of either stoichiometric, nonstoichiometric tungsten oxide, or both [96,97], and will find some applications in the development of biofuel cells. The application of ink-jet printed MXene with graphene oxide heterocomposite (Ti_3C_2/GO) was also modified with Hb [23] and applied in biosensors for the determination of H_2O_2. Sensitivity of MXenes towards pH [98] can be well exploited in the design of some biosensors based on enzymes with pH that changes during catalytic action.

4. Affinity Sensors Based on MXenes Modified by Immobilized Affinity Agents

Affinity sensors are analytical devices, which specifically recognize analyte and form stabile complexes with analytes. According to applied analyte-binding, affinity sensors are classified into immunosensors, DNA-sensors, RNA-sensors and molecularly imprinted polymer based sensors. In some recent researches it was demonstrated that MXenes can be applied in the design of various affinity sensors. A very promising direction here is to design artificial biological recognitions systems based on molecularly imprinted polymers (MIPs) which were developed for proteins [99], DNA-based structures [100], but MIP-based sensors work especially well for the determination of small molecular weight analytes such as caffeine [101], theophylline [102], et cetera. In this research direction, hierarchical porous MXene/amino carbon nanotubes-based molecular imprinting sensor for the determination of low molecular mass analyte, fisetin, has also already been reported [103]. However, larger molecular mass analytes such as proteins were also determined by some MXene-based sensors based on immobilized receptors, for example, Ti_3C_2-based MXene was modified by biological receptor after the activation with 3-aminopropyl triethoxysilane (APTES) in order to perform covalent binding, and it was applied in the design of affinity sensor [104] for the determination of cancer biomarker, carcinoembryonic antigen [105]. In this research it was reported that the carboxylic group of anti-carcinoembryonic-antibodies binds well to the amino group of f-Ti_3C_2 MXene and forms a covalent bond. Hexaammineruthenium ($[Ru(NH_3)_6]^{3+}$) was applied as a redox-probe for potentiodynamic measurement based determination of analytical signal. Authors declared extremely long linear detection range of this sensor, which was in the range from 10^{-13} to 2×10^{-6} ng/mL with great sensitivity of 37.9 mA ng/mL $\times$ cm^{-2} per one decade of concentration with extremely low LOD of 0.000018 ng/mL. This sensor operated well in human serum samples. Application of MXenes for the design of affinity sensors based on antibodies and some other affinity agents offers new avenues for the development of efficient affinity sensors. MXenes were applied for the design of chimeric DNA-functionalized sensors for mapping of some cancer biomarkers in living cells [106] and DNA-sensors suitable for the determination of label-free mismatches of DNA in real human samples [107]. RNA sensors based on the application of MXenes were also reported where a novel label-free electrochemical strategy for the determination of miRNA-182 detection based on MoS_2/Ti_3C_2 nanohybrids was applied [108]. microRNA-155 detection based on AuNPs/Ti_3C_2 MXene three-dimensional nanocomposite for exonuclease III-aided cascade target recycling was designed [109] and oncomiRs detection based on synergetic signal amplification AuNPs/MXene were reported [110]. Very different application of DNA-based structures (such as DNA-aptamers) in the design of bio-recognition elements was applied in sensors dedicated to rapid electrochemical detection of thyroxine [111]. In another research, Ti_3C_2-based MXene was modified by DNA-aptamer applied in luminol-based chemo-luminescence based affinity sensor for the determination of MCF-7 exosomes [112], which established highly sensitive electro-generated chemo-luminescence. A glassy carbon electrode was modified by poly-nisopropylacrylamide/Au, which has provided a higher concentration of carboxyl available for covalent immobilization of DNA-aptamer, which has selectively recognized MCF-7 exosomes with LOD of 125 particles per mL^{-1}.

Moreover, a label-free electrochemical biosensor for highly sensitive detection of gliotoxin based on DNA nanostructure/MXene nanocomplexes was also reported [113].

MXene-based structures are able to selectively adsorb different molecules through physical adsorption or electrostatic attraction, and lead to a measurable change in the conductivity of the material with high signal-to-noise ratio and excellent sensitivity (Figure 3). Therefore, sensors based on 2-dimensional Ti_3C_2 MXene-based nanosheets were characterized by good sensitivity and selectivity towards PGE2 and 8-HOA, which are both present in A549 lung cancer cells [86].

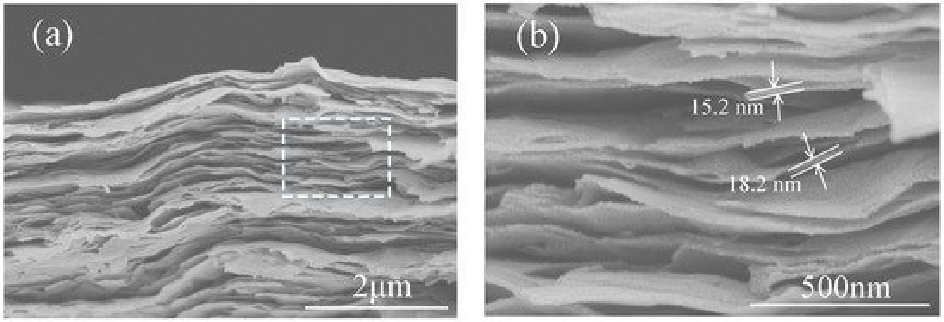

Figure 3. SEM images of (**a**) a cross-section of $Ti_3C_2T_x$ film and (**b**) an enlarged part with estimated flake thickness. Reprinted from [114].

5. Non-Enzymatic Biosensors Cell Electrodes

Non-enzymatic biosensors and biofuel cell electrodes are electrochemical systems which are suitable for the determination of biological compounds and catalyze spontaneous oxidation/reduction of various biological compounds by generation of substantial potential (in the range of 50–1200 mV) and electrical current. Nonezymatic glucose sensors based on application of Ni-nanoparticle/polypyrrole composite was reported recently by our group [33]. The application of MXenes in non-enzymatic glucose sensors also seems very promising as it was demonstrated by the application of three-dimensional porous MXene/NiCo-LDH composite in the design of high performance non-enzymatic glucose sensors [115]. However, despite mentioned achievements, until recently most glucose oxidase (GOx) based sensors used are in this area [40–46], and during catalytic action of GOx as well as by action of many other oxidases hydrogen peroxide (H_2O_2) is produced. Some recent reports in this area illustrate that hydrogen peroxide can be easily determined by non-enzymatic PB/Ti_3C_2 hybrid nanocomposite [116].

In order to design other non-enzymatic sensors, MXene was introduced into graphite composite paste in order to design (MXene/GCPE)-electrodes, which were sensitive to adrenaline by chronoamperometry with LOD of 9.5 nM [117]. Very efficient determination of adrenaline, serotonin and ascorbic acid was achieved by differential pulse voltammetry (DPV), which enabled separate characteristic DPV-peaks for adrenaline, serotonin and ascorbic acid.

Screen-printed electrodes modified by $Ti_3C_2T_x$ MXene modified (MXene/SPE) were applied for simultaneous detection of acetaminophen and isoniazid drugs [118]. DPV was applied as a detection method, which enabled distinguishing of characteristic DPV-peaks of acetaminophen and isoniazid with linear range between 0.25 and 2000 mM and LOD of 0.048 mM for acetaminophen and linear range between 0.1 and 4.6 mM and LOD of 0.064 mM for isoniazid.

Several MXene-based NH_3 sensors were developed, where the remarkable properties of MXenes to adsorb gaseous materials were well exploited [119,120]. Moreover, catalytic properties of MXenes can be exploited for catalytic determination of various chemical and biochemical compounds [69].

6. Immobilization of Enzymes and Affinity-Agents on MXenes

Oriented immobilization is a very important issue in the design of enzymatic immunosensors and biofuel cells [32]. Well oriented enzymes exhibit sufficient activity, because in such cases the substrate has good access into active sites with lower diffusional limitations in comparison, when the enzyme's active center is oriented upside down and oriented towards the electrode. The only exception is when the direct charge transfer is observed between electrode and enzyme, then the orientation is playing a different role; therefore, the active redox center should be oriented towards the electrode [40,41]. The advantage of MXenes in the application of biofuel cells would be useful for the adsorption of redox enzymes within 2D planes [121–123], because in such a system the orientation of enzymes would play a less critical role and in such a way MXene 2D planes will significantly increase the electrochemically active surface area of electrodes [3]. It is remarkable that MXenes are suitable to be applied for both anodic and cathodic potentials [124]. This property is highly appreciable for the development of biofuel cells because both electrodes can be based on very similar kinds of modifications and can be used for similar enzyme or cell immobilization procedures.

Rather unusual morphology and the ability of MXenes to be split into multiple one dimensional planes [125] (Figures 2 and 3) during the preparation of these materials, enables "to load" MXene-based matrix by high concentrations of enzymes and microorganisms, which together with remarkable metallic conductivity of MXenes increases the applicability of these materials for the design of both enzymatic and microbial biofuel cells. It is remarkable that MXenes offer a good environment for immobilized enzymes or other proteins, which enables retaining sufficient catalytic activity [69,73]. However, up to now, only rather small sheets of MXenes were developed (up to maximum 1 µm in length and width), therefore, they can just be treated as deposits on other substrates.

During the design of immunosensors and affinity sensors, the proper side of the affinity site of antibodies or other receptors should be oriented towards the solution with the analyte, which can be achieved by proper terminal groups of MXenes that are mostly suitable for covalent attachment [13–15]. Some affinity sensors have been designed by the immobilization of affinity-agents by simple adsorption on the surface of working electrode, which was modified by MXene-based sheets [31]. However, this strategy is not very efficient due to the random orientation of these affinity-agents, therefore, improved strategies, which enable orientation of antibodies should be adapted for the development of more efficient affinity sensors [126,127]. A number of such strategies were reported in a targeted review dedicated to the development of immunosensors based on oriented antibodies by Ramanaviciene and Makaraviciute [127] and in their experimental works it was well demonstrated that whole antibodies [128], receptors [129] and some particular parts of antibodies, which were chemically split into two or four pieces [126,127], can be immobilized in oriented-fashion on electrode surfaces. It should be noted that MXenes formed by chemical etching usually possess various surficial functional groups, mostly fluorine (−F) hydroxyl (−OH) or oxygen (−O) [130–132] (Figure 4). It is related to the chemical formula of MXenes, which is "Mn+1XnTx", where T indicates surficial functional groups. Ti_3C_2 MXene formed by chemical etching can be based on the following three structures: $Ti_3C_2(OH)_2$, $Ti_3C_2O_2$ and $Ti_3C_2F_2$ (Figure 4) [133]. The quantity and structure of terminal groups is mostly influenced by the synthesis protocol; therefore, the structure of terminal groups can be tailored, which is very important for the covalent immobilization of proteins (e.g., antigens or antibodies), which are used in immunosensor design as biological recognition parts [35].

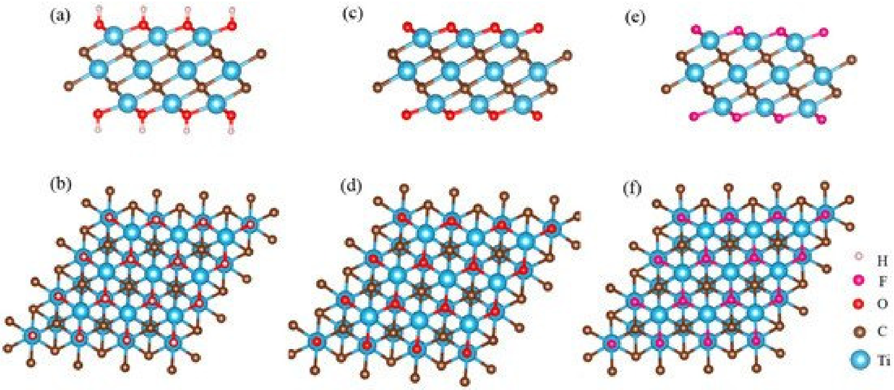

Figure 4. The structure of Ti_3C_2 nanosheets with different functional groups from side and top views: (**a**,**b**) $Ti_3C_2(OH)_2$; (**c**,**d**) $Ti_3C_2O_2$ and (**e**,**f**) $Ti_3C_2F_2$. Reprinted from [133].

Ti_3C_2-based MXene was applied in the design of biomimetic-sensors, which was based on adenosine triphosphate (ATP) deposited on MXene surface and then modified by $Mn_3(PO_4)_2$; this system was applied for amperometric determination of superoxide anions (O_2^-) [134], which were generated by HepG2 cells. In this chemical sensor, $Mn_3(PO_4)_2$ was sensing superoxide (O_2^-) in the range between 2.5 and 14 mM, sensitivity of 7.86 mA $\times$ mM^{-1} $\times$ cm^{-2} and LOD of 0.5 nM. In addition to amperometric measurements, capacitance measurements can also be applied due to high capacitance storage ability of MXenes; in this direction, Ti_3C_2 MXene nanosheet-based immunoassay with tyramine-enzyme repeating detection of prostate-specific antigens on interdigitated micro-comb electrodes was designed [135].

7. Conclusions and Future Trends

MXenes are 2D-materials, which show real potential for the application in the design of biosensors, biofuel cells and bioelectronics. MXenes are opening a new avenue for the development of conducting composites with metallic conductivity, which can advance sensing properties of amperometric enzymatic biosensors, because direct charge transfer between MXenes and heme-based redox proteins (hemoglobin) has already been reported. This finding opens a new avenue for the design of MXene-based biosensors and biofuel cells with other redox enzymes that are capable of direct charge transfer. Moreover, the advantage of MXenes in the application of biofuel cells would be their ability to adsorb redox enzymes within 2D planes (Figure 2), because in such a system the orientation of enzymes would play a less critical role, and in such way it will significantly increase electrochemically active surface areas of biofuel cell electrodes. The disadvantage of MXenes is that up now, only rather small sheets of MXenes were developed (up to maximum 1 µm in length and width).

Some terminal groups like −OH can be introduced into MXenes structures, which offers the possibility of immobilizing biological recognition exhibiting proteins in an oriented way; therefore, such ability can be well exploited for oriented immobilization of enzymes and antibodies. However, this property according to our best knowledge was never applied for the immobilization of biological recognition elements required for the design of enzymatic and affinity sensors.

Author Contributions: S.R. performed literature research, analysis, and drafted the paper. A.R. initiated and supervised the work and provided insights. All authors have read and agreed to the published version of the manuscript.

Funding: This research was funded by a grant (No. S-MIP-20-18) from the Lithuanian Research Council.

Conflicts of Interest: The authors declare no conflict of interest.

References

1. Naguib, M.; Kurtoglu, M.; Presser, V.; Lu, J.; Niu, J.; Heon, M.; Hultman, L.; Gogotsi, Y.; Barsoum, M.W. Two-Dimensional Nanocrystals Produced by Exfoliation of Ti_3AlC_2. *Adv. Mater.* **2011**, *23*, 4248–4253. [CrossRef]
2. Naguib, M.; Mashtalir, O.; Carle, J.; Presser, V.; Lu, J.; Hultman, L.; Gogotsi, Y.; Barsoum, M.W. Two-dimensional transition metal carbides. *ACS Nano* **2012**, *6*, 1322–1331. [CrossRef]
3. Naguib, M.; Mochalin, V.N.; Barsoum, M.W.; Gogotsi, Y. 25th Anniversary article, MXenes: A new family of two dimensional materials. *Adv. Mater.* **2014**, *26*, 992–1005. [CrossRef]
4. Naguib, M.; Gogotsi, Y. Synthesis of two-dimensional materials by selective extraction. *Acc. Chem. Res.* **2015**, *48*, 128–135. [CrossRef]
5. Deshmukh, K.; Kovárik, T.; Pasha, S.K.K. State of the art recent progress in two dimensional MXenes based gas sensors and biosensors: A comprehensive review. *Coord. Chem. Rev.* **2020**, *424*, 213514. [CrossRef]
6. Zhao, Y.; Watanabe, K.; Hashimoto, K. Self-supporting oxygen reduction electrocatalysts made from a nitrogen-rich network polymer. *J. Am. Chem. Soc.* **2012**, *134*, 19528–19531. [CrossRef]
7. Ghidiu, M.; Lukatskaya, M.R.; Zhao, M.Q.; Gogotsi, Y.; Barsoum, M.W. Conductive two-dimensional titanium carbide 'clay' with high volumetric capacitance. *Nature* **2014**, *516*, 78–81. [CrossRef]
8. Eklund, P.; Rosen, J.; Persson, P.O.Å. Layered ternary M n +1AX n phases and their 2D derivative MXene: An overview from a thin-film perspective. *J. Phys. D Appl. Phys.* **2017**, *50*, 113001. [CrossRef]
9. Magnusan, M.; Mattesini, M. Chemical bonding and electronic-structure in MAX phases as viewed by X-ray spectroscopy and density functional theory. *Thin Solid Films* **2017**, *621*, 108–130. [CrossRef]
10. Ma, T.Y.; Cao, J.L.; Jaroniec, M.; Qiao, S.Z. Interacting carbon nitride and titanium carbide nanosheets for high performance oxygen evolution. *Angew. Chem. Int. Ed.* **2016**, *55*, 1138–1142. [CrossRef]
11. She, Z.W.; Fredrickson, K.D.; Anasori, B.; Kibsgaard, J.; Strickler, A.L.; Lukatskaya, M.R.; Gogotsi, Y.; Jaramillo, T.F.; Vojvodic, A. Two-dimensional molybdenum carbide (MXene) as an efficient electrocatalyst for hydrogen evolution. *ACS Energy Lett.* **2016**, *1*, 589–594.
12. Ibrahim, Y.; Mohamed, A.; Abdelgawad, A.M.; Eid, K.; Abdullah, A.M.; Elzatahry, A. The Recent Advances in the Mechanical Properties of Self-Standing Two-Dimensional MXene-Based Nanostructures: Deep Insights into the Supercapacitor. *Nanomaterials* **2020**, *10*, 1916. [CrossRef]
13. Kim, H.; Wang, Z.; Alshareef, H.N. MXetronics: Electronic and photonic applications of MXenes. *Nano Energy* **2019**, *60*, 179–197. [CrossRef]
14. Khazaei, M.; Arai, M.; Sasaki, T.; Ranjbar, A.; Liang, Y.; Yunoki, S. OH-terminated two-dimensional transition metal carbides and nitrides as ultralow work function materials. *Phys. Rev.* **2015**, *B 92*, 075411. [CrossRef]
15. Tahini, H.A.; Tan, X.; Smith, S.C. The origin of low work functions in OH terminated MXenes. *Nanoscale* **2017**, *9*, 7016–7020. [CrossRef]
16. Liu, M.; He, Y.; Zhou, J.; Ge, Y.; Zhou, J.; Song, G. A "naked-eye" colorimetric and ratiometric fluorescence probe for uric acid based on Ti_3C_2 MXene quantum dots. *Anal. Chim. Acta* **2020**, *1103*, 134–142. [CrossRef]
17. Zhang, Q.; Wang, F.; Zhang, H.; Zhang, Y.; Liu, M.; Liu, Y. Universal Ti_3C_2 MXenes Based Self-Standard Ratiometric Fluorescence Resonance Energy Transfer Platform for Highly Sensitive Detection of Exosomes. *Anal. Chem.* **2018**, *90*, 12737–12744. [CrossRef]
18. Zhu, X.; Zhang, Y.; Liu, M.; Liu, Y. 2D titanium carbide MXenes as emerging optical biosensing platforms. *Biosens. Bioelectron.* **2021**, *171*, 112730. [CrossRef]
19. Liu, H.; Duan, C.; Yang, C.; Shen, W.; Wang, F.; Zhu, Z. A novel nitrite biosensor based on the direct electrochemistry of hemoglobin immobilized on MXene-Ti_3C_2. *Sens. Actuat. B* **2015**, *218*, 60–66. [CrossRef]
20. Lorencova, L.; Bertok, T.; Dosekova, E.; Holazova, A.; Paprckova, D.; Vikartoska, A.; Sasinkova, V.; Filip, J.; Kasak, P.; Jerigova, M.; et al. Electrochemical performance of $Ti_3C_2T_x$ MXene in aqueous media: Towards ultrasensitive H2O2 sensing. *Sens. Actuat. B* **2017**, *235*, 471–479. [CrossRef]
21. Wu, L.; Lu, X.; Dhanjai, Z.S.; Wu, Y.; Dong, X.; Wang, S.; Zheng, J.C. 2D transition metal carbide MXene as a robust biosensing platform for enzyme immobilization and ultrasensitive detection of phenol. *Biosens. Bioelectron.* **2018**, *107*, 69–75. [CrossRef]
22. Wang, F.; Yang, C.; Duan, C.; Xiao, D.; Tang, Y.; Zhu, J. An organ-like titanium carbide material (MXene) with multilayer structure encapsulating hemoglobin for a mediator-free biosensor. *J. Electrochem. Soc.* **2015**, *162*, B16–B21. [CrossRef]

23. Zheng, J.; Diao, J.; Jin, Y.; Ding, A.; Wang, B.; Wu, L.; Wong, B.; Chen, J. An inkjet printed Ti_3C_2-GO electrode for the electrochemical sensing of hydrogen peroxide. *J. Electrochem. Soc.* **2018**, *165*, B227–B231. [CrossRef]
24. Zhu, X.; Liu, B.; Hou, H.; Huang, Z.; Zeinu, K.M.; Huang, L.; Yuan, X.; Guo, D.; Hu, J.; Yang, J. Alkaline intercalation of Ti_3C_2 MXene for simultaneous electrochemical detection of Cd(II), Pb(II), Cu(II) and Hg(II). *Electrochim. Acta* **2017**, *248*, 46–57. [CrossRef]
25. Rasheed, P.A.; Pandey, R.P.; Rasool, K.; Mahmoud, K.A. Ultra-sensitive electrocatalytic detection of bromate in drinking water based on Nafion/$Ti_3C_2T_x$ (MXene) modified glassy carbon electrode. *Sens. Actuat. B* **2018**, *265*, 652–659. [CrossRef]
26. Zhou, L.; Zhang, X.; Ma, L.; Gao, J.; Jiang, Y. Acetylcholinesterase/chitosan transition metal carbides nanocomposites-based biosensor for the organophosphate pesticides detection. *Biochem. Eng. J.* **2017**, *128*, 243–249. [CrossRef]
27. Lorencova, L.; Bertok, T.; Filip, J.; Jerigova, M.; Elic, D.; Kasak, P.; Ahmoud, K.A.; Tkac, J. Highly stable $Ti_3C_2T_x$ (MXene)/Pt nanoparticles-modified glassy carbon electrode for H2O2 and small molecules sensing applications. *Sens. Actuat. B* **2018**, *263*, 360–368. [CrossRef]
28. Kalambate, P.K.; Gadhari, N.S.; Li, X.; Rao, Z.; Navale, S.T.; Shen, Y.; Patil, V.R.; Huang, Y. Recent advances in MXene–based electrochemical sensors and biosensors. *TrAC Trends Anal. Chem.* **2019**, *120*, 115643. [CrossRef]
29. Rasool, K.; Mahmoud, K.A.; Johnson, D.J.; Helal, M.; Berdiyorov, G.R.; Gogotsi, Y. Efficient Antibacterial Membrane based on Two-Dimensional $Ti_3C_2T_x$ (MXene) Nanosheets. *Sci. Rep.* **2017**, *7*, 1598. [CrossRef]
30. Lin, H.; Chen, Y.; Shi, J. Insights into 2D MXenes for Versatile Biomedical Applications: Current Advances and Challenges Ahead. *Adv. Sci.* **2018**, *5*, 1800518. [CrossRef]
31. Rakhi, R.B.; Nayak, P.; Xia, C.; Alshareef, H.N. Novel amperometric glucose biosensor based on MXene nanocomposite. *Sci. Rep.* **2016**, *6*, 36422. [CrossRef]
32. Ramanavicius, A.; Ramanaviciene, A. Hemoproteins in design of biofuel cells. *Fuel Cells* **2009**, *9*, 25–36. [CrossRef]
33. Emir, G.; Dilgin, Y.; Ramanaviciene, A.; Ramanavicius, A. Amperometric Nonenzymatic Glucose Biosensor based on Graphite Rod Electrode Modified by Ni-Nanoparticle/Polypyrrole Composite. *Microchem. J.* **2020**, in press. [CrossRef]
34. Kisieliute, A.; Popov, A.; Apetrei, R.M.; Cârâc, G.; Morkvenaite-Vilkonciene, I.; Ramanaviciene, A.; Ramanavicius, A. Towards Microbial Biofuel Cells: Improvement of Charge Transfer by Self-Modification of Microoganisms with Conducting Polymer—Polypyrrole. *Chem. Eng. J.* **2019**, *356*, 1014–1021. [CrossRef]
35. Ramanavicius, A.; Oztekin, Y.; Ramanaviciene, A. Electrochemical Formation of Polypyrrole-based Layer for Immunosensor Design. *Sens. Actuators B Chem.* **2014**, *197*, 237–243. [CrossRef]
36. Ramanaviciene, A.; Ramanavicius, A. Pulsed amperometric detection of DNA with an ssDNA/polypyrrole modified electrode. *Anal. Bioanal. Chem.* **2004**, *379*, 287–293. [CrossRef]
37. Ratautaite, V.; Plausinaitis, D.; Baleviciute, I.; Mikoliunaite, L.; Ramanaviciene, A.; Ramanavicius, A. Characterization of Caffeine-Imprinted Polypyrrole by a Quartz Crystal Microbalance and Electrochemical Impedance Spectroscopy. *Sens. Actuators B Chem.* **2015**, *212*, 63–71. [CrossRef]
38. Glenn, E.; Fryxell, G.C. *Environmental Applications of Nanomaterials: Synthesis, Sorbents and Sensors*, 2nd ed.; Imperial Collage Press: London, UK, 2012.
39. Yoon, J.; Shin, M.; Lim, J.; Lee, J.-Y.; Choi, J.W. Recent Advances in MXene Nanocomposite-Based Biosensors. *Biosensors* **2020**, *10*, 185. [CrossRef]
40. Oztekin, Y.; Ramanaviciene, A.; Yazicigil, Z.; Solak, A.O.; Ramanavicius, A. Direct electron transfer from glucose oxidase immobilized on polyphenanthroline modified-glassy carbon electrode. *Biosens. Bioelectron.* **2011**, *26*, 2541–2546. [CrossRef]
41. Kausaite-Minkstimiene, A.; Mazeiko, V.; Ramanaviciene, A.; Oztekin, Y.; Solak, A.O.; Ramanavicius, A. Evaluation of some redox mediators in the design of reagentless amperometric glucose biosensor. *Electroanalysis* **2014**, *26*, 1528–1535. [CrossRef]
42. Bagdžiūnas, G.; Ramanavičius, A. Towards Direct Enzyme Wiring: A Theoretical Investigation of Charge Carriers Transfer Mechanisms between Glucose Oxidase and Organic Semiconductors. *Phys. Chem. Chem. Phys.* **2019**, *21*, 2968–2976. [CrossRef] [PubMed]
43. Bagdžiūnas, G.; Žukauskas, Š.; Ramanavičius, A. Insights into Hole Transfer Mechanism between Glucose Oxidase and p-Type Organic Semiconductor. *Biosens. Bioelectron.* **2018**, *102*, 449–455. [CrossRef]

44. Ramanaviciene, A.; Nastajute, G.; Snitka, V.; Kausaite, A.; German, N.; Barauskas-Memenas, D.; Ramanavicius, A. Spectrophotometric evaluation of gold nanoparticles as red-ox mediator for glucose oxidase. *Sens. Actuators B Chem.* **2009**, *137*, 483–489. [CrossRef]
45. Ramanavicius, A.; Kausaite, A.; Ramanaviciene, A. Enzymatic biofuel cell based on anode and cathode powered by ethanol. *Biosens. Bioelectron.* **2008**, *24*, 761–766. [CrossRef] [PubMed]
46. Ramanavicius, A.; Kausaite, A.; Ramanaviciene, A. Biofuel cell based on direct bioelectrocatalysis. *Biosens. Bioelectron.* **2005**, *20*, 1962–1967. [CrossRef]
47. Peng, X.; Zhang, Y.; Lu, D.; Guo, Y.; Guo, S. Ultrathin Ti_3C_2 nanosheets based "off-on" fluorescent nanoprobe for rapid and sensitive detection of HPV infection. *Sens. Actuator B Chem.* **2019**, *286*, 222–229. [CrossRef]
48. Liu, M.; Zhou, J.; He, Y.; Cai, Z.; Ge, Y.; Zhou, J.; Song, G. "-Poly-L-lysine-protected Ti_3C_2 MXene quantum dots with high quantum yield for fluorometric determination of cytochrome c and trypsin. *Microchim. Acta* **2019**, *186*, 770. [CrossRef]
49. Zhu, X.H.; Pang, X.; Zhang, Y.Y.; Yao, S.Z. Titanium carbide MXenes combined with red-emitting carbon dots as a unique turn-on fluorescent nanosensor for label-free determination of glucose. *J. Mater. Chem. B* **2019**, *7*, 7729–7735. [CrossRef]
50. Shahzad, F.; Iqbal, A.; Zaidi, S.A.; Hwang, S.W.; Koo, C.M. Nafion-stabilized twodimensional transition metal carbide ($Ti_3C_2T_x$ MXene) as a high-performance electrochemical sensor for neurotransmitter. *J. Indus. Eng. Chem.* **2019**, *79*, 338–344. [CrossRef]
51. Lapenaite, I.; Ramanaviciene, A.; Ramanavicius, A. Current trends in enzymatic determination of glycerol. *Crit. Rev. Anal. Chem.* **2006**, *36*, 13–25. [CrossRef]
52. German, N.; Ramanaviciene, A.; Ramanavicius, A. Formation of Polyaniline and Polypyrrole Nanocomposites with Embedded Glucose Oxidase and Gold Nanoparticles. *Polymers* **2019**, *11*, 377. [CrossRef]
53. Kausaite-Minkstimiene, A.; Glumbokaite, L.; Ramanaviciene, A.; Dauksaite, E.; Ramanavicius, A. An amperometric glucose biosensor based on poly(pyrrole-2-carboxylic acid)/glucose oxidase biocomposite. *Electroanalysis* **2018**, *30*, 1642–1652. [CrossRef]
54. Bruzaite, I.; Rozene, J.; Morkvenaite-Vilkonciene, I.; Ramanavicius, A. Towards Microorganism-based Biofuel Cells: The Viability of Saccharomyces cerevisiae Modified by Multiwalled Carbon Nanotubes. *Nanomaterials* **2020**, *10*, 954. [CrossRef]
55. Kausaite-Minkstimiene, A.; Glumbokaite, L.; Ramanaviciene, A.; Ramanavicius, A. Reagent-less amperometric glucose biosensor based on nanobiocomposite consisting of poly(1,10-phenanthroline-5,6-dione), poly(pyrrole-2-carboxylic acid), gold nanoparticles and glucose oxidase. *Microchem. J.* **2020**, *154*, 104665. [CrossRef]
56. German, N.; Ramanavicius, A.; Voronovic, J.; Oztekin, Y.; Ramanaviciene, A. The effect of gold nanoparticle colloidal solution on performance of glucose oxidase modified carbon electrode. *Microchim. Acta* **2011**, *172*, 185–191. [CrossRef]
57. German, N.; Ramanavicius, A.; Voronovic, J.; Ramanaviciene, A. Glucose biosensor based on glucose oxidase and gold nanoparticles of different sizes covered by polypyrrole layer. *Colloids Surf. A Physicochem. Eng. Asp.* **2012**, *413*, 224–230. [CrossRef]
58. German, N.; Ramanaviciene, A.; Ramanavicius, A. Electrochemical deposition of gold nanoparticles on graphite rod for glucose biosensing. *Sens. Actuators B Chem.* **2014**, *203*, 25–34. [CrossRef]
59. German, N.; Kausaite-Minkstimiene, A.; Ramanavicius, A.; Semashko, T.; Mikhailova, R.; Ramanaviciene, A. The use of different glucose oxidases for the development of an amperometric reagentless glucose biosensor based on gold nanoparticles covered by polypyrrole. *Electrochim. Acta* **2015**, *169*, 326–333. [CrossRef]
60. Apetrei, R.M.; Carac, G.; Bahrim, G.; Ramanaviciene, A.; Ramanavicius, A. Modification of *Aspergillus niger* by Conducting Polymer—Polypyrrole, and the Evaluation of Electrochemical Properties of Modified Cells. *Bioelectrochemistry* **2018**, *121*, 46–55. [CrossRef]
61. Stirke, A.; Apetrei, R.M.; Kirsnyte, M.; Dedelaite, L.; Bondarenka, V.; Jasulaitiene, V.; Pucetaite, M.; Selskis, A.; Carac, G.; Bahrim, G.; et al. Synthesis of polypyrrole microspheres by *Streptomyces* spp. *Polymer* **2016**, *84*, 99–106. [CrossRef]
62. Andriukonis, E.; Stirke, A.; Garbaras, A.; Mikoliunaite, L.; Ramanaviciene, A.; Remeikis, V.; Thornton, B.; Ramanavicius, A. Yeast-Assisted Synthesis of Polypyrrole: Quantification and Influence on the Mechanical Properties of the Cell Wall. *Colloids Surf. B Biointerfaces* **2018**, *164*, 224–231. [CrossRef]

63. Apetrei, R.M.; Carac, G.; Ramanaviciene, A.; Bahrim, G.; Tanase, C.; Ramanavicius, A. Cell-Assisted Synthesis of Conducting Polymer—Polypyrrole—for the Improvement of Electric Charge Transfer through Fungi Cell Wall. *Colloids Surf. B Biointerfaces* **2019**, *175*, 671–679. [CrossRef]
64. Ramanavicius, A.; Andriukonis, E.; Stirke, A.; Mikoliunaite, L.; Balevicius, Z.; Ramanaviciene, A. Synthesis of Polypyrrole Within the Cell Wall of Yeast by Redox-Cycling of [Fe(CN)6]3-/[Fe(CN)6]4-. *Enzym. Microb. Technol.* **2016**, *83*, 40–47. [CrossRef] [PubMed]
65. Garbaras, A.; Mikoliunaite, L.; Popov, A.; Ramanaviciene, A.; Remeikis, V.; Ramanavicius, A. Isotope method for the determination of stoichiometry between compounds forming polypyrrole and glucose oxidase composite. *Phys. Chem. Chem. Phys.* **2015**, *17*, 2252–2258. [CrossRef]
66. Wang, X.; Lu, X.; Wu, L.; Chen, J. Direct electrochemical tyrosinase biosensor based on mesoporous carbon and Co3O4 nanorods for the rapid detection of phenolic pollutants. *ChemElectroChem* **2014**, *1*, 808–816. [CrossRef]
67. Kamysbayev, V.; Filatov, A.S.; Hu, H.; Rui, X.; Lagunas, F.; Wang, D.; Klie, R.F.; Talapin, D.V. Covalent surface modifications and superconductivity of two-dimensional metal carbide MXenes. *Science* **2020**, *369*, 979–983. [CrossRef]
68. Soomro, R.A.; Jawaid, S.; Zhu, Q.; Abbas, Z.; Xu, B. A mini-review on MXenes as versatile substrate for advanced sensors. *Chin. Chem. Lett.* **2020**, *31*, 922–930. [CrossRef]
69. Zhu, J.; Ha, W.; Zhao, G.; Huang, D.; Yue, G.; Hu, L.; Sun, N.; Wang, Y.; Lee, L.Y.S.; Xu, C.; et al. Recent advance in MXenes: A promising 2D material for catalysis, sensor and chemical adsorption. *Coord. Chem. Rev.* **2017**, *352*, 306–327. [CrossRef]
70. Yu, T.; Breslin, C.B. Review—Two-dimensional titanium carbide MXenes and their emerging applications as electrochemical sensors. *J. Electrochem. Soc.* **2020**, *167*, 037514. [CrossRef]
71. Koyappayil, A.; Chavan, S.G.; Mohammadniaei, M.; Go, A.; Hwang, S.Y.; Lee, M.-H. β-Hydroxybutyrate dehydrogenase decorated MXene nanosheets for the amperometric determination of β-hydroxybutyrate. *Microchim. Acta* **2020**, *187*, 277. [CrossRef]
72. Zheng, J.; Wang, B.; Ding, A.; Weng, B.; Chen, J. Synthesis of MXene/DNA/Pd/Pt nanocomposite for sensitive detection of dopamine. *J. Electroanal. Chem.* **2018**, *816*, 189–194. [CrossRef]
73. Sinha, A.; Dhanjai, H.; Zhao, Y.; Huang, X.; Lu, J.; Chen, R.J. MXene: An emerging material for sensing and biosensing. *Trends Anal. Chem.* **2018**, *105*, 424–435. [CrossRef]
74. Gu, H.; Xing, Y.; Xiong, P.; Tang, H.; Li, C.; Chen, S.; Zeng, R.; Han, K.; Shi, G. Three-Dimensional Porous $Ti_3C_2T_x$ MXene–Graphene Hybrid Films for Glucose Biosensing. *ACS Appl. Nano Mater.* **2019**, *2*, 6537–6545. [CrossRef]
75. Jiang, Y.; Zhang, X.; Pei, L.; Yue, S.; Ma, L.; Zhou, L.; Huang, Z.; He, Y.; Gao, J. Silver nanoparticles modified two-dimensional transition metal carbides as nanocarriers to fabricate acetycholinesterase-based electrochemical biosensor. *Chem. Eng. J.* **2018**, *339*, 547–556. [CrossRef]
76. Song, D.; Jiang, X.; Lu, X.; Luan, S.; Wang, Y.; Li, Y.; Gao, F. Metal_organic frameworks-derived MnO_2/Mn_3O_4 microcuboids with hierarchically ordered nanosheets and Ti_3C_2 MXene/Au NPs composites for electrochemical pesticide detection. *J. Hazard. Mater.* **2019**, *373*, 367–376. [CrossRef]
77. Lei, Y.; Zhao, W.; Zhang, Y., Jr.; He, H.; Baeumner, A.J.; Wolfbeis, O.S.; Wang, Z.L.; Salama, K.N.; Alshareef, H.N. A MXene-based wearable biosensor system for high-performance in vitro perspiration analysis. *Small* **2019**, *15*, 1901190. [CrossRef]
78. Liu, J.; Jiang, X.; Zhang, R.; Zhang, Y.; Wu, L.; Lu, W.; Li, J.; Li, Y.; Zhang, H. MXene enabled electrochemical microfluidic biosensor: Applications toward multicomponent continuous monitoring in whole blood. *Adv. Funct. Mater.* **2019**, *29*, 1807326. [CrossRef]
79. Li, Y.; Kang, Z.; Kong, L.; Shi, H.; Zhang, Y.; Cui, M.; Yang, D.P. MXene-Ti_3C_2/CuS nanocomposites: Enhanced peroxidase-like activity and sensitive colorimetric cholesterol detection. *Mater. Sci. Eng. C Mater. Biol. Appl.* **2019**, *104*, 110000. [CrossRef]
80. Li, H.; Wen, Y.; Zhu, X.; Wang, J.; Zhang, L.; Sun, B. Novel Heterostructure of a MXene@NiFe-LDH Nanohybrid with Superior Peroxidase-Like Activity for Sensitive Colorimetric Detection of Glutathione. *ACS Sustain. Chem. Eng.* **2019**, *8*, 520–526. [CrossRef]
81. Chen, K.; Qiu, N.; Deng, Q.; Kang, M.-H.; Yang, H.; Baek, J.-U.; Koh, Y.-H.; Du, S.; Huang, Q.; Kim, H.-E. Cytocompatibility of Ti3AlC2, Ti3SiC2, and Ti2AlN: In Vitro Tests and First-Principles Calculations. *ACS Biomater. Sci. Eng.* **2017**, *3*, 2293. [CrossRef]

82. Zong, L.; Wu, H.; Lin, H.; Chen, Y. A polyoxometalate-functionalized two-dimensional titanium carbide composite MXene for effective cancer theranostics. *Nano Res.* **2018**, *11*, 4149–4168. [CrossRef]
83. Xu, Y.X.; Hu, C.G.; Hu, S.S. A reagentless nitric oxide biosensor based on the direct electrochemistry of hemoglobin adsorbed on the gold colloids modified carbon paste electrode. *Sens. Actuat. B* **2010**, *148*, 253–258. [CrossRef]
84. Srivastava, P.; Mishra, A.; Mizuseki, H.; Lee, K.R.; Singh, A.K. Mechanistic Insight into the Chemical Exfoliation and Functionalization of Ti_3C_2 MXene. *ACS Appl. Mater. Interfaces* **2016**, *8*, 24256–24264. [CrossRef]
85. Alhabeb, M.; Maleski, K.; Anasori, B.; Lelyukh, P.; Clark, L.; Sin, S.; Gogotsi, Y. Guidelines for synthesis and processing of two-dimensional titanium carbide (Ti_3C_2T _ MXene). *Chem. Mater.* **2017**, *29*, 7633–7644. [CrossRef]
86. Sadiq, M.; Pang, L.; Johnson, M.; Sathish, V.; Wang, D. 2D Nanomaterial, Ti_3C_2 MXene-Based Sensor to Guide Lung Cancer Therapy and Management. *Proceedings* **2020**, *60*, 29. [CrossRef]
87. Ramanavicius, S.; Tereshchenko, A.; Karpicz, R.; Ratautaite, V.; Bubniene, U.; Maneikis, A.; Jagminas, A.; Ramanavicius, A. $TiO_{2\text{-}x}/TiO_2$-structure based 'self-heated' sensor for the determination of some reducing gases. *Sensors* **2020**, *20*, 74. [CrossRef]
88. Zhu, Q.; Peng, Y.; Lin, L.; Fan, C.M.; Gao, G.Q.; Wang, R.X.; Xu, A.W. Stable blue $TiO_{2\text{-}x}$ nanoparticles for efficient visible light photocatalysts. *J. Mater. Chem.* **2014**, *A2*, 4429–4437. [CrossRef]
89. Andersson, S.; Magneli, A. Diskrete Titanoxydphasen im Zusammensetzungsbereich $TiO_{1,75}$-$TiO_{1,90}$. *Naturwissenschaften* **1956**, *43*, 495–496. [CrossRef]
90. Liborio, L.; Mallia, G.; Harrison, N. Electronic structure of the Ti_4O_7 Magnéli phase. *Phys. Rev. B* **2009**, *79*, 245133. [CrossRef]
91. Seebauer, E.G.; Kratzer, M.C. Charged point defects in semiconductors. *Mater. Sci. Eng. R Rep.* **2006**, *55*, 57. [CrossRef]
92. Harada, S.; Tanaka, K.; Inui, H. Thermoelectric properties and crystallographic shear structures in titanium oxides of the Magnéli phases. *J. Appl. Phys.* **2010**, *108*, 083703. [CrossRef]
93. Smith, J.R.; Walsh, F.C.; Clarke, R.L. Electrodes based on Magnéli phase titanium oxides: The properties and applications of Ebonex® materials. *J. Appl. Electrochem.* **1998**, *28*, 1021. [CrossRef]
94. Walsh, F.C.; Wills, R.G.A. The continuing development of Magnéli phase titanium sub-oxides and Ebonex® electrodes. *Electrochim. Acta* **2010**, *55*, 6342. [CrossRef]
95. Wu, D.; Wang, S.; Zhang, S.; Yuan, J.; Yang, B.; Chen, H. Highly negative Poisson's ratio in a flexible two-dimensional tungsten carbide monolayer. *Phys. Chem. Chem. Phys.* **2018**, *20*, 18924–18930. [CrossRef]
96. Petruleviciene, M.; Juodkazyte, J.; Parvin, M.; Tereshchenko, A.; Ramanavicius, S.; Karpicz, R.; Samukaite-Bubniene, U.; Ramanavicius, A. Tuning of photo-luminescence properties of WO3-based layers by the adjustment of layer formation conditions. *Materials* **2020**, *13*, 2814. [CrossRef]
97. Ramanavičius, S.; Petrulevičienė, M.; Juodkazytė, J.; Grigucevičienė, A.; Ramanavičius, A. Selectivity of tungsten oxide synthesized by sol-gel method towards some volatile organic compounds and gaseous materials in a broad range of temperatures. *Materials* **2020**, *13*, 523. [CrossRef]
98. Chen, X.; Sun, X.; Xu, W.; Pan, G.; Zhou, D.; Zhu, J.; Wang, H.; Bai, X.; Dong, B.; Song, H. Ratiometric photoluminescence sensing based on Ti_3C_2 MXene quantum dots as an intracellular pH sensor. *Nanoscale* **2018**, *10*, 1111–1118. [CrossRef]
99. Ramanaviciene, A.; Ramanavicius, A. Molecularly imprinted polypyrrole-based synthetic receptor for direct detection of bovine leukemia virus glycoproteins. *Biosens. Bioelectron.* **2004**, *20*, 1076–1082. [CrossRef]
100. Ratautaite, V.; Topkaya, S.N.; Mikoliunaite, L.; Ozsoz, M.; Oztekin, Y.; Ramanaviciene, A.; Ramanavicius, A. Molecularly Imprinted Polypyrrole for DNA Determination. *Electroanalysis* **2013**, *25*, 1169–1177. [CrossRef]
101. Ramanaviciene, A.; Finkelsteinas, A.; Ramanavicius, A. Basic electrochemistry meets nanotechnology: Electrochemical preparation of artificial receptors based on a nanostructured conducting polymer, polypyrrole. *J. Chem. Educ.* **2006**, *83*, 1212–1214. [CrossRef]
102. Ratautaite, V.; Janssens, S.D.; Haenen, K.; Nesládek, M.; Ramanaviciene, A.; Baleviciute, I.; Ramanavicius, A. Molecularly Imprinted Polypyrrole Based Impedimentric Sensor for Theophylline Determination. *Electrochim. Acta* **2014**, *130*, 361–367. [CrossRef]
103. Ma, X.; Tu, X.L.; Gao, F.; Xie, Y.; Huang, X.G.; Fernandez, C.; Qu, F.L.; Liu, G.B.; Lu, L.M.; Yu, Y.F. Hierarchical porous MXene/amino carbon nanotubes-based molecular imprinting sensor for highly sensitive and selective sensing of fisetin. *Sens. Actuators B* **2020**, *309*, 127815. [CrossRef]

104. Kumar, S.; Lei, Y.; Alshareef, N.H.; Quevedo-Lopez, M.A.; Salama, K.N. Biofunctionalized two-dimensional Ti_3C_2 MXenes for ultrasensitive detection of cancer biomarker. *Biosens. Bioelectron.* **2018**, *121*, 243–249. [CrossRef]
105. Kulpa, J.; Wojcik, E.; Reinfuss, M.; Kotodiziejski, L. Carcinoembryonic antigen, squamous cell carcinoma antigen, CYFRA 21–1, and neuron-specific enolase in squamous cell lung cancer patients. *Clin. Chem.* **2002**, *48*, 1931–1937. [CrossRef]
106. Wang, S.; Wei, S.; Wang, S.; Zhu, X.; Lei, C.; Huang, Y.; Nie, Z.; Yao, S. Chimeric DNA-functionalized titanium carbide MXenes for simultaneous mapping of dual cancer biomarkers in living cells. *Anal. Chem.* **2019**, *91*, 1651–1658. [CrossRef]
107. Fang, Y.; Yang, X.; Chen, T.; Xu, G.; Liu, M.; Liu, J.; Xu, Y. Two-dimensional titanium carbide (MXene)-based solid-state electrochemiluminescent sensor for labelfree single-nucleotide mismatch discrimination in human urine. *Sens. Actuators* **2018**, *B263*, 400–407. [CrossRef]
108. Liu, L.; Wei, Y.; Jiao, S.; Zhu, S.; Liu, X. A novel label-free strategy for the ultrasensitive miRNA-182 detection based on MoS2/Ti_3C_2 nanohybrids. *Biosens. Bioelectron.* **2019**, *137*, 45–51. [CrossRef]
109. Yang, X.; Feng, M.; Xia, J.; Zhang, F.; Wang, Z. An electrochemical biosensor based on AuNPs/Ti_3C_2 MXene three-dimensional nanocomposite for microRNA-155 detection by exonuclease III-aided cascade target recycling. *J. Electroanal. Chem.* **2020**, *878*, 114669. [CrossRef]
110. Mohammadniaei, M.; Koyappayil, A.; Sun, Y.; Min, J.; Lee, M.H. Gold nanoparticle/MXene for multiple and sensitive detection of oncomiRs based on synergetic signal amplification. *Biosens. Bioelectron.* **2020**, *159*, 112208. [CrossRef]
111. Kheyrabadi, L.K.; Koyappayil, A.; Kim, T.; Cheon, Y.-P.; Lee, M.-H. A MoS2@$Ti_3C_2T_x$ MXene hybrid-based electrochemical aptasensor (MEA) for sensitive and rapid detection of Thyroxine. *Bioelectrochemistry* **2021**, *137*, 107674. [CrossRef]
112. Zhang, H.; Wang, Z.; Zhang, Q.; Wang, F.; Liu, Y. Ti_3C_2 MXenes nanosheets catalyzed highly efficient electrogenerated chemiluminescence biosensor for the detection of exosomes. *Biosens. Bioelectron.* **2019**, *124–125*, 184–190. [CrossRef]
113. Wang, H.; Li, H.; Huang, Y.; Xiong, M.; Wang, F.; Li, C. A label-free electrochemical biosensor for highly sensitive detection of gliotoxin based on DNA nanostructure/MXene nanocomplexes. *Biosens. Bioelectron.* **2019**, *142*, 111531. [CrossRef]
114. Chen, L.; Shi, X.; Yu, N.; Zhang, X.; Du, X.; Lin, J. Measurement and Analysis of Thermal Conductivity of $Ti_3C_2T_x$ MXene Films. *Materials* **2018**, *11*, 1701. [CrossRef]
115. Li, M.H.; Fang, L.; Zhou, H.; Wu, F.; Lu, Y.; Luo, H.J.; Zhang, Y.X.; Hu, B.S. Three-dimensional porous MXene/NiCo-LDH composite for high performance non-enzymatic glucose sensor. *Appl. Surf. Sci.* **2019**, *495*, 143554. [CrossRef]
116. Dang, Y.; Guan, X.; Zhou, Y.; Hao, C.; Zhang, Y.; Chen, S.; Ma, Y.; Bai, Y.; Gong, Y.; Gao, Y. Biocompatible PB/Ti_3C_2 hybrid nanocomposites for the non-enzymatic electrochemical detection of H_2O_2 released from living cells. *Sens. Actuators B* **2020**, *319*, 128259. [CrossRef]
117. Shankar, S.S.; Shereema, R.M.; Rakhi, R.B. Electrochemical determination of adrenaline using MXene/graphite composite paste electrodes. *ACS Appl. Mater. Interfaces* **2018**, *10*, 43343–43351. [CrossRef]
118. Zhang, Y.; Jiang, X.; Zhang, J.; Zhang, H.; Li, Y. Simultaneous voltammetric determination of acetaminophen and isoniazid using MXene modified screen-printed electrode. *Biosens. Bioelectron.* **2019**, *130*, 315–321. [CrossRef]
119. Yu, X.; Li, Y.; Cheng, J.; Liu, Z.; Li, Q.; Li, W.; Yang, X.; Xiao, B. Monolayer Ti_2CO_2: A promising candidate for NH_3 sensor or capturer with high sensitivity and selectivity. *ACS Appl. Mater. Interfaces* **2015**, *7*, 13707–13713. [CrossRef]
120. Xiao, B.; Li, Y.; Yu, X.; Cheng, J. MXenes: Reusable materials for NH3 sensor or capturer by controlling the charge injection. *Sens. Actuators B* **2016**, *235*, 103–109. [CrossRef]
121. Zhao, M.Q.; Ren, C.E.; Ling, Z.; Lukatskaya, M.R.; Zhang, C.; Aken, K.L.V.; Barsoum, M.W.; Gogotsi, Y. Flexible MXene/carbon nanotube composite paper with high volumetric capacitance. *Adv. Mater.* **2015**, *27*, 339–345. [CrossRef]
122. Mashtalir, O.; Naguib, M.; Mochalin, V.N.; Dall'Agnese, Y.; Heon, M.; Barsoum, M.W.; Gogotsi, Y. Intercalation and delamination of layered carbides and carbonitrides. *Nat. Commun.* **2013**, *4*, 1716. [CrossRef]
123. Lukatskaya, M.R.; Mashtalir, O.; Ren, C.E.; Dall'Agnese, Y.; Rozier, P.; Taberna, P.L.; Naguib, M.; Simon, P.; Barsoum, M.W.; Gogotsi, Y. Cation intercalation and high volumetric capacitance of two-dimensional titanium carbide. *Science* **2013**, *341*, 1502–1505. [CrossRef]

124. Choudhary, N.K.; Jin, H.; Kim, B.; Baek, D.S.; Joo, S.H.; Lee, K. MXene: An emerging two-dimensional material for future energy conversion and storage applications. *J. Mater. Chem. A* **2017**, *5*, 24564–24579. [CrossRef]
125. Ren, C.E.; Zhao, M.-Q.; Makaryan, T.; Halim, J.; Boota, M.; Kota, S.; Anasori, B.; Barsoum, M.W.; Gogotsi, Y. Porous Two-Dimensional Transition Metal Carbide (MXene) Flakes for High-Performance Li-Ion Storage. *ChemElectroChem* **2016**, *3*, 689–693. [CrossRef]
126. Baniukevic, J.; Boyaci, I.H.; Bozkurt, A.G.; Tamer, U.; Ramanavicius, A.; Ramanaviciene, A. Magnetic gold nanoparticles in SERS-based sandwich immunoassay for antigen detection by well oriented antibodies. *Biosens. Bioelectron.* **2013**, *43*, 281–288. [CrossRef]
127. Makaraviciute, A.; Ramanaviciene, A. Site-directed antibody immobilization techniques for immunosensors. (A Review). *Biosens. Bioelectron.* **2013**, *50*, 460–471. [CrossRef]
128. Morkvenaite-Vilkonciene, I.; Ramanaviciene, A.; Kisieliute, A.; Bucinskas, V.; Ramanavicius, A. Scanning electrochemical microscopy in the development of enzymatic sensors and Immunosensors. *Biosens. Bioelectron.* **2019**, *141*, 111411. [CrossRef]
129. Plikusiene, I.; Balevicius, Z.; Ramanaviciene, A.; Talbot, J.; Mickiene, G.; Balevicius, S.; Stirke, A.; Tereshchenko, A.; Tamosaitis, L.; Zvirblis, G.; et al. Evaluation of affinity sensor response kinetics towards dimeric ligands linked with spacers of different rigidity: Immobilized recombinant granulocyte colony-stimulating factor based synthetic receptor binding with genetically engineered dimeric analyte derivatives. *Biosens. Bioelectron.* **2020**, *156*, 112112.
130. Wang, X.; Garnero, C.; Rochard, G.; Magne, D.; Morisset, S.; Hurand, S.; Chartier, P.; Rousseau, J.; Cabioc'H, T.; Coutanceau, C. A new etching environment (FeF3/HCl) for the synthesis of two-dimensional titanium carbide MXenes: A route towards selective reactivity vs. water. *J. Mater. Chem. A* **2017**, *5*, 22012–22023. [CrossRef]
131. Wang, H.; Naguib, M.; Page, K.; Wesolowski, D.J.; Gogotsi, Y. Resolving the Structure of $Ti_3C_2T_x$ MXenes through Multilevel Structural Modeling of the Atomic Pair Distribution Function. *Chem. Mater.* **2015**, *28*, 349–359. [CrossRef]
132. Hope, M.A.; Forse, A.C.; Griffith, K.J.; Lukatskaya, M.R.; Ghidiu, M.; Gogotsi, Y.; Grey, C.P. NMR reveals the surface functionalisation of Ti_3C_2 MXene. *Phys. Chem. Chem. Phys.* **2016**, *18*, 5099–5102. [CrossRef]
133. Zhang, Y.; Zhang, N.; Ge, C. Review First-Principles Studies of Adsorptive Remediation of Water and Air Pollutants Using Two-Dimensional MXene Materials. *Materials* **2018**, *11*, 2281. [CrossRef]
134. Zheng, J.; Wang, B.; Jin, Y.; Weng, B.; Chen, J. Nanostructured MXene-based biomimetic enzymes for amperometric detection of superoxide anions from HepG2 cells. *Microchim. Acta* **2019**, *186*, 95. [CrossRef] [PubMed]
135. Chen, J.L.; Tong, P.; Huang, L.T.; Yu, Z.H.; Tang, D.P. Ti_3C_2 MXene nanosheet-based capacitance immunoassay with tyramine-enzyme repeats to detect prostate-specific antigen on interdigitated micro-comb electrode. *Electrochim. Acta* **2019**, *319*, 375–381. [CrossRef]

UŽRAŠAMS

UŽRAŠAMS

UŽRAŠAMS

Vilnius University Press
9 Saulėtekio Ave., Building III, LT-10222 Vilnius
Email: info@leidykla.vu.lt, www.leidykla.vu.lt
Print run copies 25